ALMA MATER STUDIORUM
UNIVERSITÀ DI BOLOGNA

DOTTORATO DI RICERCA IN FISICA

CICLO XXXVII

Settore Concorsuale: 02/A1 - FISICA SPERIMENTALE DELLE INTERAZIONI FONDAMENTALI
Settore Scientifico Disciplinare: FIS/01 - FISICA SPERIMENTALE

Measurement of the WbWb cross-section in the dilepton channel using classical and quantum computing techniques with the ATLAS detector at the LHC

CANDIDATO:
Gianluca Bianco

SUPERVISORE:
Chiar.mo Prof. Maximiliano Sioli

COORDINATORE DOTTORATO:
Chiar.mo Prof. Alessandro Gabrielli

CO-SUPERVISORI:
Dott. Marino Romano
Dott.ssa Alessia Bruni

Esame Finale - Anno 2025

"Qualunque cosa tu possa fare, qualunque sogno tu possa sognare, comincia. L'audacia reca in sé genialità, magia e forza."

Johann Wolfgang von Goethe

Alla mia anima gemella, Federica. Ai miei genitori, Daniela e Marco. A mio fratello, Edoardo.

Abstract

The top quark is the heaviest known elementary particle of the Standard Model. Thanks to its particular properties, it allows to explore unique physics domains, inaccessible otherwise: one of them is the $WbWb$ production from proton-proton collisions. Studying this process is very important for a better knowledge of the Standard Model, but also to investigate some Beyond the Standard Model phenomena.

In this work, the first ever measurement of the fiducial differential cross-sections of the $WbWb$ production in the dilepton channel is provided. The measurement is performed using the full dataset collected by the ATLAS detector from proton-proton collisions at the LHC during Run-2 at $\sqrt{s} = 13\,\text{TeV}$ corresponding to an integrated luminosity of $140\,\text{fb}^{-1}$. The differential cross-sections have been measured as a function of kinematic variables characterizing the $WbWb$ final states and one $t\bar{t}/tW$ interference-sensitive variable, defined as m_{bl}^{minimax}. The results are then compared to several Monte Carlo predictions.

We have also developed a novel unfolding method based on quantum annealing, along with a dedicated software tool, called `QUnfold`. Our implementation is the first LHC-size data analysis software capable of using quantum computation to solve the unfolding problem and therefore to measure differential cross-sections of particle physics processes. We successfully tested it on the $WbWb$ ATLAS data used for the main analysis of this work.

Contents

Introduction

The Standard Model (SM) of particle physics is, at the moment, the most complete theory to describe matter particles and their interactions. In the Standard Model, the heaviest elementary particle known so far is the top quark.

The study of the top quark properties is a fundamental particle physics topic nowadays; it is useful not only for a better understanding of the SM, but also to explore proposed Beyond the Standard Model (BSM) processes. The top quark represents one of the fundamental building blocks of our universe and is significantly different with respect to the other particles. Due to its large mass, it may undergo some kind of processes that can't be seen with the other lighter particles.

The top quark decays into a Wb pair with a branching ratio close to 100%. An interesting process to study is the $WbWb$ production which takes into account also the quantum interference between singly (tW) and doubly ($t\bar{t}$) resonant top quark productions. This production process can be studied in proton-proton collisions at the LHC.

The experimental measurement of this interference term is a fundamental test for the SM, but it also aims at improving particular BSM searches, where background regions are enriched in events in the interference region. For example, these regions need to be deeply understood in order to discriminate signal from background in several SUSY searches. This study can also help to solve a similar problem in $t\bar{t}H$ vs. tWH or $t\bar{t}\gamma$ vs $tW\gamma$ processes.

At present, the LHC is the largest and most powerful particle accelerator in the world. It hosts four main experiments and one of them is ATLAS. I contributed to the ATLAS RPC detector improvements and in particular I developed a software which helps the monitoring of the RPC detector performances and operations. This work is also useful to improve selection quality of muon events of the W decay in the Wb pair of the top decay.

Here we present the first ever complete measurement of the $WbWb$ cross-sections in the dilepton channel at the particle level. This measurement has been performed on the full data collected by ATLAS from proton-proton collisions at the LHC, during the Run-2 at $\sqrt{s} = 13\,\text{TeV}$, corresponding to an integrated luminosity of $140\,\text{fb}^{-1}$. The differential cross-sections have been measured as a function of several kinematic variables and one interference-sensitive variable, named m_{bl}^{minimax}, by using an iterative Bayesian unfolding

procedure and comparing the results to several Monte Carlo predictions.

We have also developed a novel unfolding method based on quantum annealing, along with a dedicated software tool, called `QUnfold`. In recent years, quantum computing has emerged as one of the most promising and intriguing fields at the intersection of physics and technology. Among the various quantum computing paradigms explored, quantum annealing stands out as a particularly significant approach. Our implementation is a revision and an improvement of a technique described in a previously published paper and is the first LHC-size data software capable of using quantum annealing to solve the unfolding problem. We decided to test it on simulated data as a first step, and then on the real $WbWb$ ATLAS data used for the main analysis of this work, in order to perform a full feasibility study.

This work is structured as follows:

- **Chapters 1 and 2**: here the physical foundations of the measurement are explained. Firstly, the SM of microcosm is introduced, then the top quark particle is presented and finally the $WbWb$ production and in particular the quantum interference between $t\bar{t}$ and tW is described from a theoretical point of view.

- **Chapters 3 and 4**: here the LHC collider and the ATLAS detector are introduced. Firstly, a basic introduction to LHC is provided and then a more detailed explanation of the ATLAS experiment and its components is highlighted. In **Appendix A** the work related to my contribution to the RPC detectors is shown.

- **Chapter 5**: in this chapter the reconstruction procedure of the fundamental particles detected by ATLAS is shown. The interested reconstructed objects are: electrons, muons, b-jets and missing transverse energy. An extra section about the overlap removal procedure is reported in the last part of the chapter.

- **Chapters 6, 7 and 8**: here all the fundamental steps of the analysis are pointed out. Firstly, data and Monte Carlo (MC) samples are presented. Secondly, the event-selection and the discriminating variables used for the unfolding are shown. Then, the unfolding procedure and the final results are reported. Finally, in the last part, all the work related to `QUnfold` and its results is present. Complements to this chapter are located in **Appendices B and C**.

- **Conclusions**: here discussions, conclusions and future outlooks of the work are discussed.

Chapter 1

The top quark

Particle physics is one of the main pillars of our understanding of the laws on Nature. It describes the fundamental constituents of our Universe, which are the **particles** and how they interact with each other through **forces**. The **Standard Model**, described in Section 1.1, is considered for the moment as the most powerful theory used to describe the particles and their interactions. Despite some missing pieces in the description of the Nature, it seems to be able to provide a successful picture of the current experimental data.

One of the elementary particles behaves in a different manner with respect to the others: the **top quark**, described in Section 1.2. Due to its peculiar properties (described in Section 1.2.2) it is able to participate in many interesting processes, inaccessible for the lighter particles [1].

One of the most interesting processes involving top quarks is the $WbWb$ production in proton-proton (pp) collisions. This process is the main subject of this work and will

be described from the theoretical point of view in Chapter 2.

1.1 The Standard Model of particle physics

As mentioned in the Introduction, the SM is one of the most suitable theories used to describe the nature and the behavior matter. It is currently the best and most experimentally confirmed choice to describe the microcosm.

The theory is based on three gauge groups:

$$\mathrm{SU(3)_C} \otimes \mathrm{SU(2)_L} \otimes \mathrm{U(1)_Y} \tag{1.1}$$

where the first one is associated to the strong interaction while the second and third to electroweak one.

1.1.1 Particles and forces classification

Fundamental "matter" particles of the SM are called **fermions** and have semi-integer spin. They are:

$$\left.\begin{array}{l} 6\ \textbf{Leptons}\ \text{with Spin} = \dfrac{1}{2} \\ 6\ \textbf{Quarks}\ \ \text{with Spin} = \dfrac{1}{2} \end{array}\right\} \text{with also the corresponding anti-particles.}$$

Fermions are divided into three families, each of them composed by two leptons:

$$\begin{pmatrix} e \\ \nu_e \end{pmatrix}, \begin{pmatrix} \mu \\ \nu_\mu \end{pmatrix}, \begin{pmatrix} \tau \\ \nu_\tau \end{pmatrix} \tag{1.2}$$

and two quarks:

$$\begin{pmatrix} u \\ d \end{pmatrix}, \begin{pmatrix} c \\ s \end{pmatrix}, \begin{pmatrix} t \\ b \end{pmatrix} \tag{1.3}$$

Each of the six types of quarks is available in three distinct color charges, conventionally named: *red*, *blue* and *green*. Anti-fermions have opposite-sign quantum numbers with respect to their fermions counterpart [2]. The total number of fundamental matter constituents is therefore 24 fermions and 24 anti-fermions[1].

Particles are subject to interactions, that explain the way in which matter is bound together. To allow for an action at distance that does not violate the relativity principles, it is necessary for each force to be exchanged through a mediator, which should be a particle with integer spin, namely a **boson**: this is required by the **Quantum Field**

[1] Ordinary matter is composed mainly by e, u and d.

Theory (*QFT*). The four known fundamental interactions are: **gravitational interaction**, which does not enter the SM, **electromagnetic interaction** (*QED*), **weak interaction** (*QFD*) [3, 4, 5] and **strong interaction** (*QCD*) [6, 7]. In Table 1.1 properties of each interaction mediator are shown.

Interaction	**Mediator**	**Symbol**	**Spin** ($\hbar$)	**Mass** ($\mathrm{GeV/c^2}$)
Gravitational	Graviton (1)	G	2	0
Electromagnetic	Photon (1)	γ	1	0
Strong	Gluons (8)	g	1	0
Weak	W and Z (3)	W^+, W^-, Z	1	≈ 100

Table 1.1: Representation of the 4 fundamental forces mediators and their properties. The graviton is an hypothetical particle which should participate as a mediator into the gravitational force.

Another fundamental boson of the theory is the **Higgs boson** H which is a scalar boson and, through the **Brout-Englert-Higgs mechanism** (*BEH*) [8], gives masses to the other fundamental particles.

Finally, the total number of fundamental fermions and bosons in the theory is [9]:

$$48 \text{ (fermions)} + 12 \text{ (bosons)} + 1 \text{ (Higgs)} = 61 \tag{1.4}$$

In Figure 1.1 the SM fundamental particles with some of their basic properties are shown.

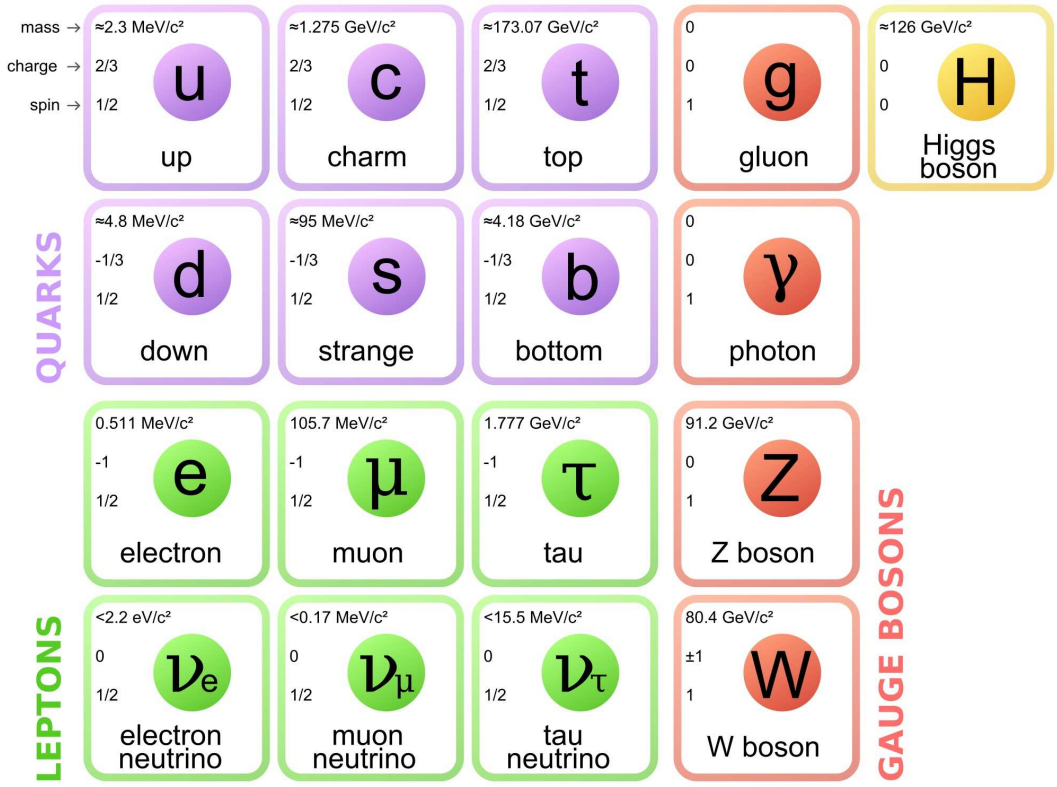

Figure 1.1: Fundamental particles of the SM with some of their basic properties.

1.1.2 Quantum Electrodynamics

The **electromagnetic** (*EM*) interaction is classically defined as the interaction between two electrically charged bodies that exchange a massless boson, called *photon*, as described by the Maxwell equations. At a fundamental level, a quantum field theory is required to describe this force, with QED being the most suitable theory developed to date [10]. It is described by the $U(1)_{EM}$ gauge group. The interaction between two charged fermions is treated as the emission of a photon by one of them, followed by the absorption by the other. See Figure 1.2 for an example of a possible EM interaction [11] represented through a Feynman diagram[2]. Since QED is an abelian gauge

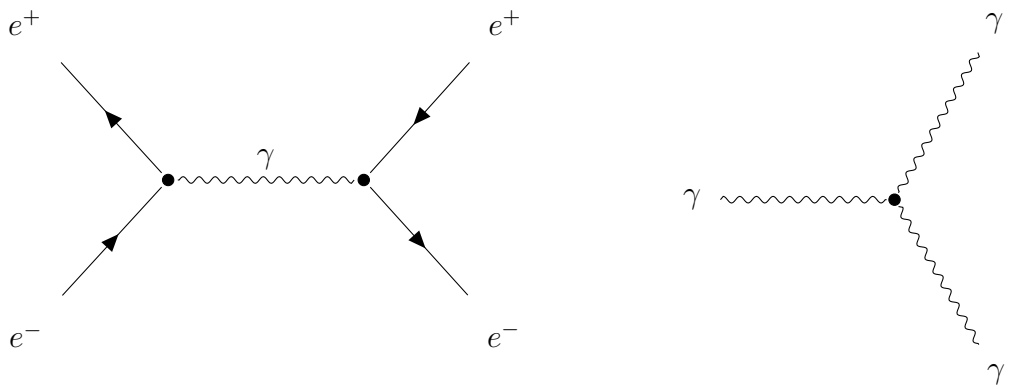

Figure 1.2: (a): example of an EM interaction between an electron and a positron through the exchange of a photon (Bhabha scattering) and (b): Triple vertex diagram with photons (not allowed in QED).

theory, it is not possible to have vertices in absence of fermionic sources, i.e. with bosons self-interactions, as shown in Figure 1.2.

The two manifestations of the EM interaction are the forces related to the **electric** and **magnetic fields**, defined in this way:

$$\vec{E} = -\vec{\nabla}\phi - \frac{\partial \vec{A}}{\partial t} \tag{1.5}$$

$$\vec{B} = \vec{\nabla} \times \vec{A} \tag{1.6}$$

where ϕ is the scalar potential, $\vec{A}$ is the vector potential and $\vec{\nabla}$ is the *nabla* operator. In general, the electromagnetic four-potential is defined as:

$$A^\mu = (\phi, \vec{A}). \tag{1.7}$$

[2]A Feynman diagram is a graphical representation used in particle physics to depict interactions between subatomic particles. Each line or vertex in the diagram corresponds to particles and their interactions, simplifying calculations in quantum field theory.

Each interaction is now represented by a **density lagrangian**, that in this case is:

$$\mathcal{L}_{EM} = -\frac{1}{4}F_{\mu\nu}F^{\mu\nu} - J_\mu A^\mu + \frac{1}{2}m^2 A^\mu A_\mu \tag{1.8}$$

where $F_{\mu\nu}$ is the EM tensor and J_μ is the current-density. The first term of the Eq. 1.8 is called *kinetic term*, the second one is called *interaction term* ($\mathcal{L}_{int}$). If the field was massive, with mass m, the third term would have represented the *mass term*.

The total QED lagrangian is obtained requiring its invariance under local gauge transformations. In fact, free fermions are described by the *Dirac lagrangian*:

$$\mathcal{L}_{free} = \bar{\psi}(x)(i\gamma^\mu\partial_\mu - m)\psi(x) \tag{1.9}$$

where ψ is a 4-component *Dirac spinor*, γ^μ are the *Dirac matrices* and $\bar{\psi} = \psi^\dagger(x)\gamma^0$. If now the covariant derivative is introduced:

$$\mathcal{D}_\mu = \partial_\mu + iqA_\mu(x) \tag{1.10}$$

Eq. 1.9 results invariant under local gauge transformations, and the new lagrangian becomes:

$$\mathcal{L} = \mathcal{L}_{free} - qA_\mu\bar{\psi}\gamma^\mu\psi \tag{1.11}$$

with $J^\mu = \bar{\psi}\gamma^\mu\psi$. This is invariant under local gauge transformations:

$$\psi(x) \to e^{iq\alpha(x)}\psi(x) \tag{1.12}$$

$$A_\mu(x) \to A_\mu(x) - \partial_\mu\alpha(x) \tag{1.13}$$

where $\alpha(x)$ is a generic function, parameter of the transformation. To obtain the final QED lagrangian it is necessary to also include the kinetic term of the Eq. 1.8 which describes the propagation of the photon associated to the field:

$$\mathcal{L}_{QED} = \mathcal{L}_{free} - qA_\mu\bar{\psi}\gamma^\mu\psi - \frac{1}{4}F_{\mu\nu}F^{\mu\nu} \tag{1.14}$$

where the mass term for the photon of the Eq. 1.8 has been omitted since it would violate the local gauge invariance and the lagrangian correctly describes a non-massive photon [12].

From the vertex of an EM interaction it is possible to extract an adimensional coupling, called **fine structure constant** which value is:

$$\alpha_{EM} \simeq \frac{1}{137.1} \tag{1.15}$$

even if it is not properly a constant, because it is a running coupling and varies with the energy scale [13].

1.1.3 Quantum Flavordynamics

The **Quantum Flavordynamics** (*QFD*) [14], or simply **weak interaction**, is different with respect to QED. The interaction is mediated by three charged bosons: $W^{\pm}$ for charged current interaction (CC), and Z for neutral current interaction (NC).

A very particular property of this kind of force is its relation with the **parity** quantum number P. Parity is represented as the γ^0 Dirac matrix operator:

$$\hat{P} = \gamma^0 = \begin{bmatrix} 1 & 0 & 0 & 0 \\ 0 & 1 & 0 & 0 \\ 0 & 0 & -1 & 0 \\ 0 & 0 & 0 & -1 \end{bmatrix} \tag{1.16}$$

Parity violation was discovered by Madame Wu in 1957, studying the nuclear β-decay of ^{60}Co [15]. From this observation, the weak interaction vertex required to have a different form with respect to the other interactions such as QED or QCD. The requirement of Lorentz invariance of the matrix element severely restricts the possible forms of the interaction. It was later demonstrated that the most general form for the interaction came only from the linear combination of 2 *bilinear covariants* giving rise to the **Axial-Vector (V-A)** current [16].

The most representative Hamiltonian of the QFD is the one associated with the β-decay of the neutron:

$$H_{V-A} = \frac{G_F}{\sqrt{2}}[\bar{\psi}_p \gamma^\mu (1-\gamma^5)\psi_n][\bar{\psi}_e \gamma^\mu (1-\gamma^5)\psi_\nu] \tag{1.17}$$

where γ^μ is the vector operator and $\gamma^\mu\gamma^5$ is the axial-vector one. See Figure 1.3 for a graphical representation of the Feynman diagram of the neutron β-decay. G_F is the *Fermi constant*, embedding the "strength" of the weak interaction:

$$\frac{G_F}{\sqrt{2}} = \frac{g_W^2}{8m_W^2} \tag{1.18}$$

This interaction is called "weak" because of the large mass ($m_W \simeq 80\,\text{GeV}$) at the denominator of the Eq. 1.18. The g_W represents the coupling constant and is useful to determine the fine structure constant of the QFD:

$$\alpha_W = \frac{g_W^2}{4\pi} \approx \frac{1}{30} > \alpha_{EM} \tag{1.19}$$

and also in this case the constant varies with the energy.

Each vertex is expressed as:

$$-\frac{ig_W}{\sqrt{2}}\frac{1}{2}\gamma^\mu(1-\gamma^5) \tag{1.20}$$

Since QFD is a non-Abelian gauge theory, vertices like the ones shown in Figure 1.4 are allowed.

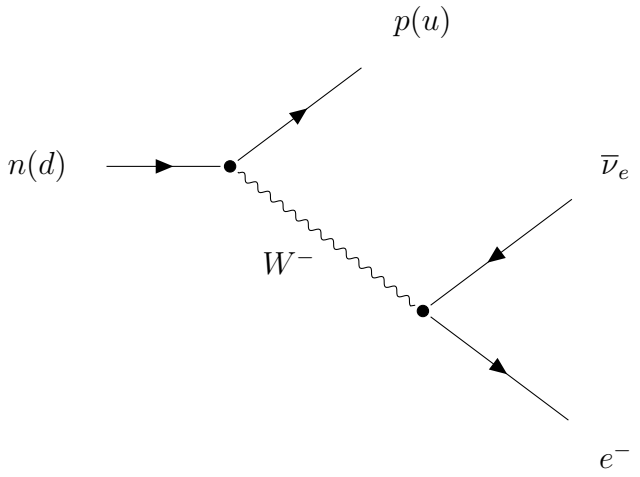

Figure 1.3: Feynman representation of the β-decay of the neutron: $n \to p + e^- + \bar{\nu}_e$.

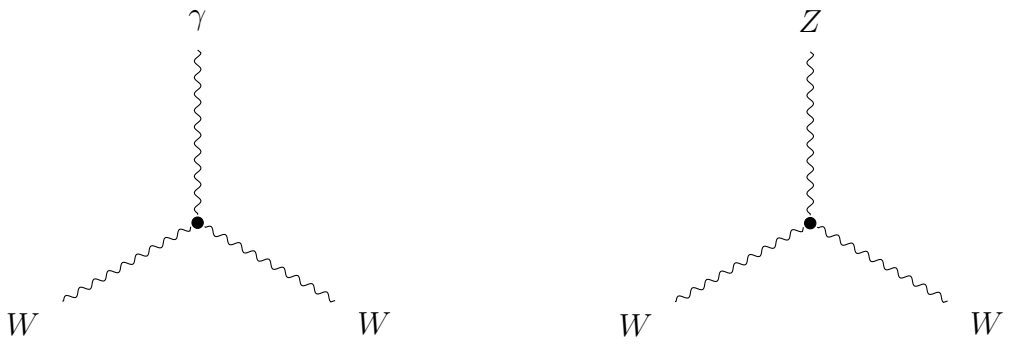

(a) γWW vertex. (b) ZWW vertex.

Figure 1.4: Allowed vertices in QFD theory.

1.1.4 Quantum Chromodynamics

The **Quantum Chromodynamics** (QCD), also called **strong interaction**, is the last of the three fundamental interactions mentioned in the introduction. It involves only quarks and is related to the $SU(3)_C$ gauge group, where the label C stands for *color*. The energy scale[3] of this force varies with the energy and the number of considered quark flavors, but usually the value 250 MeV is used to represent the necessary energy to confine two quarks in a pion [17].

The property that distinguishes quarks from leptons is the **color** quantum number, so it is natural to construct a theory of the strong interactions among quarks based upon a local color gauge symmetry.

Interactions among quarks are mediated by **gluons**, that are massless vector bosons and are 8 in total.

The six quarks presented in Section 1.1.1 (see Figure 1.1) are color triplets.

To construct a theory (and a lagrangian) of the strong interaction we have to start from the description of a free quark lagrangian. It can be described by the Eq. 1.9. The Dirac spinor is composed by three different components associated to the three colors:

$$\psi(x) = (\psi_{red}, \psi_{green}, \psi_{blue}). \tag{1.21}$$

Let's now consider the covariant derivative, defined in Eq. 1.10, with a new field B_μ, and the strong coupling constant g_s:

$$\mathcal{D}_\mu = \partial_\mu + i g_s B_\mu \tag{1.22}$$

where B_μ is a 3×3 matrix in color space, that depends on the eight color gauge fields b^l_μ and the generators $\lambda^l/2$ of the $SU(3)_C$ gauge group:

$$B_\mu = \frac{1}{2}\vec{\lambda} \cdot \vec{b}_\mu = \frac{1}{2}\lambda^l b^l_\mu \tag{1.23}$$

where λ are the Gell-Mann λ-matrices. Adding also a kinetic term to the lagrangian, determined by the $G_{\mu\nu}$ gluon field-strenght tensor, the new lagrangian becomes:

$$\mathcal{L}_{QCD} = \bar{\psi}(x)(i\gamma^\mu \mathcal{D}_\mu - m)\psi(x) - \frac{1}{2}\mathrm{tr}\,(G_{\mu\nu}G^{\mu\nu}) \tag{1.24}$$

As for the QFD, QCD is a non-Abelian gauge theory and 3 or 4 gluon vertices are allowed in the theory (see Figure 1.5). For energies of $\approx 100\,\mathrm{GeV}$, $\alpha_s \approx 0.1$, this is called *asymptotic freedom* regime in which perturbative approach is possible; instead, for smaller energies ($\approx 1\,\mathrm{GeV}$), $\alpha_s \approx 1$. This is called *confinement* regime. An example of a possible strong interaction is the one shown in Figure 1.6.

[3] The energy scale in physics refers to the characteristic range of energies at which a particular physical phenomenon or interaction becomes significant or dominant.

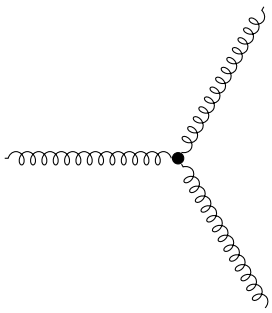

(a) Triple-boson vertex.

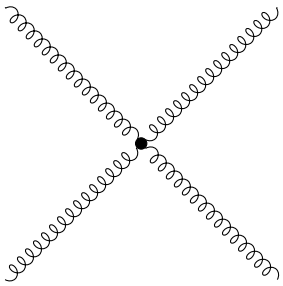

(b) Tetra-boson vertex.

Figure 1.5: Allowed vertices in the QCD theory.

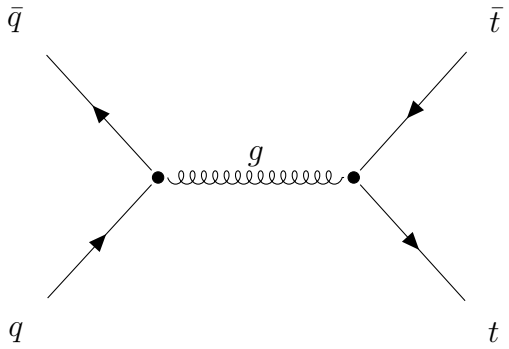

Figure 1.6: Production of $t\bar{t}$ via $q\bar{q}$ annihilation.

1.1.5 Electroweak theory

In the SM all fermions are decomposed into *left-handed* and *right-handed* **chiral** states. In general each fermion family can be written as:

$$\begin{pmatrix}\nu_l\\ l^-\end{pmatrix}_L,\ \begin{pmatrix}q_u\\ q_d\end{pmatrix}_L,\ l_R^-,\ q_{uR},\ q_{dR} \tag{1.25}$$

where ν_l is the neutrino associated to the charged lepton l^- and q_u and q_d are the up-type and down-type quarks. The left-handed fields are $\mathrm{SU}(2)_L$ doublets, while their right-handed partners transform as SU(2) singlets [18].

To describe a unified theory of electromagnetic and weak interactions (this forces are unified at $\simeq 246\,\mathrm{GeV}$) it is necessary to have massive gauge bosons $W^\pm$ and Z and massless QED boson γ. The simplest group to describe this interaction is:

$$G = \mathrm{SU}(2)_L \otimes \mathrm{U}(1)_Y \tag{1.26}$$

where Y is the *hypercharge*, defined from this equation:

$$Q = I_3 + \frac{Y}{2} \tag{1.27}$$

with Q electromagnetic charge and I_3 third component of the weak isospin.

Let's start by considering a lagrangian as in QED and QCD:

$$\mathcal{L}_0 = \sum_{j=1}^{3} i\bar{\psi}_j(x)\gamma^\mu\partial_\mu\psi_j(x) \tag{1.28}$$

where $\psi_1(x)$ is the up-down spinor doublet of the quark or lepton sector, $\psi_2(x)$ is the right-handed spinor singlet of the up-component and $\psi_3(x)$ is the right-handed spinor singlet of the down-component. This lagrangian is invariant under global gauge transformations in flavor space. If we replace fermion derivatives with covariant derivatives we get local gauge invariance. Firstly, it is necessary to build a kinetic term, starting with the introduction of two field strenght tensors:

$$B_{\mu\nu} = \partial_\mu B_\nu - \partial_\nu B_\mu \tag{1.29}$$

$$\widetilde{W}_{\mu\nu} = \partial_\mu W^i_\nu - \partial_\nu W^i_\mu - g\epsilon^{ijk}W^j_\mu W^k_\nu \tag{1.30}$$

where B_μ is the gauge field of QED, $\widetilde{W}_\mu$ are the gauge fields of QFD, g is the coupling constant of the $\mathrm{SU}(2)_\mathrm{L}$ group and ϵ^{ijk} is the Levi-Civita tensor. Both fields of Eq. 1.29 and 1.30 are invariant under gauge transformations. Therefore, the kinetic term becomes:

$$\mathcal{L}_{kin} = -\frac{1}{4}B_{\mu\nu}B^{\mu\nu} - \frac{1}{2}tr\left[\widetilde{W}_{\mu\nu}\widetilde{W}_{\mu\nu}\right] = -\frac{1}{4}B_{\mu\nu}B^{\mu\nu} - \frac{1}{4}W^i_{\mu\nu}W_i^{\mu\nu}. \tag{1.31}$$

The gauge symmetry forbids a mass term for the gauge bosons and also fermionic masses are not allowed since they would link the left- and right-handed fields, which have different transformation properties and therefore would provide an explicit breaking of the symmetry. Now this lagrangian contains only massless fields and generates also cubic and quadratic terms that have to be taken into account.

The lagrangian of Eq. 1.28 contains interactions of fermion fields with gauge bosons, so they describe possible charged-current interactions with the boson fields W_μ and its complex-conjugate $W_\mu^\dagger$ for a single family of quarks and leptons:

$$\mathcal{L}_{CC} = -\frac{g}{2\sqrt{2}}\{W_\mu^\dagger[\bar{u}\gamma^\mu(1-\gamma_5)d + \bar{\nu}_e\gamma^\mu(1-\gamma_5)e] + h.c.]\} \tag{1.32}$$

where $h.c.$ are hermitian conjugates terms. However also neutral current interactions

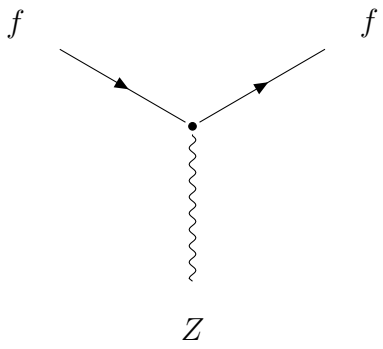

(a) NC interaction vertex.

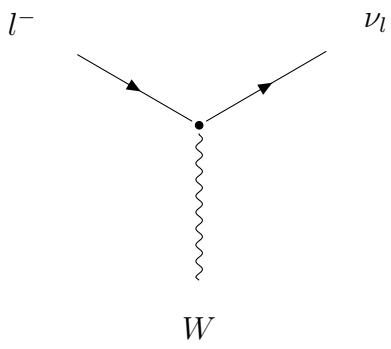

(b) CC interaction vertex.

Figure 1.7: Examples of CC and NC allowed electroweak processes. In (a): NC vertex of a generic fermion f. In (b): CC vertex of a generic lepton l^- and the corresponding neutrino ν_l.

based on the W_μ^3 and B_μ fields are allowed, and a NC term of the lagrangian is necessary:

$$\mathcal{L}_{NC} = \mathcal{L}_{QED} - \frac{e}{2\sin\theta_W\cos\theta_W} J_Z^\mu Z_\mu \tag{1.33}$$

where $\mathcal{L}_{QED}$ is the lagrangian of QED, $e = g\sin\theta_W$, θ_W is the *Weinberg angle* that mixes W_μ^3 and B_μ with the physical fields Z_μ and A_μ and J_Z^μ is the neutral fermionic current. See Figure 1.7 for some examples of CC and NC electroweak processes.

The problem of this lagrangian is that it does not contain mass terms for the fermions nor for the vector bosons. The issue of fermion and boson masses can be solved with the introduction of the **spontaneous symmetry breaking (SSB)** via the BEH mechanism (mentioned in Section 1.1.1) in the case of a lagrangian with local gauge symmetry. After the application of this theory, the gauge bosons of the weak interaction and the fermions became massive and a new massive scalar field called *Higgs boson* is introduced.

The measured masses of the weak bosons are [19]:

$$M_Z \simeq 91\,\text{GeV},\ M_W \simeq 80\,\text{GeV} \tag{1.34}$$

1.2 Top quark physics

The top quark is one of the most particular elementary particles observed so far. As mentioned in the introduction of Section 1.1, it has very singular properties that let his behaving in a completely different manner with respect to the lightest elementary components. In this section a brief overview on the top quark physics at the LHC will be introduced, explaining its properties and its importance in current studies.

1.2.1 The top

The most significant dates for the discovery of the top quark t are the following:

- 1964: quark model proposed by Gell-Mann and Zweig [20].
- 1970: *GIM Mechanism* $\Rightarrow$ introduction of the fourth quark, the *charm* [21].
- 1975: discovery of the $\tau \Rightarrow$ 3 generations of leptons [22].
- 1977: discovery of the Υ and the introduction of the fifth quark, the *bottom* [23].
- 1984: t not observed at $Sp\bar{p}S$ accelerator $\Rightarrow$ limit on the t mass: $m_t > 44\,\text{GeV}$ [24].
- 1990: t not observed at LEP collider $\Rightarrow$ limit on the t mass: $m_t > 69\,\text{GeV}$ [25].

The discovery was announced at Fermilab on March 3, 1995 [26], with an integrated luminosity $L \simeq 60\,\text{fb}^{-1}$, yielding very few events, but with 5σ discovery significance, corresponding to a probability of 10^{-6}, which corresponds to the likelihood that the observed result is due to background fluctuation, implying a very high confidence level in the discovery.

From the studies and further measurements followed along the years, at present we know that:

- It is an elementary particle.
- It is massive.
- It has spin $\frac{1}{2}$.
- It is produced both strongly and weakly.

- It decays immediately before hadronizing.
- It is the particle more intensively coupled with the Higgs boson through the *Yukawa coupling*, even if, for the moment, we only have quite imprecise measurements of the top Yukawa coupling.

With a mass of $\simeq$ 173 GeV, above the Wb threshold, the decay width of the top is expected to be dominated by the two-body decay channel:

$$t \to Wb \tag{1.35}$$

Neglecting terms of order m_b^2/m_t^2, α_s^2 and those of the order $\frac{\alpha_s m_W^2}{\pi m_t^2}$ in the decay amplitude, the width predicted through the SM theory is [27, 28]:

$$\Gamma_t = \frac{G_F m_t^2}{8\pi\sqrt{2}}\left(1-\frac{m_W^2}{m_t^2}\right)^2\left(1+2\frac{m_W^2}{m_t^2}\right)\left[1-\frac{2\alpha_s}{3\pi}\left(\frac{2\pi^2}{3}-\frac{5}{2}\right)\right] \approx 1.33\text{GeV}. \tag{1.36}$$

We can see that the G_F constant contains the largest part of the one-loop electroweak radiative corrections, providing an expression accurate to better than 2% and this width increase with the mass of the top. From the Eq. 1.36 it is possible to compute the top quark lifetime:

$$\tau_t \simeq 0.5 \times 10^{-24}\text{s} \tag{1.37}$$

and due to this very short lifetime the t is expected to decay before top-flavoured hadrons or $t\bar{t}$-quarkonium bound states can form. Also, other QCD corrections can be applied to the Eq. 1.36, reducing the theoretical error to 1%. Other Ws or Wd decays are suppressed because of the values of the *CKM matrix* elements [29].

The W boson decays as well and its possible decay channels are:

$$W \to l\nu_l,\ W \to qq^{'} \tag{1.38}$$

where l is a lepton, ν_l is the corresponding neutrino and q and $q^{'}$ are two different quarks See Figure 1.8 for a schematic view of an example of a top-quark decay Feynman diagram.

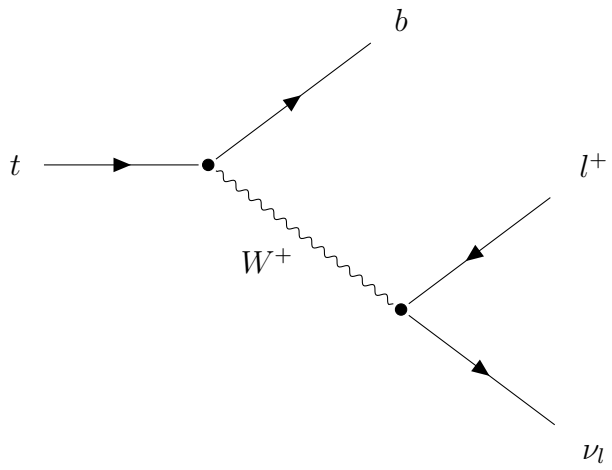

Figure 1.8: Example of decay channel of t quark into W^+ and b with subsequent decay: $W^+ \to l^+\nu_l$.

1.2.2 Fundamental properties of the top quark

Some of the most important top quark properties are:

- **Mass**: the mass of the top quark is larger than that of any other known fundamental particle. Usually the top-quark mass value is given as a top *pole-mass*, that is defined as the real part of the pole in the top quark propagator:

$$\sqrt{p^2} = m_t^{pole} - \frac{i}{2}\Gamma \tag{1.39}$$

  where p is the 4−momentum and Γ is the decay rate [30]. This pole-mass is defined up to an intrinsic ambiguity of the order of $\Lambda_{QCD} \approx 200\,\text{MeV}$. Masses of top, W and H particles are linked by a relation (see radiative correction formula in Eq. 1.43 later), therefore, better precision in the estimation of the top mass is given also by better precision in the measurement of W and H masses (see Figure 1.9). Summary of the ATLAS and CMS direct m_{top} measurements[4] compared with the LHC and Tevatron+LHC m_{top} combinations are shown in Figure 1.10. The combination m_{top} value of ATLAS and CMS gives the following top mass value [32]:

$$m_t = 172.52 \pm 0.33 \text{ GeV} \tag{1.40}$$

- **Electric charge**: the top quark in the SM is an up-type quark, so the charge is predicted to be +2/3; this has found confirmation experimentally by dedicated measurements [27].

[4] In this case the *MC-mass* is usually measured instead of the pole-mass.

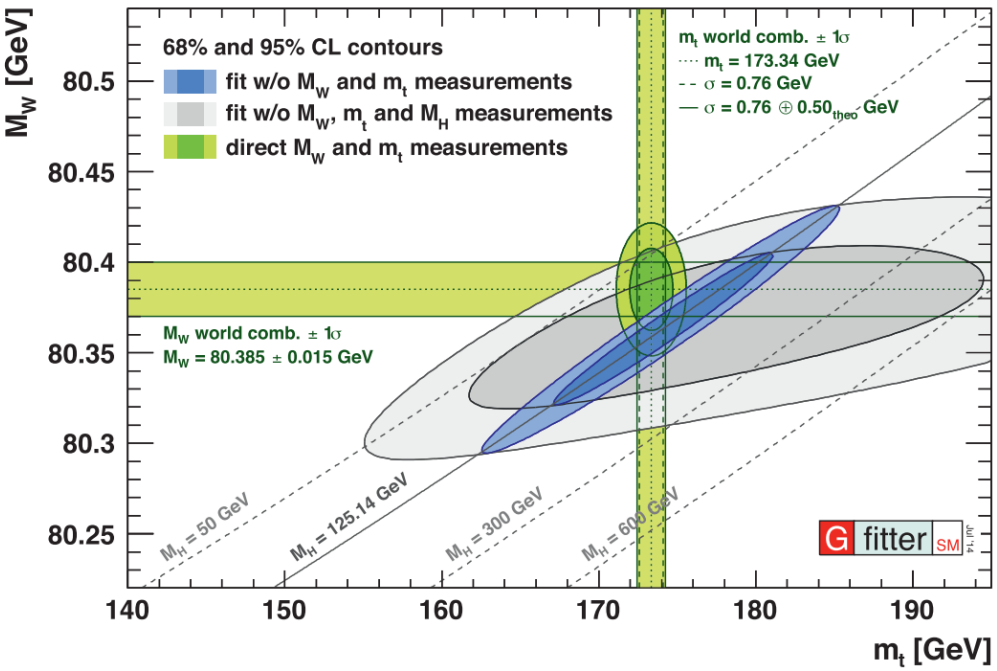

Figure 1.9: Plot of m_W vs m_t. In figure the 68% and 95% CL contours for the indirect determination of m_t and m_W from global SM fits to EW precision data are shown [31].

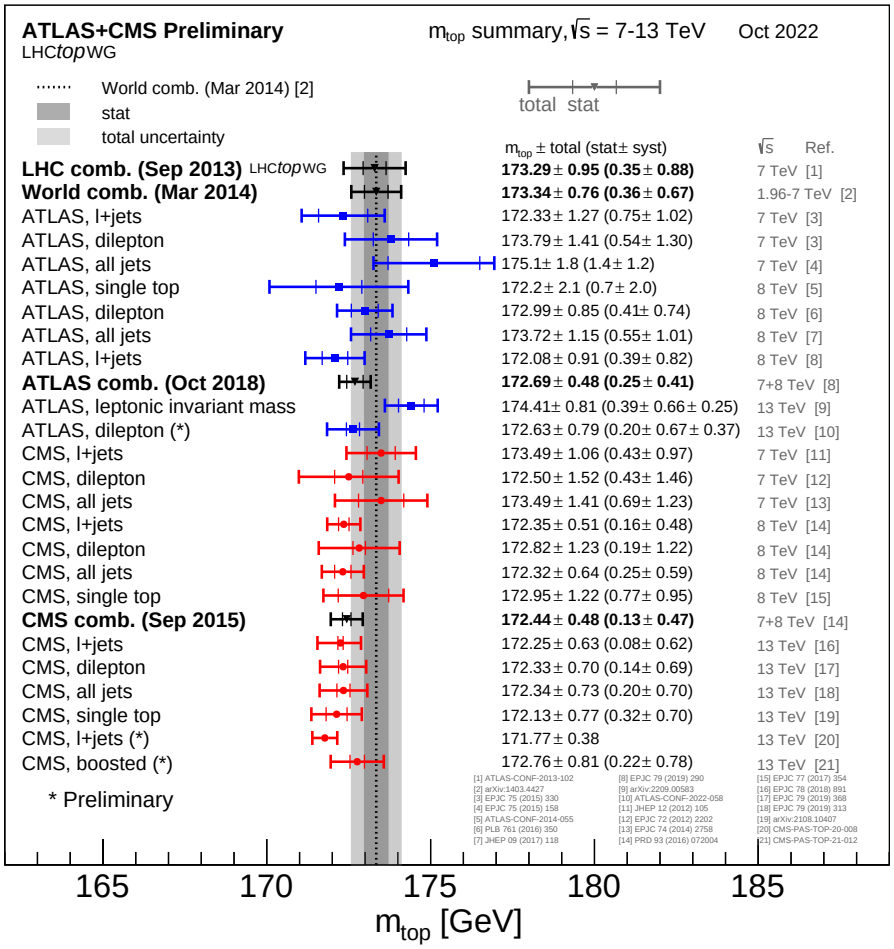

Figure 1.10: Summary of the ATLAS and CMS direct m_{top} measurements. The results are compared with the LHC and Tevatron+LHC m_{top} combinations. For each measurement, the statistical uncertainty includes the jet scale factor (JSF) and b-jet scale factor (bJSF) contributions (when applicable), while the sum of the remaining systematic uncertainties is reported separately. The JSF and bJSF contributions are statistical in nature and apply to analyses performing in-situ (top quark pair based) jet energy calibration procedures.

- **Helicity of the W boson in top quark decay**: the SM implies that the top quark has the same V-A charged-current weak interaction as all the other fermions (see Section 1.1.3):

$$-i\frac{g}{\sqrt{2}}V_{tb}\gamma^{\mu}\frac{1}{2}(1-\gamma_5) \tag{1.41}$$

where V_{tb} is the CKM matrix element. Due to angular momentum conservation, the W boson from the t decay cannot have right-handed (RH) helicity (see Figure 1.11). If the W boson were RH, then the component of total angular momentum

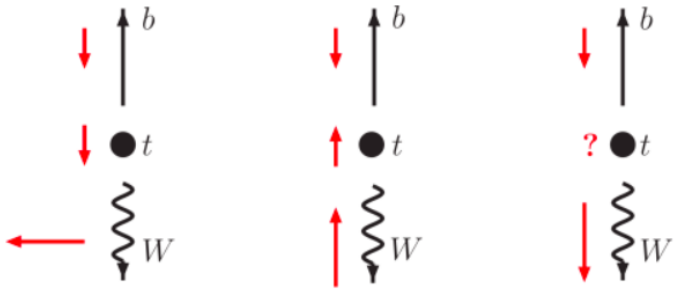

Figure 1.11: In order from left to right: longitudinal W-boson case (left), left-handed W-boson case (center) and forbidden right-handed W-boson case (right).

along the decay axis would be $+3/2$, but the initial t quark has spin angular momentum $\pm 1/2$ along this axis, so this decay is forbidden by conservation of angular momentum. The t prefers to decay into left-handed (LH) W boson with a branching ratio of 0.7.

- **Spin correlation in strong $t\bar{t}$ production**: on average, the top quark decays before there is time for its spin to be depolarized in the strong interaction. The top quark polarization is directly observable via the angular distribution of its decay products. The spins of the t and $\bar{t}$ are correlated in $t\bar{t}$ production processes even if the tops are not polarized in the $t\bar{t}$ production. This correlation can be measured and SM predictions can be tested. Another interesting motivation for the study of this property is the detection of the entanglement between the spins of $t\bar{t}$ pairs, that represents the first possibility of entanglement detection in a pair of quarks, and also the entanglement observation at the highest energy scale so far. This entanglement can be observed by direct measurement of the angular separation between the leptons arising from the decay of the $t\bar{t}$ pair.

- **Yukawa coupling**: Yukawa coupling of the Higgs boson with the top quark is defined as:

$$y_t = \frac{\sqrt{2}m_t}{v} \tag{1.42}$$

where $v \approx 246\,\text{GeV}$ is the vacuum expectation energy. The value of this coupling is very close to unity. This value leads to numerous speculations related to new physics that can be accessed with the study of the top quark.

1.2.3 Impacts of top quark in SM and BSM physics

Precise measurements of top quark parameters are fundamental to constrain BSM physics. First of all, the mass of the top quark, m_t , is one of the most interesting parameters. It plays a central role in the SM, since the top quark participates to radiative corrections of higher order for the bosonic propagator and, for example, it modifies the mass of the W (see Figure 1.12). The theoretical prediction of m_W is [33]:

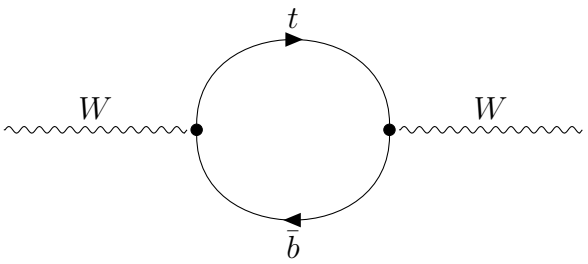

Figure 1.12: Radiative corrections from the top quark of higher order for the bosonic propagator of W.

$$m_W^2 = \frac{\pi \alpha_{EM}}{\sqrt{2} G_F \sin^2 \theta_W} \frac{1}{1 - \Delta r} \tag{1.43}$$

where α_{EM}, G_F and θ_W have been already defined in previous sections and Δr can be approximated with:

$$\Delta r \simeq \Delta \rho_0 - \frac{\Delta \rho}{\tan^2 \theta_W} \approx 3\% \tag{1.44}$$

where the first term is the running of the strong coupling constant α_s and the second one represents the one-loop corrections [34]. Then:

$$\Delta \rho = \frac{3 G_F m_t^2}{8\sqrt{2}\pi^2} \tag{1.45}$$

As mentioned in Figure 1.9, the top quark mass depends on the coupling to the Higgs boson through loops with H; therefore, a combined measurement of m_W and m_t can constrain the possible values of m_H:

$$\Delta m_W \propto \Delta m_t^2 \tag{1.46}$$

$$\Delta m_W \propto \log \Delta m_H^2 \tag{1.47}$$

or, having discovered the Higgs boson, test the global consistency of the SM. Measuring accurately m_H vs m_t provides a test of the stability of the vacuum state of the SM and the ultimate fate of our Universe. Present estimates suggest that we're in a region of meta-stability, with important cosmological limitations, but in a time far larger than the present age of the Universe. See Figure 1.13 for a graphical representation of this problem [35].

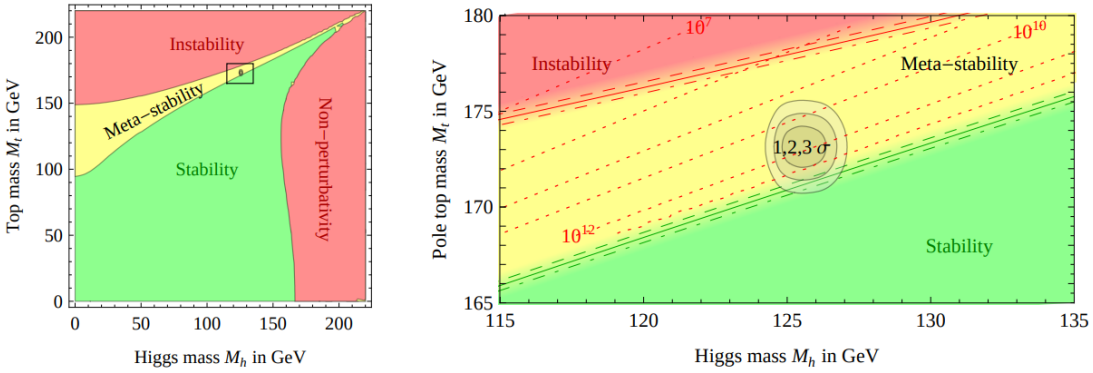

Figure 1.13: Regions of absolute stability, meta-stability and instability of the SM vacuum in the m_t vs m_h (Higgs boson mass) plane. The gray areas denote the allowed region at 1, 2, and 3 σ [35].

1.2.4 Top quark production cross-sections

Another fundamental quantity measured from the top physics is the **cross-section** σ of the production processes involving the top quark itself. For example, the cross section of $t\bar{t}$ production process at the LHC, that will be discussed in Section 2.1, is given by:

$$\sigma(pp \to t\bar{t}) = \sum_{i,j} \int d\vec{x}_i f_i(\vec{x}_i, \mu^2) \int d\vec{x}_j f_j(\vec{x}_j, \mu^2) \hat{\sigma}_{ij}(\hat{s}, \mu^2, m_t) \tag{1.48}$$

where the sum is extended over partons i and j, f are the parton density functions (PDFs) of light quarks and gluons, $\vec{x}$ is the momentum fraction, $\hat{s}$ is the center-of-mass energy of partons and $\hat{\sigma}$ is the partonic cross-section. A representative Feynman diagram is illustrated in Figure 1.14, this is only one of the possible diagrams at LO. The cross-section depends on the mass of the top and on the factorization scale μ, because calculations are carried on some finite order. Measurements of a cross-section are fundamental to extract useful constraints to some theory parameters. For example, in this case, a constraint on the PDFs is provided and also a determination of α_s and m_t; but also a characterization of the soft radiation, in production and decay, and a constrain on parton shower and hadronization models is provided [36].

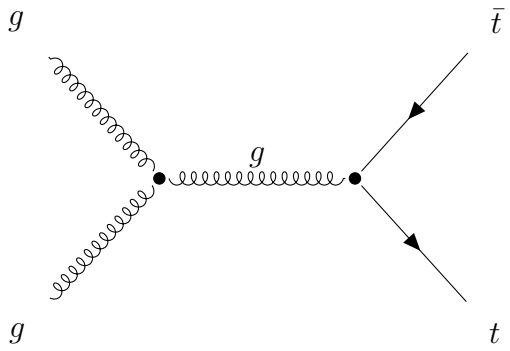

Figure 1.14: Production of $t\bar{t}$ pair at the LHC, through gluon-gluon fusion.

However, to make more realistic comparisons with theoretical models it is important to measure **differential cross-sections**. These cross-sections are measured at two possible levels:

- **Particle level**: Refers to quantities that can be directly measured in the detector, including simultaneous observations of particles.
- **Parton level**: Refers to the intrinsic kinematic properties of the produced top quarks, as predicted by the underlying theoretical model.

These cross sections are always measured as a function of one or more variables. Deviations from the model prediction could spot the presence of possible BSM physics hints.

Top quark production and decay processes are also important to measure three parameters of the CKM matrix, namely $|V_{td}|$, $|V_{ts}|$ and $|V_{tb}|$.

Chapter 2

The $WbWb$ production

At the LHC, the top quark is produced mainly through gluon-gluon fusion, giving $t\bar{t}$ pair (see Figure 1.14); but there is also the possibility to be produced singly, with an associated W boson and a b quark. The latter is a rarer process than the previous one. It happens that at next-to-leading order (NLO) in QCD the two previous mentioned processes quantum-mechanically interfere and this interference may provide important contributions to other SM and BSM physics processes. In particular, several BSM searches have developed selections that are enriched in tW events in the interference region (see Section 1.2.3). So, the spread in model prediction for this process is large and this results in large systematic uncertainties [37]. The production process given by $t\bar{t}+tWb$ is called $WbWb$, it also includes non resonant di-boson and two b-quark production, as explained below.

Better knowledge on the interference is also useful to discriminate among triple Higgs boson vertices like $t\bar{t}H$ and tWH or $t\bar{t}\gamma$ and $tW\gamma$. The latter is important because $t\bar{t}\gamma$ probes $t\gamma$ coupling and is sensitive to anomalous dipole-moment and *Effective Field Theory* (EFT) operators.

To account for the interference process and avoid double counting when simulating $t\bar{t}$ and tW samples, two main approaches are generally used. The first approach involves studying tW at NLO and $t\bar{t}$ at LO using *removal* techniques (as explained in Section 2.3). The second approach focuses directly on the study or measurement of the $WbWb$ final state, treating it as a combined process that includes contributions from both $t\bar{t}$ and tW without attempting to separate them.

2.1 The $t\bar{t}$ top pair production process

The top quark is currently studied at CERN by the two experiments ATLAS and CMS. At LHC, the dominant mechanism for the production of a top quark through a pair of $t\bar{t}$ is the gluon-gluon fusion. The relative contributions to this production at LHC are:

$$B(q\bar{q} \to t\bar{t}) < 20\% \tag{2.1}$$

$$B(gg \to t\bar{t}) > 80\% \tag{2.2}$$

The first process was the dominant one at Tevatron. In Figure 1.14 a LO diagram for the top pair-production is shown, while in Figure 2.1 the dominant contributing diagram is given. The $t\bar{t}$ production is described by perturbative QCD: in this approach a hard

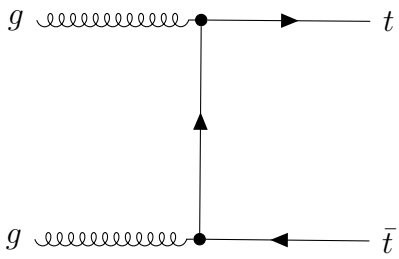

Figure 2.1: LO dominant diagram for the $t\bar{t}$ production process through gluon-gluon fusion at the LHC.

scattering process between two hadrons is the result of an interaction between the quarks and the gluons, which are the constituents of the incoming hadrons. The incoming proton provides broad band beams of partons carrying fractions x of the momentum of the parent hadron. Perturbative expansions of the calculations related to the partonic cross section (see Eq. 1.48) are fundamental to get more sensitivity on important parameters when comparing data with theoretical models. In higher order calculations infinites such as ultraviolet divergences appear; they are removed by the renormalization procedure.

To produce a top-quark pair at rest, it is required a minimum amount of center-of-mass energy:

$$\hat{s} \geq 4m_t^2 \tag{2.3}$$

and therefore:

$$x_i x_j = \frac{\hat{s}}{s} > \frac{4m_t^2}{s} \tag{2.4}$$

Setting $x_i = x_j = x$ one gets the result shown in Eq. 2.5.

If we consider the ratio between the mass of the top m_t and the energy of the proton E_p in the collision:

$$x_{min} = \frac{m_t}{E_p} \simeq 0.043 \tag{2.5}$$

with $E_p \approx 6500\,\text{GeV}$, we see that x_{min} is quite small and therefore gluon PDF dominates (see Figure 2.2). The production rate for $\sqrt{s} = 13\,\text{TeV}$ and $\mathcal{L} \simeq 1 \times 10^{33}\,\text{cm}^{-2}\text{s}^{-1}$ is about

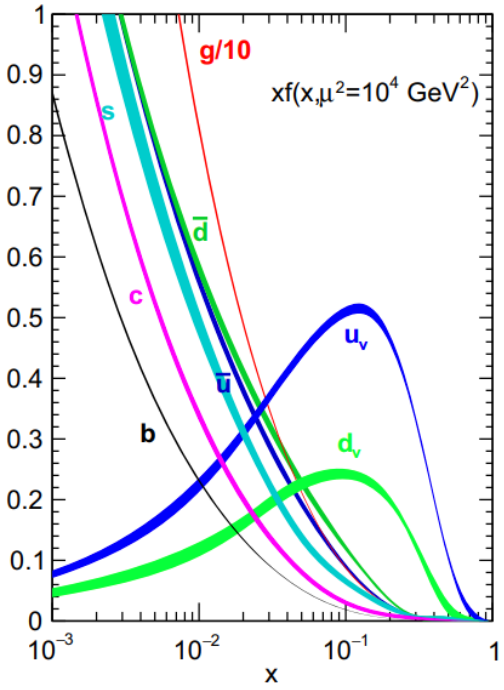

Figure 2.2: The `NNPDF3.1` NNLO PDFs, evaluated at $\mu^2 = 10^4\text{GeV}^2$ [38].

1 Hz, giving a production cross-section of $\sigma_{t\bar{t}}^{13\,\text{TeV}} \simeq 8 \times 10^{-34}\,\text{cm}^2$. This is equivalent to the production of 2 million $t\bar{t}$ events per month, when LHC is on.

An accurate calculation of this cross-section is a necessary ingredient for the measurement of the $|V_{tb}|$ element of the CKM matrix since $t\bar{t}$ production is an important background for the EW single-top production. More importantly, this cross-section is sensitive to new physics in top quark production and decay.

Given that the top quark decays almost 100% of the times into a W boson and a b-quark, typical final states for the pair-production process can be divided into three classes:

$$t\bar{t} \to W^+bW^-\bar{b} \to q\bar{q}'bq''\bar{q}'''\bar{b} \tag{2.6}$$

$$t\bar{t} \to W^+bW^-\bar{b} \to q\bar{q}'bl\bar{\nu}_l\bar{b} + \bar{l}\nu_l bq\bar{q}'\bar{b} \tag{2.7}$$

$$t\bar{t} \to W^+bW^-\bar{b} \to \bar{l}\nu_l bl'\bar{\nu}_{l'}\bar{b} \tag{2.8}$$

where the branching ratios are respectively: 46.2%, 43.5% and 10.3% [9]. The three processes are referred to as the all hadronic, semileptonic and di-leptonic channels, respectively. The l refers to e, μ or τ, but most of the results to date rely on e and μ

channels. The initial and final states can also radiate gluons that can be detected as additional jets.

Recent summary plots for $t\bar{t}$ production cross-section measurements done at LHC and Tevatron are shown in Figures 2.3 and 2.4.

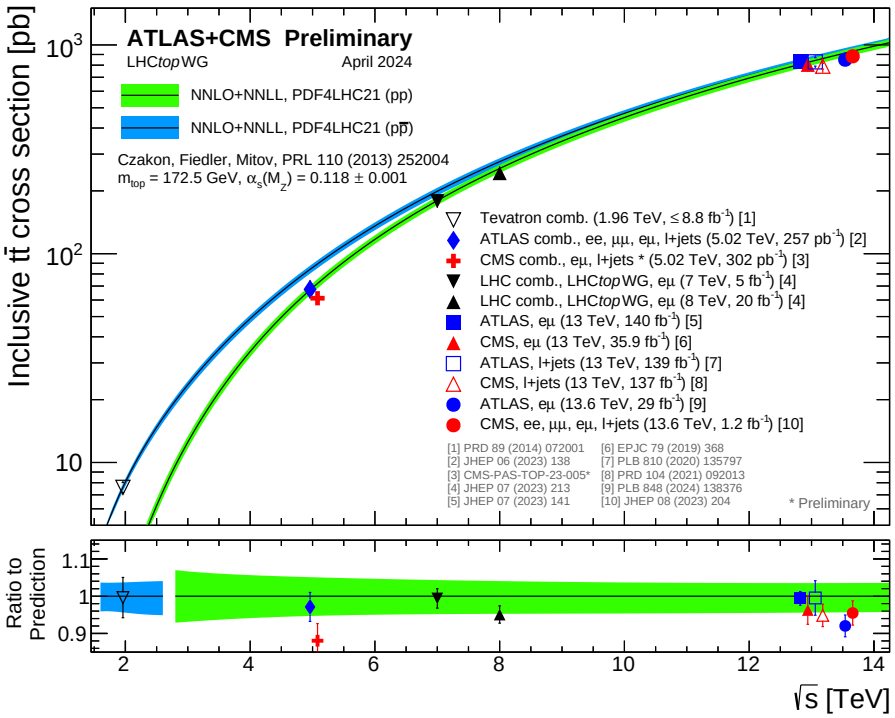

Figure 2.3: Summary of LHC and Tevatron measurements of the $t\bar{t}$-pair production cross-section as a function of the centre-of-mass energy compared to the NNLO QCD calculation complemented with NNLL resummation (`top++2.0` [39]). The theory band represents uncertainties due to renormalization and factorization scale, parton density functions and the strong coupling. The measurements and the theory calculation are quoted at $m_{\text{top}} = 172.5\,\text{GeV}$. Measurements made at the same centre-of-mass energy are slightly offset for clarity. [40].

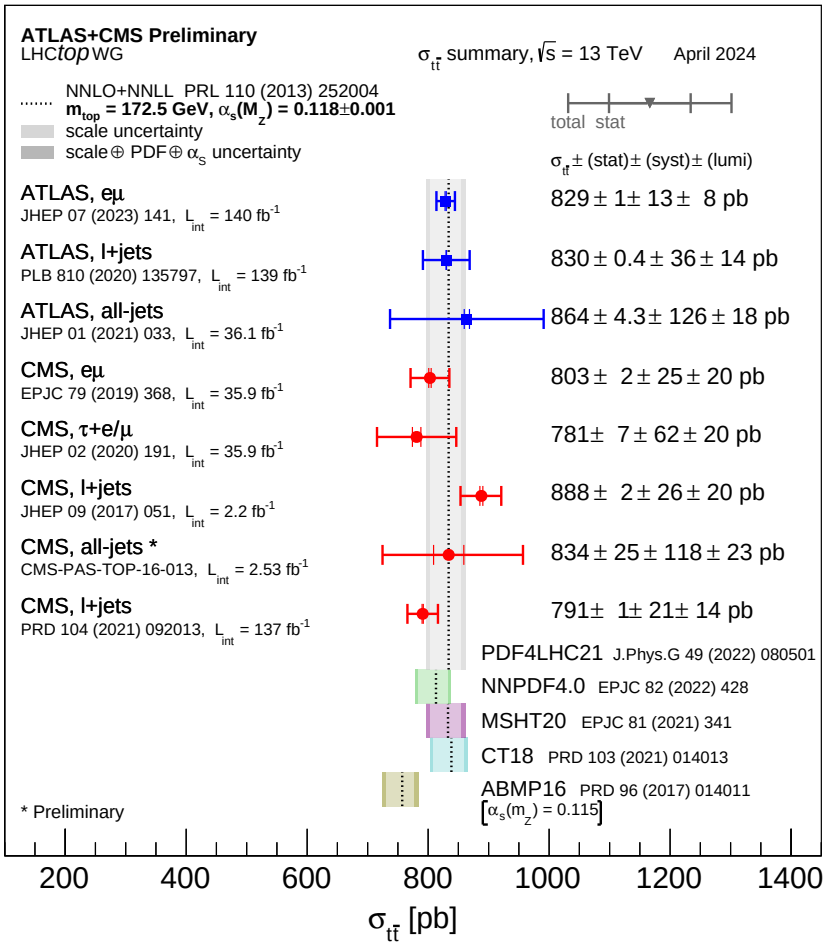

Figure 2.4: Summary of measurements of the $t\bar{t}$-pair production cross-section at 13 TeV compared to the exact NNLO QCD calculation complemented with NNLL resummation (`top++2.0`). The theory band represents uncertainties due to renormalization and factorization scale, parton density functions and the strong coupling. The measurements and the theory calculation are quoted at $m_{\text{top}} = 172.5\,\text{GeV}$.

2.2 The tW single top production process

The best way to study the properties of the tWb vertex and to directly measure the $|V_{tb}|$ matrix element at the LHC is via the measurement of the EW single-top quark production (see Figure 2.5 for the Feynman diagram for this process at LO). Measurements of the

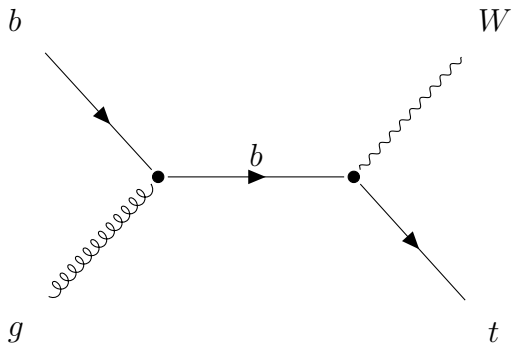

Figure 2.5: Wt channel single-top production process at the LHC at LO.

process cross-section are proportional to $|V_{tb}|^2 g_W^2(tb)$. The large production rate at the LHC allows a measurement of the matrix element with negligible statistical uncertainty, differently from what happens in other channels.

There are two approaches to treat the single-top production at the NLO. In the **5 flavor scheme (5F)** a massless b-quark contributes to the proton PDF and therefore b-initiated diagrams contribute at the lowest order in the calculation (see Eq. 2.9 and Figure 2.6b). In the **4 flavor scheme (4F)** the b-quark is treated as massive and the initial-state b-quarks result from gluons via explicit $g \to b\bar{b}$ splittings (see Eq. 2.10 and Figure 2.6a) [41]. The two processes are represented by the following equations:

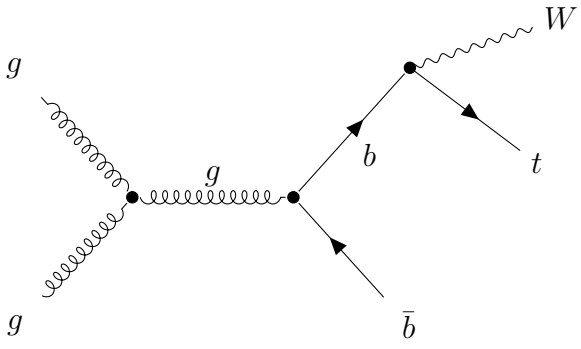

(a) 4 flavor scheme diagram.

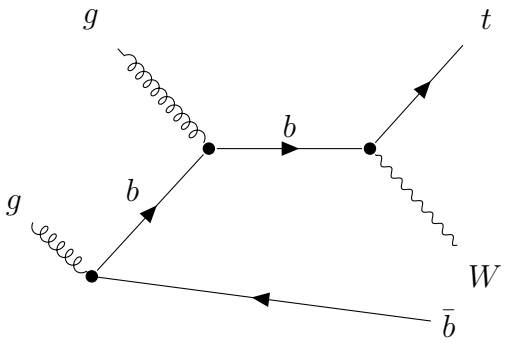

(b) 5 flavor scheme diagram.

Figure 2.6: Example of NLO diagram contributions to the tWb single-top production.

$$gb \to W^- W^+ b \tag{2.9}$$
$$gg \to W^- W^+ \bar{b} b \tag{2.10}$$

The presence of a single b-jet at LO represents a clearly distinctive feature with respect to the $t\bar{t}$ decay, but this separation ceases to exist beyond the LO, since the $t\bar{t}$ process enters also the NLO corrections to tW production. This will be deeply explained later in Section 2.3.

Let's start from the *Born Level* computation of the cross-section at LO. In this treatment all the quarks are taken as massless, including the b quark. The σ can be written as:

$$d\sigma^{(0)} = \mathcal{M}^{(0)} d\phi_2 \tag{2.11}$$

where $d\phi_2$ is the two-body final state phase space and $\mathcal{M}^{(0)}$ is the Born-level matrix element, defined as:

$$\mathcal{M}^{(0)} = \frac{1}{2s}\frac{1}{4}\frac{1}{N(N^2-1)} g_s^2 \frac{g_W^2}{8} \left|\mathcal{A}^{(0)}\right|^2 \tag{2.12}$$

with: g_s and g_W respectively the strong and weak coupling constants, s squared center-of-mass energy, N number of colors and $\mathcal{A}^{(0)}$ spin-number Born-level matrix element [42].

To get a NLO description of the process, it is necessary to introduce two kind of corrections:

- **Virtual corrections**: in this case one-loop virtual diagrams in $d = 4 - 2\epsilon$ dimensions are calculated. Virtual corrections are Laurent series in the parameter ϵ with different poles and singularities. To solve the problem, some quantities as the strong coupling g_s and the top mass m_t are renormalized providing a contribution to the amplitude from the expansion of the renormalized top quark propagator, where there are terms proportional to the Born amplitude $\mathcal{A}^{(0)}$ and the modified amplitude $\mathcal{A}'^{(1)}$ involving the squared top quark propagator. Therefore, in terms of the *finite reminder* the cross-section receives the contribution:

$$d\sigma^{1,V}_{\delta m_t} = (\delta m_t)_{finite} d\sigma^{(0)} (\mathcal{A}^{(0)} \mathcal{A}'^{\dagger(1)} + \mathcal{A}'^{(1)} \mathcal{M}^{\dagger(0)}). \tag{2.13}$$

- **Real corrections**: for this correction, the matrix elements are computed by the fictitious W boson decays:

$$W(q) \to Q(p) + \bar{b}_3(q_3) + g_4(q_4) + g_5(q_5) \tag{2.14}$$
$$W(q) \to Q(p) + \bar{b}_3(q_3) + b_4(q_4) + \bar{b}_5(q_5) \tag{2.15}$$

  where Q denotes generally the only quark with mass different from zero. This corrections come from gluon-radiation and initial-gluon diagrams. In particular, for gluon radiation:

$$\sigma^{gr} = \sigma^{gr}_s + \sigma^{gr}_c + \sigma^{gr}_{fin} \tag{2.16}$$

where the three terms are respectively contributions from: soft, collinear and non collinear regions [43].

For the initial gluon process:

$$\sigma^{ig} = \sigma_c^{ig} + \sigma_{fin}^{ig} \tag{2.17}$$

the two terms represent the contributions in the collinear and non-collinear regions.

Finally, it's necessary to construct a Monte Carlo (MC) subtraction term for the matching of the NLO computation with event generators. MC subtraction terms can be written as:

$$d\sigma\big|_{MC} = \sum_i \sum_L \sum_l d\sigma_i^{(L,l)}\big|_{MC} \tag{2.18}$$

where i indicates the different partonic subprocesses, L labels the parton leg from which the parton is emitted and l runs over different color structures. There are also short-distance contributions that have to be taken into account for the subtraction term.

See Figure 2.7 for a summary of the ATLAS and CMS collaboration measurements of the single-top tW production cross-section at 13 TeV center-of-mass energy.

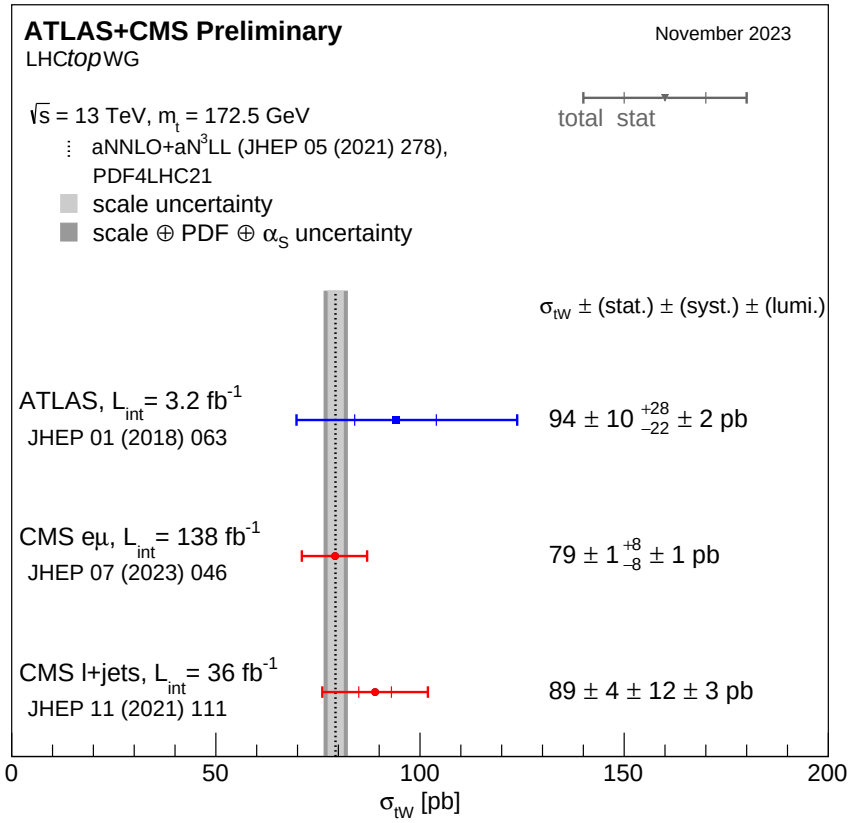

Figure 2.7: Cross-section measurements for the associated production of a top quark and a W boson performed by ATLAS and CMS at 13 TeV, and combined result compared with the NLO+NNLL prediction (gray bands). Statistical and total uncertainties are represented by red and blue error bars, respectively. The uncertainties in the theoretical prediction are represented by dark and light gray bands for renormalization / factorization scale and PDF (evaluated using `MSTW2008`), respectively [44].

2.3 The quantum interference between $t\bar{t}$ and tWb processes

At LO, in the 5 FS, the tW process is represented by the following process:

$$bg \to tW \tag{2.19}$$

This process has a smaller cross-section than top-pair production by a factor of about 15. Beyond the LO, some other Feynman diagrams contribute and they produce the same output state of a $t\bar{t}$ pair at LO, see Figure 2.8 for an example of this kind of diagrams[1]. Therefore, from this observations, the set of diagrams contributing to the

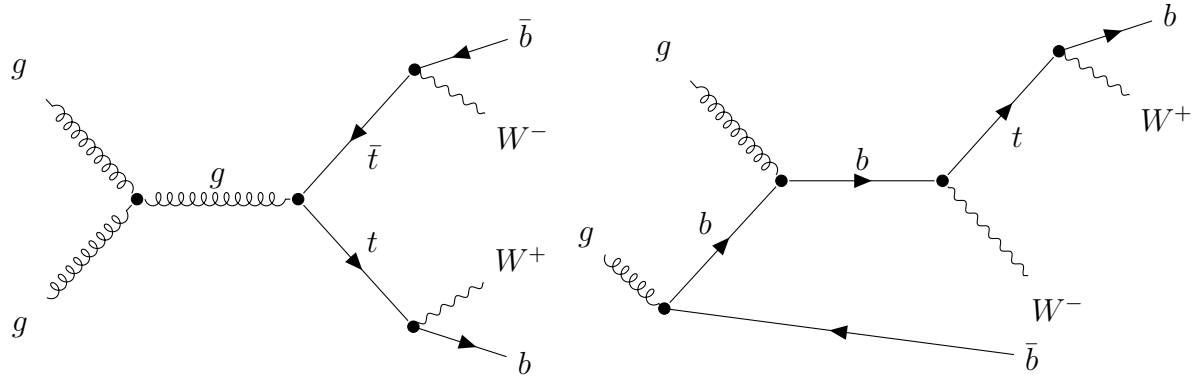

(a) Doubly-resonant diagram.

(b) Singly-resonant diagram.

Figure 2.8: Examples of quantum-mechanical interfering LO doubly-resonant diagram (a) and NLO singly-resonant diagram (b).

beyong LO version of Eq. 2.19 can be divided into two subsets denoted as **doubly resonant** (see Figure 2.8a) and **singly resonant** (see Figure 2.8b). Also non-resonant diagrams contribute to the $WbWb$ cross-section (see Figure 2.9), but their contribution is negligible with respect to the others. The interference, briefly mentioned before, may happen between these two subsets of diagrams and may be physically interpreted as the interference between tW and $t\bar{t}$ productions [45]. This process enters only at NLO contributions.

We introduce the notation $\mathcal{A}_{\alpha\beta}$ as the $\mathcal{O}(g_W\alpha_s)$ amplitude of the process:

$$\alpha + \beta \to t + W + \delta \tag{2.20}$$

where δ is the parton (identified as the b-quark), that can be omitted in the notation. The total amplitude is therefore:

$$\mathcal{A}_{\alpha\beta} = \mathcal{A}^{(Wt)}_{\alpha\beta} + \mathcal{A}^{(t\bar{t})}_{\alpha\beta} \tag{2.21}$$

[1]From now on, only the case of top quarks produced through gluon-gluon fusion will be considered.

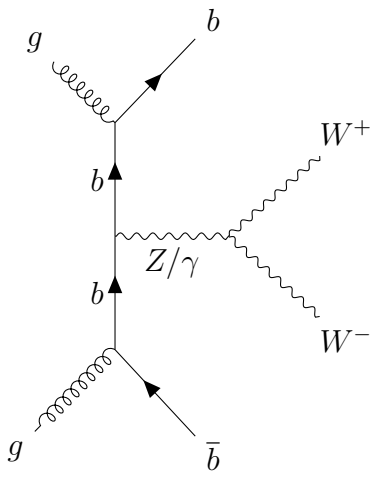

Figure 2.9: Example of non-resonant contribution to the $WbWb$ cross-section.

where the two terms are respectively the singly and doubly resonant contributions diagrams to the Wt cross-section. In the computation of the final cross-section, this term appears in the NLO part:

$$|\mathcal{A}_{\alpha\beta}|^2 = \left|\mathcal{A}_{\alpha\beta}^{(Wt)}\right|^2 + 2\,\mathrm{Re}\{\mathcal{A}_{\alpha\beta}^{(Wt)}\mathcal{A}_{\alpha\beta}^{(t\bar{t})}\} + \left|\mathcal{A}_{\alpha\beta}^{(t\bar{t})}\right|^2 \equiv \mathcal{S}_{\alpha\beta} + \mathcal{I}_{\alpha\beta} + \mathcal{D}_{\alpha\beta} \tag{2.22}$$

where the first term is associated to the singly resonant diagrams, the second term is the quantum interference and the third term is the doubly resonant contribution.

It is important to find a way to separate out the tW and $t\bar{t}$ productions and recover a workable definition of the tW channel beyond the LO[2].

When dealing with this kind of phenomena one of the most important problems to deal with is defining the tW channel in a way that it is applicable in an event generator context where both initial- and final-state parton showers are present.

One solution, called Diagram Removal (DR), is to remove from the computations the contributions of those processes which contain doubly-resonant diagrams.

There are other methods, designed in such a way that, by comparing them, one can directly assess the impact of the interference with $t\bar{t}$. Therefore, if the two results from the two definitions agree we can be confident of having isolated the tW channel. Some of the most used methods are [42]:

- **Diagram Removal** (DR): where all the doubly resonant diagrams in the NLO tW process amplitude are removed. This technique is different from the removal of the gg initiated process, because diagrams with this initial state are kept if they aren't doubly-resonant.

[2]At LO the definition is not problematic.

- **Diagram Subtraction** (DS): where NLO tW cross-sections are modified by implementing a subtraction term designed to cancel only locally the $t\bar{t}$ contribution.

These two schemes needs to be well explained. The NLO real-emission contribution to the subtracted short-distance partonic cross-section including the flux factor and phase space is:

$$d\hat{\sigma}_{\alpha\beta} = \frac{1}{2s}\left(\mathcal{S}_{\alpha\beta} + \mathcal{I}_{\alpha\beta} + \mathcal{D}_{\alpha\beta}\right) d\phi_3 \tag{2.23}$$

where $d\phi_3$ is the three-body final state phase-space and the hat denotes that the infra-red singularities have been subtracted. The hadroproduction cross-section resulting from the Eq. 2.23 is:

$$d\sigma = d\sigma^{(2)} + \sum_{\alpha\beta}\int dx_1 dx_2 \mathcal{L}_{\alpha\beta} d\hat{\sigma}_{\alpha\beta} \tag{2.24}$$

with $d\sigma^{(2)}$ that indicates the contribution to the cross-sections that are not already included (Born, soft-virtual etc. . .) and $\mathcal{L}_{\alpha\beta}$ parton-level luminosity. But, when NLO is matched to parton showers, the equation needs to be modified by the subtraction of MC counterterms. It is possible to choose to absorb this terms in $\hat{\mathcal{S}}_{\alpha\beta}$, because is the only piece that contains particular singularities. So the DR and DS cross sections become:

$$d\sigma^{(DR)} = d\sigma^{(2)} + \sum_{\alpha\beta}\int \frac{dx_1 dx_2}{2x_1 x_2 s}\mathcal{L}_{\alpha\beta}(\hat{\mathcal{S}}_{\alpha\beta} + \mathcal{I}_{\alpha\beta} + \mathcal{D}_{\alpha\beta} - \widetilde{\mathcal{D}}_{\alpha\beta}) d\phi_3 \tag{2.25}$$

$$d\sigma^{(DS)} = d\sigma - d\sigma^{subt} \tag{2.26}$$

where $d\sigma^{subt}$ is designed to remove numerically the doubly-resonant contribution and $\widetilde{\mathcal{D}}_{\alpha\beta}$ is defined such that $\mathcal{D}_{\alpha\beta} - \widetilde{\mathcal{D}}_{\alpha\beta}$ will vanish when $m^2_{\bar{b}W} \to m^2_t$. The DR cross-section has the problem to be not gauge invariant, but this is not a problem in practice, by repeating the DR calculation in a number of alternative gauges. Then, the difference between the two Eq. 2.26 and 2.25 is:

$$d\sigma^{(DS)} - d\sigma^{(DR)} = \sum_{\alpha\beta}\int \frac{dx_1 dx_2}{2x_1 x_2 s}\mathcal{L}_{\alpha\beta}(\mathcal{I}_{\alpha\beta} + \mathcal{D}_{\alpha\beta} - \widetilde{\mathcal{D}}_{\alpha\beta}) d\phi_3 \tag{2.27}$$

that depends on the interference term and the $\mathcal{D}_{\alpha\beta} - \widetilde{\mathcal{D}}_{\alpha\beta}$ difference.

A gauge invariant subtraction term can be found by choosing an appropriate value of the $\widetilde{\mathcal{D}}_{\alpha\beta}$.

Writing all this calculations in amplitudes notation we get:

$$|\mathcal{A}_{\alpha\beta}|^2_{DR} = \left|\mathcal{A}^{tW}_{\alpha\beta}\right|^2 \tag{2.28}$$

$$|\mathcal{A}_{\alpha\beta}|^2_{DS} = \left|\mathcal{A}^{tW}_{\alpha\beta} + \mathcal{A}^{t\bar{t}}_{\alpha\beta}\right|^2 - C^{SUB} \tag{2.29}$$

with C^{SUB} cross-section level subtraction term. From this equations we get:

$$|\mathcal{A}_{\alpha\beta}|^2_{DR} - |\mathcal{A}_{\alpha\beta}|^2_{DS} = 2\,\mathrm{Re}\{\mathcal{A}^{(Wt)}_{\alpha\beta}\mathcal{A}^{t\bar{t}}_{\alpha\beta}\} \tag{2.30}$$

There is also another approach, called **Diagram Removal 2 (DR2)** in which doubly resonant amplitudes are only included in the interference term, but it is less used with respect to the previous ones [37].

It exists also a dedicated *bb4l* process simulation which will be described in Section 6.2.2.

Chapter 3

The LHC collider

In December 1951 in Paris, after an intergovernmental meeting of UNESCO, was taken the first decision about the establishment of a European Council for Nuclear Research. Two months later, an agreement was signed, establishing the provisional council: the acronym CERN (*Conseil Européen pour la Recherche Nucléaire* in French) was born. After 18 months, the Council produced the first formal Convention. During the years, the main research topics of CERN moved from Nuclear Physics to High Energy Physics. Due to these reasons, its laboratory is often referred to as the European Laboratory for Particle Physics [46].

It hosts the largest proton accelerator of the world: the LHC (*Large Hadron Collider*). The latter contains four experiments, among which one of them is the ATLAS (*A Toroidal LHC ApparatuS*) experiment (described in Chapter 4). See Figure 3.1.

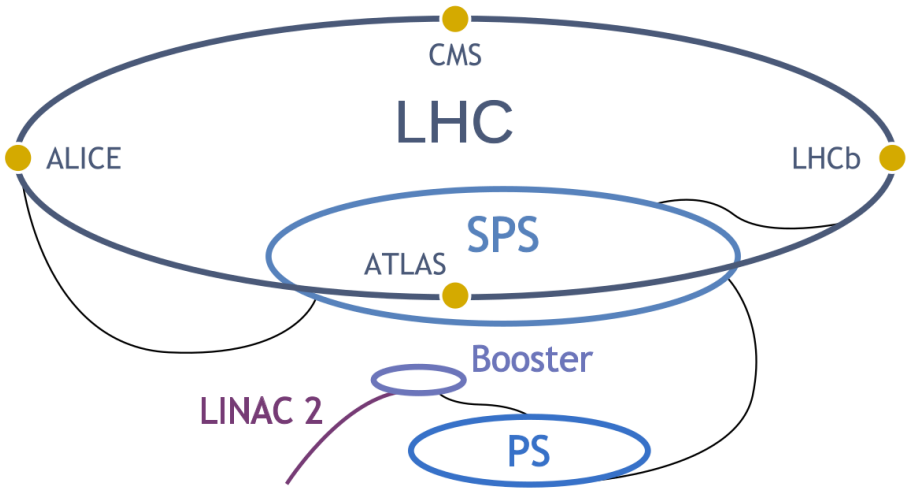

Figure 3.1: A sketch showing the complete structure of the LHC facility at CERN. There are the 4 main experiments (ATLAS, CMS, LHCb and ALICE) and the small accelerators that feed protons into the collider (PS, SPS, LINAC 2 and Booster) [47].

3.1 The collider layout

The LHC is situated in a 27 km tunnel that was constructed between 1984 and 1989 for the LEP (*Large Electron-Position*) collider at CERN, in Geneva. It is a two-ring-superconducting-hadron accelerator and collider. This tunnel has 8 straight sections and 8 arcs and lies between 45 m and 170 m below the surface of the *Léman lake*. There is a pair of tunnels that links the LHC to the CERN complex, each of them of approximately 2.5 km.

In December 1994, the CERN Council approved the LHC project. After exactly 2 years, in 1996, the Council approved the construction of the 14 TeV accelerator.

The previous accelerator (the LEP) needed almost 344 superconducting RF cavities, due to the high energy loss for radiation, caused by the small mass of the electron-positron (almost 500 keV) used as beam component:

$$E_{\text{loss}} \propto \frac{1}{m^4} \tag{3.1}$$

LHC collides protons that have masses of almost 10^3 times larger than the one of the electrons, so it needs only 8 superconducting RF cavities [48].

The collider contains two adjacent parallel beam pipes, separated by 194 mm, where beams circulate in opposite directions. The two pipes intersect only at four interaction points, where four experiments have been placed to detect particles produced in the collisions (see Figure 3.2). These experiments are:

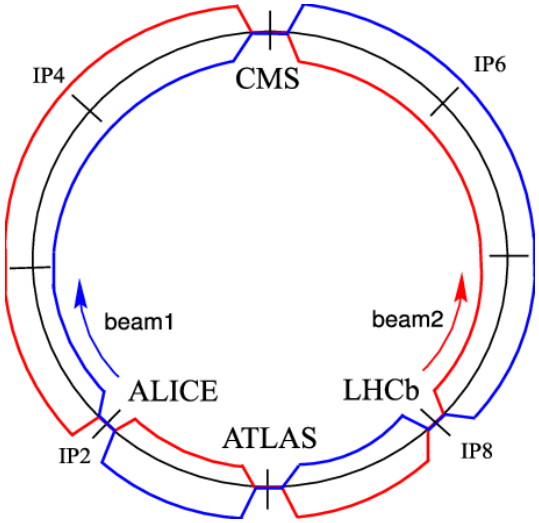

Figure 3.2: Minimal layout of the LHC structure: there are 8 interaction points (IPs) in total, which only 4 of them host the detectors (ATLAS, CMS, ALICE and LHCb). Beam 1 and beam 2 are circulating in opposite direction [49].

- ATLAS (*A Toroidal LHC ApparatuS*): designed for "general purposes" in particle physics.
- CMS (*Compact Muon Solenoid*): designed for purposes similar to ATLAS.
- LHCb (*Large Hadron Collider beauty*): dedicated to bottom quark physics and CP violation studies.
- ALICE (*A Large Ion Collider Experiment*): is dedicated to the study of collisions of heavy ions (Pb-Pb collisions), for quark-gluon plasma studies.

Proton or heavy-ion beams circulate along the LHC ring inside vacuum tubes, "driven" by magnets. The vertical magnetic field in the dipoles curves the beams by the Lorentz force and keeps them on a circular trajectory. To maintain in orbit these high energy beams, superconducting magnets are used, cooled by a huge cryogenic system.

3.2 Luminosity

A very important quantity in colliders is the **luminosity**. The **instantaneous luminosity** $\mathcal{L}$ is defined as the ratio between the rate of produced events R and the cross-section of the considered process, σ:

$$\mathcal{L} = \frac{R}{\sigma} \tag{3.2}$$

Units of measurement are $\mathrm{cm}^{-2}\mathrm{s}^{-1}$. The instantaneous luminosity depends on beam properties:

$$\mathcal{L} = \frac{N_p^2 n_b f \gamma}{4\pi\epsilon_n \beta^*} F \tag{3.3}$$

where N_p is the number of protons, n_b is the number of bunches per beam, f is the revolution frequency, $\gamma = E/m$ is the relativistic factor (E is the energy), ϵ_n is the normalized beam emittance, β^* is the beam beta function or focal length at the collision point and F is the luminosity reduction factor due to the crossing angle at the interaction point (IP). The latter is defined as:

$$F = \left(1 + \frac{\theta_c \sigma_z}{2\sigma_{xy}}\right) \tag{3.4}$$

where θ_c is the beam crossing angle and σ_z and σ_{xy} are the longitudinal and transverse RMS beam sizes at the interaction point.
ATLAS is one of the highest luminosity experiments at the LHC and aims at a peak luminosity of:

$$\mathcal{L} = 1 \times 10^{34}\ \mathrm{cm}^{-2}\mathrm{s}^{-1} \tag{3.5}$$

The high beam intensity required for such a high luminosity excludes the use of anti-proton beams and hence exclude the particle-antiparticle ($p\bar{p}$) collision in this case. The LHC is designed as a proton-proton (or ion) collider, with separate magnetic fields and vacuum chambers in the main arcs and with common sections only in the regions in which the detector lies. The two beams share a 130 m long common beam pipe along the interaction points.

The number of circulating protons (N_p) is usually of the order of $O(10^{11})$. Together with the large number of bunches (n_b), that corresponds to $\approx$ 2808 for each proton beam, and a nominal bunch spacing of 25 ns, other nominal parameter values are: $N_b = 1.1 \times 10^{11}$ (particles per bunch), $f = 11.2$ kHz, $\epsilon_n = 3.75$ µm, $\beta^* = 0.55$ m, $\theta_c = 285$ μrad, $\sigma_{xy} = 16.7$ µm and $\sigma_z = 7.55$ cm.

The peak beam energy depends on the integrated dipole field around the storage ring, which implies a peak dipole field of 8.33 T for the 7 TeV in the LHC and the use of superconducting magnet technology.

Another very important parameter is the **luminosity integrated in time** (T), defined as the ratio of the number of events N produced at a rate R with a certain cross section σ:

$$L = \int_0^T \mathcal{L}\ dt = \frac{N}{R} \tag{3.6}$$

which is measured in fb^{-1}. LHC delivered an integrated luminosity of $5.6\,\mathrm{fb}^{-1}$ of $p\bar{p}$ collision data at the CM energy of 7 TeV in 2010 and 2011. In 2012 the energy was increased up to 8 TeV and the LHC luminosity was upgraded significantly; in that period

ATLAS recorded an amount of luminosity around 14.3 fb^{-1} [50]. During the Run-2 period, from 2015 to 2018, at a CM energy of 13 TeV, it collected a total integrated luminosity of 140 fb^{-1}. In Figure 3.3 the total integrated luminosities collected by ATLAS and the recorded luminosities in function of the number of interactions per crossing of each year of Run-2 are shown.

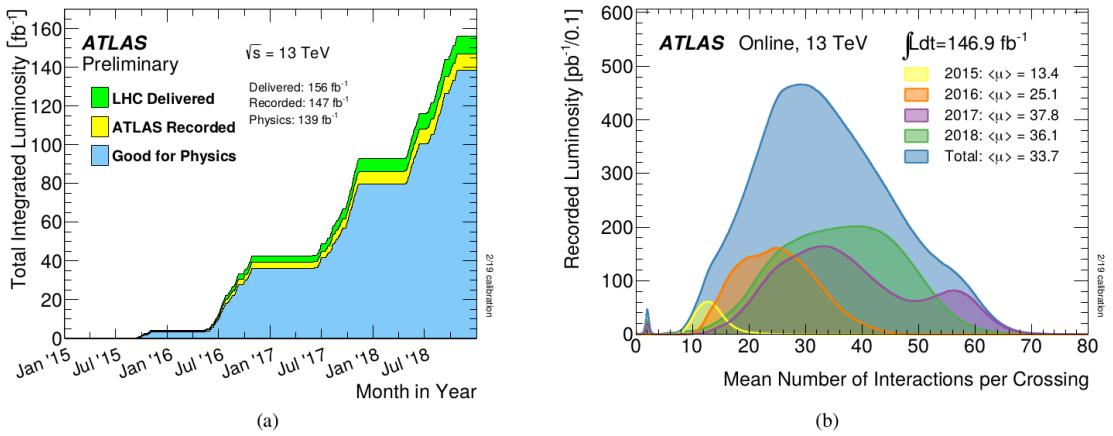

(a) (b)

Figure 3.3: Figure (a): total integrated luminosity collected by ATLAS in Run-2. Figure (b): recorded luminosity as a function of the number of interactions per crossing in each year of Run-2 [51].

3.3 Magnets

The LHC relies on **superconducting magnets**, that are at the edge of the present technology. It makes use of the well-proven technology based on NbTi Rutherford cables and cools the magnets to a temperature below 2 K, with superfluid He operating at magnetic fields above 8 T. Such a reduced temperature leads to a significant reduction of the heat capacity of the cable by almost an order of magnitude, therefore the energy deposit that can trigger a quench[1] is substantially reduced. This means that the temperature margin must be larger and is needed a tight control of movements and heat dissipation inside cables. Due to the increasing of the electromagnetic forces (that increase with the square of the magnetic field), the structure retaining the conductor motion must be stronger than the previous designs.

The major part of the LHC magnets adopt the so called "two-in-one" structure: the windings for the two beam channels lie in a common cold mass and cryostat, with

[1] A quench is an abnormal termination of magnet operation that occurs when part of the superconducting coil enters the normal resistive state.

magnetic flux circulating in the opposite sense through the two channels. A cross-section of one of the LHC magnet with its components is shown in Figure 3.4. In this

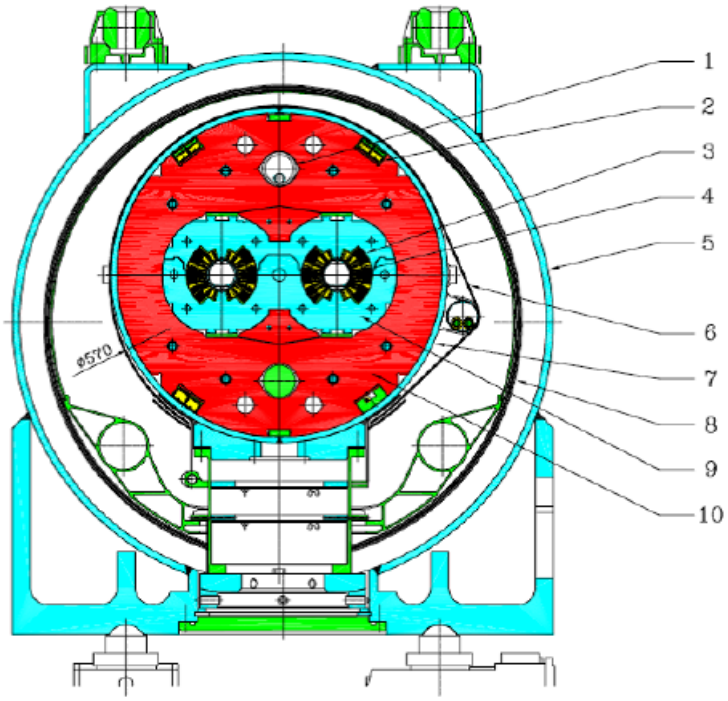

Figure 3.4: Cross-section of an LHC magnet. It consists of the following parts: (1) heat exchanger pipe, (2) superconducting busbars, (3) superconducting coils, (4) beam screen, (5) vacuum vessel, (6) radiation screen, (7) shrinking cylinder, (8) thermal shield, (9) non magnetic collars and (10) iron yoke [52].

configuration there are $O(1000)$ dipoles to guide the beam and $O(400)$ quadrupoles to focus it. Dipole magnets are done by copper-clad steel (CCS) with cables of NbTi, as mentioned above. For a 8 T field a $O(1200)$ Ampère current and a 2 in 1 magnet design are required.

3.4 Beam injection and acceleration

The injection of particle beams into the LHC is performed in the **injection insertions**, that are the IP2 and IP8 (see Figure 3.2). In both the insertions, the beam approaches the LHC from outside and below the machine plane. Then, a series of dipoles direct the beam in the injection line towards five magnets, which deflect the beam horizontally by 12 mrad under the outer ring. A series of four kicker magnets deflects the beam vertically by 0.85 mrad onto the closed orbit. It is also used an injection beam stopper

(TDI) placed 15 m upstream of the superconducting recombination dipole, supplemented by an additional shielding element in a way to facilitate the procedure and to protect the collider in case of problems related to kickers. To complete the protection, also two collimators are used. The geometrical layout is very similar for both the IP regions, however optics vary between them, due to displaced interaction point in IP8.

Protons at the LHC are provided from the following injectors: **Linac2**, **PSB** (*Proton Synchrotron Booster* or simply *Booster*), **PS** (*Proton Synchrotron*) and **SPS** (*Super Proton Synchrotron*); see Figure 3.1 for their representation in the LHC structure. This accelerators have been upgraded to satisfy all the LHC requirements (see Section 3.2). There are many conditions that have to be satisfied for the beam, the most important are:

- Beam emittance[2] has to fit the small aperture of the LHC superconducting magnets.
- Beam intensity has to be limited by the synchrotron radiation which is absorbed by the cryogenic system.
- Spread in betatron tunes caused by the beam-beam effect during beams collision needs to be kept under control.
- Space-charge limits in the injector have to be respected.

The intensity that SPS is able to accelerate (almost 4×10^{13} protons per cycle) limits the number of PS pulses per SPS cycle to a maximum of 4. The momentum spread acceptance of the PS-SPS line is about $\pm 0.2\%$ in $\Delta p/p$ and the total bunch lenght has to be below 4 ns to fit the SPS accelerating system. This last requirement implies a longitudinal emittance of 0.35 eV per PS bunch. During the SPS acceleration, the longitudinal emittance is increased up to 1 eV.

PSB is composed by 4 rings, all them are normally ejected and sequentially transferred to fill the PS in one go, for example, for the SPS beam with two bunches per ring [54].

[2]Beam emittance is defined as the area covered by the beam. There can be both horizontal and vertical beam emittance [53].

Chapter 4

The ATLAS detector

As mentioned at the beginning of Chapter 3, the LHC hosts 4 big experiments which one of them is the ATLAS experiment. ATLAS is a multipurpose detector, built for probing proton-proton collisions at very high energies [55]. It is forward-backward symmetric with respect to the interaction point. Its main **sub-components** are:

- Magnetic System (Section 4.2).
- Tracking system (Section 4.3).
- Electromagnetic and hadronic calorimeters (Section 4.4).
- Muon spectrometer (Section 4.5).

It contains also an inner solenoid, an outer toroidal magnetic field and trigger, readout, DAQ (Data Acquisition) and control Systems (Section 4.6). Its dimensions are 25 m in height and 44 m in length. The weight of the whole detector is almost 7000 t (see Figure 4.1). It is located at almost 100 m underground at IP1 of the LHC ring (see Figure 3.2). In addition to the main just mentioned components, there are also three smaller sets of detectors with the purpose of providing a good coverage in the forward region; from here, the name **forward detectors**. They are:

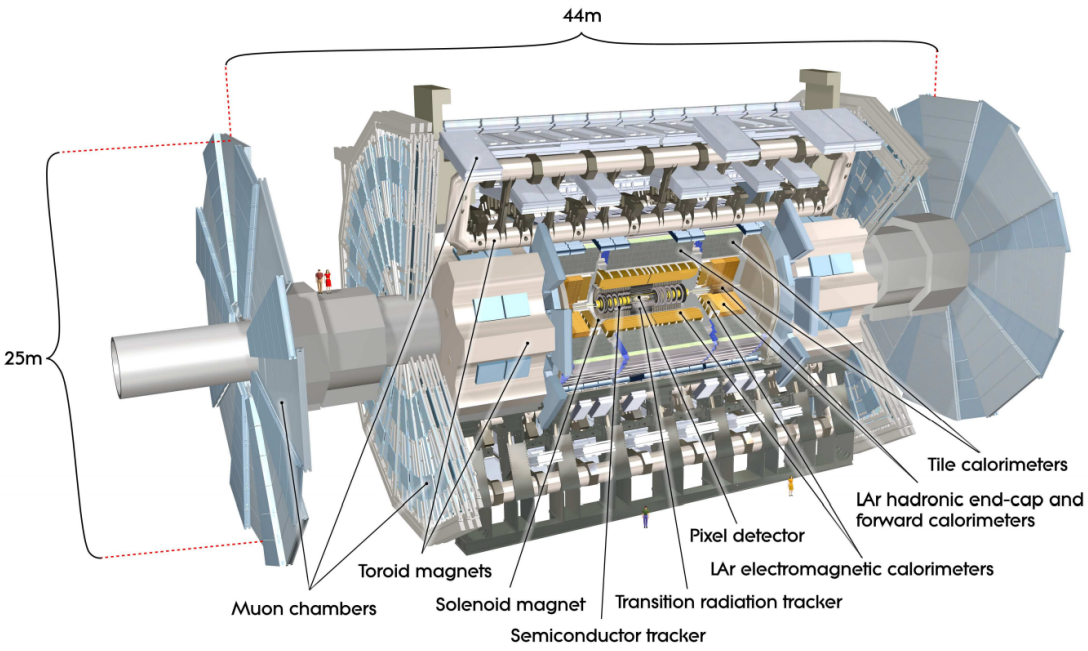

Figure 4.1: View of the main components of the ATLAS detector. The dimensions are 25 m in height $\times$ 44 m in length. It is composed by: muon chambers, toroid magnets, solenoid magnet, tracker system (pixel detector, semiconductor tracker and transition radiation tracker), liquid Argon electromagnetic and hadronic calorimeters and tile calorimeters [56].

- **LUCID** (*LUminosity measurement using Cherenkov Integrating Detector*): it is a Cherenkov detector.
- **ZDC** (*Zero Degree Calorimeter*): located at ±140 m from the IP. It detects forward neutrons in heavy-ion collisions.
- **ALFA** (*Absolute Luminosity For ATLAS*): it consists of scintillating-fibre trackers located at a distance of ±240 m from the IP. It is dedicated to total cross-section measurement.

Also additional proton-tagging detectors are considered at an even greater distance from the IP of about ±420 m.

4.1 Detector reference frame and requirements

In ATLAS a **right-handed Cartesian reference frame** is used. Collisions are produced in the origin, centered in the interaction point:

- The horizontal x-axis is pointing towards the center of the LHC ring.
- The vertical y-axis is pointing upwards.
- The z-axis is tangent to the beam line.

The x-y plane, orthogonal to the beam pipe, is called the **transverse plane** while the z-axis direction is called **longitudinal plane**. Due to the cylindrical symmetry polar coordinates can be used (see Figure 4.2 for a graphical representation):

- $\vec{r}$ is the distance from the interaction point, in the transverse plane x-y:

$$\vec{r} = \sqrt{x^2 + y^2} \tag{4.1}$$

- ϕ is the azimuthal angle, measured from the x-axis in the transverse plane and takes value from $-\pi$ to $+\pi$.
- θ is the polar angle, measured from the z-axis in the longitudinal plane z-y and takes values from 0 to $+\pi$.

Most used variables are:

- The **transverse momentum** $p_T = |\vec{p}| \sin\theta$. "Invisible" particles that escape along the beam pipe have $p_T \approx 0$, so they are out of acceptance. The "visible" p_T is conserved ($\sum_i p_{t,i} \approx 0$). However $\vec{p}$ and θ are not Lorentz invariant along z.

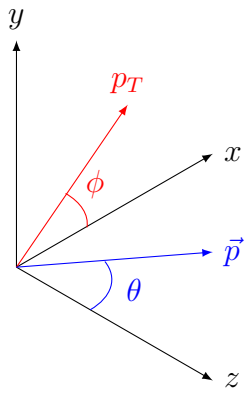

Figure 4.2: Graphical representation of the right-handed Cartesian reference frame: the x-axis is pointing towards the center of the LHC, the y-axis is pointing upwards and the z-axis is tangent to the beam line. The angles ϕ and θ are respectively the azimuthal angle from the x-axis in the transverse plane and the polar angle measured from the z-axis in the x-y longitudinal plane. Furthermore, $\vec{p}$ is the momentum and p_T its transverse component.

- The **rapidity** y:
$$\vec{\mathrm{y}} = \frac{1}{2}\ln\frac{E+p_z}{E-p_z} = \frac{1}{2}\ln\frac{1+\beta\cos\theta}{1-\beta\cos\theta} \tag{4.2}$$

- The **pseudo-rapidity** η, which for $\beta \to 1$ ($m << p_t$):
$$\eta = -\ln\left(\tan\frac{\theta}{2}\right) \tag{4.3}$$
It is commonly used to describe the relative angle between a particle and the beam axis. Forward direction refers to the region which is close to the beam axis, corresponding to high values of $|\eta|$ (see Figure 4.3).

The Δy and $\Delta\phi$ are invariant for Lorentz boosts along z-axis. The pseudo-rapidity is useful also to describe the angular distance between 2 particles:
$$\Delta R = \sqrt{\Delta\eta^2 + \Delta\phi^2} \tag{4.4}$$

Global **requirements** that ATLAS must satisfy for the LHC collider are:

- Fast, radiation-hard electronics and sensor elements. High detector granularity[1] is needed to handle the particle fluxes and to reduce the overlapping of events.
- Large acceptance in pseudo-rapidity with almost full azimuthal angle coverage.

[1]The granularity is defined as how much is sensitive the detector for unit cell (related to the tracker).

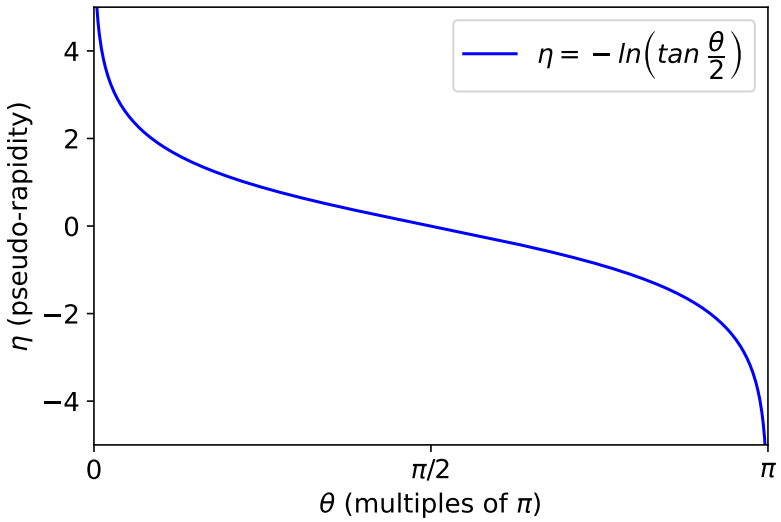

Figure 4.3: Pseudo-rapidity as a function of the polar angle θ.

- Good resolution for charged-particle momentum and efficiency in the tracking system.
- Very good electromagnetic calorimetry for electron and photon identification, complemented by an hadronic calorimetry for jets and missing transverse energy measurements.
- Good muon identification and momentum resolution and the ability to determine unambiguously the charge of high p_T muons.
- Excellent trigger system for low transverse momentum objects with a good background rejection.

Electromagnetic calorimeters cover the pseudo-rapidity range $|\eta| < 3.2$. The hadronic calorimetry covers the range $|\eta| < 1.7$ and $|\eta| > 1.5$, matching the outer limits of endcap electromagnetic calorimeters. The forward calorimeters provide both electromagnetic and hadronic energy measurements and extend the pseudo-rapidity to $|\eta| = 4.9$. General performance goals of the ATLAS detector are shown in Table 4.1.

Detector Component	Required Resolution	η coverage	
		Measurement	Trigger
Tracking	$\sigma_{p_T}/p_T = 0.05\%\ p_T \oplus 1\%$	± 2.5	
EM Calorimetry	$\sigma_E/E = 10\%/\sqrt{E} \oplus 0.7\%$	± 3.2	± 2.5
Hadronic Calorimetry (jets)			
barrel and end-cap	$\sigma_E/E = 50\%/\sqrt{E} \oplus 3\%$	± 3.2	± 3.2
forward	$\sigma_E/E = 100\%/\sqrt{E} \oplus 10\%$	$3.1 < \lvert\eta\rvert < 4.9$	$3.1 < \lvert\eta\rvert < 4.9$
Muon Spectrometer	$\sigma_{\vec{p}_T}/\vec{p}_T = 10\%$ at $\vec{p}_T = 1\,\text{TeV}$	± 2.7	± 2.4

Table 4.1: General performance goals of the ATLAS detector: the required resolution and the η coverage (for measurement and trigger) of each main component of the ATLAS experiment are shown.

4.2 Magnet system

The ATLAS unique hybrid magnet system is composed by 4 **superconducting magnets**. The dimensions of the system are 22 m in diameter for 26 m in lenght, with a stored energy of 1.6 GJ. Superconducting magnets provide a magnetic field over a total volume of almost 12 000 m^3. This is defined as the region in which the field exceeds, with an intensity of 50 mT. The system is composed mainly by:

- A **solenoid**: it is aligned on the beam axis and provides an axial magnetic field of 2 T for the inner tracker and minimize the radiative thickness in front of the barrel electromagnetic calorimeter.
- A **barrel toroid** and **two end-cap toroids**: they provide a total toroidal magnetic field of 0.5 T and 1 T for the muon detector, respectively in the central and end-cap regions. Each end cap toroid contains eight racetrack coils, mounted as a single cold mass in a cryostat vessel of approximately 10 m diameter [57].

A brief representation of the position of the magnets in the detector is shown in Figure 4.1. A more representative geometry of the magnet system is shown in Figure 4.4.

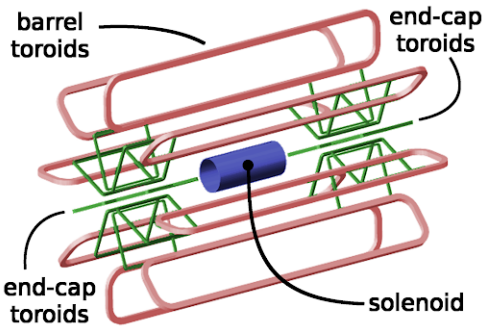

Figure 4.4: Geometrical representation of the magnet system. It is formed by: barrel toroids, solenoid and two end-cap toroids. The eight barrel toroid coils with the end-cap coils interleaved are visible. The solenoid winding lies inside the calorimeter volume [58].

4.3 Tracking system

The **Inner Detector** (*ID*) constitutes an important part of the tracking system of ATLAS. Its purpose is to reconstruct charged particles tracks and vertices (its tracking measurements are in a range matched by precision measurements of the electromagnetic calorimeter) and to measure their momentum, which must lie above a given value of the transverse momentum and within the pseudo-rapidity range $|\eta| < 2.5$. Its dimensions are 2.1 m in height and 6.2 m in lenght. It consists of three types of sub-detectors: **Pixel Detector**, **Semiconductor Tracker** (*SCT*) and **Transition Radiation Tracker** (*TRT*) (see Figure 4.5). All the sub-detectors are contained within a cylindrical envelope of 3512 mm lenght and radius 1150 mm in the barrel region. While, in the end-cap regions they're located on disks perpendicular to the beam axis. This setup is surrounded by a magnetic field of 2 T.

The Pixel Detector is the one with the highest granularity and is situated very close to the interaction point. It has 1744 modules that are arranged in three barrel layers and two end-caps each with three disk layers. Its intrinsic spatial resolution[2] is 10 µm in $R-\phi$ and 115 µm in z. All pixel sensors are identical and have a minimum pixel size in $R-\phi \times z$ of 50×400 µm.

The Semiconductor Tracker is a silicon detector with microstrips which surrounds the Pixel Detector layers. It provides 8 measurements per track with resolution of 16 µm in $R-\phi$ and 580 µm in z. It consists of 4088 modules tiling four coaxial cylindrical layers in the barrel region and two end-caps each containing nine disk layers.

The TRT is the outermost and provides typically more than 30 hits per track. It has a very good pattern recognition and contributes also to particle identification. It is composed by gaseous counter, filled with Xe, CO_2 and O_2 mixtures. It contains up to 73 layers of tubes interleaved with fibres and 160 straw planes interleaved with foils

[2]Pixel layers are segmented in $R-\phi$ and z with typically three pixel layers crossed by each track.

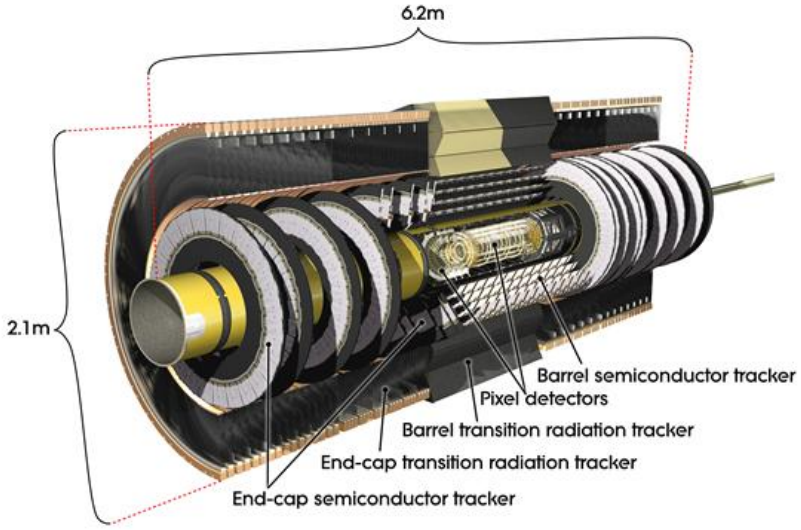

Figure 4.5: Layout of the ATLAS Inner Detector. It is formed by: semiconductor tracker, transition radiation tracker and pixel detectors.

(end-cap), which provide transition radiation for electron identification.

Tracks above a given p_T threshold are reconstructed offline within the full acceptance range $|\eta| < 2.5$ of the whole Inner Detector, using multi-stage track identification algorithms.

4.4 Calorimetry

ATLAS has an **electromagnetic** (*EM*) and an **hadronic** (*HAD*) **calorimeters**. EM calorimeter is divided into a *barrel part* and two *end-cap* components; instead HAD calorimeter is composed by *tile*, *end-cap* and *forward* calorimeter regions (see Figure 4.6). All them cover the range $|\eta| < 4.9$ using different techniques, related to the physics processes. Over the η region matched to the inner detector, the EM calorimeter fits ideally for the measurements of electrons and photons. The rest of the calorimeter is useful for the reconstruction of the jets topology and the measurement of the missing transverse energy E_T^{miss}.

The main purpose of calorimeters is to contain electromagnetic and hadronic showers; this implies that the depth is a very important parameter. The total thickness of the EM calorimeter is more than 22 X_0 (radiation lengths) in the barrel with 9.7 λ interaction lengths and more than 24 X_0 in the end-caps, with 10 interaction lengths. The total thickness is 11 λ at $\eta = 0$.

As mentioned before, the EM calorimeter has a barrel part, that covers the region $|\eta| < 1.475$ and two end-cap components, covering the region $1.375 < |\eta| < 3.2$. The

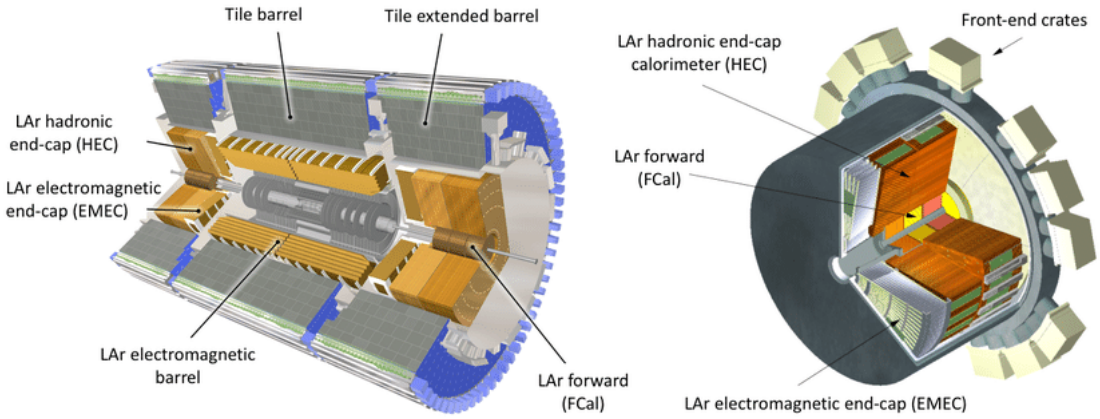

Figure 4.6: "Cut-away" view of the ATLAS calorimetry. EM calorimeter is divided into a barrel part and two end-caps components. HAD calorimeter is composed by tile, end-cap and forward calorimeter regions [59].

central solenoid is in front of the EM calorimeter. As a consequence, the latter and the calorimeter share a common vacuum vessel. The barrel EM calorimeter is composed by two coaxial wheels: an outer wheel that covers the region $1.375 < |\eta| < 2.5$ and an inner one for the region $2.5 < |\eta| < 3.2$. Over the region devoted to precision physics ($|\eta| < 2.5$) the whole calorimeter is segmented into three sections in depth. Regarding the end-cap inner wheel, the calorimeter is segmented into two sections in depth. In the region $|\eta| < 1.8$ a pre-sampler detector is used; it consists of an active layer of LAr, which is used to absorb the energy lost by electrons and photons upstream the calorimeter.

HAD calorimeter is composed by:

- **Tile calorimeter**: placed directly outside the EM calorimeter envelope. It has a barrel that covers the region $|\eta| < 1.0$ and two extended barrels in the range $0.8 < |\eta| < 1.7$. It is a sampling calorimeter which uses steel as absorber and scintillating tiles as active material. The tile calorimeter extends radially from an inner radius of 2.28 m to an outer one of 4.25 m. It is segmented into three layers of approximately 1.5, 4.1 and 1.8 λ for the barrel and 1.5, 2.6 and 9.7 λ at $\eta = 0$.

- **LAr hadronic end-cap calorimeter**: it consists of two wheels per end-cap which are located behind the EM calorimeter. It extends out to $|\eta| = 3.2$ to reduce the transition between the end-cap and the forward calorimeter, which lies at $|\eta| = 3.1$. It overlaps also the tile calorimeter ($|\eta| < 1.7$) by extending up to $|\eta| = 1.5$. The wheels closest to the interaction point are built from 25 mm parallel copper plates, each of them with an outer radius of 2.03 m; while those further away use 50 mm copper plates, with an inner radius of 0.475 m.

- **LAr forward calorimeter**: provides coverage in the region $3.1 < |\eta| < 4.9$

[60].It is integrated into the end-cap cryostats and provides benefits in terms of the calorimetric coverage, by reducing radiation background levels in the muon spectrometer. It has approximately 10 λ depth and consists of three modules in each end-cap: one, in copper, is for electromagnetic measurements, while the other two, in tungsten, are for the measurement of the hadronic interaction energy.

4.5 Muon spectrometer

The muon spectrometer of the ATLAS detector is composed by the following sub-detectors: **monitored drift tubes** (*MDTs*), **cathode strip chambers** (*CSC*), **resistive plate chambers** (*RPCs*) and **thin gap chambers** (*TGCs*). See Figure 4.7 for a cut-away view of the sub-detector. This detector is based on the magnetic deflection

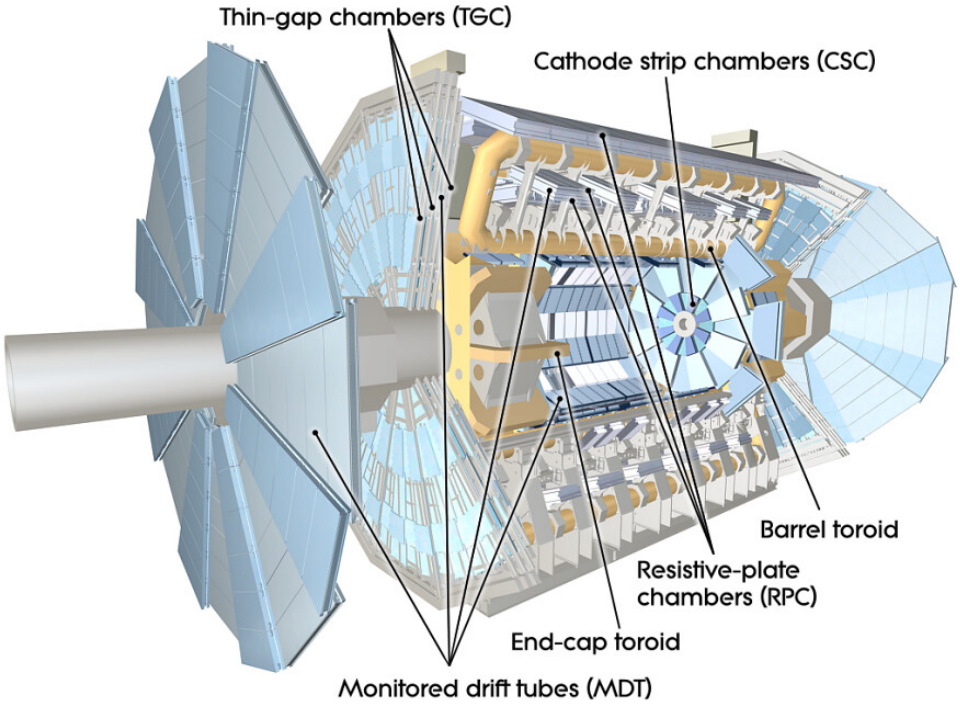

Figure 4.7: Cut-away view of the ATLAS muon spectrometer. The spectrometer is composed by: monitored drift tubes (MDTs), cathode strip chambers (CSC), resistive plate chambers (RPCs) and thin gap chambers (TGCs). It has also a barrel and an end-cap toroid. Its dimensions are 24 m in diameter by 44 m in length.

of muon tracks in the large superconducting air-core toroid magnets, instrumented with separate trigger and high-precision tracking chambers in which is is ensured a three-point measurement of tracks [61]. Its momentum resolution is $2-3\%$ at $10-100\,\mathrm{GeV/c}$ and

10% at 1 TeV. The latter quantity is estimated by taking into account also the high-level background environment, the inhomogeneous magnetic field and the large size of the apparatus, that is 24 m in diameter and 44 m in lenght.

The barrel toroid provides a magnetic bending for $|\eta| < 1.4$. In the region $1.6 < |\eta| < 2.7$ muon tracks are bent by two smaller end-cap magnets, inserted into both ends of the barrel toroid, mentioned before. Finally, in the transition region $1.4 < |\eta| < 1.6$ magnetic deflection is provided with the barrel and end-cap fields together. Thanks to this magnet configuration, the field is orthogonal to the muon trajectories and minimizes the degradation of resolution due to multiple scattering.

The choice of some performance parameters like the rate capability, the granularity, the ageing properties and the radiation hardness is affected by the high level of particle flux in the geometrical region covered.

In the barrel region, all the tracks are measured in detector chambers arranged in three cylindrical layers around the beam axis, instead, in the transition and end-cap regions, the chambers are situated in planes perpendicular to the beam, always in three layers.

Precision measurement of the muon tracks in the main bending direction of the magnetic field are performed by the MDTs. The three stations of the RPCs provide the trigger function, the bunch-crossing identification and the second coordinate measurements in the end-cap regions. Chambers in the barrel are placed at three different radii with respect to the beam line.

Regarding the MDTs each sense wire of the drift tubes is isolated in a way to guarantee a reliable operation. The higher granularity CSCs in the innermost plane are used in the region $2 < |\eta| < 2.7$ to front the demanding rate and background conditions.

The overall performance over the large areas, in particular at highest momenta, depends on the alignment of the muon chambers with respect to each other and with respect to the overall detector. The singular muon momentum measurement needs a precision of 30 µm on the alignment, both within each projective tower and between consecutive layers in immediately adjacent towers. Relative positions of the MDT chambers are monitored by 12000 sensors. The accuracy needed for the relative positioning of non adjacent towers to obtain a good mass resolution for multi-muon final states lies in the range of few mm.

During my PhD I worked on the operation and performance of the RPC detector system and my activity is reported in A.

4.6 Trigger and DAQ system

The ATLAS **TDAQ** (*Trigger and Data Acquisition*) system is responsible for *online processing* and selecting and storing of the events of interest. Events are selected using a two-stage trigger system, composed by: **Level-1** (*L1*) and **High-Level Trigger** (*HLT*)

steps [62]. A diagram of the whole TDAQ system is shown in Figure 4.8. The L1

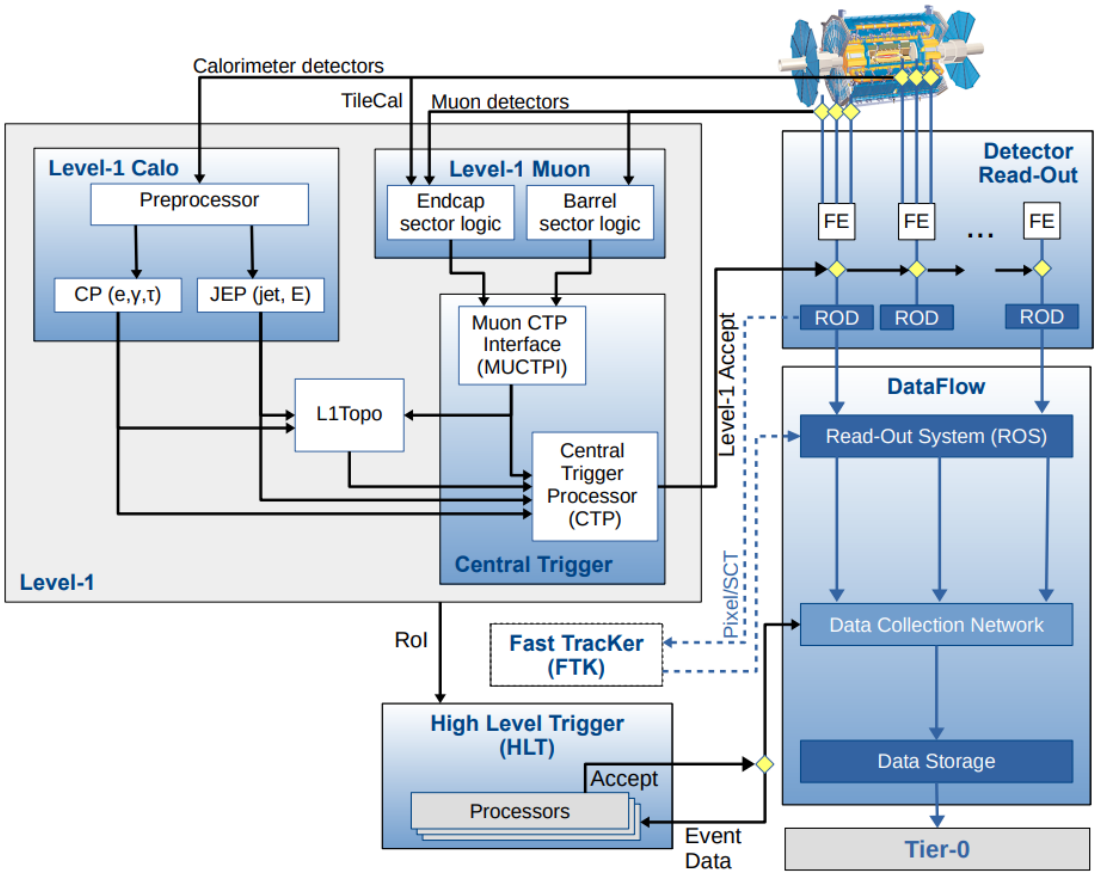

Figure 4.8: Block diagram of the ATLAS TDAQ system. It is possible to see the two-stage trigger system (L1 and HLT) and the detector read-out with data flow.

trigger is an hardware-based system that uses custom electronics to trigger on reduced-granularity information from the calorimeter and muon detectors. The **L1 calorimeter** (*L1Calo*) trigger takes signal from the calorimeter detectors as input. The analogue detector signals are digitized and calibrated by the preprocessor and sent in parallel to the *Cluster Processor* (*CP*) and *Jet/Energy-sum Processor* (*JEP*). This CP system identifies electrons, photons and τ-leptons candidates above a certain threshold, while the JEP identifies jets candidates and produces global sums of total and missing transverse energy (MET). Some objects with narrow clusters, such as electronics, aren't too much affected by small energy shifts, but the missing transverse momentum is very sensitive to small systematic shifts in energy over the entire LAr calorimeter. These effects are treated in the L1Calo trigger with a dedicated correction algorithm.

The **L1 muon trigger** (*L1Muon*) uses hits from the RPCs in the barrel and TGCs in the endcaps, in order to determine the deviation of the hit pattern from that of a muon with infinite momentum.

The **L1 trigger decision** is composed by: the *Central Trigger Processor* (*CPT*), which receives inputs from the L1Calo trigger, the *L1Muon Central Trigger Processor Interface* (*MUCTPI*) and the *L1 topological trigger* (*L1Topo*) [63]. In this decision also trigger signals from detector subsystems (LUCID Cherenkov for example) are considered. The CPT is responsible for applying the *dead time*, which is a mechanism used to limit the number of L1 accepts to be within constraints on the detector read-out latency.

The L1 trigger can also select events by considering event-level quantities (such as the total energy in the calorimeter), the multiplicity of objects above thresholds (such as the p_T of a muon) and the topological requirements (invariant masses for example). The L1 trigger accept events up to a rate of 100 MHz, down from the bunch crossing rate of 40 MHz, within a latency of 2.5 µs.

For each L1-accepted event, the **Front-End** (*FE*) detector electronics reads out the event data for all detectors. Events are sent first to the *ReadOut Drivers (RODs)*, for the preprocessing and then to the *ReadOut System (ROS)* for the data buffering. The L1 trigger defines also the so called **Regions of Interest** (*RoI's*) in which interesting events are selected and identified with η and ϕ coordinates.

After passing the first stage, selected events enter the second stage of the triggering, which is the software-based HLT trigger. For this reconstruction sequence dedicated fast trigger algorithms are used. These algorithms are executed on a computing farm, composed by 40000 selection applications called *Processing Units* (*PUs*). In this selection part, in some cases, information from the full detector are requested in order to reconstruct physics objects. The physics output rate of the HLT during an ATLAS data-taking run is on average 1.2 kHz with an average physics throughput to permanent storage of 1.2 GB/s.

Once the event passes the L1 and HLT, the *Sub-Farm Output* (*SFO*) sends the data to permanent storage for offline reconstruction and exports the data to the *Tier-0* facility at CERN computing center.

Chapter 5

Objects reconstruction

The **object reconstruction** is a fundamental step in particle physics analyses. It consists on the reconstruction and identification of particles produced after the pp collision in the detector. For our analysis, the most important objects we have to take into account are *electrons* (described in Section 5.1) and *muons* (described in Section 5.2). Other important objects are: *jets* (described in Section 5.3) and *missing transverse energy* E_T (described in Section 5.4). Finally in Section 5.5 the *overlap removal* problem is treated.

5.1 Electron reconstruction

As mentioned in Chapter 2, electrons are fundamental ingredients for the study of the $WbWb$ process final state, in the ee and $e\mu$ channels for example. They are reconstructed

combining EM calo and tracking information. The total efficiency for the charged electron reconstruction is given by[1]:

$$\epsilon_{\text{total}} = \epsilon_{\text{reco}} \cdot \epsilon_{\text{id}} \cdot \epsilon_{\text{iso}} \cdot \epsilon_{\text{trig}} \tag{5.1}$$

which depends on the *reconstruction efficiency* ϵ_{reco}, the *identification efficiency* ϵ_{id}, the *isolation efficiency* ϵ_{iso} and the *trigger efficiency* $\epsilon_{\text{trigger}}$. Only for the electrons, a factor ϵ_{EMclus} which indicates the efficiency to reconstruct in the EM calorimeter by the EM-cluster candidates (which are localized energy deposits) associated with all produced electrons is added.

A **scale factor**, defined as the ratio between data and MC predictions is used to correct the efficiencies in the MC simulation, to match those observed in data[2] [64].

Electrons from the process of interest are difficult to discriminate from other large backgrounds as misidentified hadrons, electrons from photon conversion and non-isolated electrons originating from heavy-flavor decays. The fraction of each background event is reduced by imposing the different ID/isolation criteria.

Electrons can lose a significant amount of their energy due to bremsstrahlung when they interact with nuclei of the material they cross. Photons radiated through the process may convert into an electron-positron pair that can interact with the detector material. All this objects (positrons, electrons and photons) are usually emitted in a collimated beam and are reconstructed as part of the same EM cluster. These interactions can occur inside the inner tracker volume or even in the beam pipe, by generating tracks in the inner detector, or can occur downstream of the inner tracker, by impacting the shower only in the EMCAL. So, it is possible to produce and match multiple tracks to the same EM cluster, all them originating from the same primary electron.

The electron reconstruction in the ATLAS precision region ($|\eta| < 2.47$) is given by the EMCAL and the inner tracker. It is based on three components, characterizing the signature of electrons: localized clusters of energy deposits found within the EMCAL, charged-particle tracks identified in the inner tracker and close matching in $\eta \times \phi$ space of the tracks to the clusters to form the final electron candidates. See Figure 5.1 for a schematic view of the path of an electron through the detector.

[1] The procedure is the same also for the other leptons.

[2] It is a multiplicative scale factor for the simulation.

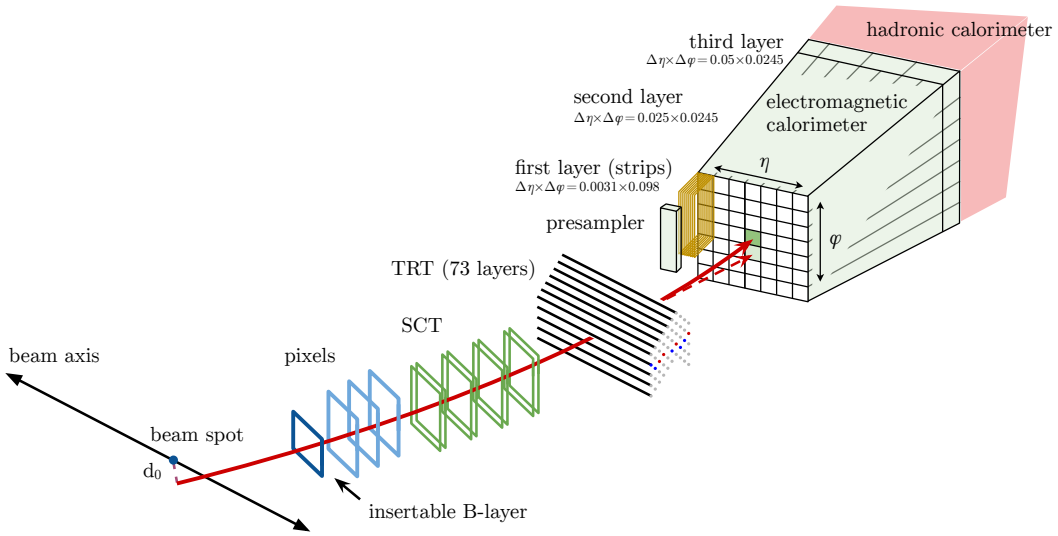

Figure 5.1: Schematic view of the path of an electron through the detector. The red line is the hypothetical trajectory of an electron traversing first the tracking system and then entering the EMCAL. The dashed line indicates the path of a photon produced via bremsstrahlung in the tracking system [65].

5.1.1 Electron identification

To select electrons entering the $|\eta| < 2.47$ region a **likelihood-based identification (LH)** is used. All the inputs to the LH include measurements from the tracking system, the calorimeter system and quantities that combine both their information. Also probability density function (pdf) based on simulated events are constructed.

The LH is based on the products for signal L_S and for background L_B of n pdfs and is given by:

$$L_{S(B)}(\vec{x}) = \prod_{i=1}^{n} P_{S(B),i}(x_i) \tag{5.2}$$

where $\vec{x}$ are n-component input vectors, $P_{S,i}(x_i)$ is the value of the signal pdf for quantity i at value x_i and $P_{B,i}(x_i)$ is the corresponding value of the background pdf. The signal is given by prompt electrons, while the background comes from the combination of jets that have a similar signature of prompt electrons, electrons from photon conversion in the detector material and non-prompt electrons given from the decay of hadrons containing heavy flavours.

For each electron candidate a discriminant d_L is formed, in order to combine L_S and L_B:

$$d_L = \frac{L_S}{L_S + L_B}. \tag{5.3}$$

This discriminant presents a sharp peak at unity for signal electrons and at zero for background.

In order to derive the PDFs for the electron LH, each one of them is determined for each identification quantity in separate bins of electron-candidate E_T and η. This pdfs are created from finely binned histograms of the individual identification quantities. Pdfs histograms are smoothed using an adaptive *kernel density estimators (KDE)* to avoid non-physical fluctuations. The PDFs for the transverse energy E_T range from 4.5 GeV to 15 GeV and are determined using $J/\psi \to ee$ MC simulations while the others for $E_T > 15$ GeV are determined using $Z \to ee$ MC simulation.

In order to cover all the required prompt-electron signal efficiencies and background rejection factors (needed by the considered physics analyses), four fixed values of the LH discriminant are used, in order to define four **operating points**, which are: *Very-Loose*, *Loose*, *Medium* and *Tight*. These correspond to increasing thresholds for the LH discriminant. The efficiencies for identifying a prompt electron with $E_T > 40$ GeV are 93%, 88% and 80% for the Loose, Medium and Tight operating points, respectively. The identification is optimized in bins of cluster η and bins of E_T[3]. All this points need some tracking criteria requirements: Loose, Medium and Tight points require at least two hits in the pixel detector and seven hits total in the pixel and silicon strip detectors combined; while for Medium and Tight points one of these pixel hits must be in the innermost pixel layer. VeryLoose operating point does not include an explicit requirement on the innermost pixel layer and requires only one hit in the pixel detector. The latter point provides identification requirements for background studies.

Efficiencies for the LH-based electron identification for the Loose, Medium and Tight operating points for data and data-to-simulation ratios are shown in Figure 5.2 and 5.3. The measurement of efficiencies of the electron identification and isolation cuts are performed with the data using tag and probe techniques with large statistical sample of $Z \to ee$ and $J/\psi \to ee$ decays [66].

[3]Bins are selected by taking into account detector characteristics.

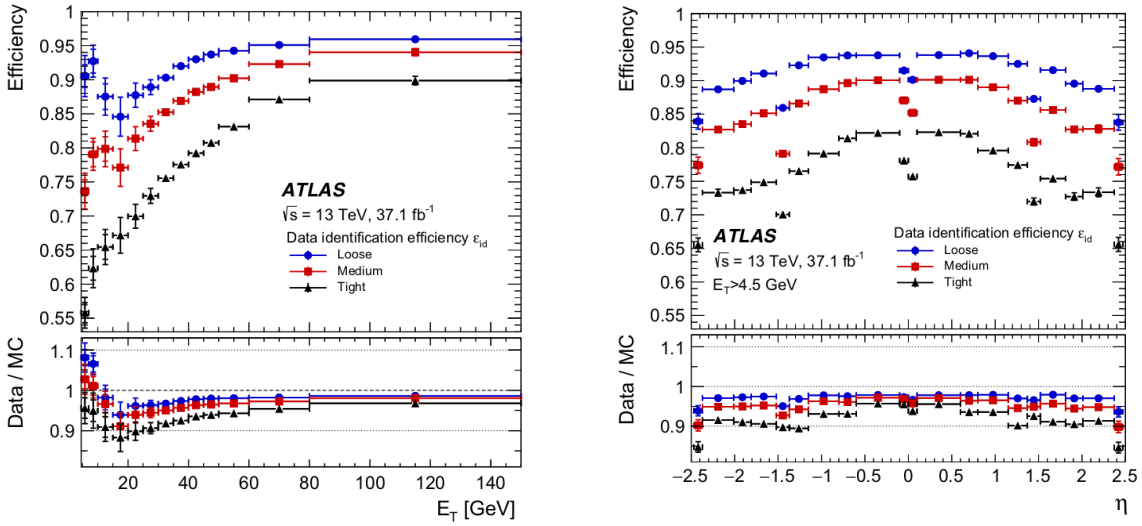

(a) Efficiencies as a function of P_T.

(b) Efficiencies as a function of η.

Figure 5.2: Measured LH electron-identification efficiencies in $Z \to ee$ events for the Loose, Medium and Tight operating points, as a function of E_T and η. Vertical bars represent the statistical and total uncertainties. Bottom panel shows the data-to-simulation ratios.

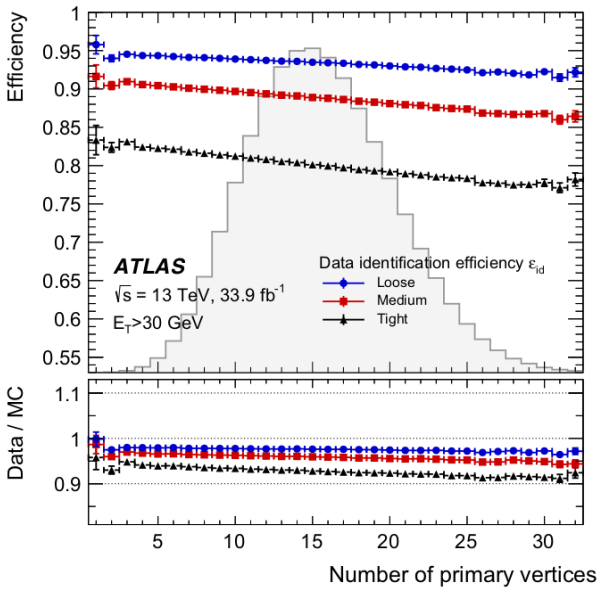

Figure 5.3: LH electron-identification efficiencies for electron candidates with $E_T >$ 30 GeV for the Loose, Medium and Tight operating points, as a function of primary vertices in the 2016 data taking, using the $Z \to ee$ process. The histogram shows the distribution of the number of primary vertices for the data. Inner uncertainties are statistical, while the total ones include both statistical and systematics components. Bottom panel shows the data-to-simulation ratios.

5.1.2 Electron isolation

In the differentiation of the reconstructed object in sinal processes, a hint of the signal is represented by a small activity, both in the calorimeter and in the inner detector, in a region of $\Delta\eta \times \Delta\phi$ surrounding the candidate object. However, the production of boosted particles decaying, for example, into collimated electron-positron pairs or the production of prompt electrons, muons and photons such as $t\bar{t}$ production can spoil the signal. Some variables are constructed in order to quantify the amount of activity close to the candidate object. They are built summing up transverse energies of clusters in the calorimeter or transverse momenta of tracks in a cone of radius $\Delta R = \sqrt{(\Delta\eta)^2 + (\Delta\phi)^2}$ around the direction of the electron candidate, excluding the candidate itself.

Some of the fundamental steps entering the structure of this isolation variables are: identify the candidate object itself, its direction and its contribution to the activity within the cone and summing, in a pile-up and underlying event robust way, the other activity found within the cone. Isolation variables can be divided in two classes:

- **Calorimeter-based isolation**: the computation of calorimeter-based isolation in the early running period of ATLAS simply summed the E_T of the calorimeter cells (from EMCAL and HADCAL) within a cone aligned with the electron direction, excluding the candidate's contribution. A good improvement is obtained by using E_T of topological clusters instead of cells, applying a significant noise-suppression algorithm to the collection cells. In Figure 5.4 a sketch of the calorimeter isolation method is shown. This method is simple and robust thanks to the stable subtraction scheme for both the signal and background candidates. A disadvantage of this method is that the candidate object may deposit energy outside of this fixed rectangular area which may be incorrectly assigned as additional activity.

- **Track-based isolation**: to compute track-based isolation variables, tracks with $p_T > 1\,\text{GeV}$, reconstructed with a fiducial region of the inner detector $|\eta| < 2.5$, that satisfy basic track-quality requirements, are used. This track selection includes a minimum number of hits identified in the silicon detectors and a maximum number of inoperable detector regions crossed by the track. To reduce the contribution of pile-up, a cut $|z_0 \sin\theta| < 3\,\text{mm}$ is required, where z_0 is the *longitudinal impact parameter*. This requirement aims to select tracks that originate from the vertex. Some track-based isolation variables are constructed by summing the transverse momenta of the tracks found within a cone of radius ΔR aligned with the electron track, excluding the candidate's own contribution. Then the track-p_T contribution of the candidate electron to the track-isolation variable must be subtracted from the cone. The resulting track-isolation variable is called p_T^{isol}.

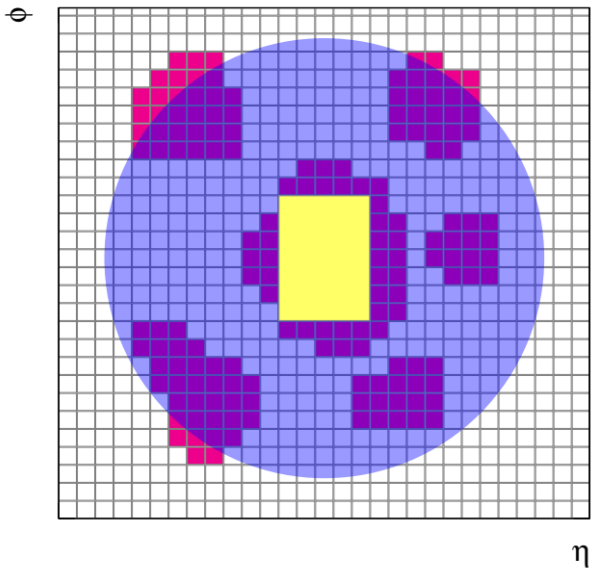

Figure 5.4: Sketch of the calorimeter isolation method: the grid represents the second-layer calorimeter cells in the η and ϕ directions. The electron candidate is located in the center of the purple circle representing the isolation cone. All topological clusters are represented in red. The yellow-rectangle cells correspond to the subtracted cells in the core subtraction method (subtraction of the core energy around the candidate).

5.1.3 Electron triggers

ATLAS trigger system has been introduced in Section 4.6. The electron (and photon) reconstruction at the HLT stage is performed on each EM RoI, provided by L1, which satisfies E_T and isolation requirements as specified by the trigger menu [67]. To run precision algorithms at a reduced rate, later in the trigger sequence, the HLT fast algorithms are executed first. They operate by using calorimeter and ID (Inner Detector) information within the RoI to perform the initial selection and identification of the electron candidates (and achieve early background rejection).

If a particle passes the fast selection criteria, the precision algorithms in the HLT are executed, if it is possible to access detector information outside the RoI. Therefore, the two main trigger selections are:

- **The L1 trigger** for electrons uses calorimeter information in the central region $|\eta| < 2.5$ to build an EM RoI. Within the window, the algorithm uses the maximum E_T from the four possible pairs of nearest-neighbour EM towers in a 2×2 central region[4]. Also a nominal E_T threshold and optionally a selection to reject hadronic activity below 50 GeV can be applied. Final step is an EM isolation requirement, in which candidate electrons are rejected if the sum of E_T in the 12 towers surrounding the 2×2 central region in the EM layer is at least 2 GeV and exceeds the value $E_T/8.0 - 1.8\,\text{GeV}$.

- Also the **HLT electron reconstruction** has fast and precision steps. The fast calorimeter reconstruction and selection steps for electrons have two implementations: a cut-based algorithm and a neural network based *Ringer* algorithm[5]. The former is used for electron triggers with $E_T < 15$ GeV, the latter is used for triggering electrons with $E_T \geq 15$ GeV. Electron candidates are required to have tracks from the fast track reconstruction step, performed inside the RoI only, matching the corresponding cluster. In the precision calorimeter reconstruction step, precision tracks within the RoI are extrapolated to the second layer of the EM calorimeter and are required to match the clusters within $|\Delta\eta(\text{track, cluster})| < 0.05$ and $|\Delta\phi(\text{track, cluster})| < 0.05$ rad. Here, the electron selection relies on a multivariate technique using a LH discriminant with four operating points, similar to the ones of Section 5.1.1.

5.2 Muon reconstruction

Like electrons, also muons are fundamental objects in our analysis because they form both the $e\mu$ and $\mu\mu$ final states of the decay. The muon reconstruction is performed

[4] This is used for EM E_T reconstruction.

[5] This algorithm exploits the property of EM showers to develop in the lateral direction in an approximately conical structure around the initial particle.

independently in ID and MS (Muon Spectrometer). The information is then combined to form muon tracks, used for physics analyses. In the ID, muons are reconstructed as the other charged particles [68].

For the **MS reconstruction**, the algorithm starts with a search for hit patterns inside each muon chamber, to form segments. The MDT segments are reconstructed by performing a straight-line fit with the hits found in each layer. The RPC or TGC measure the coordinate orthogonal to the bending plane. The segments in the CSC detectors are built using a separate combinatorial search in the η and ϕ detector planes. Muon track candidates are built by fitting together hits from segments in different layers. At least two matching segments are required to built a track, except in the barrel-endcap transition region where a single high-quality segment with η and ϕ information can be used. The hits associated with each track candidate are fitted using global χ^2 fit.

Information from ID and MS tracks are then joint to perform a ID-MS combined reconstruction. This procedure is performed according to various algorithms, based on the information provided by ID, MS and calorimeters. Depending on the sub-detector used in the reconstruction, there are four muon types:

- **Combined** (*CB*) **muons**: here the track reconstruction is performed independently in the ID and MS, and a combined track is formed with a global refit that uses the hits from both ID and MS sub-detectors.

- **Segment-tagged** (*ST*) **muons**: in this case a track in the ID is classified as a muon if, once extrapolated to the MS, it is associated with at least one local track segment in the MDT or CSC chambers.

- **Calorimeter-tagged** (*CT*) **muons**: here a track in the ID is identified as a muon if it can be matched to an energy deposit in the calorimeter, compatible with a minimum-ionizing particle. The criteria for the identification of this muons are optimized for the region $|\eta| < 0.1$ in the momentum range $1.5 < p_T < 100\,\text{GeV}$.

- **Extrapolated** (*ME*) **muons**: for this muons the trajectory is reconstructed based only on the MS track and on a loose requirement on compatibility originating from the interaction point. This muons are mainly used to extend the acceptance for muon reconstruction into the region $2.5 < |\eta| < 2.7$ (not covered by the ID).

The overlaps between different kind of muons are resolved before producing the final reconstructed muons for the analysis. A scheme of all the reconstructed muon candidates is shown in Figure 5.5.

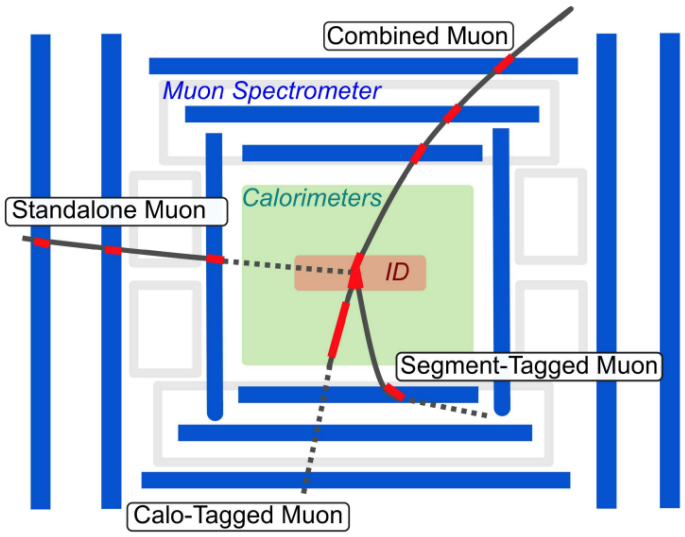

Figure 5.5: Scheme of all the reconstructed muon candidates [69].

5.2.1 Muon identification

Muon identification is performed by applying quality requirements that suppress background. To guarantee a robust momentum measurement, specific requirements on the number of hits in the ID and MS are used. Four muon identification selections, namely *Medium*, *Loose*, *Tight* and *High-*p_T, are provided to address the specific needs of different physics analyses:

- **Medium muons**: the Medium identification criteria is the default selection for muons in ATLAS. In this case only CB and ME tracks are used. The first ones are required to have at least 3 hits in at least two MDT layers, except for tracks in the $|\eta| < 0.1$ region, where tracks with at least one MDT layer, but no more than one MDT hole layer, are allowed. Instead, the latter are required to have at least three MDT/CSC layers, and are employed only in the $2.5 < |\eta| < 2.7$ region, to extend the acceptance outside the ID geometrical coverage.

- **Loose muons**: this criteria are designed to maximize the reconstruction efficiency while providing good-quality muon tracks. In this case all muon types are used. All CB and ME muons satisfying the Medium requirements are included in the Loose selection. CT and ST muons are restricted to the $|\eta| < 0.1$ region. In the $|\eta| < 2.5$ region almost all muons are CB.

- **Tight muons**: this muons are selected to maximize the purity of muons at the cost of some efficiency. Here, only CB muons with hits in at least two stations of the MS

and satisfying the Medium selection criteria are considered. In the $2.5 < |\eta| < 2.7$ region muons are reconstructed using only the MS detector.

- **High-p_T muons**: this selection aims to maximize the momentum resolution of tracks with $p_T > 100\,\text{GeV}$. CM muons that have passed the Medium selection and have at least three hits in three MS stations are selected.

5.2.2 Muon isolation

Muons originating from heavy particles are usually produced isolated from other particles and are well separated from them in the event. Therefore, the muon isolation is a powerful tool for background rejection in physics analyses. To define muon isolation, two variables are defined: a **track isolation variable** and a **calorimeter-based isolation variable**. The former is called $p_T^{\text{varcone30}}$ and is defined as the scalar sum of the p_T of the tracks with $p_T > 1\,\text{GeV}$ in a cone with size:

$$\Delta R = \min\left(10\,\text{GeV}/p_T^{\mu}, 0.3\right) \tag{5.4}$$

around the muon transverse momentum p_T^{μ}, excluding the muon track itself.

The calorimeter-based variable $E_T^{\text{topcone20}}$, is defined as the sum of the E_T of topological clusters in a cone of size $\Delta R = 0.2$ around the muon, after subtracting the contribution from the energy deposit of the muon itself and correcting for pile-up effects.

The real isolation criteria are constructed using the so-called *relative isolation variables*: they are defined as the ratio of track or calorimeter based isolation variables to the p_T of the muon. The distribution of this variables for muons coming from $Z \to \mu\mu$ events are shown in Figure 5.6. Some isolation criteria, called *isolation working points*, are defined; each of them is optimized for different physics analyses. The efficiencies of this points are measured in data and simulation in $Z \to \mu\mu$ decays, by using the *tag-and-probe* method[6].

[6]This method is employed to measure the efficiency of the muon identification selections within the acceptance of the ID ($|\eta| < 2.5$). $Z \to \mu\mu$ events are used, with one of the two muons considered as a tag by requiring to match the single-muon trigger, and the other acting as a probe, in order to measure trigger efficiency.

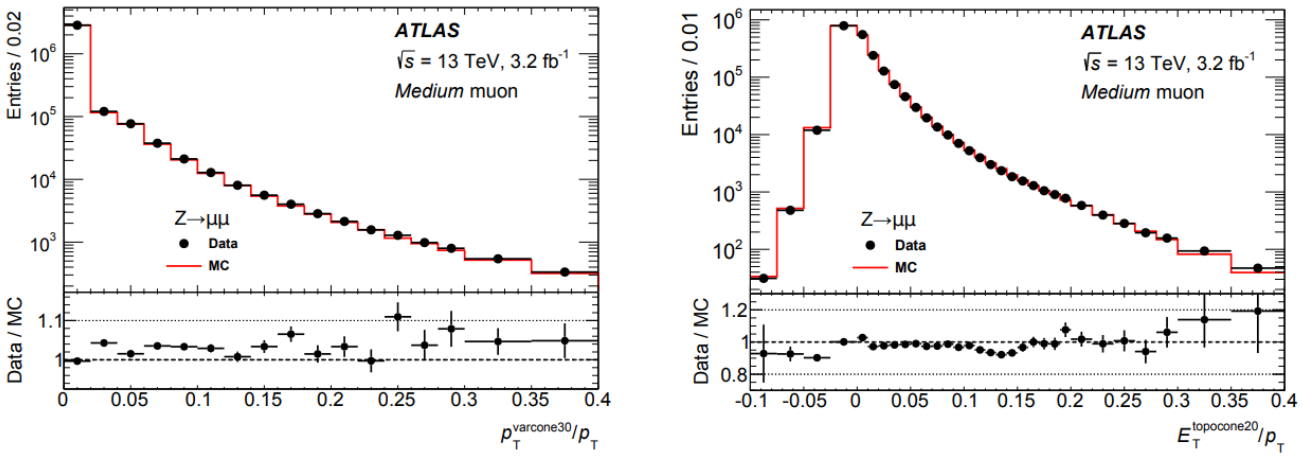

Figure 5.6: Left: distribution of the track based relative isolation variable. Right: distribution of the calorimeter-based relative isolation variable. Variables are measured in $Z \to \mu\mu$ events. Muons included in the plots satisfy Medium identification criteria and are well separated from the other muon from the Z boson, that have $\Delta R_{\mu\mu} > 0.3$. Bottom panel shows the ratio to data to simulation. Dots show the distribution of data, while histograms show distribution from simulation.

5.2.3 Muon triggers

The L1 muon trigger uses TGCs and RPCs hardware in order to select events by means of coarse p_T information. The L1 trigger also defines the RoIs[7]. The HLT muon trigger employs dedicated softwares to reconstruct muons in the RoIs defined by the L1, using information from precision trackers, MDTs, CSCs and ID [70]. In addition to precise p_T measurements, for some triggers, isolation criteria are also applied to reject non-prompt muons. Muon trigger performances are studied by means of a tag-and-probe method. In Figure 5.7 the absolute efficiencies for muons with respect to the offline muon p_T in the barrel ($|\eta| < 1.05$) and endcap ($1.05 < |\eta| < 2.4$) regions are shown. Relative efficiency of the HLT with respect to L1 is superimposed in the plots with blue line. Values of efficiency in endcap are lower than in the barrel: this loss is due to uncovered detector regions.

The ATLAS muon trigger performance has been stable during Run 2. The L1 trigger decision in the barrel region is based on the coincidence of hits from three concentric RPC stations for the three high-p_T thresholds. To reach optimal performance for the ATLAS trigger, an effective rejection of fake muon triggers in region $1.05 < |\phi| < 1.3$ has been possible by exploiting a coincidence between the TGC chambers and the tile HADCAL. To verify the performance of the muon trigger in different pile-up conditions,

[7]They are defined in terms of the pseudorapidity η and the azimuthal angle ϕ.

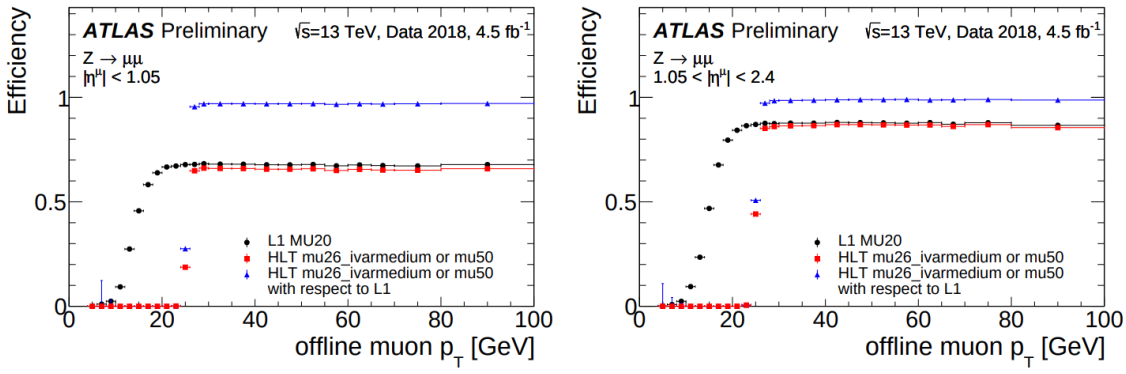

Figure 5.7: Absolute efficiencies for muons with respect to the offline muon p_T in the barrel ($|\eta| < 1.05$, left panel) and endcap ($1.05 < |\eta| < 2.4$, right panel) regions. Relative efficiency of the HLT with respect to L1 is superimposed in the plots with blue line.

the efficiency has been tested as a function of the number of reconstructed vertices (see Figure 5.8).

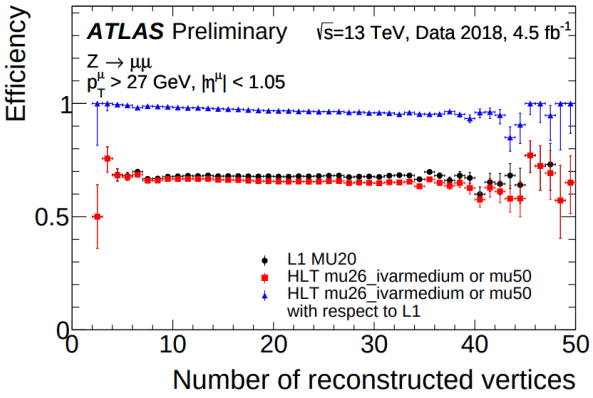

Figure 5.8: Muon trigger efficiency in the barrel region as a function of the number of reconstructed vertices. Efficiencies of L1, HLT and the total efficiency are shown for offline muons reconstructed in the barrel region with $p_T > 27\,\text{GeV}$.

5.3 Jet reconstruction and calibration

In ATLAS, different jets definitions are used, in particular for the study of QCD jets and jets containing the hadronic decay of boosted massive particles[8]. These different kind of jets are calibrated through some sequential steps. Jets are only a representation of the underlying physical process: the use of different jet definitions is adopted regarding the considered phenomena. ATLAS usually considers mostly small-R jets for physics results with quarks and gluons. The resulting jet is calibrated, in order to provide an accurate representation of the event.

The jet reconstruction is mainly divided into three parts:

- **Jet inputs**: in ATLAS *particle-flow* algorithm [71] is used to remove calorimeter energy deposits due to charged hadrons from consideration during jet reconstruction. This improves the accuracy of the charged-hadron measurement, while retaining the calorimeter measurements of neutral-particle energies.

- **Jet algorithms**: ATLAS uses the *anti-k_t algorithm* algorithm [72] for jet reconstruction. Two different distance parameters R are typically used, corresponding to different intended uses. Jets representing quarks and gluons are called small-R jets and are reconstructed with $R = 0.4$. Instead, jets representing hadronically decaying massive particles are typically called large-R jets and are reconstructed with $R = 1.0$.

- **Jet grooming**: the usage of large-R jets is necessary to fully contain the hadronic massive particle decays, but it comes with a substantially increased sensitivity to pile-up effects due to the larger fraction of the calorimeter enclosed within the jet volume. While pile-up may be low energy and thus not charge, the total jet kinematics by a large amount is randomly distributed and can thus unknown the angular structure within the jet that is the key to identifying massive particle decays. In order to solve this limitations, large-R jets are typically groomed[9].

The jet **calibration** procedure is divided into three steps: first, pile-up contributions are suppressed at the jet level, for small-R jets, then the jet is calibrated to the MC truth scale and finally the differences between MC and data are considered.

5.3.1 b-tagging algorithms

The purpose of b-tagging algorithms is to identify jets containing b-flavored hadrons. For each selected jet, this algorithms provide b-weights, reflecting the probability that this

[8] Hadronic jets are collimated streams of hadrons produced in high-energy collisions. These jets result from the fragmentation and aggregation of quarks and gluons released in strong interactions.

[9] *Grooming* is a class of algorithms that take a jet and throw away constituents following a defined strategy, rebuilding the final jet from the remaining constituents.

jet originates from a b-quark.

The discrimination of b-quark jets from light quark jets is possible mainly thanks to the relatively long lifetime of b-flavored hadrons, resulting in a significant flight path length L of the order of some millimeter. This leads to measurable secondary vertices and impact parameters of the decay products. Various b-tagging algorithms are used in ATLAS, based on these discriminating variables (L, d_0 and z_0), on secondary vertex properties and on the presence of leptons within b-jets.

Each tagging algorithm defines a discriminant w, associated to the probability for a given jet to have been originated from a b-quark. For each tagging algorithm, different "working points", corresponding to different threshold on the w variable, can be used.

The choice of the working point sets the tagging efficiencies for b-, c- and light quark jets [73]. For our analysis the *DL1 algorithm* with a working point of 60% efficiency with veto on 3rd b-tagged jets at 85% efficiency is used [74].

The DL1 algorithm is based on a *deep feed-forward neural network* (*NN*). The DL1 NN has a multidimensional output corresponding to the probabilities for a jet to be a b-jet, a c-jet or a light-flavour jet.

Training with multiple output nodes offers additional flexibility when constructing the final output discriminant by combining the b-jet, c-jet and light-flavour jet probabilities. Since all flavours are treated equally during training, the trained network can be used for both b-jet and c-jet tagging. The final DL1 b-tagging discriminant is defined as:

$$D_{\mathrm{DL1}} = \ln\left(\frac{p_b}{f_c \cdot p_c + (1 - f_c) \cdot p_{\mathrm{light}}}\right) \tag{5.5}$$

where p_b, p_c, p_{light} and f_c represent respectively the b-jet, c-jet and light-flavour jet probabilities, and the effective c-jet fraction in the background training sample. Using this approach, the c-jet fraction in the background can be chosen "a posteriori" in order to optimize the performance of the algorithm.

5.4 MET reconstruction

The missing transverse energy is reconstructed as the negative vector sum of transverse momenta p_T of reconstructed physics objects. The physical objects considered in the E_T^{miss} calculation are electrons, photons, muons, $\tau-$leptons and jets (**hard terms**) [75]. The E_T^{miss} components in the $x-y$ transverse plane are:

$$E_{x(y)}^{\mathrm{miss}} = E_{x(y)}^{\mathrm{miss,e}} + E_{x(y)}^{\mathrm{miss},\mu} + E_{x(y)}^{\mathrm{miss},\gamma} + E_{x(y)}^{\mathrm{miss},\tau} + E_{x(y)}^{\mathrm{miss,jets}} + E_{x(y)}^{\mathrm{miss,soft}} \tag{5.6}$$

and each term is defined as:

$$E_{x(y)}^{\mathrm{miss}} = -\sum_{i}^{n} p_{x(y)}(i) \tag{5.7}$$

where i are electron or muon or other interested objects. Instead, the reconstructed momentum not associated to any of the hard terms is referred as the **soft term**. There exist several algorithms used to reconstruct the E_T^{miss} soft term using calorimeter energy deposits or tracks. The main used algorithm for this purpose (used by ATLAS at Run-2) is the so-called *Tracks Soft Term* (TST), which fully relies on tracks. This algorithm misses the contribution from neutral particles, but it's robust against lots of pile-up conditions.

The removal of pile-up jets is essential for the E_T^{miss} resolution: this is done with the *Jet Vertex Tagger (JVT)* technique[10] [76]. Also a *novel forward pileup tagging technique (fJVT)*, that exploits the correlation between central and forward jets originating from pile-up interactions is developed. This latter technique improves the E_T^{miss} resolution in high pile-up conditions (see Figure 5.9). The TST systematic uncertainties are evaluated

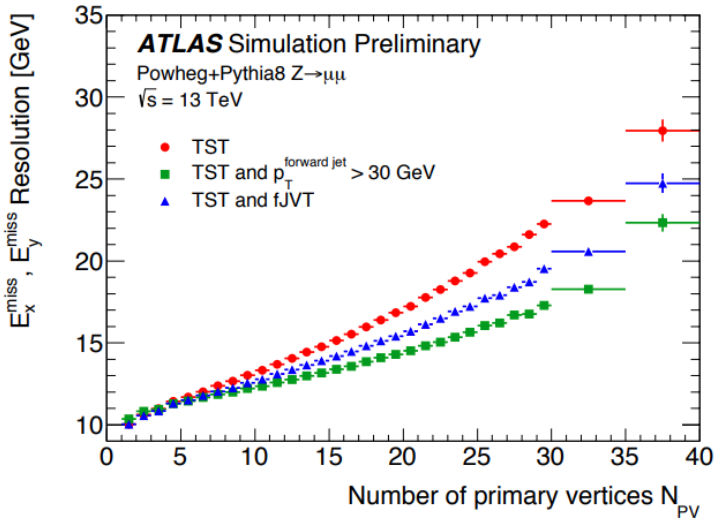

Figure 5.9: TST E_T^{miss} resolution as a function of the number of primary vertices, measured in MC simulated $Z \to \mu\mu$ events using different strategies for pile-up suppression.

exploiting the differences between data and MC using the balance of a soft term and a calibrated physics object. The mean of the TST distribution as a function of the hard p_T term has been measured using $36.5\,\text{fb}^{-1}$ Run-2 ATLAS data and agrees with MC simulation within the systematic uncertainty.

[10]This technique extracts the pile-up jets using track-to-vertex association method.

5.5 Overlap removal

To avoid cases where detector response to a single physical object is reconstructed as two separate final-state object, several steps are followed to remove these overlaps:

1. Calo-tagged muons sharing a track with an electron are removed, followed by the removal of any remaining electron sharing a track with a muon[11].

2. The closest jet to each electron within an $y - \phi$ cone of size $\Delta R = 0.2$ is removed to reduce the proportion of electrons being reconstructed as jets. In particular, this jets must pass the JVT requirements (mentioned at the end of the Section 5.4), in addition to the standard p_T and $|\eta|$ requirements, to be used to remove an overlapping object.

3. Electrons with a distance $\Delta R < 0.4$ from any of the remaining non-pileup jets are removed to reduce backgrounds from non-prompt, non-isolated electrons coming from heavy-flavor hadron decays.

4. Jets with fewer than three tracks and distance $\Delta R < 0.2$ from a muon are then removed to reduce jet fakes from muons depositing energy in the calorimeters.

5. Muons with a distance $\Delta R < 0.4$ from any of the surviving jets are removed to avoid contamination of non-prompt muons from heavy flavor hadron decays.

[11] This step is useful to avoid cases where a muon mimics an electron through radiation of a hard photon.

Chapter 6

Analysis data, samples and definitions

In this chapter, the data, MC samples and some common objects definitions used in the analysis are described.

In Section 6.1 the dataset is presented, while in Section 6.2 the Monte Carlo simulated samples used for comparison with results are provided. In Section 6.3 the event selection details of the analysis are introduced and finally in Section 6.4 the particle-level objects and the interested phase-space are explained.

6.1 Data samples

For this work the full dataset collected by the ATLAS detector during Run 2 operations (2015-2018) has been used. This dataset consists of data from proton-proton collision at

a center-of-mass energy of 13 TeV, sampled at a total integrated luminosity of 140 fb^{-1}.

Only data collected during stable beam LHC operations and with the ATLAS detector fully functioning is included. Events are considered only if they are accepted by at least one of the single-muon or single-electron triggers described in [77, 78, 79, 80, 81]. A matching between online objects firing the trigger and the offline reconstructed object is required.

6.2 Monte Carlo simulated samples

The contribution of SM processes is evaluated from MC simulated samples [82].

Multiple overlaid proton-proton collisions are simulated with the soft QCD processes of `Pythia8` [83] using the A2 tune [84] and the `MSTW2008LO` PDF [85]. The detector response is simulated with `Geant4` [86]. As a full simulation of the detector response is computationally expensive, for some of the modelling uncertainties estimation, the fast-simulation package AtlFast-II [82] is used, which parametrises hadronic showers in the electromagnetic and hadronic calorimeter, in order to speed up the simulation.

Simulation samples are reweighted so that their pile-up profile, based on the actual pile-up, matches the one observed in data [87].

The signal samples are defined as the sum of the $t\bar{t}$ and the tW samples from the same combination of generators and parton showers.

Monte Carlo events are further categorized based on the presence of non-prompt leptons. For all processes, besides those contributing to the fakes/non-prompt background, it is required that the two selected leptons are prompt.

6.2.1 Nominal signal sample

$t\bar{t}$ production

The production of the nominal $t\bar{t}$ events is modelled using the `PowhegBox` [88, 89, 90, 91] generator which provides matrix elements at NLO in the strong coupling constant α_s with the NNPDF3.0NLO [92] parton distribution function (PDF) and the h_{damp} parameter, which controls the matching in `Powheg` and effectively regulates the high-p_{T} radiation against which the $t\bar{t}$ system recoils, set to 1.5 m_{top} [93]. The functional form of the renormalization and factorization scale is set to the default scale $\sqrt{m_{\text{top}}^2 + p_{\text{T}}^2}$. The events are interfaced with `Pythia8` for the parton shower and hadronization, using the A14 set of tuned parameters [94] and the `NNPDF2.3lo` set of PDFs [95]. The decays of the bottom and charm hadrons are simulated using the `EvtGen` program [96].

The nominal $t\bar{t}$ sample is normalized to the cross-section prediction at NNLO in QCD including the resummation of NNLO soft-gluon terms calculated using Top++ [97, 98, 99, 100, 101, 39, 102]. For proton–proton collisions at a center-of-mass energy of

$\sqrt{s} = 13\,\text{TeV}$, this cross-section corresponds to:

$$\sigma(t\bar{t})_{\text{NNLO+NNLL}} = 834^{+21}_{-30}(\text{scale}) \pm 21(\text{PDF}+\alpha_s) \pm 23(m_{\text{top}})\ \text{pb} \tag{6.1}$$

using a top-quark mass of $m_{\text{top}} = 172.5$ GeV. The uncertainties on the cross-section due to PDF and α_s are calculated using the PDF4LHC prescription [103] with the MSTW2008 68% CL NNLO [85, 104], CT10 NNLO [105, 106] and NNPDF 5f FFN PDF sets, and are added in quadrature to the scale uncertainty.

tW production

The nominal single-top tW associated production is modelled using the `PowhegBox` v2 [107] generator which provides matrix elements at NLO in the strong coupling constant α_s in the five-flavour scheme with the NNPDF3.0NLO parton distribution function set. The functional form of the renormalzation and factorization scale is set to $H_T/2$[1]. The diagram removal scheme (see Section 2.3) is employed to handle the interference with $t\bar{t}$ production. The events are interfaced with `Pythia8` using the A14 tune and the NNPDF23LO PDF set. The decays of the bottom and charm hadrons are simulated using the `EvtGen` program.

The inclusive cross-section is corrected to the theory prediction calculated at NLO in QCD with NNLL soft gluon corrections [108, 109]. For proton–proton collisions at a center-of-mass energy of $\sqrt{s} = 13\,\text{TeV}$, this cross-section corresponds to:

$$\sigma(tW)_{\text{NLO+NNLL}} = 71.7 \pm 3.8\ \text{pb} \tag{6.2}$$

using a top-quark mass of $m_{\text{top}} = 172.5$ GeV. The uncertainty on the cross-section due to PDF is calculated using the `MSTW2008nnlo` 90% CL PDF set, and is added in quadrature to the scale uncertainty.

6.2.2 Alternative signal samples

Several additional $t\bar{t}$ and tW samples are considered for modelling systematics evaluation and to make comparison with data.

Samples for systematic uncertainties and comparison with data

- ***tW* PWG+PY8 (DS)**: it is similar to the nominal PWG+PY8 sample but using the DS scheme. It is combined with the nominal $t\bar{t}$ sample, and is labelled in the legends of figures and tables as PWG+PY8 (DS).

[1] H_T is related to an energetic scale associated to transverse momenta of the final particles involved in a given event.

- **$t\bar{t}$ and tW PWG+PY8 ($h_{\text{damp}} = 3m_t$)**: they are produced with the same settings as the nominal PWG+PY8 sample but with the h_{damp} parameter set to $3m_t$. The short name used in the paper is PWG+PY8 (h_{damp}).

- **$t\bar{t}$ and tW PWG+H7**: for them, events were generated using the same Powheg-Box v2 set-up using the NNPDF3.0NLO [92] parton distribution function (PDF), interfaced to HERWIG 7.1.3 [110, 111], which includes an angular-ordered parton-shower model. This sample was generated using the HERWIG 7.1 default set of tuned parameters and the MMHT2014LO PDF set [112]. For the tW process, events were generated with the POWHEG BOX v2 generator were interfaced to HERWIG 7.0.4, using the same parton shower tune and PDF as the $t\bar{t}$ sample. The functional form of the renormalization and factorization scales was set fixed to the default scale, which is equal to the top-quark mass. The decays of the bottom and charm hadrons were simulated using the EVTGEN 1.6.0 program [96]. The short name used in the paper is *PWG+H7 (fix)*.

- **$t\bar{t}$ and tW PWG+PY8 (pThard)**: it is similar to the nominal PWG+PY8 sample but using $p_{\text{T,hard}} = 1$ instead of $p_{\text{T,hard}} = 0$ [113, 114]. This parameter regulates the definition of the vetoed region of the showering, important to avoid hole/overlap in the phase space filled by POWHEG and PYTHIA. The short name for this sample is PWG+PY8 (pThard).

- **$t\bar{t}$ PWG+PY8 (recoil)**: similar to the nominal PWG+PY8 sample but with a different recoil strategy. In the nominal sample, the modelling of second and subsequent gluon emission is performed recoiling the gluon against b-quarks while in the alternative sample the top-quark itself works as the recoiler.

Samples only for comparison with data

- **PWG+PY8 *bb4l***: this sample [115] is not given from the sum of $t\bar{t}$ and tW separate simulations. The process is modelled using a generalization of `Powheg` which produces $\ell^+ v_\ell l^- \bar{v}_l b\bar{b}$ final states that take into account quantum interference effects between the $t\bar{t}$ and tW production modes as well as off-shell and non-resonant effects [116].Events are generated using the POWHEG BOX RES framework [117], with matrix elements at NLO in the strong coupling constant. A general NLO+PS matching technique that allows for a consistent treatment of resonances, referred to as 'resonance-aware matching' [118], is employed. The functional form of the renormalisation and factorisation scales is set to $\left[\left(m_t^2 + p_{T,t}^2\right)\left(m_{\bar{t}}^2 + p_{T,\bar{t}}^2\right)\right]^{\frac{1}{4}}$ where the (anti)top masses and transverse momenta are defined in the underlying Born phase space in terms of final state (off-shell) decay products. For diagrams containing an intermediate Z boson, the scales are set to $\frac{\sqrt{p_Z^2}}{2}$, with $p_Z = p_{l^+} +$

$p_{l^-} + p_\nu + p_{\bar{\nu}}$. The h_{damp} parameter is set to $1.5m_t$. Events are interfaced with PYTHIA 8.245 [83] using the A14 tune [94] and the NNPDF2.3LO PDF set [95]. For the POWHEG-PYTHIA matching, a special UserHook (`PowhegBB4Ltms`) is used.

- ***tW* PWG+PY8 with fixed scales (both DR and DS)**: it is similar to the nominal PWG+PY8 sample but with the renormalization and factorization scales fixed to the default scale, $m_t = 172.5$ GeV. It is combined with the nominal $t\bar{t}$ sample and both are presented in legends of figures and tables as PWG+PY8 (fix) and PWG+PY8 (fix, DS) respectively.

- ***tt̄* PWG+PY8 NNLO reweighting**: in order to evaluate the extent to which the NNLO corrections improve the agreement between data and simulation, the events of the nominal PWG+PY8 $t\bar{t}$ sample are reweighted at parton-level to match the NNLO QCD + NLO EW parton level prediction presented in [119]. The reweighting is performed on the three variables $p_{\text{T}}(t)$, $m(t\bar{t})$ and $p_{\text{T}}(t\bar{t})$, using the kinematics of the top quarks in the MC samples after initial- and final-state radiation. The predictions for $p_{\text{T}}(t)$ and $m(t\bar{t})$ are calculated at NNLO in QCD with NLO electroweak (EW) corrections [119] with the NNPDF3.0QED PDF set using the dynamic renormalisation and factorisation scales $m_{\text{T}}(t)/2$ for $p_{\text{T}}(t)$ and $H_{\text{T}}/4$ for $m(t\bar{t})$ as proposed in Ref. [119]. The prediction for $p_{\text{T}}(t\bar{t})$ is calculated at NNLO in QCD [120, 121] with the NNPDF3.0 PDF set and with μ_{r} and μ_{f} set to $H_{\text{T}}/4$. All the predictions use $m_t = 173.3$ GeV. The reweighting was performed iteratively [122, 123], such that at the end of the procedure the reweighted MC sample agrees well with the higher-order prediction for each of the three variables. The re-weighted predictions themselves are not equivalent to complete NNLO+parton shower calculations and are used to estimate the effect of the NNLO contributions on the measured observables. Such kind of reweighting is currently unavailable for the tW production, so for this process we keep the nominal tW DR PWG+PY8 MC. The short name for this sample is PWG+PY8 (NNLO rew.).

All the alternative samples are normalized to the same total cross-section as the nominal, except for the top-quark mass variations, which are normalized to the corresponding higher-order cross-sections.

6.2.3 Background samples

Below a list of the background samples used in the analysis is presented.

$t\bar{t}X$ production The associated production of a top-quark pair with a heavy boson ($W/Z/H$) is referred to as $t\bar{t}X$.

The production of $t\bar{t}W/Z$ events is modelled using the `MadGraph5_aMC@NLO` v2.3.3 generator [124] which provides matrix elements at NLO in the strong coupling constant α_{s}

with the NNPDF3.0nlo PDF. The functional form of the renormalization and factorization scale is set to the default of $0.5 \times \sum_i \sqrt{m_i^2 + p_{\mathrm{T},i}^2}$, where the sum runs over all the particles generated from the matrix element calculation. Top quarks are decayed at LO using MadSpin [125, 126] to preserve spin correlations. The events are interfaced with Pythia8.210 for the parton shower and hadronization, using the A14 set of tuned parameters and the NNPDF2.3lo PDF set. The decays of the bottom and charm hadrons are simulated using the EvtGen v1.2.0 program.

The cross-sections are calculated at NLO QCD and NLO EW accuracy using MadGraph5_aMC@NLO as reported in [127]. The $t\bar{t}Z$ cross section is further supplemented with an off-shell correction (down to 5 GeV) calculated in [128]. The predicted values at 13 TeV are $0.88^{+0.09}_{-0.11}$ pb and $0.60^{+0.08}_{-0.07}$ pb for $t\bar{t}Z$ and $t\bar{t}W$ respectively, where the uncertainties are estimated from variations of the renormalization and factorization scales as well as the strong coupling α_s.

The production of $t\bar{t}H$ events was modelled using the Powheg Box v2 [88, 89, 90, 91, 129] generator, which provided matrix elements at NLO in the strong coupling constant α_s, in the five-flavour scheme with the NNPDF3.0nlo [92] PDF set. The functional form of the renormalization and factorization scales was set to $\sqrt[3]{m_{\mathrm{T}}(t) \cdot m_{\mathrm{T}}(\bar{t}) \cdot m_{\mathrm{T}}(H)}$. The events were interfaced to Pythia 8.230 [83] using the A14 tune [94] and the NNPDF2.3lo [92] PDF set. The decays of bottom and charm hadrons were performed by EvtGen 1.6.0 [96].

The cross-section was calculated at NLO QCD and NLO EW accuracy using MadGraph5_aMC@NLO as reported in [127]. The predicted value at $\sqrt{s} = 13$ TeV is 507^{+35}_{-50} fb, where the uncertainties were estimated from variations of α_s and the renormalisation and factorisation scales.

Z+jets and W+jets production In the phase space region used in the analysis, the Z+jets process contributes via events where the Z boson decays in two τ leptons, which in turn decay in an electron and a muon; the W+jets process contributes only via fake leptons.

The production of V+jets (Z+jets and W+jets) was simulated with the Sherpa 2.2.1 [130] generator using NLO matrix elements for up to two partons, and LO matrix elements for up to four partons calculated with the Comics [131] and OpenLoops [132, 133, 134] libraries. They were matched with the Sherpa parton shower [135] using the MEPS@NLO prescription [136, 137, 138, 139] using the set of tuned parameters developed by the Sherpa authors. The NNPDF3.0nnlo set of PDFs [92] was used and the samples were normalised to a NNLO prediction [140]. For the Z+jets samples, a cut-off of $m_{ll} > 40$ GeV was applied at generator level.

Diboson production This production has been simulated with Sherpa v2.2.2 and v2.2.1 generator, depending on the process, including off-shell effects and Higgs boson

contributions, where appropriate. The samples were generated using matrix elements at NLO accuracy in QCD for up to one additional parton and at LO accuracy for up to three additional parton emissions. Samples for the loop-induced processes $gg \to VV$ were generated using LO-accurate matrix elements for up to one additional parton emission for both the cases of fully leptonic and semileptonic final states. In this setup, multiple matrix elements (NLO for up to one additional parton and LO for up to three additional partons) are matched and merged with the `Sherpa` parton shower based on Catani-Seymour dipole using the MEPS@NLO prescription. The virtual QCD corrections for matrix elements at NLO accuracy are provided by the OpenLoops library. The NNPDF3.0nnlo set of PDFs was used, along with a dedicated set of tuned parton-shower parameters developed by the Sherpa authors.

Non-prompt production This sample is estimated using MC by selecting events with non-prompt leptons, based on truth level information (from inclusive tW, non-full-hadronic $t\bar{t}$, Z + jets, W +jets, diboson and $t\bar{t}V$) and assuming all fakes come from modeled processes.

6.3 Event selection

The event selection comprises a set of requirements based on the general event quality and on the reconstructed objects, defined in Chapter 5, that characterize the final-state event topology.

The sample is collected using a logical or of the lepton triggers. To ensure events originate from proton-proton collisions, events are required to have at least one vertex with at least two tracks. The primary vertex is defined as the vertex with the highest $\sum p_{\mathrm{T}}^2$ where the sum extends over all associated tracks with $p_{\mathrm{T}} > 0.4\,\mathrm{GeV}$. Each event is required to contain exactly one good electron and one good muon, with $p_{\mathrm{T}} > 28$ GeV, as defined in the previous chapter.

The trigger object fired in the event must be matched to the corresponding reconstructed lepton. This matching is based on angular distance between the fully-reconstructed lepton and the one reconstructed by the trigger algorithm. Finally, at least two jets, with $p_{\mathrm{T}} > 25\,\mathrm{GeV}$, and at least two b-jets at 70% WP are required.

6.3.1 2b-inclusive signal region

In Figures 6.1 and 6.2 detector-level control plots for the kinematic variables of base objects, are shown.

The data and simulated distributions (obtained employing both the DR and DS schemes) generally agree well, but the lepton transverse momentum distribution observed in data is softer than in the nominal signal and background simulation, as has

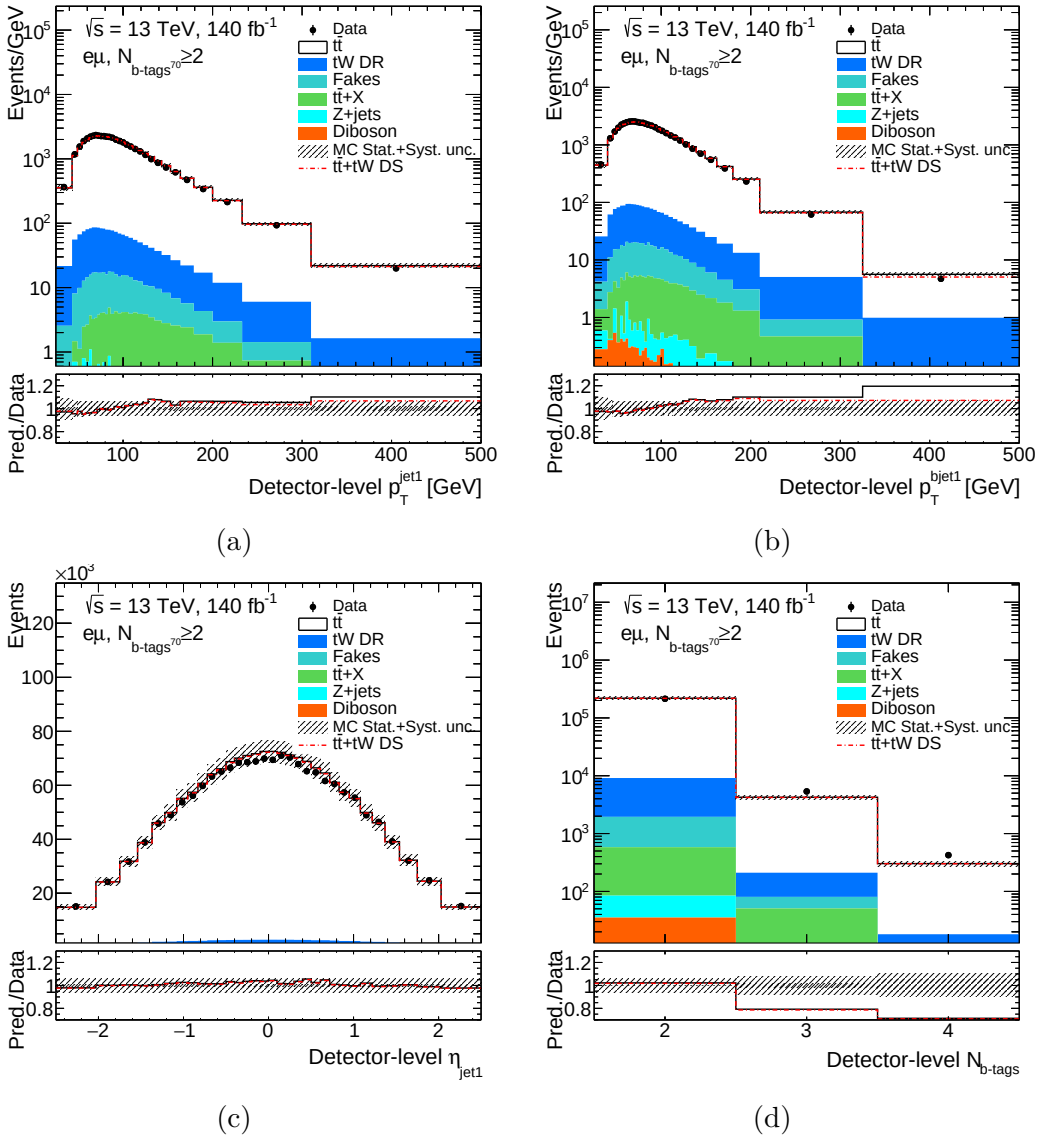

Figure 6.1: Comparison of data and MC predictions for the p_{T} of a the leading jet and b the leading b-jet, c the η of the leading jet and d the number of b-jets in the $2b$-inclusive region. The hatched area indicates the combined statistical and systematic uncertainties in the total prediction, excluding systematic uncertainties related to the signal modelling. Events beyond the range of the horizontal axis are included in the last bin.

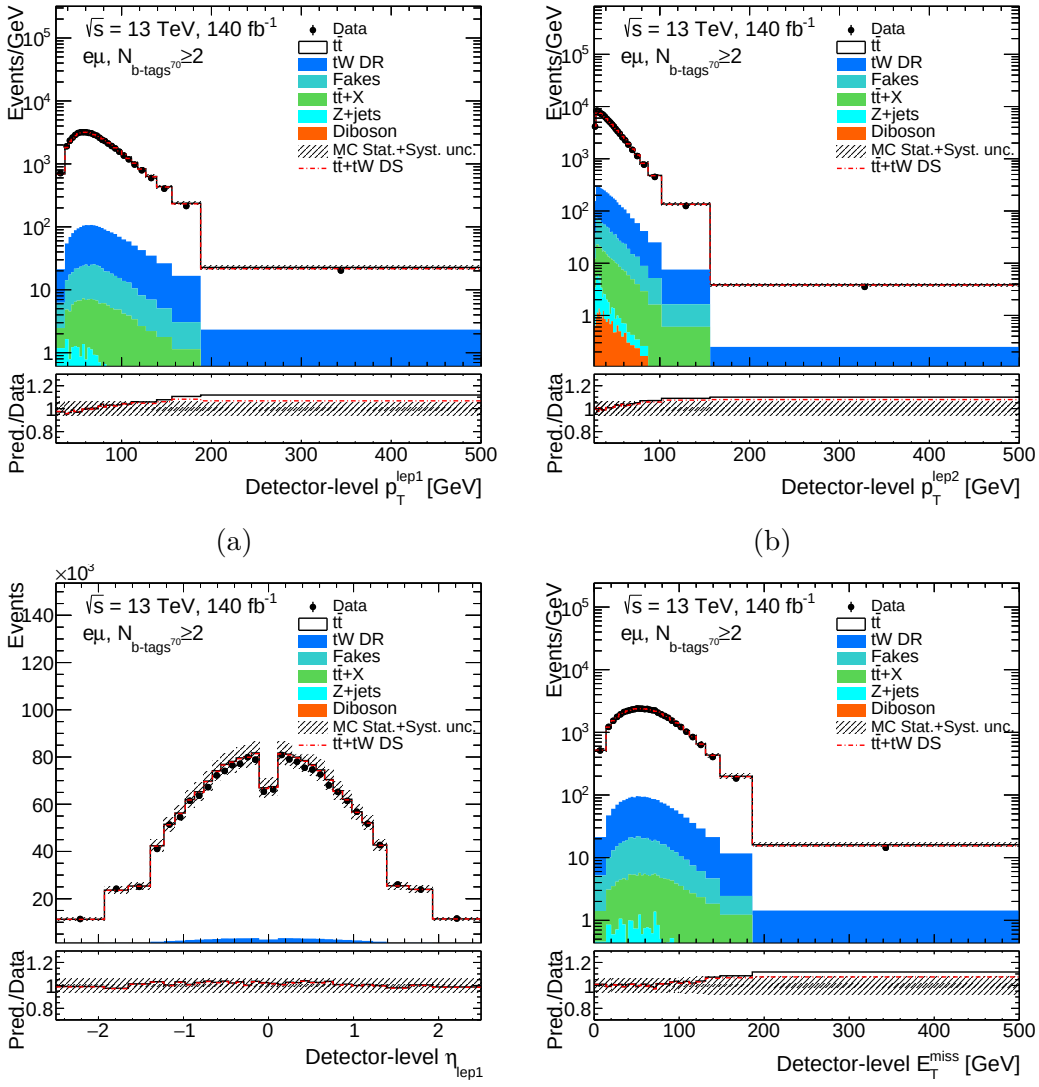

Figure 6.2: Comparison of data and MC predictions for the p_{T} of a the leading and b the subleading lepton, c the η of the leading lepton and d the $E_{\mathrm{T}}^{\mathrm{miss}}$ in the 2b-inclusive region. The hatched area indicates the combined statistical and systematic uncertainties in the total prediction, excluding systematic uncertainties related to the signal modelling. Events beyond the range of the horizontal axis are included in the last bin.

also been observed in previous measurements at $\sqrt{s} = 13$ TeV [141, 142]. For most of the distributions, no significant differences are observed between the DR and DS schemes. To enhance the sensitivity to the interference between the $t\bar{t}$ and tW processes, a new variable is defined, m^{bl}_{minimax} , in a region with a veto on additional b-tagged jets, as described in the next section.

Values of observed and expected number of events in the channel after the full event selection are shown in Table 6.1.

Sample	$e\mu$, $N_{bjets^{70}} \geq 2$			
$t\bar{t}$	214000	$\pm$	13000	($\pm$6%)
tW (DR)	7300	$\pm$	400	($\pm$6%)
$t\bar{t}V$	800	$\pm$	110	($\pm$13%)
Diboson	36	$\pm$	15	($\pm$40%)
Z+jets	51		$^{+20}_{-19}$	($\pm$40%)
Fakes	1400	$\pm$	700	($\pm$50%)
Expected	224000	$\pm$	13000	($\pm$6%)
Purity	0.9898	$\pm$	0.0032	($\pm$0.32%)
Observed	219882			
MC/Data	1.02	$\pm$	0.06	($\pm$6%)

Table 6.1: Observed and expected number of events in the 2b-inclusive signal region after the full event selection. The uncertainties include the Monte Carlo statistic uncertainties and all systematic uncertainties except for the signal modelling ones.

Additional detector-level control plots for different variables in this phase space are presented in Appendix B.1.2.

6.3.2 2b-exclusive signal region

The observable that is most sensitive to the interference between double and single top production is m^{bl}_{minimax} , which is described in detail in Appendix B.2. Its definition is shown in Eq. 6.3:

$$m_{bl}^{\text{minimax}} \equiv \min\{\max(m_{b_1 l_1}, m_{b_2 l_2}), \max(m_{b_1 l_2}, m_{b_2 l_1})\} \tag{6.3}$$

where b_i and l_i represent the two b-jets and leptons, respectively[2]. A deeper description of this variable is shown in Section 6.3.3. This variable is sensitive to the interference

[2]The first and only measurement of the $WbWb$ cross-section as a function of m^{bl}_{minimax} variable has been provided by ATLAS in 2018 [37].

for high mass values (above about 180 GeV) due to the suppression of doubly resonant contribution. However, this region of the phase space is also sensitive to the presence of additional b-jets that can result in a value in the high mass region due to the combinatorial between b-jets and leptons. Therefore, the veto on additional b-jets is essential to achieve a good sensitivity. The best selection is achieved by requiring a veto on additional b-jet at 85% WP with $p_{\mathrm{T}} > 25$ GeV.

The procedure and motivations that led to this optimisation are described in detail in Appendix B.3.

In Figure 6.3 detector-level control plots for the $m^{bl}_{\mathrm{minimax}}$ variable, is shown. The comparison between predictions obtained with the DR and DS schemes shows the region of the distribution that is sensitive to the interference

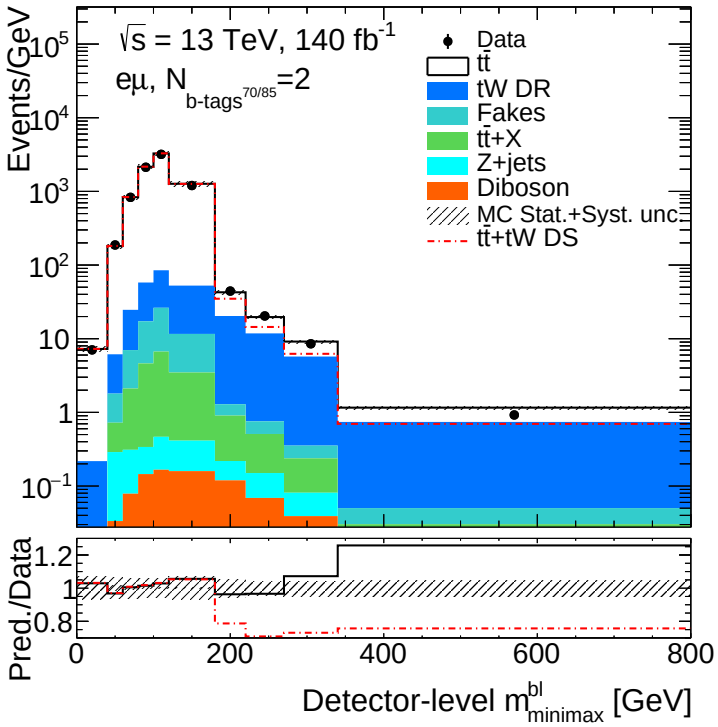

Figure 6.3: Comparison of data and MC predictions for the $m^{bl}_{\mathrm{minimax}}$ variable for the 2b-exclusive signal region. The hatched area indicates the combined statistical and systematic uncertainties in the total prediction, excluding systematic uncertainties related to the signal modeling. Events beyond the range of the horizontal axis are included in the last bin.

In Figures 6.4 and 6.5 detector-level control plots for the kinematic variables of interference-sensitive objects, are shown. In this case, no major impact is observed

between the DR and DS schemes and the same level of agreement between data and MC predictions is observed as in the $2b$-inclusive signal region.

Values of observed and expected number of events in the channel after the full event selection are shown in Table 6.2.

$t\bar{t}$	200000	$\pm$	12000	($\pm$6%)
tW (DR)	6900	$\pm$	400	($\pm$6%)
$t\bar{t}V$	500	$\pm$	70	($\pm$13%)
Diboson	32	$\pm$	13	($\pm$40%)
Z+jets	47	$\pm$	18	($\pm$40%)
Fakes	1300	$\pm$	700	($\pm$50%)
Expected	209000	$\pm$	12000	($\pm$6%)
Purity	0.9910	$\pm$	0.0031	($\pm$0.32%)
Observed	202738			
MC/Data	1.03	$\pm$	0.06	($\pm$6%)

Table 6.2: Observed and expected number of events in the $2b$-exclusive signal region after the full event selection. The uncertainties include the Monte Carlo statistic uncertainties and all systematic uncertainties except for the signal modelling ones.

Additional detector-level control plots for different variables in this phase space are presented in Appendix B.1.1.

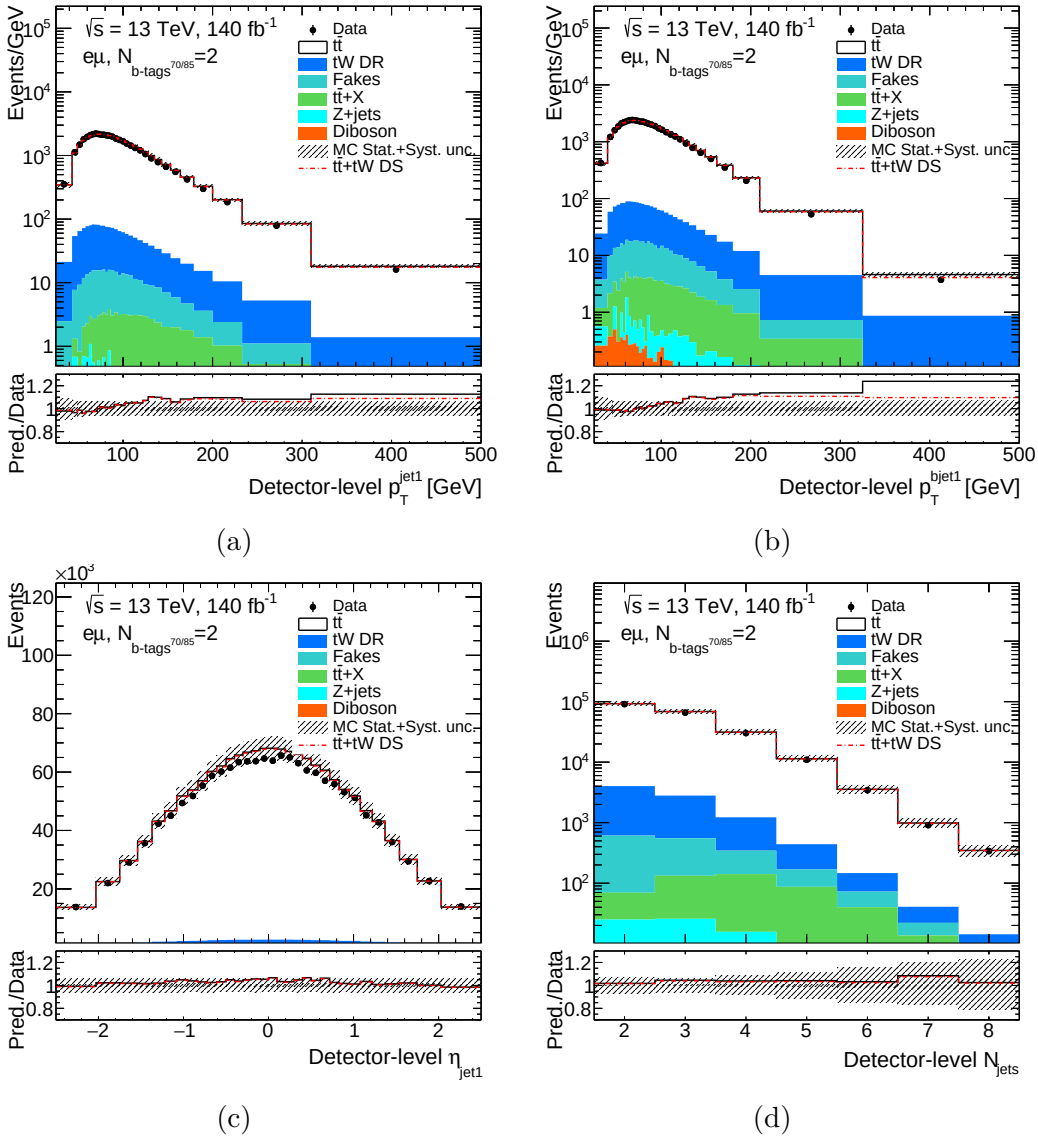

Figure 6.4: Comparison of data and MC predictions for the p_{T} of a the leading jet and b the leading b-jet, c the η of the leading jet and d the number of jets for the $2b$-exclusive region. The hatched area indicates the combined statistical and systematic uncertainties in the total prediction, excluding systematic uncertainties related to the signal modelling. Events beyond the range of the horizontal axis are included in the last bin.

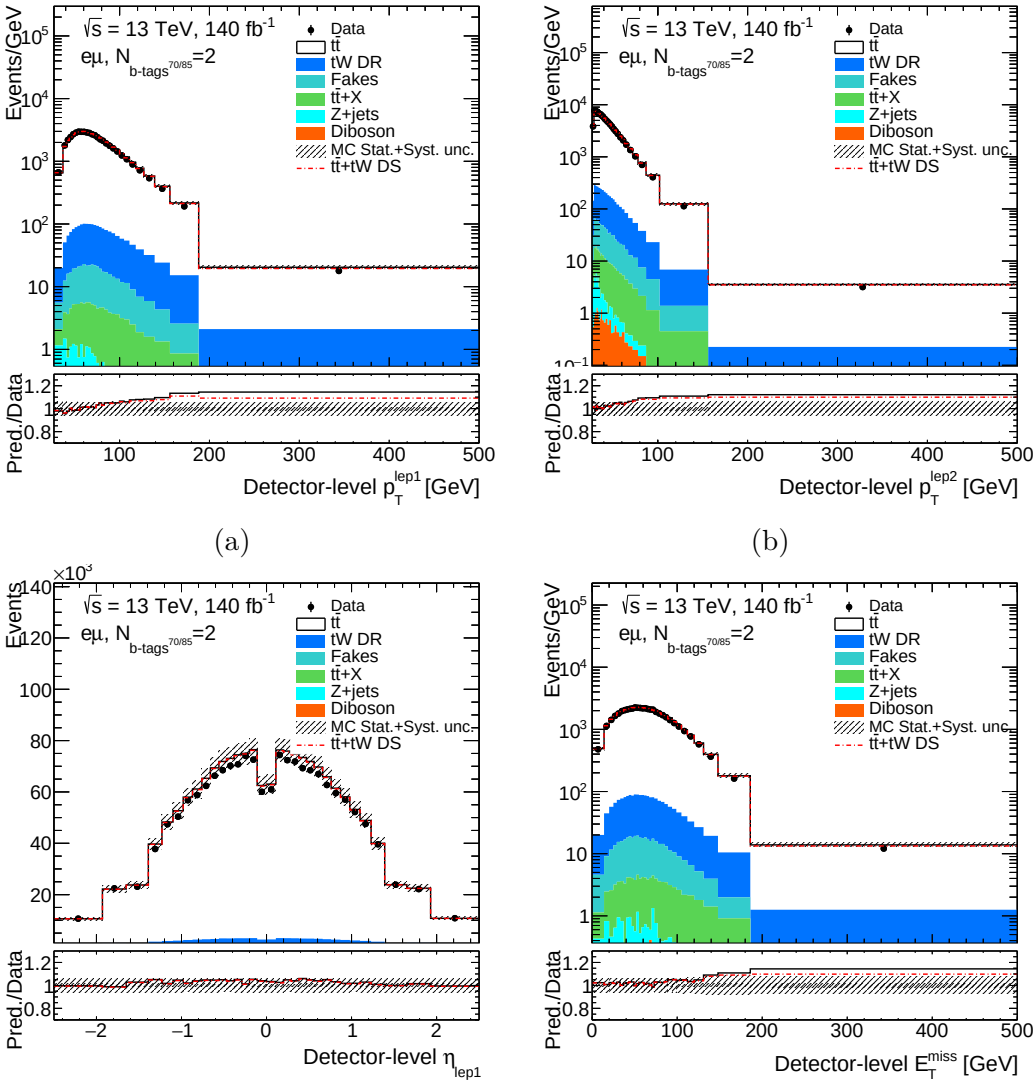

Figure 6.5: Comparison of data and MC predictions for the p_{T} of a the leading and b the subleading lepton, c the η of the leading lepton and d the $E_{\mathrm{T}}^{\mathrm{miss}}$ for the $2b$-exclusive region. The hatched area indicates the combined statistical and systematic uncertainties in the total prediction, excluding systematic uncertainties related to the signal modelling. Events beyond the range of the horizontal axis are included in the last bin.

6.3.3 The m_{bl}^{minimax} variable physical interpretation

The m^{bl}_{minimax} variable represents the invariant mass of a specific pairing of a b-jet and a lepton. Let's assume that two leptons and b-jets are reconstructed in an event, labelling them b_1, b_2, l_1 and l_2. Then one can create pairs to reconstruct four unique masses $m_{ij} = m(b_i, l_i)$ where $i, j = 1, 2$. In doubly resonant $t\bar{t}$ events, two of the masses are guaranteed to be below the top mass bound due to the not-reconstructed neutrino. But in singly-resonant $t\bar{t}$ events, only a single pair must satisfy the top mass bound. The m^{bl}_{minimax} is constructed to efficiently take advantage of this difference (see Eq. B.2).

There are two ways to match b-jets and leptons. Assuming that one has correctly paired the objects[3], we are interested in the larger of the two masses, hence the *maximum*. This mass will be lower than the top mass bound for doubly-resonant events, while it can "evade the top mass endpoint" for singly-resonant tWb events. However, one cannot know a priori the correct way to make the b-jet-lepton pairing, so one is forced to take the *minimum* over the possible ways to assign the objects. An illustration of this procedure is shown in Figure 6.6. Thanks to this construction the $t\bar{t}$ process mainly

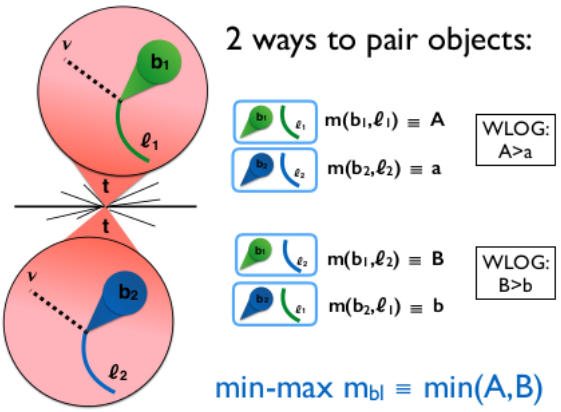

Figure 6.6: A scheme demonstrating the assignment of the leptons and b-jets to form the m^{bl}_{minimax} variable. Two possible pairings are considered: the *A-type* and the *B-type* and for each of them one can build two possible m_{bl} values. The minimum of the larger m_{bl} values from each pairing is selected as m^{bl}_{minimax}. In $t\bar{t}$ events this choice has a kinematic endpoint at $m^{bl}_{\text{minimax}} < \sqrt{m_t^2 - m_W^2}$ while for single-top events there is no such bound.

populates the region where m^{bl}_{minimax} is less than the top mass bound. Single top events populated the entirety of the m^{bl}_{minimax} distribution including the region where the variable is significantly beyond the top mass. As a result of this effect, the region of large m^{bl}_{minimax}

[3]So as to correctly group the decay products originating from the same top quark.

is highly pure in single top events and is very sensitive to the interference effect, as shown in Figure 6.7. At present, this is considered as the most interference-sensitive variable.

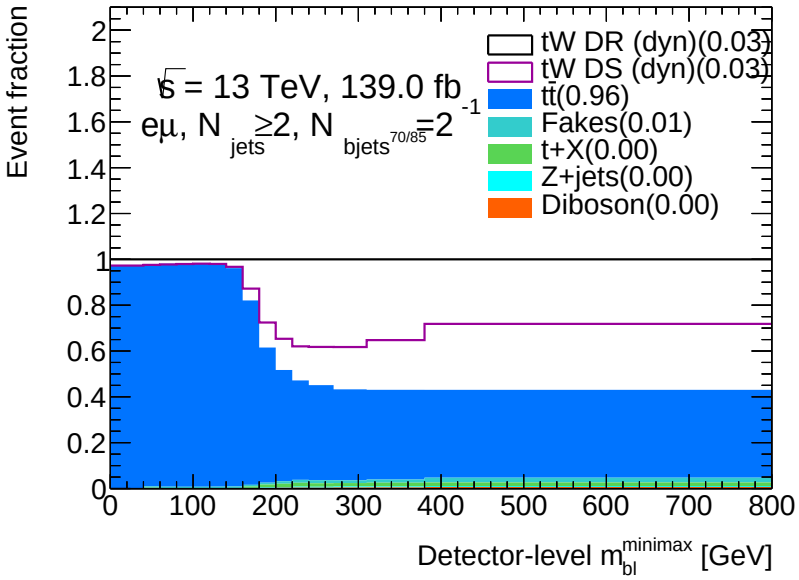

Figure 6.7: The event fraction composition of the m^{bl}_{minimax} distribution in the interference-sensitive region is shown. The $t\bar{t}$ contribution is suppressed in the region of large m^{bl}_{minimax} while the single top contribution is enhanced.

6.4 Particle-level objects

Particle-level objects are reconstructed using generator-level information from MC simulation. The physics objects are built from stable particles in the generator record, defined as those that satisfy: $c\tau > 10\,\text{mm}$ where τ is the mean lifetime of a particle.

Particle-level electrons and muons from the signal sample are selected from the stable particles and are required not to have been originated by an hadron, either directly or via an intermediate τ decay. Their momentum is calculated to include the radiation loss due to *final-state radiation* (*FSR*) photons, classified as photons with $\Delta R < 0.1$ that do not originate from hadron decays. p_T and η requirements are the same of the detector-level signal objects. Baseline leptons are defined with looser p_T requirements of 4 GeV (muons) and 5 GeV (electrons) for the overlap removal (see Section 5.5).

Particle-level jets are reconstructed by clustering truth particles (excluding those identified as baseline leptons or neutrinos from electroweak boson decays), with the anti-k_t algorithm with radius parameter of $R = 0.4$. Baseline jets have to satisfy $p_T > 20\,\text{GeV}$ and $|\eta| < 2.8$, while signal jets have to satisfy $p_T > 25\,\text{GeV}$ and $|\eta| < 2.5$.

B-hadrons are matched to jets by using the *ghost-association procedure* [143] in which truth jet clustering is run as usual, except with the energy of all B-hadrons set to a negligible value. All the particle jets containing a constituent B-hadron are b-tagged after this procedure.

An identical overlap removal procedure as the one illustrated in Section 5.5 is performed with the truth-level objects.

6.4.1 Particle-level selection

Using particle-level baseline objects, two fiducial regions are defined by applying additional cuts that replicate the detector-level selections as closely as possible:

- one electron and one muon with $p_{\mathrm{T}} > 28\,\mathrm{GeV}$;
- at least two jets with $p_{\mathrm{T}} > 25\,\mathrm{GeV}$;
- at least two b-jets, tagged with the B-hadron ghost-association matching;
- $m^{bl}_{\mathrm{minimax}}$ **region only**: exactly two b-jets, tagged with the B-hadron ghost-association matching.

These requirements define the particle-level fiducial regions. The measured observables are unfolded to this phase space.

Chapter 7

Analysis strategy

In this chapter the analysis strategy used to measure the differential cross-sections of the $WbWb$ production is presented. In Section 7.1 the main classical unfolding technique

is explained. In Sections 7.2 and 7.3 binning choice and unfolding tests are shown. In Section 7.4 uncertainties are highlighted. Finally, in Section 7.5 a novel unfolding method, developed by us, based on quantum annealing and its related implementation software, called `QUnfold`, are presented. This latter software is tested on the same data presented in Chapter 6 and results are shown in the next final chapter.

7.1 The unfolding method

A common problem in particle physics is the distortion of physical observables measurements due to the finite resolution and limited geometrical acceptance of the particle detector. Therefore the reconstructed distributions of physical quantities cannot be compared to theoretical distributions, or among different experiments. Data need to be corrected for these effects using the so-called **unfolding** procedure.

The purpose of this method is to return a distribution $f(x)$ of a physical quantity x, starting from the experimental measurement y with its distribution $g(y)$, that is different with respect to the *true distribution*, because of detector effects.

It is possible to classify detector effects in two categories:

- **Limited acceptance effect**: it means that not all the events are used in the measurement of the physical quantity we are interested in, because of geometrical acceptance and trigger selection efficiency.
- **Limited resolution effect**: it means that it is impossible to measure any physical quantity with an infinite amount of accuracy. The true value of an observable "migrates" in another piece of the observed distribution.

Therefore, y will be different from x, and the $g(y)$ distribution will be smeared with respect to $f(x)$. The relation that links $f(x)$ and $g(x)$ is given by:

$$g(y) = \int A(y,x) f(x) dx \tag{7.1}$$

where $A(y,x)$ is the *smearing function* and describes the detector effects on the measurement.[1] MC simulations can be used to estimate $A(y,x)$ and allow to evaluate detector effects on $f(x)$ using Eq. 7.1.

Basically, the unfolding procedure tries to infer the true distribution starting from the reconstructed one. To solve this problem it is better to use binned values of x and y and represent $f(x)$ and $g(y)$ as histograms.

The unfolding equation con be described as follows:

$$\vec{g} = \mathbf{R}\vec{f} \tag{7.2}$$

[1] It describes the probability to reconstruct a true x value as y.

where $\mathbf{R}$ is a $m \times n$ matrix, called **response matrix** that contains the acceptance and smearing informations of the reconstruction process[2], $\vec{f}$ is an n-dimensional vector, called *true spectrum* and $\vec{g}$ is an m-dimensional vector, called *reconstructed spectrum*.

Starting from the response matrix, it is possible to construct another matrix, called **migration matrix**, which is obtained through this relation:

$$M_{ij} = \frac{1}{A_j} R_{ij} \tag{7.3}$$

where A_j is the reconstruction efficiency in the true bin j. This matrix represents the probability that an event generated and selected in bin j is reconstructed in bin i. Usually, this matrix is constructed in a way that columns elements are normalized to unity in a way that, once the acceptance is accounted for, the probability to reconstruct an event in any bin is 1.

If we would have infinite resolution and therefore no migrations (ideal situation), the response matrix would be diagonal with the elements representing the reconstruction efficiency of the x quantity in the j-th bin[3]. In this ideal case, the unfolded spectrum could be extracted from the reconstructed one, by simply dividing each bin in the reconstructed spectrum by the reconstructed efficiency.

7.1.1 Iterative Bayesian approach

For this analysis it has been used a particular unfolding approach, called **iterative Bayesian** unfolding. This procedure can be described as a "cause and effect" model, based on the Bayes theorem [144, 145].

If we suppose to have, for the studied variables, n reconstructed bins and m truth bins, we can define the "effect" E_i as the n_j events in the reconstructed bin j, while the "cause" C_i as the n_i events in the truth bin i. The effect is measured, but the cause is impossible to identify, so it needs to be estimated. We define the probability for an effect to come from a particular cause as $P(E_j|C_i)$ and can be estimated by assuming some information of the migration matrix and a measurement efficiency and resolution calculated from MC.

This procedure can be performed by using a standard Bayesian inference analysis [146]. The probability of a cause, given a particular effect, is given by the Bayes theorem:

$$P(C_i|E_j) = \frac{P(E_j|C_i) \cdot P_0(C_i)}{\sum_{l=1}^{n_C} P(E_j|C_l) \cdot P_0(C_l)} \tag{7.4}$$

[2]The R-matrix is generally not diagonal, due to the fact that some events generated in bin j could be reconstructed in bin $i \neq j$. This phenomena is called *bin migration*.

[3]In this case the migration matrix would be the identity matrix.

and the number of expected events in the i-th cause bin is:

$$\hat{n}(C_i) = \frac{1}{\epsilon_i} \sum_{j=1}^{n_E} P(C_i|E_j) n(E_j) \tag{7.5}$$

where $n(E_j)$ is the number of events in the effect bin j, $P_0(C_i)$ is the a priori probability (prior) of the cause C_i (usually taken from the MC simulation) and ϵ_i is the efficiency of the selection in the bin i.

The population in the cause bins can be written in terms of the *unfold matrix*, defined as:

$$\hat{n}(C_i) = \sum_{j=1}^{n_E} \mathcal{M}_{ij}^{-1} n(E_j). \tag{7.6}$$

Here, the $\mathcal{M}_{ij}^{-1}$ it is defined as:

$$\mathcal{M}_{ij}^{-1} = \frac{P(E_j|C_i) \cdot P_0(C_i)}{\sum_{l=1}^{n_E} P(E_l|C_i) \sum_{l=1}^{n_C} P(E_j|C_l) \cdot P_0(C_l)} \tag{7.7}$$

that is different from the inverse of M_{ij}.

The posterior probability of each cause C_i is evaluated as:

$$\hat{P}(C_i) = \frac{\hat{n}(C_i)}{\sum_j \hat{n}(C_j)} \tag{7.8}$$

In the Iterative Bayesian unfolding method, $n(C_i)$ is obtained iteratively, applying Eqs 7.6 and 7.7 a number of times, each time replacing the prior probabilities in 7.7 with the posterior probabilities from 7.8, after a polynomial fit.

Each of this iteration will give an improved estimation of the actual distribution, until the algorithm reached a certain stability where each new result does not differ significantly from the previous one.

This unfolding procedure is implemented in the analysis by using the package `RooUnfold` [147, 148].

For the unfolding we also need to define the following variables:

- $\vec{b}$: the expected background events distribution with n bins.
- $f_{\text{acc}}^i = \dfrac{N_{\text{reco}\wedge\text{part}}^i}{N_{\text{reco}}^i}$ *acceptance factors*: for each bin of the reconstructed distribution, which corrects for reconstructed-level events which did not fall into the fiducial region defined at particle-level and thus have no associated particle-value which can be used during the unfolding. Therefore, it is defined as the fraction of signal events reconstructed in this bin that also pass the particle-level selection. The bin i here is defined by the *reconstructed-level* value of the variable.

- $\epsilon^i = \frac{N^i_{\text{part}\wedge\text{reco}}}{N^i_{\text{part}}}$ *efficiency factors*: for each bin of the unfolded distribution, which account for efficiency and acceptance losses on going from truth to reco. The bin i here is defined by the *truth-level* value of the variable.

For our analysis, the unfolding procedure acts as follows: for each observable, the procedure starts from the number of events observed in data at reconstruction level in bin j of the distribution (N^j_{reco}), from which the background contribution N^j_{bkg} is subtracted. Then the acceptance, migration and efficiency corrections are applied. All corrections are evaluated using the MC simulation of the signal sample.

The first step is the application of the acceptance correction f^j_{acc}. The resulting distribution is then unfolded to the particle level. The unfolding procedure uses as input the migration matrix derived from the simulated signal sample which maps the particle-level bin i in which an event falls to the bin j in which it is reconstructed. The probability for particle-level events to be reconstructed in the same bin is represented by the elements on the diagonal, and the off-diagonal elements represent the fraction of particle-level events that migrate into other bins. Therefore, the elements of each row sum to unity. For each observable, the number of bins is optimised such that the fraction of events in the diagonal bins is always greater than 50%.

The last step is the application of the efficiency correction factor ϵ to the unfolded spectrum, correcting the result with a bin-by-bin factor into the fiducial phase-space.

An important application of the unfolding method is the measurement of the differential cross-section $d\sigma$ of a process. The differential cross-section of interest is a function of a kinematic variable X and the procedure to measure it can be summarized as follows:

$$\frac{\mathrm{d}\sigma^{\text{fid}}}{\mathrm{d}X^i} \equiv \frac{1}{\mathcal{L}\cdot\Delta X^i}\cdot\frac{1}{\epsilon^i}\cdot\sum_j \mathcal{M}^{-1}\cdot f^j_{\text{acc}}\cdot\left(N^j_{\text{obs}} - N^j_{\text{bkg}}\right), \tag{7.9}$$

where the index j runs over bins of observable X at reconstruction level while the index i labels bins at particle level, ΔX^i is the bin width, $\mathcal{L}$ is the integrated luminosity, and the inverted migration matrix as obtained with the iterative unfolding procedure is symbolised by M^{-1}.

In this method, the initial prior probabilities are obtained from a reference truth distribution.

The integrated fiducial cross-section σ^{fid} is obtained by integrating the differential cross-section over the bins, and its value is used to compute the normalised differential cross-sections:

$$\frac{1}{\sigma^{\text{fid}}}\cdot\frac{\mathrm{d}\sigma^{\text{fid}}}{\mathrm{d}X^i}. \tag{7.10}$$

Examples of acceptance, efficiency and migration matrices for the m^{bl}_{minimax} variable are shown in Figure 7.1. The full list of plots for each variable are presented in Appendix C.1.

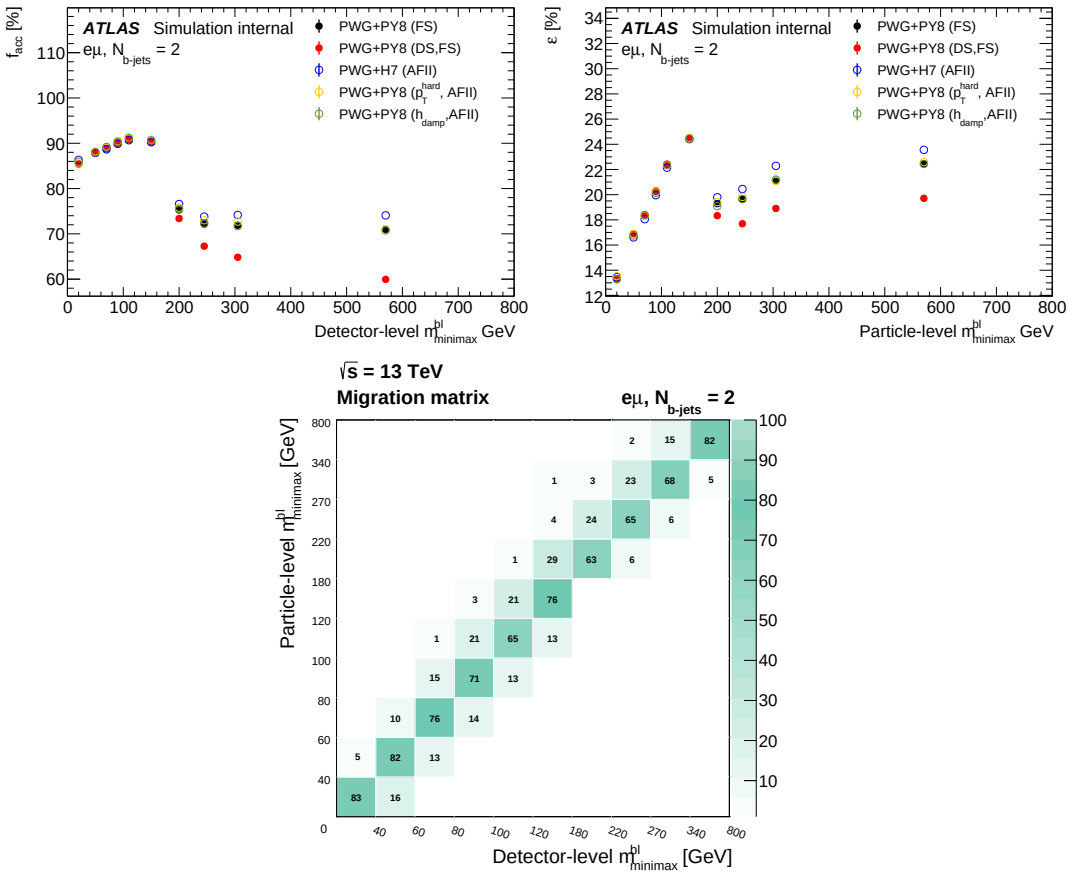

Figure 7.1: The (left) acceptance (f_{acc}) and (right) efficiency ε corrections and (bottom) the migration matrix for the m^{bl}_{minimax} variable. The nominal acceptance and efficiency corrections, in black, are compared to the corrections obtained with some MC generators used to evaluate the signal modelling uncertainties. In the migration matrix, only bins where the migration is greater than 1% are shown.

7.2 Binning choice and resolution studies

The binning optimization is based on the resolution of the ATLAS detector and reconstruction algorithms and is performed for each variable separately. The influence of the resolution is described by a matrix which relates a given variable at particle level and the difference between the reconstructed level and particle level. Resolution matrices were evaluated on simulation using a fine binning. The resolution is evaluated in each particle level bin of the migration matrix by looking at the profile distribution and is defined as the standard deviation of the difference between the reconstructed and particle level values. In the case of a resolution perfectly gaussian the 68% of the events would lie in ± 1 RMS.

This resolution-based binning has been derived by the following iterative formula from the profile distributions:

$$\delta \cdot \mathrm{Resol}(y_{\mathrm{N}}) \geq \frac{x_{N+1} - x_N}{2}, \tag{7.11}$$

where $\mathrm{Resol}(y_N)$ is the resolution function ($\mathrm{RMS}(y_{\mathrm{particle}} - y_{\mathrm{reco}})$) for a given variable in the specified bin and x_{N+1}, x_N are bin edges. The parameter δ is a parameter to account for the possible non-gaussian shape of the resolution distributions. A scan over different values of δ has been performed to asses its impact of the binning choice. In most of the case values of δ smaller than 1 already yields good results in terms of diagonality of the migration matrix and stability against closure and stress tests, which are described in Sections 7.3.1 and 7.3.2 respectively. An additional requirement of an expected statistical error on the number of reconstructed events (using a rough definition of $\sigma_{\mathrm{stat.}} = \sqrt{N_{\mathrm{events}}}$) in the given bin lower than 5% is applied.

For these studies, overflow bins have been ignored, but a special treatment was introduced for the last bin during the computation: if the last bin was small, but not due to the tight resolution, instead due to the reaching of the range limit of the histogram, last and second to last bins were merged.

7.2.1 Unfolded distributions

A total of 11 observables have been chosen for the differential cross-section measurement. The $m^{bl}_{\mathrm{minimax}}$ variable, described in Appendix B.2, is unfolded in the $2b$-exclusive fiducial phase-space, while variables related to the number of jets and the kinematics of jets, leptons and $E_{\mathrm{T}}^{\mathrm{miss}}$, are unfolded in the $2b$-inclusive fiducial phase-space. Specifically:

$p_{\mathbf{T}}^{\mathbf{jet}_{1/2}}$: transverse momentum of the leading and subleading jet.

$p_{\mathbf{T}}^{\mathbf{lep}_{1/2}}$: transverse momentum of the leading and subleading lepton.

$p_{\mathbf{T}}^{bb}$: transverse momentum of the b-jet pair. The pair is built using the leading and subleading b-jets.

p_{T}^{bbll} : transverse momentum of the *bbll* system. The system is built using the leading and subleading *b*-jets and the two charged leptons.

m^{bbll} : invariant mass of the *bbll* system.

m_{T}^{bb4l} : transverse mass of the *bb4l* system. The system is built using the leading and subleading *b*-jets, the two charged leptons and the $E_{\mathrm{T}}^{\mathrm{miss}}$ as a proxy for the neutrinos.

p_{T}^{bb4l} : transverse momentum of the *bb4l* system.

N_{jets} : number of jets.

Final binning choice of our variables can be found in Table 7.1.

Variable	**Bin edges**
$m_{\mathrm{minimax}}^{bl}$	0,40,60,80,100,120,180,220,270,340,800
p_{T}^{jet1}	25,40,60,75,105,145,200,260,400
p_{T}^{jet2}	25,40,60,75,105,145,200,260,400
p_{T}^{lep1}	28,34,39,45,52,61,71,83,97,115,134,158,188,223,268,338,400
p_{T}^{lep2}	28,32,37,44,51,61,73,88,105,123,150,182,400
p_{T}^{bb4l}	0,30,55,85,115,150,200,250,320,400,500,800
m^{bbll}	40,160,190,220,255,290,330,375,425,485,555,635,725,825,1000,1300,2000
m_{T}^{bb4l}	120,225,275,325,380,450,520,600,700,820,960,1150,1400,2000
p_{T}^{bb}	0,30,55,80,110,145,190,260,360,700
p_{T}^{bbll}	0,30,55,85,115,150,200,250,320,400,500,800
N_{jets}	2,3,4,5,6,7,$\geq$ 8

Table 7.1: Binning choice for the unfolded variables. All variables, besides the number of jets, are measured in GeV.

7.3 Unfolding validation tests

Some unfolding validation tests have been performed in order to test the efficiency of the unfolding method used in the analysis. In Section 7.3.1 closure tests are described while in Section 7.3.2 stress tests are presented.

Both closure and stress tests have been performed to assess the reliability and stability of the chosen unfolding method. Non-closure was found to be at a sub-per-mill level and is not used as a systematic uncertainty. Similarly, stress tests are extreme tests of the unfolding procedure where spectra are reweighted much more than the typical data/prediction differences, thus, no systematics is applied either.

7.3.1 Closure tests

The POWHEG +PYTHIA 8 $t\bar{t} + tW$ sample is used to perform closure tests to demonstrate that the unfolding procedure is stable with respect to statistical fluctuations in the reconstructed spectrum. To perform these tests, the signal sample is split in two statistically-independent sub-samples generated by assigning each event of the signal sample to the two subsamples. The first sub-sample (`half0`) is filled with even-numbered events, while, the second sub-sample (`half1`) is filled with odd-numbered events. One of these sub-samples is used as pseudo-data (`half1`), the other one, is considered as MC signal (`half0`) and used for the evaluation of the unfolding corrections. The first step of the closure tests consists of unfolding the pseudo-data sample by applying the corrections obtained with the MC signal sample. Then the unfolded pseudo-data are compared to the corresponding particle level spectra. For these tests two source of uncertainties are defined: a 'data stat.' to account for the limited statistics in the pseudo-data sample and a 'MC stat.' to account for the limited statistics in the sample used to model the corrections. The first is treated with the same procedure as the actual data statistical uncertainty described in Section 7.4.5 with a difference in how the pseudo-experiments are performed, since in this case instead of using a Poisson distribution centered on the event count (weighted sum of the MC events) in each bin, a Gaussian distribution is used, with mean the event count and RMS the square root of the sum of the weights squared. The second component, MC stat., is defined in the same way of the MC stat. systematic uncertainty described in Section 7.4.5. Using this two source of uncertainties, a covariance matrix is built by summing up the two individual covariance matrices. Finally, the compatibility of the unfolded pseudo-data and its corresponding particle level spectrum is evaluated using a χ^2 test.

The plots show that the unfolded results are within the uncertainties and this is also confirmed by the χ^2 values in the tables below. In the first column of each table the names of the observables are listed. The second and the third column respectively show the χ^2 compatibility divided by the degrees of freedom and the p-values between the unfolded pseudo-data and the corresponding particle level spectrum in the case of `half0` as the prediction (column 2) or `half1` (column 3). The covariance matrix used to calculate the χ^2 includes both the covariance matrix of the pseudo-data sample and the covariance matrix of the MC sample. The number of degrees of freedom (NDF) is equal to the number of bins in the (absolute) distribution.

In Figure 7.2 the closure tests for the m^{bl}_{minimax} variable with `half0` as pseudo-data and `half1` as MC sample in the $2b$-exclusive signal region are shown.

The other closure tests for the $2b$-inclusive signal region are shown in Appendix C.2.

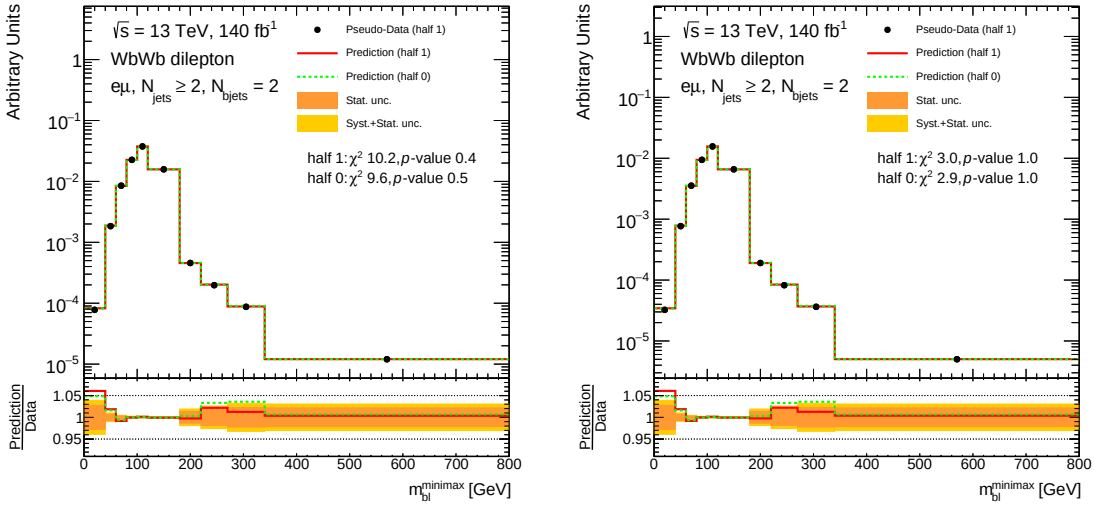

Figure 7.2: Unfolding closure tests for the absolute (left) and relative (right) cross-section measurement of the m^{bl}_{minimax} variable. The yellow band includes both the statistical uncertainty on the pseudo-data sample (`half0`) and the uncertainty on the MC sample (`half1`).

7.3.2 Stress tests

Due to the specific choice of the Monte Carlo sample for the training of the unfolding, it is necessary to check whether this choice could introduce a bias via the unfolding. To do this check the MC reweighting is required, in order to change the shapes of the distributions and get a varied distribution used as pseudo-data. The obtained reweighted MC is then unfolded with the nominal MC response and the result is compared to the reweighted MC at particle-level. Non-closure would indicate that the unfolding introduces a bias towards the training particle-level spectrum.

The final reweighted histograms have been then scaled by $N_{\text{nominal}}/N_{\text{reweighted}}$ where N_{nominal} and $N_{\text{reweighted}}$ are evaluated before any selection cuts, in order to preserve the total cross-section. In general, the reweighting shapes have been chosen extreme enough to put the unfolding procedure under a significant stress. As in the case of the closure tests, two sources of uncertainties are taken into account: a 'data stat.' and 'MC stat.' uncertainties. Their treatment is described in Section 7.3.1.

In Figure 7.3 the stress tests for the m^{bl}_{minimax} variable, using a reweighting function based on the data/MC discrepancy for the m^{bl}_{minimax} spectrum are shown as an example. In Figures 7.4 - 7.5 same tests are shown using respectively the $p_{\text{T}}^{\text{lep1}}$ and $p_{\text{T}}^{\text{bjet1}}$ reweighting functions.

The full list of the stress tests performed on the other variables are shown in Appendix C.3.

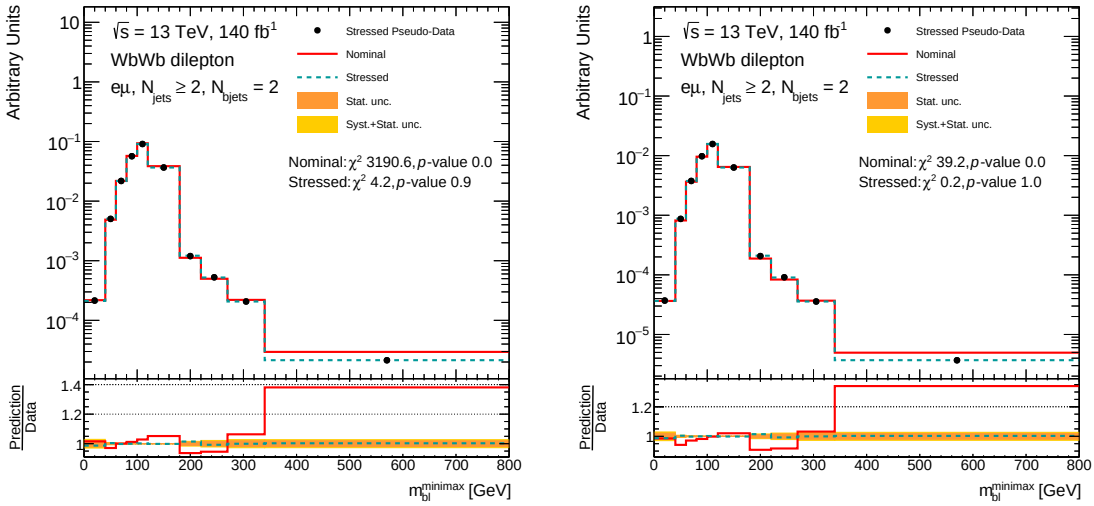

Figure 7.3: Unfolding stress tests for the absolute (left) and relative (right) cross-section measurement of the m^{bl}_{minimax} variable, using the m^{bl}_{minimax} reweighting function. The yellow band includes both the statistical uncertainty on the pseudo-data sample and the uncertainty on the MC sample.

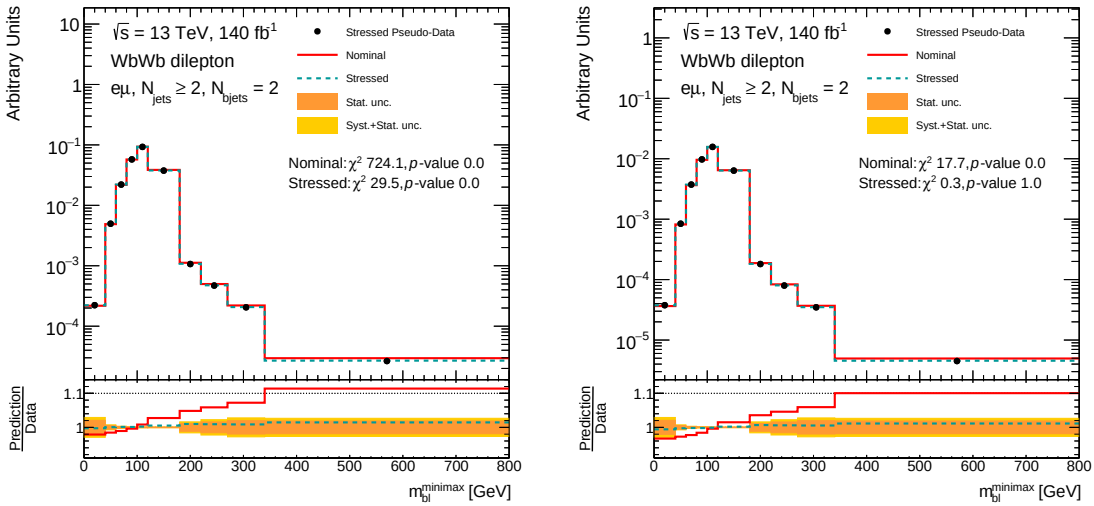

Figure 7.4: Unfolding stress tests for the absolute (left) and relative (right) cross-section measurement of the m^{bl}_{minimax} variable, using the $p_{\text{T}}^{\text{lep1}}$ reweighting function. The yellow band includes both the statistical uncertainty on the pseudo-data sample and the uncertainty on the MC sample.

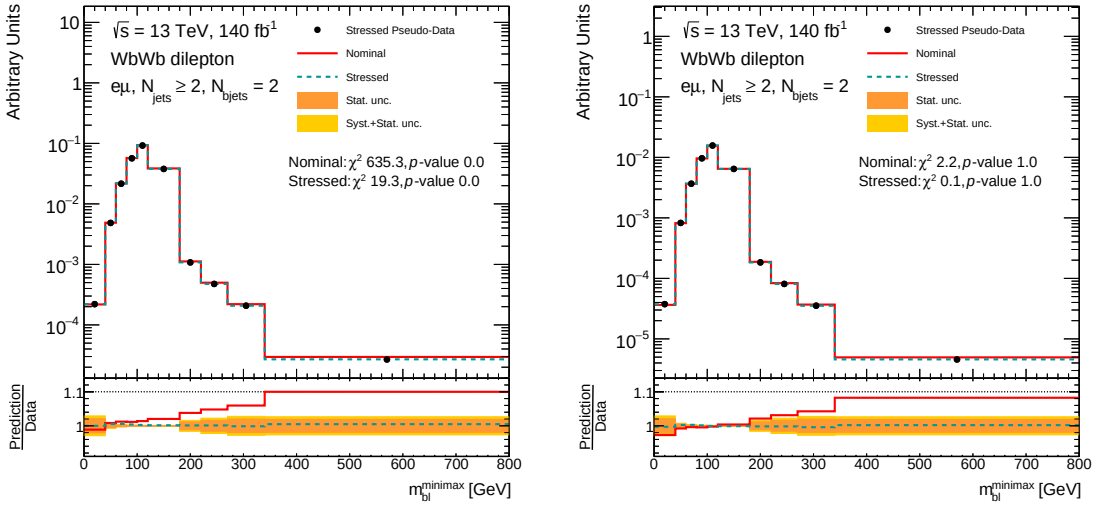

Figure 7.5: Unfolding stress tests for the absolute (left) and relative (right) cross-section measurement of the m^{bl}_{minimax} variable, using the $p_{\text{T}}^{\text{jet1}}$ reweighting function. The yellow band includes both the statistical uncertainty on the pseudo-data sample and the uncertainty on the MC sample.

Stressed data, unfolded with nominal (black marker) overlap with the truth of the stress tests; this means that the unfolding lead us to the ”right” truth distribution.

7.4 Uncertainties

Several sources of uncertainties affect the measured differential cross-sections. The statistical and systematic uncertainties due to detector effects and the ones related to the modelling of the signal and background MC components, which were found to be the most relevant ones, are described in this Section.

7.4.1 Uncertainty propagation

Each systematic uncertainty was evaluated at detector-level and then propagated through the unfolding procedure (described in Section 7.1). Deviations from the nominal predictions were evaluated separately for the upward and downward variations (or in the case of a single variation by symmetrizing the single deviation) for each bin of each observable.

In general, the impact on the measurement of each source of uncertainty is evaluated by unfolding the varied MC detector level spectra with nominal corrections and comparing the unfolded result to the particle-level distribution of the generator corresponding to the detector-level spectrum, which was unfolded (in essence, looking into a non-closure

under different assumptions at the detector and the corrections levels). The relative uncertainties evaluated with this procedure are directly applied to unfolded data.

The signal modeling systematic uncertainties are evaluated in a different way due to the need to compare to different predictions (particle-level distributions). The alternative MC (MC B) is used as the pretend data and is unfolded using the corrections coming from the nominal sample (using the AFII corrections if MC B is AFII). The unfolded result is compared to the truth spectrum of MC B, and the relative uncertainty is finally applied to the unfolded data.

The detector-related uncertainties are briefly described in Section 7.4.2, while the uncertainties on the signal modelling are described in Section 7.4.3 and the ones related to background modelling are discussed in Section 7.4.4. Finally, in Section 7.4.6 the systematics uncertainties breakdown is presented.

7.4.2 Detector-related systematics

The detector systematics can be split into two types: one type where the systematic is assessed by applying event weights to the simulated events (e.g. trigger efficiency uncertainties) and the second type where the systematic is assessed by modifying the four-vector(s) of some of the selected objects (e.g. jet energy scale uncertainties).

Leptons

Electrons and muons both have uncertainties associated with the understanding of the energy / momentum scale and resolution. These variations modify the momentum of the leptons. The calibration of the efficiency of the lepton reconstruction and identification comes with associated uncertainties and these are propagated via changes to the scale factors for the leptons. In a similar way, the scale factors for the trigger efficiencies are varied to account for uncertainties in the measurements of the trigger efficiencies of the lepton triggers.

Uncertainties affecting the momentum scale, resolution and trigger, reconstruction, identification and isolation efficiency of the electrons and muons are estimated using $Z \to ee/\mu\mu$ and $W \to e\nu$ samples, with the procedure described in [149, 150].

Jets

The impact of the uncertainty on the jet-energy scale and resolution was estimated by varying the jet energies according to the uncertainties derived from simulation and in-situ calibration measurements, following the final recommendations for the full Run 2 data reprocessed with the ATLAS software release 21 [151].

The uncertainty originating from the JVT requirement on jets is assessed by varying the scale factor associated with the JVT requirement [76].

b-tagging

The identification of jets which originate from a b-hadron is performed using a multivariate algorithm, `DL1r` [152]. Scale factors are applied to simulations to correct the jet flavour tagging efficiencies to match those in data [153, 154, 155]. The corrections are applied for the tagging efficiency of b-jets and the mis-tag rates of c- and light-jets, in bins of the PCB scores, with corresponding uncertainties derived for each jet flavour. A principle component analysis is performed to diagonalize the covariance matrix given the input systematic uncertainties considered in the calibration of the tagging efficiencies. This results in a number of orthogonal eigen-variations for each jet flavour, which are then used as nuisance parameters in this analysis. These nuisance parameters are labelled as `b-tagging DL1r [B, C, Light]`.

Three additional components labelled as `Jet PCBT high` p_{T} `[lj,bj,cj]` correspond to the uncertainties associated with the efficiency extrapolation to high jet p_{T} The uncertainties for the high jet p_{T} are derived separately for b-jets, c- and light-jets.

Missing transverse energy

The uncertainties on the energy scales and resolutions of the reconstructed leptons and jets are propagated to the missing transverse momentum in a correlated way.

In addition, there are scale and resolution uncertainties associated with the soft term that are independent uncertainty components [156, 157]. These uncertainties modify the magnitude and direction of the missing transverse momentum vector. These contributions were evaluated using $Z \to \mu\mu$ events from the $E_{\mathrm{T}}^{\mathrm{miss}}$ data/MC ratio in events without jets and from the balance between soft terms and hard objects using methods similar to those used in Ref. [157].

Pileup modelling

The uncertainty on the reweighting procedure used to correct the pile-up profile in MC to match the data is obtained by varying by $\pm 1\sigma$ the scale factors.

7.4.3 Signal modelling systematics

Our limited understanding of the generators modelling the signal processes is a significant source of uncertainty. The impact of this kind of uncertainties has been evaluated using alternative predictions that are described in Chapter 6, following the procedure described in Section 7.4.1.

tW and $t\bar{t}$ normalization

Differential cross-section measurements are typically insensitive to the overall normalization of the signal sample. This is because the signal sample contributes to the unfolding only through efficiency, acceptance, and migration corrections. These corrections, being yield ratios, do not depend on the total cross-section. This principle holds when the signal sample consists of a single process, as in the case of $t\bar{t}$ differential cross-sections. However, in this analysis, the signal comprises the sum of two processes: the tW and $t\bar{t}$ production. This composition makes the unfolding corrections sensitive to the relative normalization between the two processes. For instance, the dependence on the total cross-section in the case of the efficiency correction can be explicitly shown as follows:

$$\begin{aligned}\varepsilon_{tW+t\bar{t}} &= \frac{N_{tW}^{\text{truth,reco}} + N_{t\bar{t}}^{\text{truth,reco}}}{N_{tW}^{\text{truth}} + N_{t\bar{t}}^{\text{truth}}} \\ &= \frac{N_{tW}^{\text{truth,reco}}}{N_{tW}^{\text{truth}} + N_{t\bar{t}}^{\text{truth}}} + \frac{N_{t\bar{t}}^{\text{truth,reco}}}{N_{tW}^{\text{truth}} + N_{t\bar{t}}^{\text{truth}}} \\ &= \frac{\sigma_{tW}}{\sigma_{tW} + \sigma_{t\bar{t}}}\varepsilon_{tW} + \frac{\sigma_{t\bar{t}}}{\sigma_{tW} + \sigma_{t\bar{t}}}\varepsilon_{t\bar{t}}. \end{aligned} \tag{7.12}$$

Consequently, we consider two sources of systematic uncertainty: '$t\bar{t}$ normalization' and 'tW normalization'. These uncertainties are defined by independently varying the normalization of the $t\bar{t}$ and tW samples, while keeping the rest at their nominal normalization. The variations are defined by rescaling the samples by $1 \pm \delta_{xs}$, where δ_{xs} is the relative error on the $t\bar{t}$ (NNLO+NNLL) and tW (NLO+NNLO) cross-sections, as described in Section 6.2.1.

Hadronization model

The uncertainty due to the choice of the hadronization model and other non-perturbative aspects of the parton shower is evaluated using the POWHEG+`Herwig7`.1.3 and POWHEG+`Herwig7`.0.4 samples for the $t\bar{t}$ and tW processes, respectively. Since the tW process in POWHEG+`Herwig7` is produced with fixed scales, this uncertainty is evaluated by employing the tW POWHEG+PYTHIA8 sample produced with fixed scales.

Scales

The uncertainty due to the choice of the μ_{r} and μ_{f} scales in the hard-scatter and in the showering is evaluated using a prediction obtained with POWHEG+PYTHIA8, where μ_{r} and μ_{f} in the hard scatter are varied independently by a factor 0.5 and 2.0 and the scales in the showering are varied accordingly to the Var3c eigentune of the A14 tune [158]. These variations affect mainly ISR.

Final state radiation

The uncertainty due to the FSR simulation is obtained using a POWHEG+PYTHIA8 sample where the renormalization scale used in the final-state shower is varied by a factor 2 and 0.5 with respect to the nominal value.

h_{damp}

Another parameter affecting the additional radiation is h_{damp}. The uncertainty due to the choice of this parameter is estimated independently from the other ISR components using a dedicated POWHEG+PYTHIA8 sample where h_{damp} is multiplied by a factor 2 with respect to the nominal value.

Matrix-element matching

The matrix-element matching uncertainty is evaluated by comparing the nominal sample with an alternative sample obtained setting the $p_{\text{T,hard}}$ parameter in `Pythia8` to 1 and comparing it to the nominal sample, in which the parameter is set to 0. This parameter regulates the definition of the vetoed region of the showering, which is important to avoid hole/overlap in the phase space filled by `PowhegBox` and `Pythia8`. This prescription is based on the studies described in [113, 114].

Recoil uncertainty

The recoil uncertainty of the top pair system is evaluated by comparing the nominal sample with an alternative sample using a different recoil strategy described in Section 6.2.2. Similarly to the above uncertainty, only the top pair component of the signal is modified in the alternative sample.

Top-quark mass

The top-quark mass is known with a precision of around 0.5 GeV [159]. This can impact the analysis because the kinematics of the decay products (and hence the probability to pass the selection requirements) depends on the top-quark mass. The uncertainty is estimated by using two additional simulated samples with varied top-quark mass values of 169 GeV and 176 GeV. These samples otherwise have the same setup as the nominal $t\bar{t}$ sample and are used to evaluate an uncertainty via the unfolding result, identically to other modelling effects. The final uncertainty is then scaled by 1/7 to match the effect of a ± 0.5 GeV shift in the top-quark mass. The uncertainty of 0.5 GeV is obtained from events in the full phase-space. As the top-quark mass is Lorentz invariant, it is appropriate to apply this top-quark mass value and uncertainty to the limited phase-space used in the analysis.

PDF

The effect of a different PDF choice modifies the efficiency, acceptance and the response matrix, i.e. the corrections used to correct the spectrum at the detector level to the particle level. The impact of the choice of different PDF sets has been assessed by applying an event-by-event reweighting procedure to the nominal POWHEG+PYTHIA8 $t\bar{t}$ and tW samples following the PDF4LHC15 prescription [160]. The 30 variations PDF4LHC15 set were combined to define a relative uncertainty as

$$\delta_{\text{PDF}} \equiv \frac{\sqrt{\sum_{i \in \text{sets}} (U_i \cdot R_0 - T_0)^2}}{T_0}$$

where the 0 (i) subscripts denote the PDF4LHC15 central (varied) PDF set, R represents the distribution at the detector level while T symbolizes the distribution at the particle level, and the unfolding procedure is shortened into the U operator, with subscript on each characterizing the PDF set used to evaluate the spectrum or the corrections. The resulting uncertainties are found to be at the sub-percent level, with few excesses to 1 or 2% in low statistics bins.

Treatment of the $t\bar{t}/tW$ interference

Another component of the uncertainty is represented by the difference between the two approaches diagram removal and diagram subtraction, used to remove the overlap between the $t\bar{t}$ and tW productions. This uncertainty only affects the tW component of the signal; the tW_{DS} sample is used instead of the tW_{DR} to form the alternative signal, with $t\bar{t}$ remaining the nominal for the alternative sample.

7.4.4 Uncertainties on the background processes

Several backgrounds enter the signal region estimation, therefore several uncertainties are associated to them.

Z+jets

A global uncertainty, based on α_s, PDF and scale variations and calculated in [161], is applied to the MC prediction of the Z+jets background components. These uncertainties, evaluated in bins of jet multiplicity, take into account variations of PDFs, α_s, μ_F and μ_R.

Diboson and $t\bar{t}V$

The uncertainty on the cross-section calculation for the processes $t\bar{t}Z$, $t\bar{t}W$ and $t\bar{t}H$ composing the $t\bar{t}V$ sample are respectively 13.3%, 12.5% and 9.9% [127]. In the analysis a conservative uncertainty of 13.3% is considered for all the three processes.

Background from fake and non-prompt leptons

A 50% normalization uncertainty is assigned to this background to reflect the uncertainty in evaluating it from MC. This has been validated in regions with similar kinematic cuts as the signal regions but with the two leptons of the same charge, where the contribution of events with fake/non-prompt leptons is expected to dominate.

7.4.5 Other uncertainties

Finite MC sample statistics

To account for the limited statistics of the Monte Carlo samples, pseudo experiments are used to evaluate the impact of finite statistics. The number of events in each bin is smeared by a Gaussian shift with mean equal to the yield of the bin, and standard deviation equal to the uncertainty of the bin. Then, the smeared spectrum is unfolded. The procedure is replicated 10k times, then the final statistical uncertainty is evaluated from the RMS over the 10k toys. The resulting systematic uncertainty was found to be typically below 0.5%, increasing to $1-2\%$ in the tails of some distributions.

Integrated luminosity

The uncertainty in the combined 2015–2018 integrated luminosity is 0.83% [162], obtained using the LUCID-2 detector [163] for the primary luminosity measurements, complemented by measurements using the inner detector and calorimeters. This uncertainty is propagated to the unfolded results by varying the luminosity by $\pm 0.83\%$ in the reconstructed simulated spectra and unfolding them using the nominal corrections.

Data statistics

The uncertainty due to the data statistics is propagated through the unfolding by creating Poisson smeared pseudo-experiments that are passed through the unfolding procedure.

7.4.6 Systematic uncertainties breakdown

In this section summary plots of the uncertainties on the measured differential cross-section in the $2b$-exclusive and inclusive signal regions are presented.

The plots show the fractional uncertainties on the measured differential cross-sections, for the absolute and relative measurements, for the different observables. The uncertainties are grouped in the following categories:

- Parton shower: uncertainties related to the parton shower modelling, as described in Section 7.4.3.
- Hard scattering: uncertainties related to the hard scattering modelling, which include the matching uncertainties, as described in Section 7.4.3.
- Generator parameters: uncertainties related to the choice of the generator parameters, such as the h_{damp} parameter, the top-quark mass, the renormalization and factorization scales, the ISR and FSR parameters, the PDF and the Monte Carlo statistics, as described in Sections 7.4.3 and 7.4.5.
- Jets: uncertainties related to the jet energy scale and resolution, as well as the JVT scale factor, as described in 7.4.2.
- $t\bar{t}$ modelling: uncertainties that affect the modelling of the $t\bar{t}$ component of the signal such as the $t\bar{t}$ normalization and the recoil to top, as described in Sections 6.2.1 and 7.4.3.
- tW modelling: uncertainties that affect the modelling of the tW component of the signal, specifically the uncertainty on the tW cross-section and the uncertainty on the tW diagram removal procedure, as described in Section 7.4.3.
- Flavour tagging: uncertainties related to the b-tag scale factors, as described in Section 7.4.2.
- Background: uncertainties related to the background modelling, as described in Section 7.4.4.

The statistical and total uncertainties are shown as well. Minor sources of uncertainties, such as those related to the leptons and $E_{\text{T}}^{\text{miss}}$, are not shown in the plots.

The summary of the fractional uncertainties on the measured absolute and relative differential cross-sections as a function of m^{bl}_{minimax} is presented in Figure 7.6.

Summary plots of the fractional uncertainties for the measured normalised differential cross-sections in the $2b$-inclusive signal region are shown in Figures 7.7 - 7.9. The corresponding plots for the absolute differential cross-sections are shown in Appendix C.4.1.

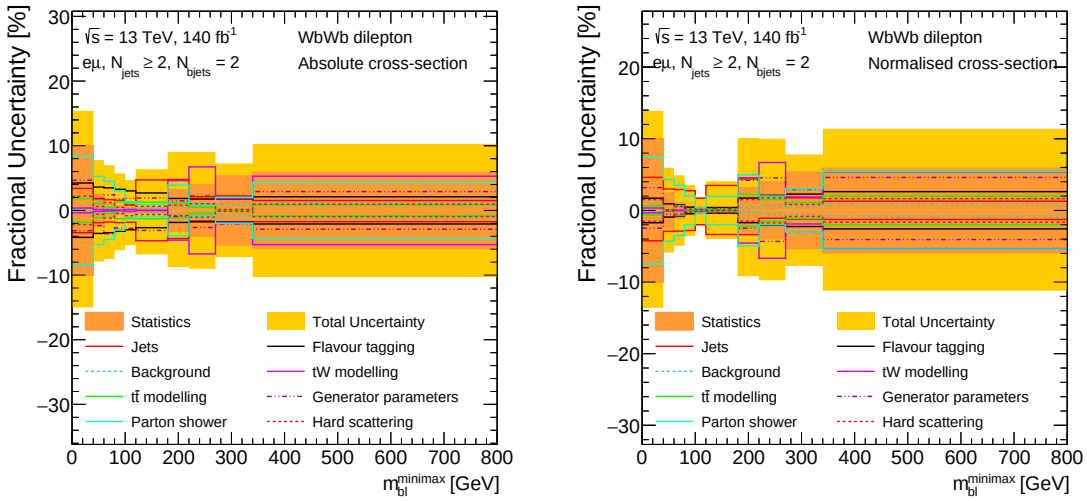

Figure 7.6: Uncertainties breakdown for the absolute (left) and relative (right) cross-section measurement of the m^{bl}_{minimax} observable.

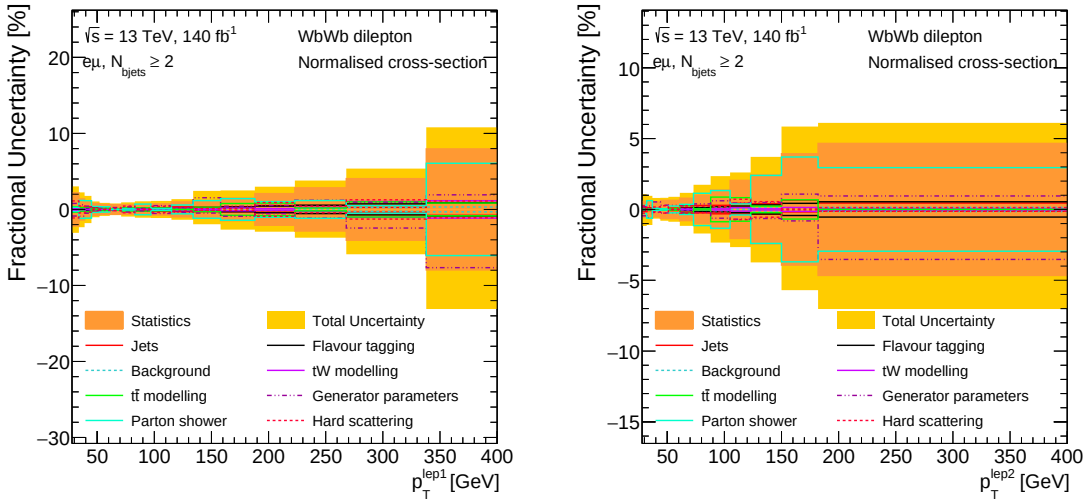

Figure 7.7: Uncertainties breakdown for the relative cross-section measurement of the leading (left) and subleading (right) lepton p_{T}.

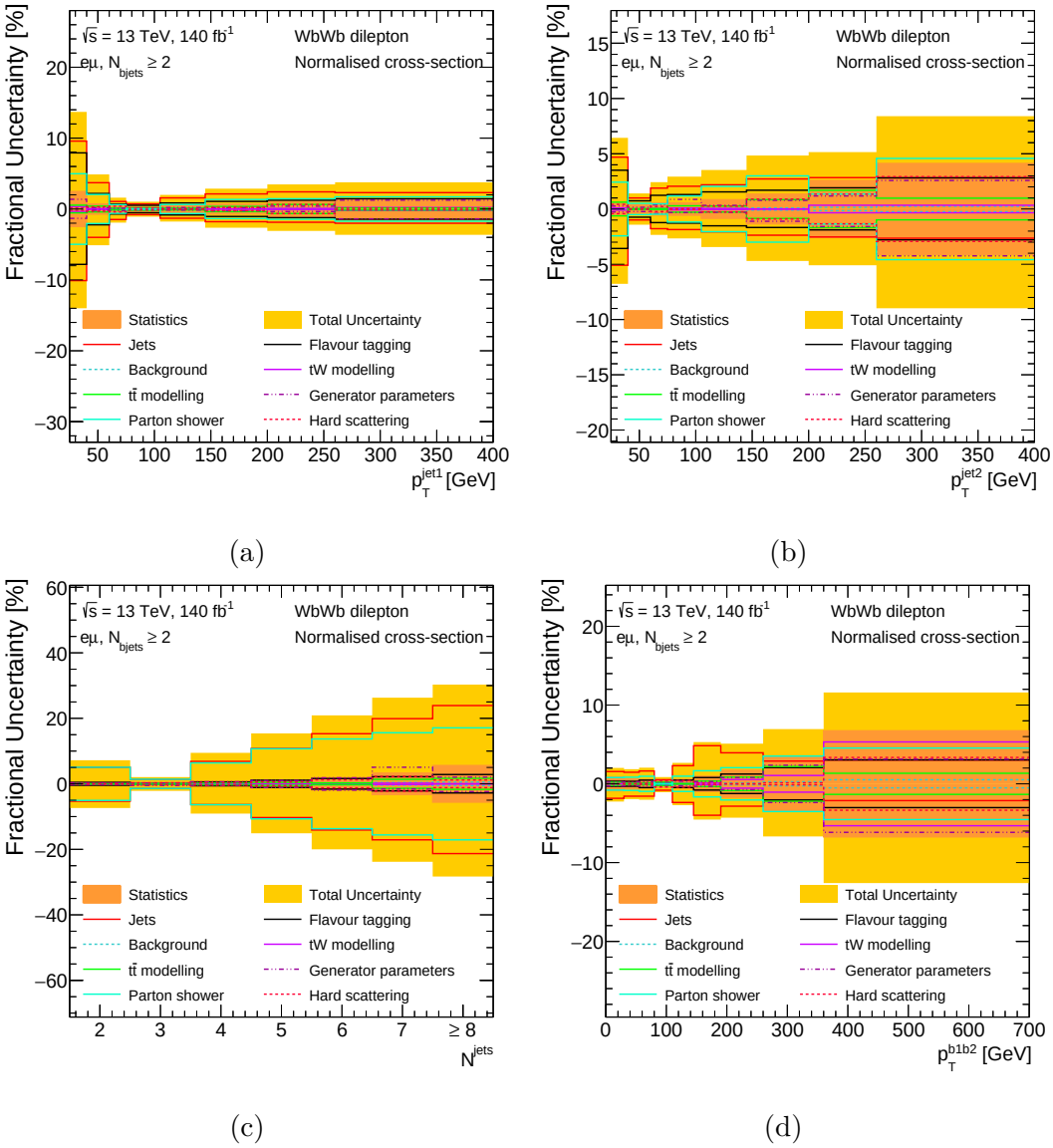

Figure 7.8: Uncertainties breakdown for the relative cross-section measurement of the a leading and b subleading jet p_{T}, c number of jets and d the p_{T} of the bb system.

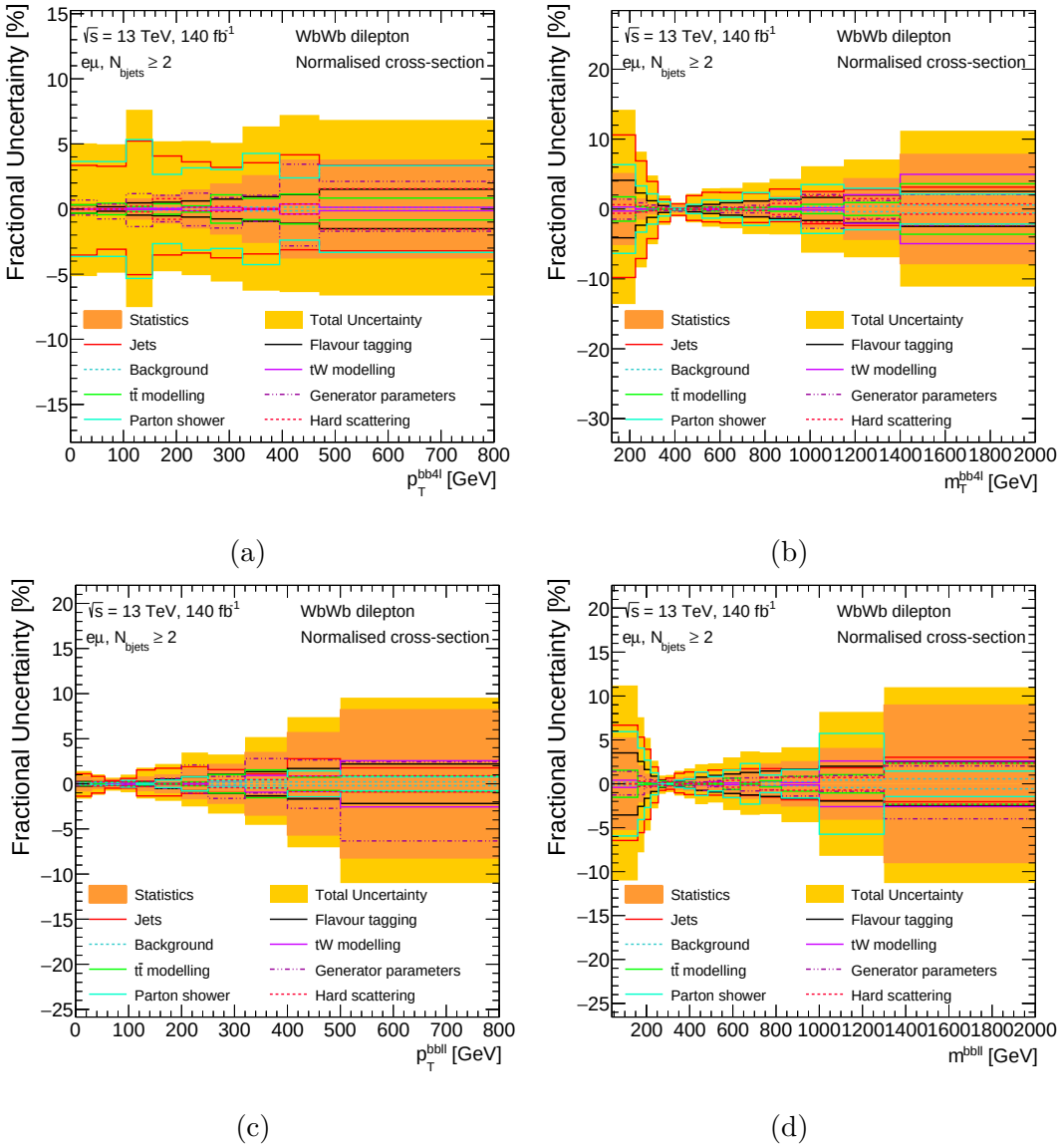

Figure 7.9: Uncertainties breakdown for the relative cross-section measurement of the a p_{T} and b m_{T} of the *bb4l* system, and c p_{T} and d mass of the *bbll* system.

7.4.7 Covariance matrices

The **covariance matrix** incorporates the statistical uncertainty and the systematic uncertainties from detector, signal and background modelling, described in the previous sections.

For each source of systematic uncertainty, the corresponding covariance matrix is computed using this formula:

$$c_{ij} = \begin{pmatrix} c_{11} & c_{12} & \dots & c_{1n} \\ c_{21} & c_{22} & \dots & c_{2n} \\ \vdots & \vdots & \ddots & \vdots \\ c_{n1} & c_{n2} & \dots & c_{nn} \end{pmatrix} \tag{7.13}$$

where $c_{ij} = \sigma_i \cdot \sigma_j$, with σ_i defined as:

$$|\sigma_i| = \frac{|\delta u_i| + |\delta d_i|}{2} \tag{7.14}$$

where δu_i is the "up" variation of a given uncertainty in bin i and δd_i is the respective "down" variation.

The sign of σ is defined in the following way:

- If $\delta u \cdot \delta d < 0$: $\text{sign}(\sigma) = \text{sign}(\delta u)$.
- Else if $\delta u \cdot \delta d > 0$ and $|u| > |d|$: $\text{sign}(\sigma) = \text{sign}(\delta u)$.
- Else if $\delta u \cdot \delta d > 0$ and $|u| < |d|$: $\text{sign}(\sigma) = -\text{sign}(\delta u)$.

The statistical components (both for data statistics and Monte carlo statistics) are obtained performing pseudo-experiments, as described in Section 7.4.5. Each pseudo-experiment is unfolded and the covariance c_{ij} is defined as:

$$c_{ij} = \langle (x_i - \langle x_i \rangle)\,(x_j - \langle x_j \rangle) \rangle \tag{7.15}$$

where x_i and x_j are the post-unfolding values of the pseudo-experiments in bins i and j.

The systematic component of the covariance matrix is defined as the sum of each covariance matrix for each systematic and the total covariance matrix is defined as the sum of the systematic and the statistical components.

7.5 The QUnfold package

Along with the main analysis work, I developed (along with two other collegues) a new unfolding method based on quantum annealing and a software related to it, called `QUnfold`. A deep explanation about its structure and functionalities are explained in the following subsections.

7.5.1 Quantum computing

Quantum computing is a science based on principles of quantum mechanics and information theory. *Quantum algorithms* are particular algorithms that exploit some properties deriving from quantum mechanics; some examples are the Shor [164] and Groover [165] algorithms. In order to work, quantum algorithms need to operate through computers capable of manipulating objects in which the quantum component is sufficiently manifest: such computers are called **quantum computers** [166].

Quantum computations is based on 3 fundamental quantum concepts:

- Superposition principle
- Quantum entanglement
- Tunneling effect

In classical computing the unit of measurement of the information is the *bit*, which can assume values 0 or 1. Classical computing is performed by creating classical circuits which are processed by the *Central Processing Unit* (CPU).

On the other side, the unit of measurement of the quantum information is the *qubit* (quantum bit) which is represented by a mix of 0 and 1 states. Qubit manifests evidence of quantum computing properties like superposition and can be represented by an atom, a trapped ion or other similar entities.

Quantum computation is represented through quantum circuits which make use of gates which do not have a counterpart in classical logical circuits. An example is shown in Figure 7.10. These quantum circuits are processed by the *Quantum Processing Unit* (QPU).

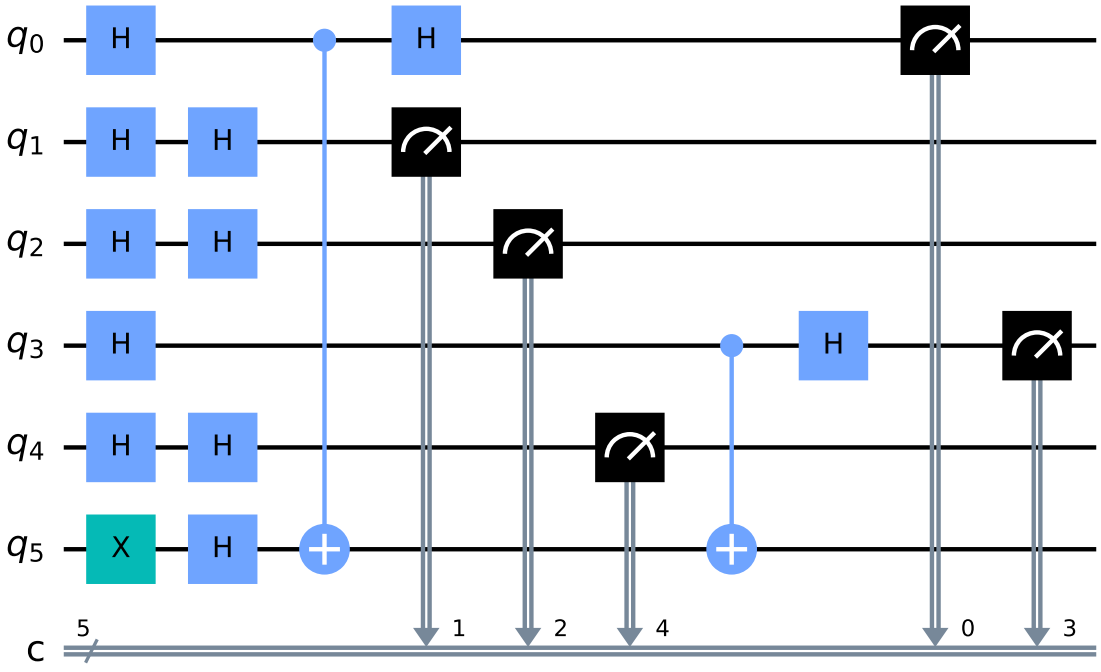

Figure 7.10: Example of quantum circuit of the *Bernstein-Vazirani algorithm*, drawn using the `Qiskit` package [167].

7.5.2 Quantum annealing and D-Wave

Quantum annealing is a particular quantum algorithm which does not make use of quantum gates in order to perform computations. This algorithm is based on the minimization of a cost function which has the form of an Hamiltonian, which represents the energy of a system and is commonly used to solve optimization problems.

In an optimization problem you search for the best of many possible combinations. These problems include scheduling challenges, such as "What is the most efficient route a traveling salesperson should take to visit different cities?".

Physics can help solve these sort of problems because you can frame them as energy minimization problems. A fundamental rule of physics is that everything tends to seek a minimum energy state; this behavior is also true in the world of quantum physics. Quantum annealing simply uses quantum physics to find low-energy states of a problem and therefore the optimal or near-optimal combination of elements [168].

Quantum annealing algorithm works in the following way: the quantum mechanical system is prepared in the known ground-state of an initial hamiltonian H_{init} while the target solution is encoded in the ground-state of a final Hamiltonian H_{fin}, written as the cost function of a *Quadratic Unconstrained Binary Optimization* (QUBO) problem [169]. The system evolution is controlled by the following time-dependent Hamiltonian:

$$H(t) = A(t)H_{\text{init}} + B(t)H_{\text{fin}} \tag{7.16}$$

At the time $t = 0$, $B(t) = 0$ while at $t = t_{\text{anneal}}$, $A(t) = 0$ where t_{anneal} is called *annealing time* and represents the time needed to reach the low energy state. In Figure 7.11 the evolution of the Hamiltonian $H(t)$ coefficients $A(t)$ and $B(t)$ over time is shown. Thanks to the **quantum adiabatic theorem**, if the evolution is slow enough, the quantum-mechanical system stays close the ground-state of the instantaneous Hamiltonian [170]. In Figure 7.12 a sketch of the evolution of the Hamiltonian $H(t)$ is presented. The QUBO Hamiltonian must have the following form in order to ensure the convergence of the annealing procedure into the required solution:

$$H_{\text{fin}} = H_{\text{QUBO}} = \sum_i a_i x_i + \sum_{i,j} b_{i,j} x_i x_j \tag{7.17}$$

where $x_i \in \{0, 1\}$ and $a_i, b_{i,j} \in \mathbb{R}$.

A QUBO problem is defined using an upper-diagonal matrix $\mathbf{Q}$, which is an $N \times N$ upper-triangular matrix of real weights, where $a_i = Q_{i,i}$ and $b_{i,j} = Q_{i,j}$. The purpose of the annealing is to minimize the QUBO Hamiltonian and extract the ground-state energy solution, which represents the solution of the combinatorial problem.

This formulation can also be expressed in a most concised form:

$$\min_{x \in \{0,1\}^n} \vec{x}^T \mathbf{Q} \vec{x}. \tag{7.18}$$

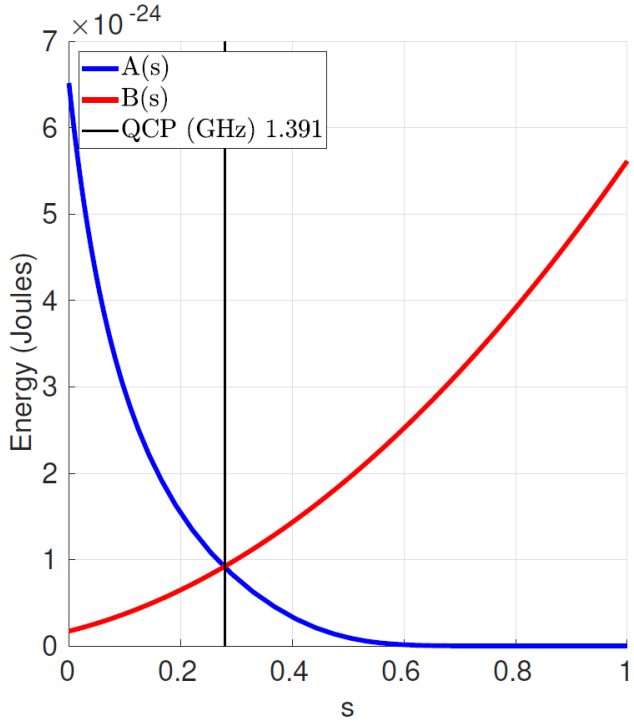

Figure 7.11: Evolution of the Hamiltonian $H(t)$ coefficients $A(t)$ and $B(t)$ over time. Annealing begins at $t = 0$ (called also s) with $A(t) \gg B(t)$ and ends at $s = 1$ with $A(t) \ll B(s)$. Data shown are representative of D-Wave 2X systems.

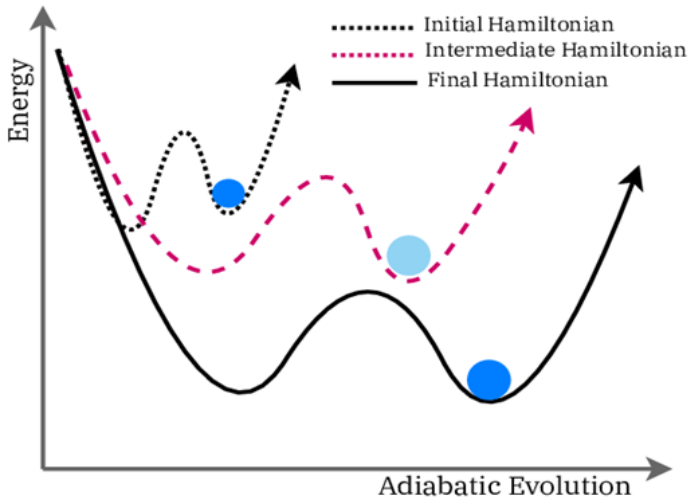

Figure 7.12: Evolution of the Hamiltonian $H(t)$ of a quantum mechanical system during quantum annealing.

Figure 7.13: Sketch of one of the D-Wave quantum annealers.

The D-Wave company is the only commerical quantum annealing machines provider so far (see Figure 7.13). The D-Wave QPU is a lattice of interconnected superconducting qubits [171] operating at around 15 mK and with a fixed limited topology. While some qubits connect to others via couplers, the D-Wave QPU is not fully connected. Instead, the qubits of D-Wave annealing quantum computers interconnect in some particular topologies. In Figure 7.14 an example of the *Pegasus* topology in D-Wave *Advantage* is shown. D-Wave Advantage is currently their best quantum annealer and counts more than 5000 qubits with more than 35.000 couplers.

This company gives also the possibility to run 1 min/month of jobs in its QPU for free. In order to get more QPU resources we got a collaboration with the CINECA company[4].

[4] https://www.cineca.it/

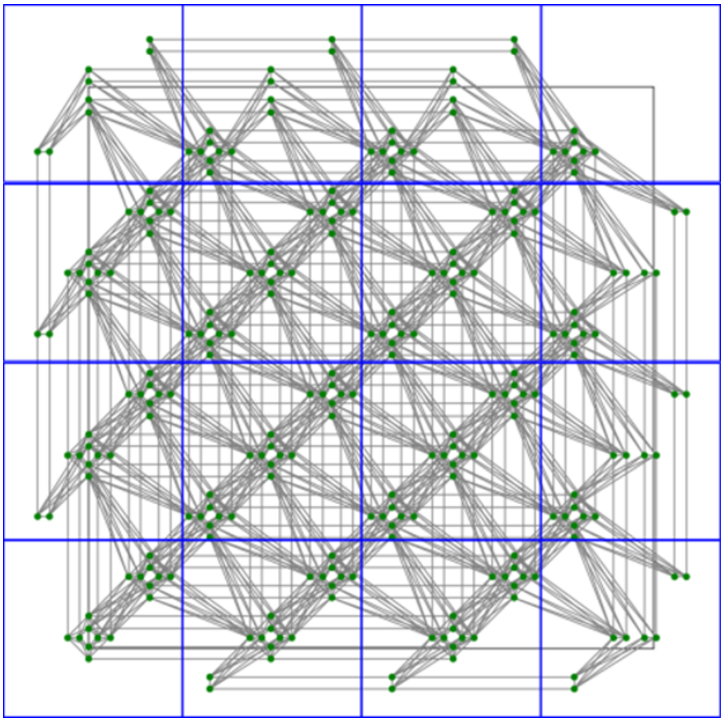

Figure 7.14: *Pegasus* topology of D-Wave *Advantage*.

7.5.3 Unfolding with quantum annealing

The unfolding method has been already introduced and explained in Section 7.1. In this section we will present a novel approach which makes use of the power of quantum annealing in order to solve the unfolding problem. A first proposal to this approach has been already presented in a 2019 work, in which a smaller version of D-Wave (2000Q) was used [172].

Before introducing benefits of quantum annealing into unfolding, we will introduce another possible approach to solve Eq. 7.2 based on a log-likelihood maximization.

This approach consists of constraining the truth-level distribution $\widehat{\theta}$ by maximizing a likelihood function $\mathcal{L}(\mu|d)$ that depends on the estimated reco-level spectrum $\mu = \mu(\widehat{\theta})$ and observed data d. In the case of a counting experiment, the likelihood is usually the product of Poisson or Gaussian, in the limit of large μ, distributions for each bin. The truth-level unfolded distribution $\widehat{\theta}$ is expected to ideally show a good degree of regularity. The most usual way to achieve this behaviour is to impose an additional constraint in the form of a Lagrange multiplier, added to the likelihood function, whose effect is to favour smooth solutions. The strength of the regularization parameter can be controlled by an additional parameter β. A common measure of smoothness to be minimized is the second derivative of the distribution, but any other order derivative can be used. This

procedure is called *Tikhonov regularization*.

The likelihood to be minimized is thus:

$$\mathcal{L}(\vec{\mu}|\vec{d}) = \left(\prod_i^N \text{Poiss}\left(\mu_i, d_i\right)\right) \times e^{-\beta\rho} \tag{7.19}$$

where:

$$\text{Poiss}(\mu_i, d_i) = \frac{\mu_i^{d_i}}{d_i!} e^{-\mu_i}, \tag{7.20}$$

$$\mu_i = \sum_j^N R_{ij}\hat{\theta}_j, \tag{7.21}$$

$$\rho = \sum_j^{N-1} (\hat{\theta}_{j+1} + \hat{\theta}_{j-1} - 2\hat{\theta}_j)^2. \tag{7.22}$$

The logarithm of the likelihood is preferrable to be minimized for numerical stability reasons.

At this point the unfolded distribution can be obtained in this way:

$$\max_{\vec{x}}(\log \mathcal{L}(\vec{\mu}|\vec{d}) + \lambda\mathcal{S}(\vec{\mu})) \tag{7.23}$$

where the second term is called *regularization term* and λ is the *regularization parameter*.

Before implementing quantum annealing in this machinery, we need to express the Eq. 7.19 in terms of a binary optimization, becase a QUBO model requires binary variables in order to work (see Eq. 7.17).

First of all, the maximization described in Eq. 7.23 can be rewritten into a minimization procedure, following the steps explained in [173] and assuming a normal distribution in each bin (*Gaussian approximation*). We get:

$$\min_{\vec{x}}(\|\mathbf{R}\vec{x} - \vec{d}\|^2 + \lambda\|\mathbf{D}\vec{x}\|^2) \tag{7.24}$$

where $\mathbf{R}$ is the response matrix and $\mathbf{D}$ is the Laplacian operator.

Thus, the objective function to be minimized is:

$$\vec{y} = \|\mathbf{R}\vec{x} - \vec{d}\|^2 + \lambda\|\mathbf{D}\vec{x}\|^2 \tag{7.25}$$

Through computations [172] it is possible to obtain two coefficients:

$$\vec{a} = -2\mathbf{R}^T\vec{d} \tag{7.26}$$

$$\mathbf{B} = \mathbf{R}^T\mathbf{R} + \lambda\mathbf{G}^T\mathbf{G} \tag{7.27}$$

which are part of the final reformulation of the objective function:

$$\vec{y} = \vec{a} \cdot \vec{x} + \vec{x}^T \mathbf{B} \vec{x} \tag{7.28}$$

Eq. 7.28 has the same form of Eq. 7.17 but it is not yet a QUBO hamiltonian because $\vec{x}$ variables are still integers (bin contents). Before rewriting it as a QUBO hamiltonian we need to encode variables from integer to binary. A binarization process based on the *logarithmic encoding* of the variables has been performed and the `PyQUBO` library [174] has been used for this purpose.

Finally, the number of variables, and therefore the number of logical qubits needed to solve Eq. 7.28 is given by:

$$N_{\text{qubits}} \propto \sum_{i=1}^{N^{\text{bins}}} \log_2 \left(N^i_{\text{entries}} \right) \tag{7.29}$$

where N_{bins} is the number of bins of the given histogram while N_{entries} is the vector of the number of entries in each bin. Eq. 7.29 is very important to have an idea of how many logical qubits are required to solve the unfolding problem on a given distribution. For example, for a Gaussian distribution with $N_{\text{bins}} = 20$ and $N_{\text{entries}} = 5.000.000$, $N_{\text{qubits}} \approx 350$. This implies that almost every unfolding problem related to LHC-size data can be afforded, because D-Wave currently counts around 5000 physical qubits[5].

7.5.4 The `QUnfold` library

We developed an open-source `Python` library capable of unfolding statistical distributions using the approach described in Section 7.5.3. This library name is `QUnfold` [175].

`QUnfold` relies on `NumPy` [176] library for linear algebra computation and on the D-Wave `Ocean` SDK to interface with quantum annealing[6] and is designed to work with real-scale HEP applications. This means that it can be used in every existing analysis since the implemented model is capable of working with LHC-size data, as explained at the end of Section 7.5.3.

The library is publicly available on GitHub[7] and `PyPi`[8] and is designed to be very intuitive and simple: an example of its interface usage is shown in Listing 7.1. After preparing the model for unfolding it is possible to choose which solver method to use. Currently there are three solver methods available on `QUnfold` which are based on the D-Wave SDK samplers:

[5] The number of physical qubits is different from the number of logical qubits, but having the number of logical qubits is still a good starting point to have an idea of the complexity of a given problem.

[6] The library is also fully compatible with `ROOT` [177] since converters from `NumPy` to `ROOT` are available in the utils modules.

[7] https://github.com/JustWhit3/QUnfold

[8] https://pypi.org/project/QUnfold/

```
# Import QUnfold base class and plotter
from QUnfold import QUnfoldQUBO

# Read numpy data from a file or sample them
truth = ... # truth distribution
measured = ... # measured distribution
response = ... # response matrix
binning = ... # binning of the distributions

# Run unfolding
unfolder = QUnfoldQUBO(response, measured, lam=0.1)
unfolder.initialize_qubo_model()
unfolded_SA, cov_matrix_SA =
   unfolder.solve_simulated_annealing(num_reads=10,
   num_toys=100)
```

Listing 7.1: Example of `QUnfold` usage using simulated annealing solver.

- Simulated annealing sampler (CPU).
- Quantum annealing sampler (QPU).
- Hybrid sampler (CPU + QPU).

In 2024 a bachelor's thesis about this library has been produced [178].

7.5.5 Tests on simulated data

To test our software in a realistic frame we decided to simulate a common physics process widely studied at the LHC: the $t\bar{t}$ process. This process can be obtained by the interaction of a top and anti-top quarks. We selected the dileptonic channel which is the one with two leptons and at least two b-jets in the final state. The final choice is represented by the following process:

$$pp \to t\bar{t} \to Wb\bar{W}\bar{b} \to l_1 b \nu_{l_1} \bar{l_2} \bar{b} \bar{\nu_{l_2}} \tag{7.30}$$

where p are protons, t are top quarks, W are weak interaction bosons, b are top quarks, l are leptons and ν are neutrinos, particles with a bar represents the corresponding anti-particle.

We generated ≈ 2.5 million events using the `Madgraph` generator (truth distribution) and we interfaced it with the `Delphes` simulator [179] to simulate detector-level data (measured distribution).

Our techniques consisted of using simulated and hybrid solvers of our library and compare them with two common HEP unfolding methods: matrix inversion[9] and IBU, which are implemented in the RooUnfold framework [147]. Some MC-based pseudo-experiments were run to compute the covariance matrix for evaluating the quality of the result, using χ^2 test-statistic[10], and estimating the statistical errors associated to the unfolding method. At the end we decided to unfold only four observables which are interesting to analyze: the leading and subleading lepton p_T and the leading and subleading lepton ηs. Results are shown in Figure 7.15. From the plots it is possible to observe that QUnfold works very well compared to IBU and sometimes even better, particularly in scenarios where the classical methods struggle with instability or noise. The hybrid solver solution is a bit unstable, but this is due to the D-Wave hybrid solver which is constrained to hardware limitations.

[9] As mentioned in Section 7.1 the matrix inversion method is never used in practice, but we decided to show him since from the theoretical point of view is interesting to see.

[10] The smaller the χ^2 is, the better the unfolding method has been to reconstruct the unfolded distribution.

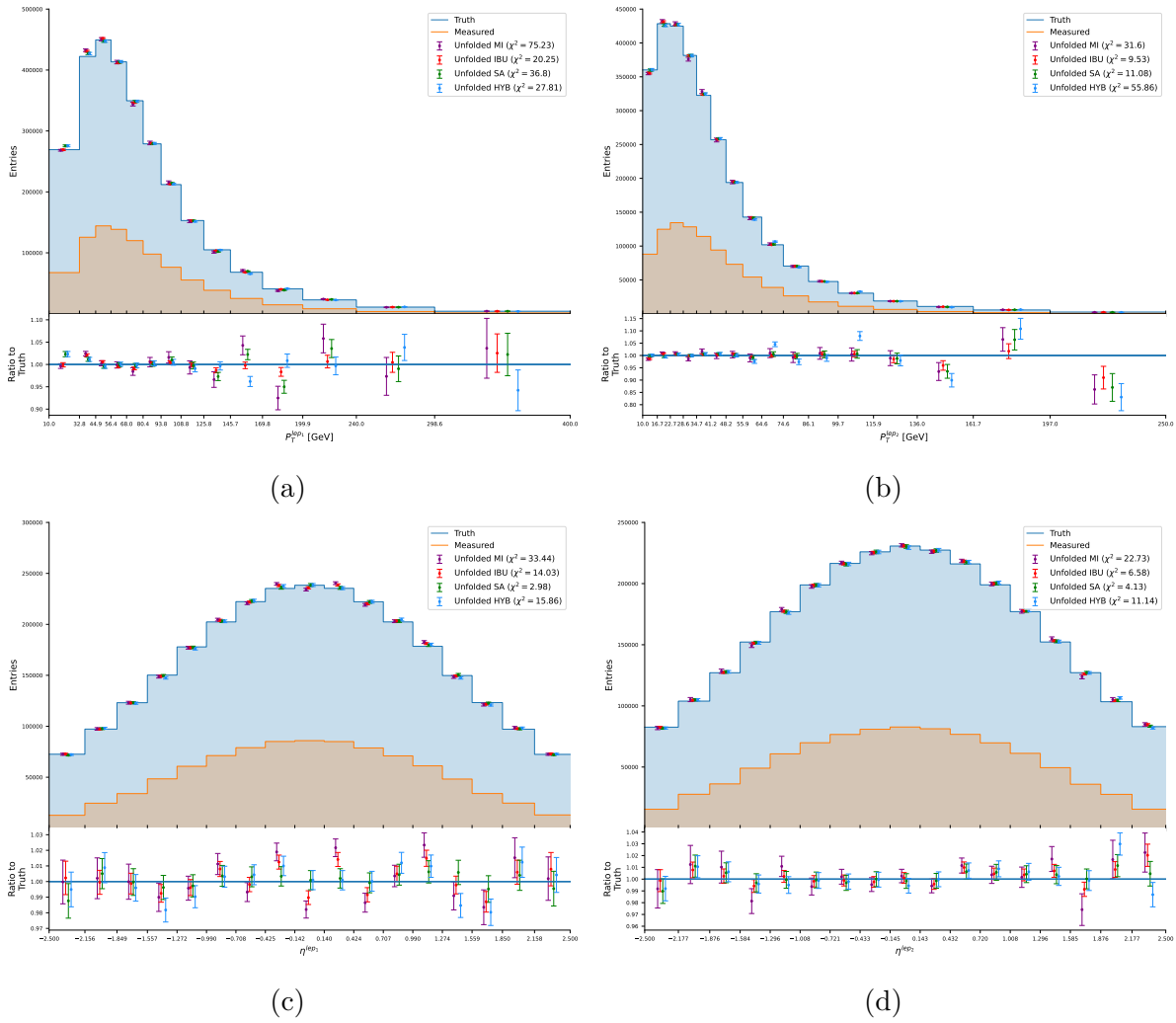

Figure 7.15: Unfolding of (a) leading lepton p_T, (b) subleading lepton p_T, (c) leading lepton η and (d) subleading lepton η.

7.5.6 The PyXSec framework

The QUnfold library is designed to work with plain unfolding, without taking into account other possible applications like its usage in the measurement of differential cross-sections of particle physics processes. In order to make QUnfold useful for measuring differential cross-sections we decided to design another Python framework which makes use of QUnfold to perform this task.

This framework is called PyXSec and is open source and publicly available on GitHub[11].

The main purpose of this software is basically to solve Eq. 7.9 using classical and quantum computing techniques and is mainly used to obtain results presented in Section 8.3.

[11] https://github.com/JustWhit3/PyXSec

Chapter 8

Results

In this chapter the main results of the analysis are presented. The metric used to assess the level of agreement between the measured cross-sections and the NLO+PS predictions is shown in Section 8.1. The measured differential cross-sections in the 2b-exclusive and 2b-inclusive regions are presented in Sections 8.2.1 and 8.2.2 respectively. To better compare the data with the different predictions, each distribution is presented twice; in Figures (a), the unfolded data are compared with theoretical predictions from different generators with variations sensitive to different interference models, while in Figure (b) the other MC used in the analysis are presented. The agreement of the different models with the measured differential cross-sections is assessed by computing the χ^2, and corresponding p-values, of the unfolded data with respect to the theoretical predictions employing the full covariance matrix.

Finally, in Sections 8.3.1 and 8.3.2 the measured differential cross-sections in the 2b-exclusive and 2b-inclusive regions performed using the `QUnfold` software are shown as a feasibility study. These latter plots are performed using the simulated annealing backend of DWave, described in Section 7.5.4. This choice is lead by the fact that hybrid and quantum solvers are unstable due to hardware limitations and, nowadays, are not

enough powerful to solve LHC-size problems. The purpose of these results is not to demonstrate that `QUnfold` works better than the standard classical cases, but to show that it is possible to perform such analysis using quantum computation, therefore this needs to be considered as a pure feasibility study.

8.1 χ^2 calculation

The level of agreement between the measured cross-sections and the predictions is evaluated using a χ^2 test-statistic. The p-value is extracted from the reduced χ^2 distribution. The χ^2 are computed using this formula:

$$\chi^2 = V^T \times \mathrm{Cov}^{-1} \times V \tag{8.1}$$

where Cov is the covariance matrix, described in Section 7.4.7 and V represents the vector of residuals, defined as the difference between the measured differential cross-section and the prediction.

For normalised differential cross-sections the vector of differences between data and predictions V_{N_b} is replaced with V_{N_b-1}, which is the same quantity, but obtained discarding the last one of the N_b elements and, consequently, Cov_{N_b-1} is the $(N_b-1)\times(N_b-1)$ sub-matrix derived from the full covariance matrix of the normalised measurements by discarding the corresponding row and column. The sub-matrix obtained in this way is invertible and allows the χ^2 to be computed. The χ^2 value does not depend on the choice of the element discarded for the vector V_{N_b-1} and the corresponding sub-matrix Cov_{N_b-1}. In this case, the NDF becomes $N_b - 1$

The full list of the correlation matrices can be found in Appendix D.1.

8.2 Results

8.2.1 Differential cross-sections in the 2b-exclusive region

The absolute and relative cross-section measurement as a function of $m^{bl}_{\mathrm{minimax}}$ are shown in Figures 8.1 - 8.2. The measurement is compared with predictions obtained with different MC generators and different interference schemes.

For each plot shown below, in the top panel, the unfolded data are shown as black points, while lines indicate the MC predictions. Uncertainties are shown by the shaded bands. The lower panel shows the ratio of the MC predictions to the unfolded data.

χ^2 and p-values of results are shown in Tables 8.1 and 8.2 for the different predictions.

The tW DR sample with dynamic scale is the only model compatible with data; none of the other predictions can reproduce the shape of the tail of the $m^{bl}_{\mathrm{minimax}}$ distribution. A special mention should be given to $bb4l$ as this should be the best model to describe the

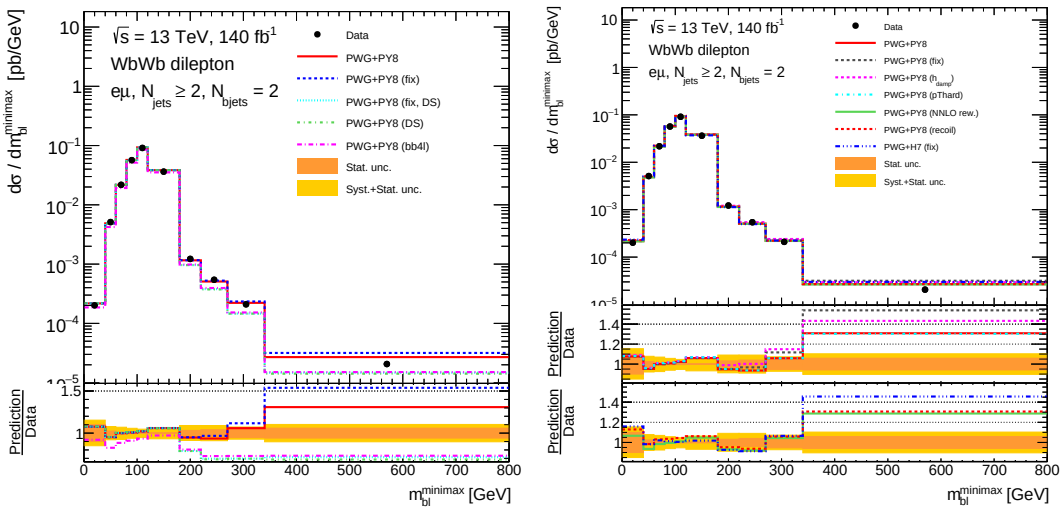

(a) (b)

Figure 8.1: Absolute differential cross-section measurement as a function of the m^{bl}_{minimax} variable. The unfolded data are compared with a predictions provided by POWHEG +PYTHIA 8 with different schemes for handling the $t\bar{t}/tW$ interference and b with predictions obtained with different MC generators.

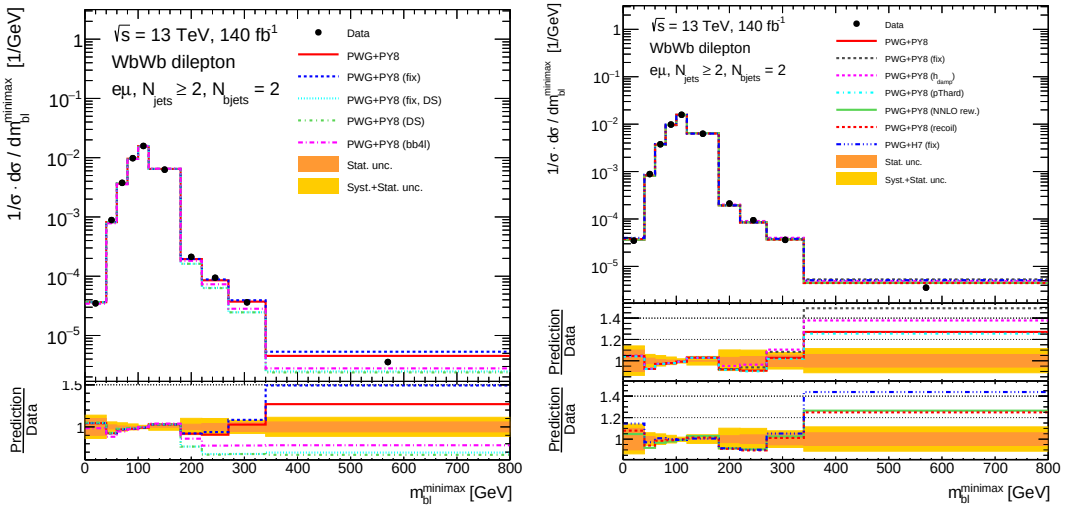

(a) (b)

Figure 8.2: Relative differential cross-section measurement as a function of the m^{bl}_{minimax} variable. The unfolded data are compared with a predictions provided by POWHEG +PYTHIA 8 with different schemes for handling the $t\bar{t}/tW$ interference and b with predictions obtained with different MC generators.

Observable	PWG+PY8 (h_{damp})		PWG+PY8 ($p_{\text{T,hard}}$)		PWG+PY8 (NNLO REW.)		PWG+PY8 (RECOIL)		PWG+H7 (fix)	
	χ^2/NDF	p-value	χ^2/NDF	p-value	χ^2/NDF	p-value	χ^2/NDF	p-value	χ^2/NDF	p-value
m^{bl}_{minimax} (norm.)	19.1/9	0.02	12.1/9	0.21	12.8/9	0.17	11.4/9	0.25	28.3/9	<0.01
m^{bl}_{minimax} (abs.)	25.3/10	<0.01	14.2/10	0.17	13.6/10	0.19	14.4/10	0.16	30.9/10	<0.01

Table 8.1: χ^2 and p-values quantifying the level of agreement between the measured differential cross-sections and predictions provided by different MC generators.

Observable	PWG+PY8		PWG+PY8 (FIX)		PWG+PY8 ($bb4l$)		PWG+PY8 (FIX, DS)		PWG+PY8 (DS)	
	χ^2/NDF	p-value	χ^2/NDF	p-value	χ^2/NDF	p-value	χ^2/NDF	p-value	χ^2/NDF	p-value
m^{bl}_{minimax} (norm.)	12.7/9	0.18	30.7/9	<0.01	28.9/9	<0.01	40.9/9	<0.01	39.1/9	<0.01
m^{bl}_{minimax} (abs.)	14.4/10	0.16	36.8/10	<0.01	49.4/10	<0.01	60.4/10	<0.01	57.5/10	<0.01

Table 8.2: χ^2 and p-values quantifying the level of agreement between the measured differential cross-sections and predictions provided by POWHEG+PYTHIA 8 with different schemes for handling the $t\bar{t}/tW$ interference.

interference but unfortunately this is not the case. In the absolute cross-section shown in Figure 8.1, the $bb4l$ prediction has a visible offset in the predictions; this is due to the lack of corrections (k-factors) that are used to normalize all other samples to the higher order prediction. Unfortunately, even in the normalized cross-section (shown in Figure 8.2b) where this effect is removed, the $bb4l$ prediction underestimates the cross-section in the tail of the distribution where the impact of the interference is larger. This measurement will be crucial for improving future versions of the $bb4l$ generator. It must also be noted that the PWG+PY8 (DS) predictions are almost identical for both dynamic and fixed scales; they are the least compatible with the data and the only ones being incompatible with the data from $\simeq 173\,\text{GeV}$.

8.2.2 Differential cross-sections in the 2b-inclusive region

The relative cross-sections measurements as a function of the kinematic variables of the $WbWb$ final-state objects are presented in Figures 8.3 - 8.4 for leading lepton and sub-leading lepton p_{T} and in Figures 8.5 - 8.6 for leading jet and sub-leading jet p_{T}. Cross-sections as a function of the additional jet multiplicity are shown in Figure 8.7. The distributions of the p_{T} and m_{T} of the $bb4l$ system, defined as the magnitude and transverse mass[1] of the vector sum of p_{T} of the two leading b-jets, the two leptons and the MET, is shown in Figures 8.8 - 8.9 respectively. Finally, normalised cross-section as a function of the mass and p_{T} of the $bbll$ system and the p_{T} of the bb system are shown in Figures 8.10 - 8.12; the two leading b-jets are used in these variables. These variables were chosen as they are sensitive to many MC parameters and in some cases have been used extensively for MC optimisation.

The corresponding plots, for the absolute differential cross-sections, are presented in

[1] $m_{\text{T}} = \sqrt{E^2 - p_z^2}$

Appendix D.2.

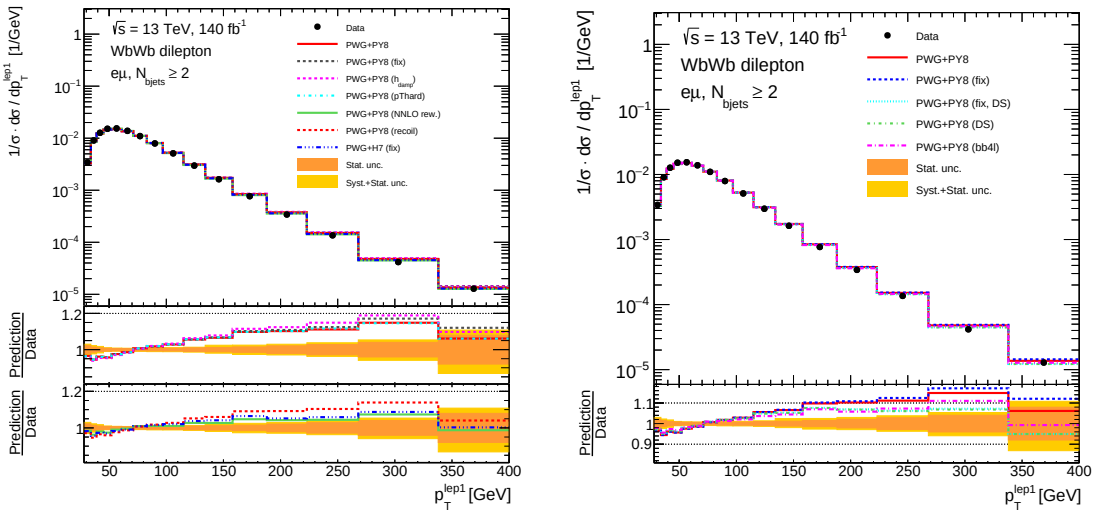

Figure 8.3: Relative differential cross-section measurement as a function of the leading lepton p_{T} compared to interference generators (right) and MC generators (left).

χ^2 and p-values of results are shown in Tables 8.3 and 8.4 for the different predictions.

Observable	PWG+PY8 (h_{damp})		PWG+PY8 ($p_{\mathrm{T,hard}}$)		PWG+PY8 (NNLO REW.)		PWG+PY8 (RECOIL)		PWG+H7 (FIX)	
	χ^2/NDF	p-value	χ^2/NDF	p-value	χ^2/NDF	p-value	χ^2/NDF	p-value	χ^2/NDF	p-value
$p_{\mathrm{T}}^{\mathrm{jet}_1}$	41.6/8	<0.01	19.5/8	0.01	7.1/8	0.53	13.6/8	0.09	9.9/8	0.27
$p_{\mathrm{T}}^{\mathrm{jet}_2}$	22.3/8	<0.01	11.7/8	0.17	3.2/8	0.92	5.7/8	0.68	2.1/8	0.98
$p_{\mathrm{T}}^{l_1}$	64.3/16	<0.01	47.6/16	<0.01	13.4/16	0.64	42.6/16	<0.01	20.9/16	0.18
$p_{\mathrm{T}}^{l_2}$	32.7/12	<0.01	30.3/12	<0.01	9.5/12	0.66	25.3/12	0.01	15.5/12	0.21
N^{jets}	9.2/7	0.24	24.5/7	<0.01	5.7/7	0.57	10.6/7	0.16	25.2/7	<0.01
p_{T}^{bb4l}	79.2/9	<0.01	46.1/9	<0.01	12.8/9	0.17	53.9/9	<0.01	45.1/9	<0.01
m_T^{bb4l}	24.8/13	0.02	18.9/13	0.13	17.4/13	0.18	17.1/13	0.20	25.8/13	0.02
m^{bbll}	32.7/16	<0.01	31.6/16	0.01	26.3/16	0.05	27.9/16	0.03	39.0/16	<0.01
p_{T}^{bbll}	91.5/11	<0.01	29.1/11	<0.01	13.5/11	0.26	35.9/11	<0.01	29.7/11	<0.01
p_{T}^{bb}	39.3/9	<0.01	12.8/9	0.17	4.7/9	0.86	13.9/9	0.13	18.0/9	0.04

Table 8.3: χ^2 and p-values quantifying the level of agreement between the measured normalized differential cross-sections and predictions provided by different MC generators.

In general, none of the predictions can describe all observables (none of them shows p-values larger than 0.05). This has been the case in other publications both in dilepton and semi-leptonic final states. One of the best predictions, as in the above publications, is PWG+H7 which is the only NLO+PS MC able to describe the leading jet and lepton p_{T}. After applying the NNLO reweighting, described in Section 6.2.2 the predictions obtained with the nominal PWG+PY8 improve notably, which is reflected by the p-values increasing systematically for all variables, making it the only prediction which can describe simultaneously all the variables in an acceptable way. This effect is minor

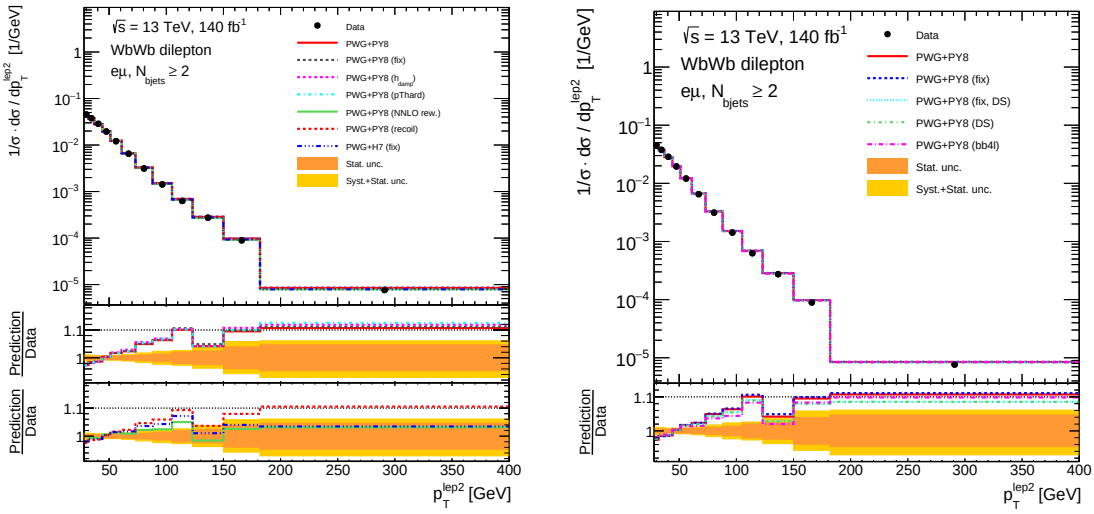

Figure 8.4: Relative differential cross-section measurement as a function of the subleading lepton p_{T} compared to interference generators (right) and MC generators (left).

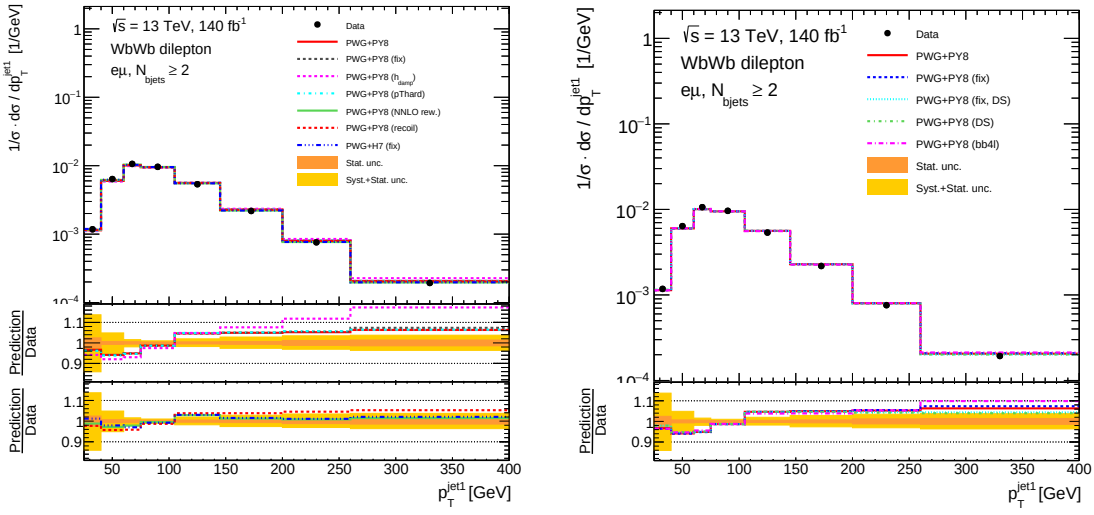

Figure 8.5: Relative differential cross-section measurement as a function of the leading jet p_{T} compared to interference generators (right) and MC generators (left).

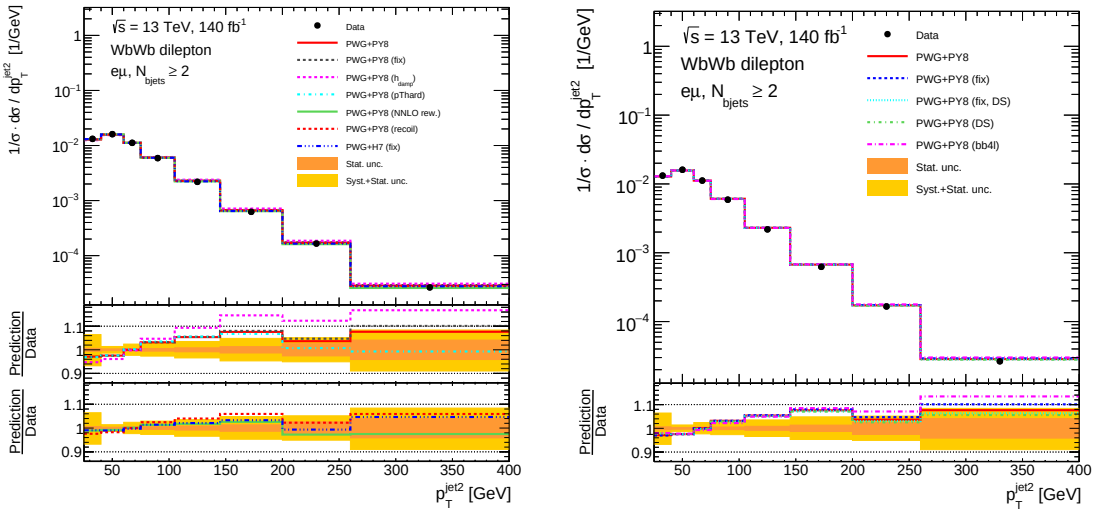

Figure 8.6: Relative differential cross-section measurement as a function of the subleading jet p_{T} compared to interference generators (right) and MC generators (left).

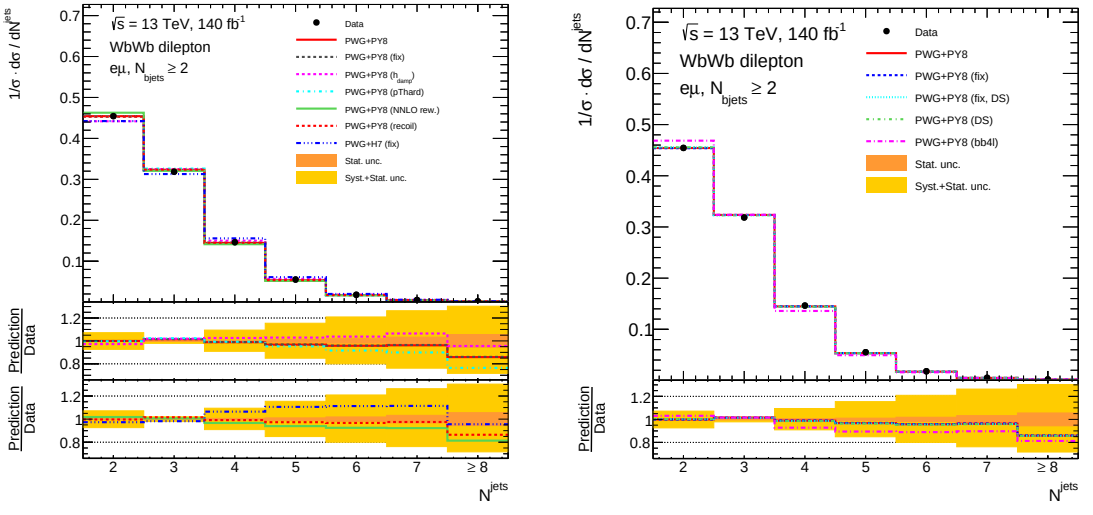

Figure 8.7: Relative differential cross-section measurement as a function of the additional jet multiplicity compared to interference generators (right) and MC generators (left).

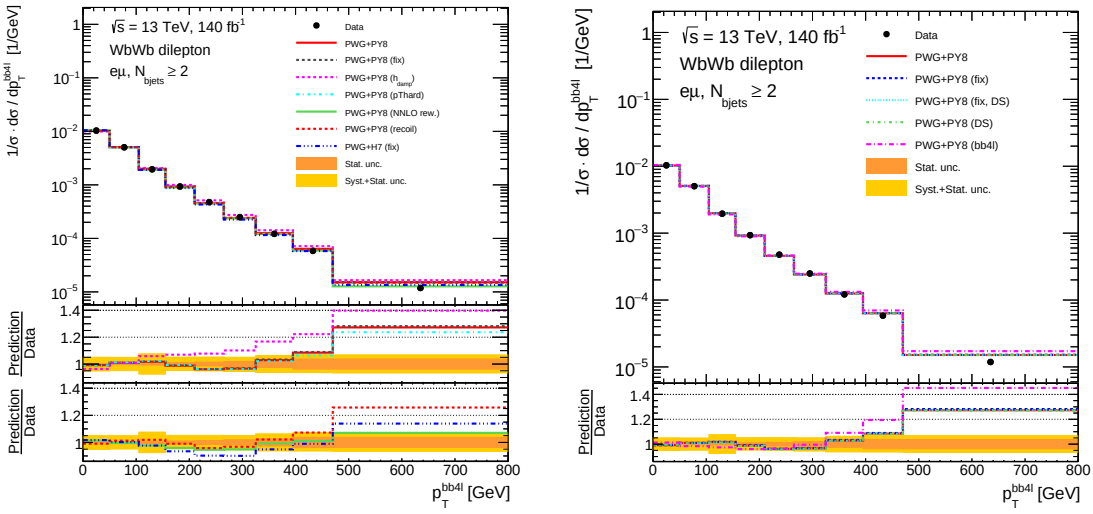

Figure 8.8: Relative differential cross-section measurement as a function of the p_{T} of the *bb4l* system compared to interference generators (right) and MC generators (left).

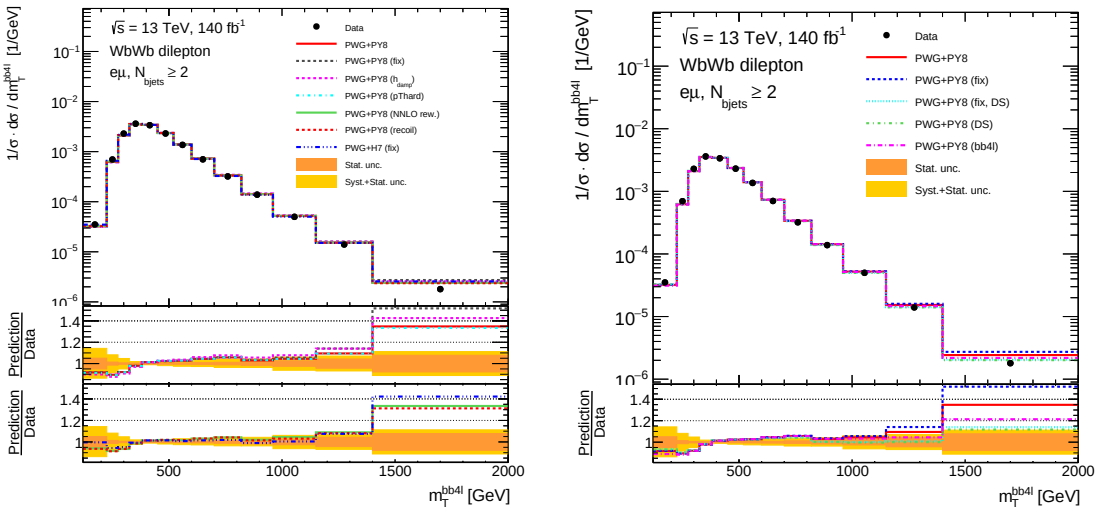

Figure 8.9: Relative differential cross-section measurement as a function of the m_{T} of the *bb4l* system compared to interference generators (right) and MC generators (left).

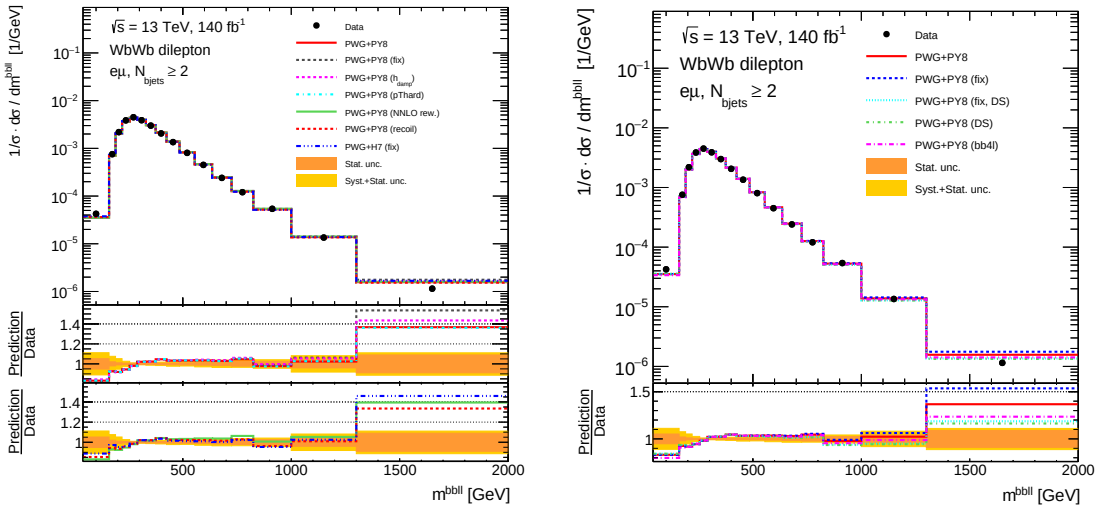

Figure 8.10: Relative differential cross-section measurement as a function of the mass of the *bbll* system compared to interference generators (right) and MC generators (left).

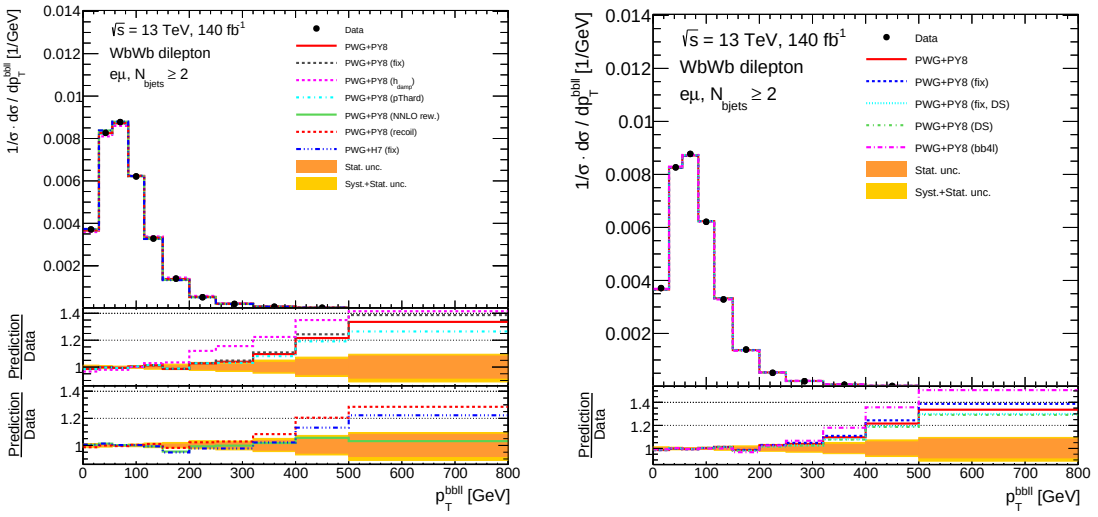

Figure 8.11: Relative differential cross-section measurement as a function of the p_{T} of the *bbll* system compared to interference generators (right) and MC generators (left).

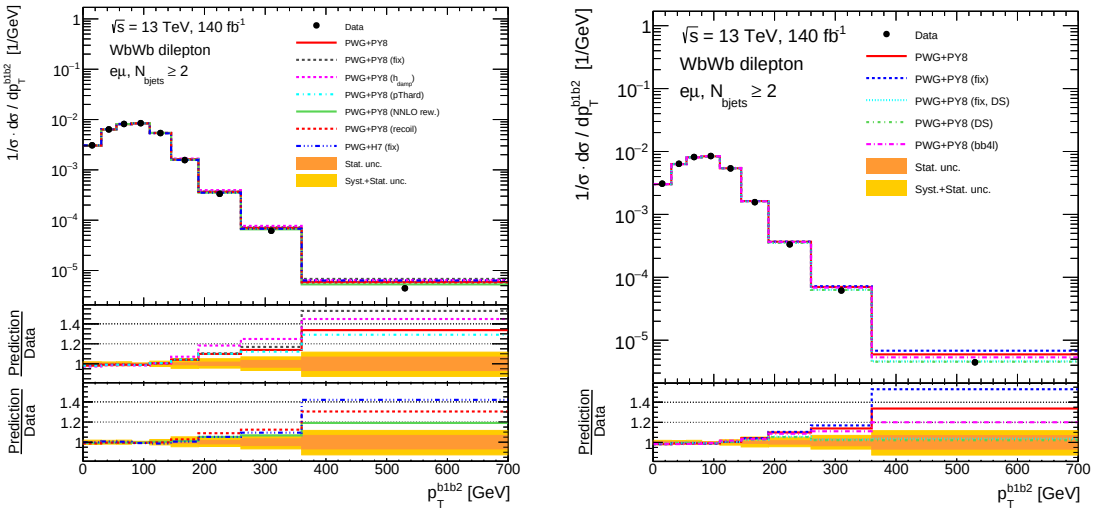

Figure 8.12: Relative differential cross-section measurement as a function of the p_{T} of the bb system compared to interference generators (right) and MC generators (left).

Observable	PWG+PY8		PWG+PY8 (FIX)		PWG+PY8 ($bb4l$)		PWG+PY8 (FIX, DS)		PWG+PY8 (DS)	
	χ^2/NDF	p-value	χ^2/NDF	p-value	χ^2/NDF	p-value	χ^2/NDF	p-value	χ^2/NDF	p-value
$p_{\mathrm{T}}^{\mathrm{jet}_1}$	16.8/7	0.02	17.3/7	0.02	15.9/7	0.03	17.0/7	0.02	17.0/7	0.02
$p_{\mathrm{T}}^{\mathrm{jet}_2}$	5.6/7	0.59	5.6/7	0.58	6.4/7	0.49	5.8/7	0.57	5.8/7	0.57
$p_{\mathrm{T}}^{l_1}$	44.3/15	<0.01	46.8/15	<0.01	23.8/15	0.07	31.4/15	<0.01	31.8/15	<0.01
$p_{\mathrm{T}}^{l_2}$	26.0/11	<0.01	27.5/11	<0.01	16.7/11	0.12	20.6/11	0.04	21.3/11	0.03
N^{jets}	8.8/6	0.19	8.8/6	0.19	21.0/6	<0.01	7.5/6	0.28	7.5/6	0.27
p_{T}^{bb4l}	51.0/8	<0.01	53.1/8	<0.01	124.3/8	<0.01	51.2/8	<0.01	52.2/8	<0.01
m_T^{bb4l}	18.9/12	0.09	31.1/12	<0.01	12.2/12	0.43	13.2/12	0.36	13.3/12	0.35
m^{bbll}	28.3/15	0.02	39.3/15	<0.01	23.9/15	0.07	26.9/15	0.03	26.2/15	0.04
p_{T}^{bbll}	36.1/10	<0.01	44.4/10	<0.01	93.5/10	<0.01	30.4/10	<0.01	31.5/10	<0.01
p_{T}^{bb}	12.7/8	0.12	25.2/8	<0.01	7.2/8	0.52	2.5/8	0.96	2.7/8	0.95

Table 8.4: χ^2 and p-values quantifying the level of agreement between the measured normalized differential cross-sections and predictions provided by POWHEG+PYTHIA 8 with different schemes for handling the $t\bar{t}/tW$ interference.

for m^{bl}_{minimax} in the $2b$-exclusive phase space, since the NNLO reweighting does not change significantly the shape of the $t\bar{t}$ component, which anyway populates mostly the low m^{bl}_{minimax} region which is already well modelled. The worse models are those with alternative h_{damp} and $p_{\text{T,hard}}$ variations, that are compatible with only one observable. The other models have intermediate results. No NLO+PS Monte Carlo can describe the p_{T} of the $bbll$ and $bb4l$ systems, which arguably are more sensitive to higher order effects and additional radiation.

8.2.3 Total fiducial cross-section

The total fiducial cross-section has been measured in both phase spaces, by applying the unfolding procedure described in Section 7.1 to a single-bin distribution. In this case, the unfolding matrix is a 1×1 matrix, and the unfolding procedure from Eq. 7.9 is equivalent to a simple division of the acceptance-corrected, background-subtracted reconstructed events in data by the efficiency.

The total fiducial cross-sections in the two phase-spaces are measured to be:

$2b$-exclusive region $\sigma_{\text{fid}} = 5.77 \pm 0.01\ (\text{stat.}) \pm 0.05\ (\text{lumi.})^{+0.27}_{-0.29}\ (\text{syst.})$ pb;

$2b$-inclusive region $\sigma_{\text{fid}} = 5.97 \pm 0.01\ (\text{stat.}) \pm 0.05\ (\text{lumi.})^{+0.27}_{-0.30}\ (\text{syst.})$ pb.

The measured cross-sections are compared with theoretical predictions from different Monte Carlo generators in Figure 8.13. All the $t\bar{t}$ and tW theoretical predictions are normalised respectively to the NNLO+NNLL and NLO+NNLL cross-sections as described in Section 6.2.1. All differences among the shown predictions are due to how differently the MC generators model the acceptance of the fiducial phase-spaces with respect to the full phase-space.

As shown in 8.5, the measurements in both the $2b$-inclusive and exclusive phase-spaces are limited by the uncertainties in the signal modeling and flavor-tagging efficiency. Other significant sources of uncertainties are related to the lepton isolation and jet energy scale.

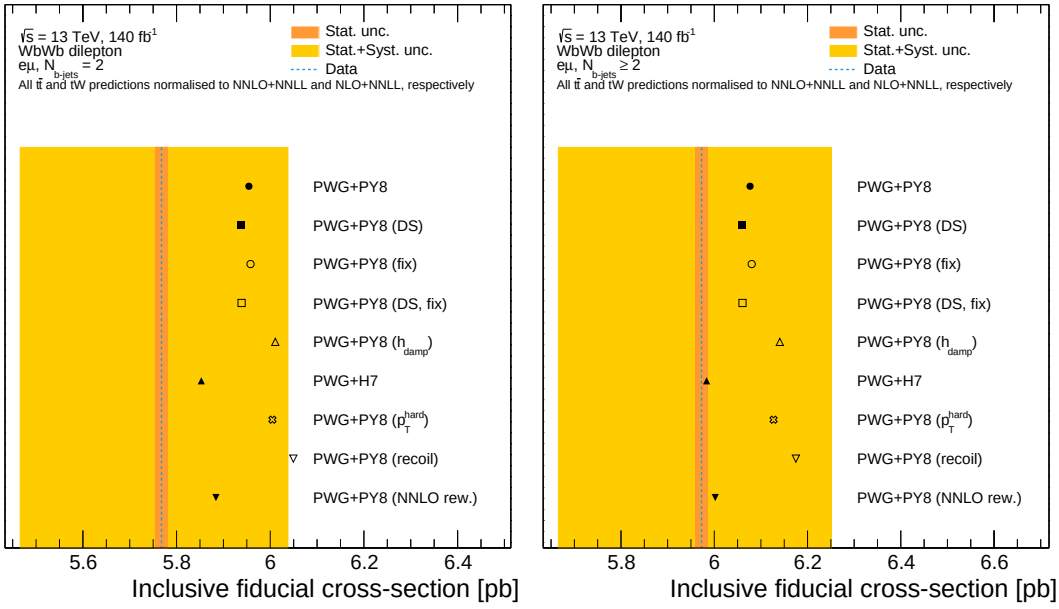

(a) (b)

Figure 8.13: Total fiducial cross-section measurement in a the 2b-exclusive and b the 2b-inclusive regions. The measured cross-sections are compared with theoretical predictions from different Monte Carlo generators.

Phase space	$e\mu, N_{\text{b-jets}} = 2$	$e\mu, N_{\text{b-jets}} \geq 2$
Fiducial cross-section [pb]	5.77	5.97
Total Uncertainty [%]	$^{+4.68}_{-5.23}$	$^{+4.67}_{-5.14}$
Statistics [%]	± 0.22	± 0.21
Systematics [%]	$^{+4.68}_{-5.23}$	$^{+4.66}_{-5.14}$
Jets [%]	$^{+1.62}_{-1.76}$	$^{+1.82}_{-1.92}$
Pile-up [%]	$^{+0.56}_{-0.62}$	$^{+0.53}_{-0.59}$
Flavour tagging [%]	$^{+2.92}_{-2.90}$	$^{+2.99}_{-2.97}$
Background [%]	± 0.31	± 0.32
Leptons and $E_{\text{T}}^{\text{miss}}$ [%]	$^{+1.80}_{-1.81}$	± 1.81
Luminosity [%]	± 0.83	± 0.83
tW modeling [%]	± 0.11	± 0.11
$t\bar{t}$ modeling [%]	± 1.06	± 1.02
Generator parameters [%]	$^{+1.89}_{-2.94}$	$^{+1.68}_{-2.69}$
Parton shower [%]	± 1.07	± 0.83
Hard scattering [%]	± 0.69	± 0.74

Table 8.5: Summary of all the uncertainty sources for the total cross section in the fiducial phase spaces.

8.3 Results with QUnfold

In this section the measured differential cross-sections in the $2b$-exclusive and $2b$-inclusive regions performed using the simulated annealing backend of QUnfold software are shown. For these results we decided to not use the pure quantum backend of QUnfold because, for the moment, the D-Wave hardware which gives the quantum resources to QUnfold is not enough powerful to deal with large-size data.

As mentioned at the beginning of this chapter, the purpose of these results is not to demonstrate that QUnfold works better than the standard classical cases afforded with RooUnfold, but to show that it is possible to perform such analysis using a quantum computation based unfolding method.

8.3.1 Differential cross-sections in the $2b$-exclusive region

The absolute and relative cross-section measurement as a function of m^{bl}_{minimax} using the QUnfold software are shown in Figures 8.14 - 8.15. The measurement is compared with predictions obtained with different MC generators and different interference schemes. The corresponding systematic breakdown plots for the relative and absolute cross-sections are shown in Appendices C.4.2 and C.4.3.

These plots show the same level of agrement among data/MC with respect to the

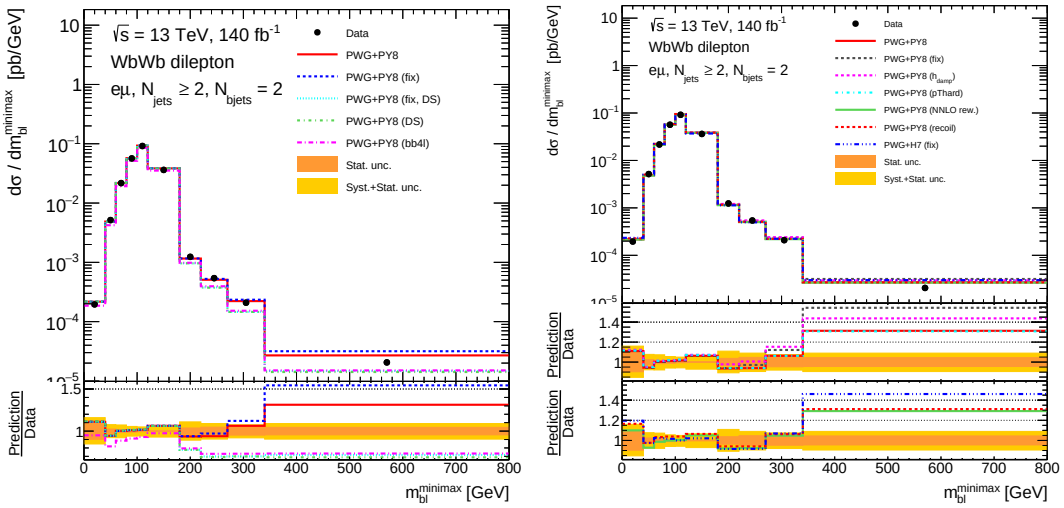

(a) (b)

Figure 8.14: Absolute differential cross-section measurement through QUnfold as a function of the m^{bl}_{minimax} variable. The unfolded data are compared with a predictions provided by POWHEG +PYTHIA 8 with different schemes for handling the $t\bar{t}/tW$ interference and b with predictions obtained with different MC generators.

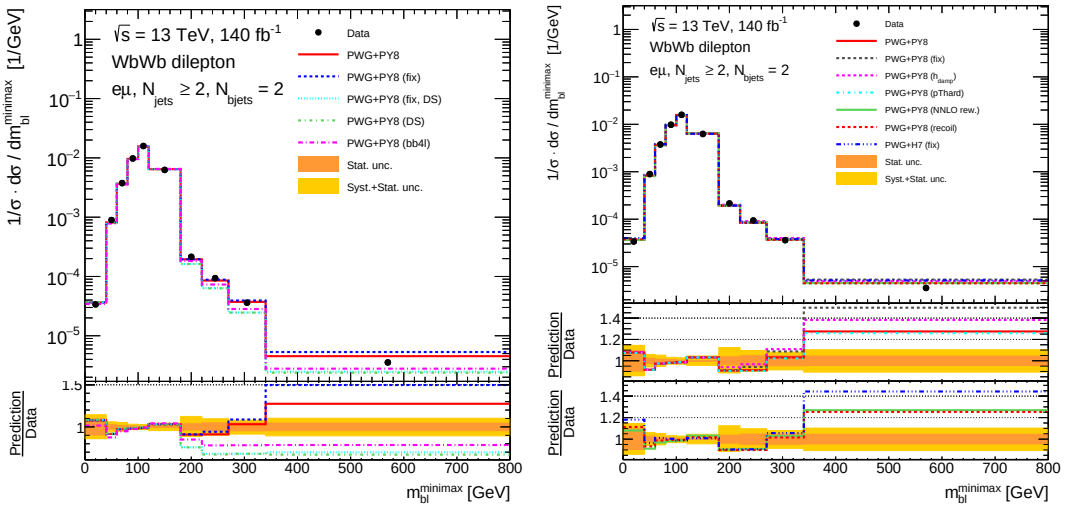

(a) (b)

Figure 8.15: Relative differential cross-section measurement through QUnfold as a function of the m^{bl}_{minimax} variable. The unfolded data are compared with a predictions provided by POWHEG +PYTHIA 8 with different schemes for handling the $t\bar{t}/tW$ interference and b with predictions obtained with different MC generators.

ones performed using classical unfolding techniques (see Section 8.2.1). This means that the unfolding gave same results in this case and that the techniques based on QUnfold converged to the correct output.

8.3.2 Differential cross-sections in the 2b-inclusive region

The relative cross-sections measurements through QUnfold as a function of some of the kinematic variables of the $WbWb$ final-state objects introduces in Section 8.2.2 are presented in Figures 8.16 - 8.22. The corresponding systematic breakdown plots for the relative and absolute cross-sections are shown in Appendices C.4.3 and C.4.2.

For each plot shown below, in the top panel, the unfolded data are shown as black points, while lines indicate the MC predictions. Uncertainties are shown by the shaded bands. The lower panel shows the ratio of the MC predictions to the unfolded data.

The corresponding plots, for the absolute differential cross-sections, are presented in Appendix D.2.

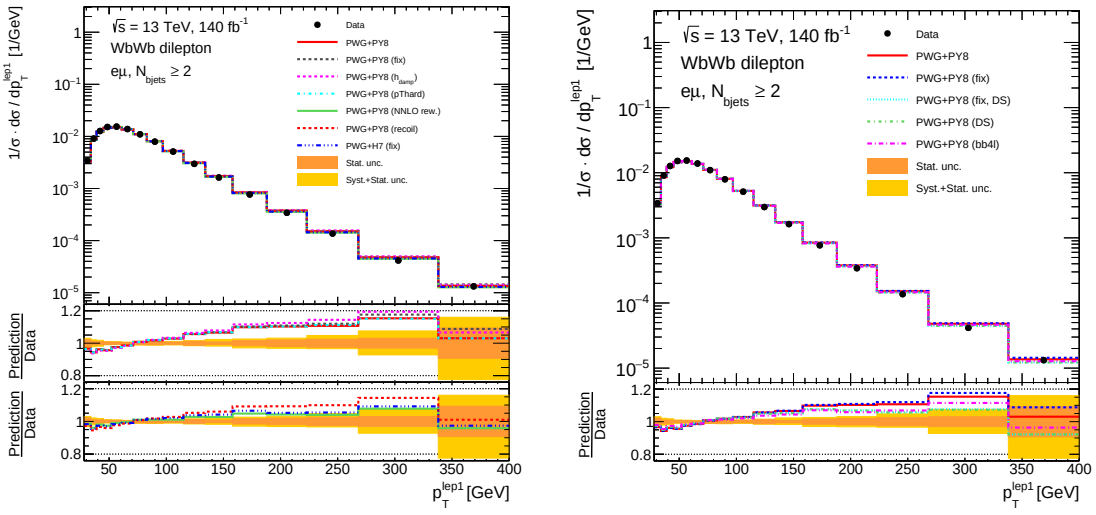

Figure 8.16: Relative differential cross-section measurement through QUnfold as a function of the leading lepton p_{T} compared to interference generators (right) and MC generators (left).

Also in this case these plots show the same level of agreement among data/MC with respect to the ones performed using classical unfolding techniques (see Section 8.2.2). This means that the unfolding gave same results even in this case and that the techniques based on QUnfold converged to the correct output.

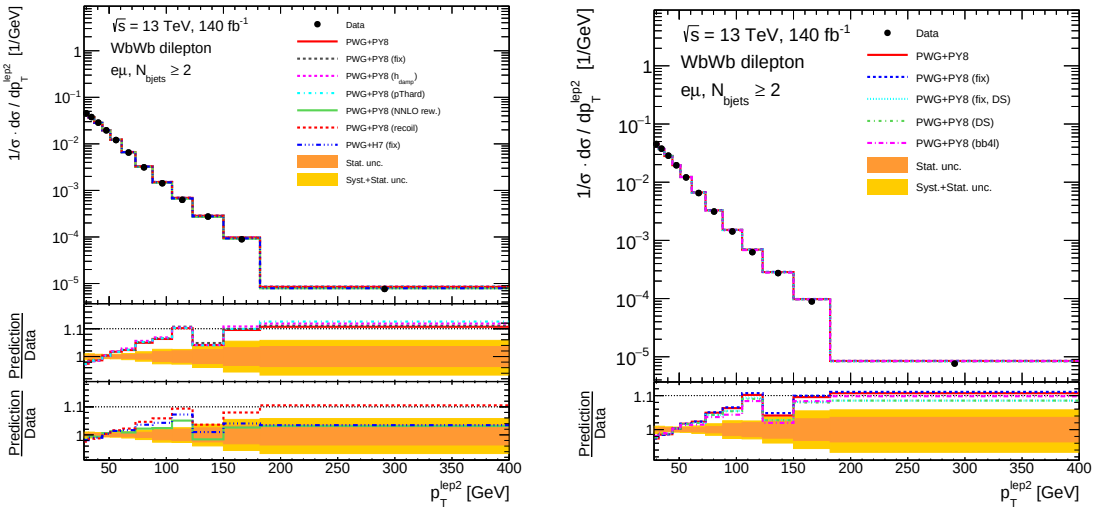

Figure 8.17: Relative differential cross-section measurement through QUnfold as a function of the sub-leading lepton p_{T} compared to interference generators (right) and MC generators (left).

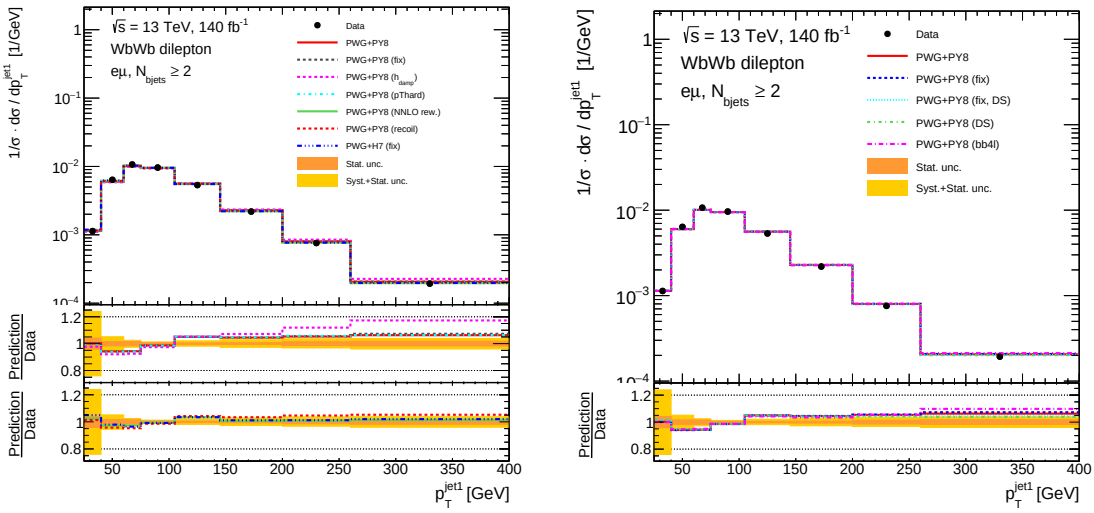

Figure 8.18: Relative differential cross-section measurement through QUnfold as a function of the leading jet p_{T} compared to interference generators (right) and MC generators (left).

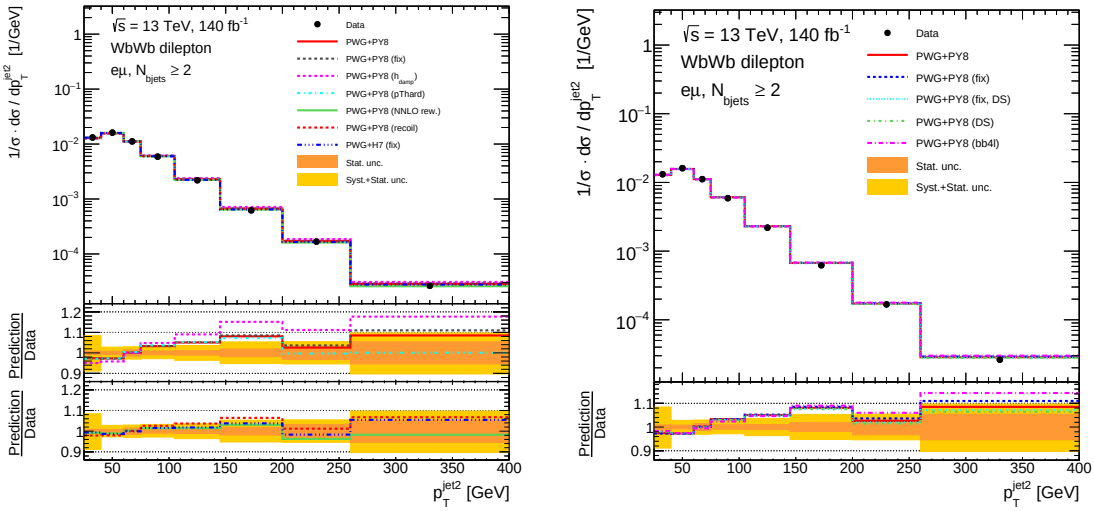

Figure 8.19: Relative differential cross-section measurement through QUnfold as a function of the sub-leading jet p_{T} compared to interference generators (right) and MC generators (left).

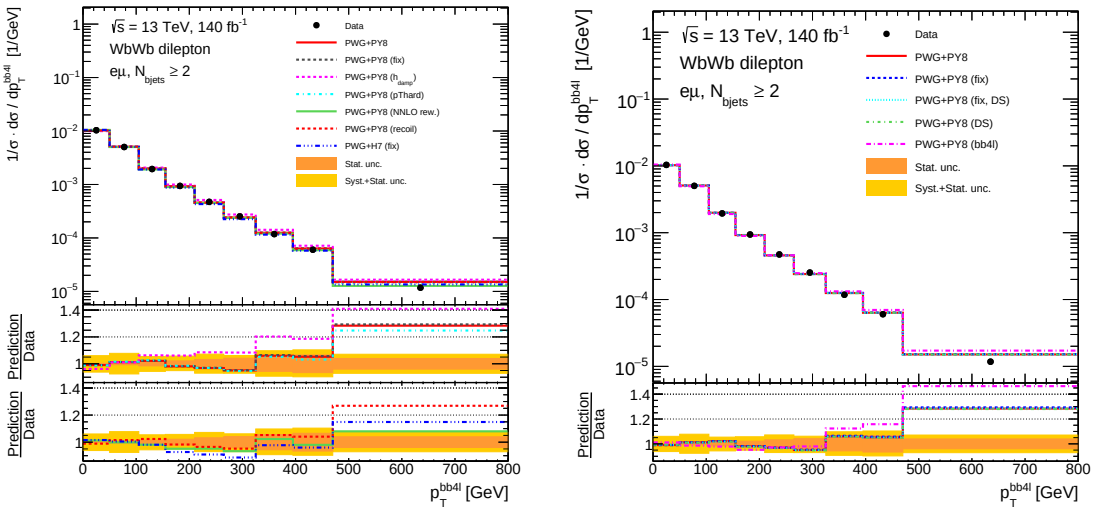

Figure 8.20: Relative differential cross-section measurement through QUnfold as a function of the p_{T} of the *bb4l* system compared to interference generators (right) and MC generators (left).

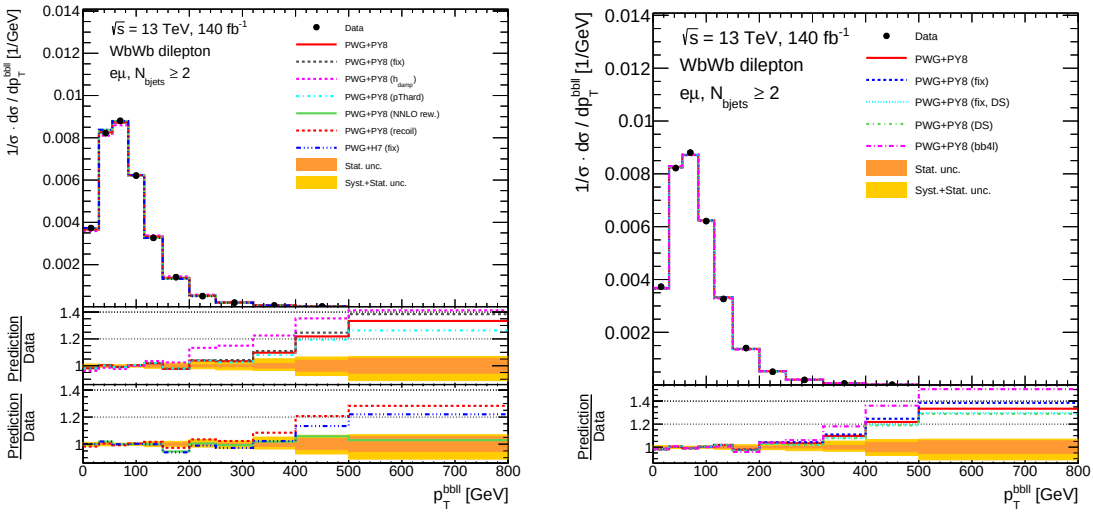

Figure 8.21: Relative differential cross-section measurement through QUnfold as a function of the p_{T} of the *bbll* system compared to interference generators (right) and MC generators (left).

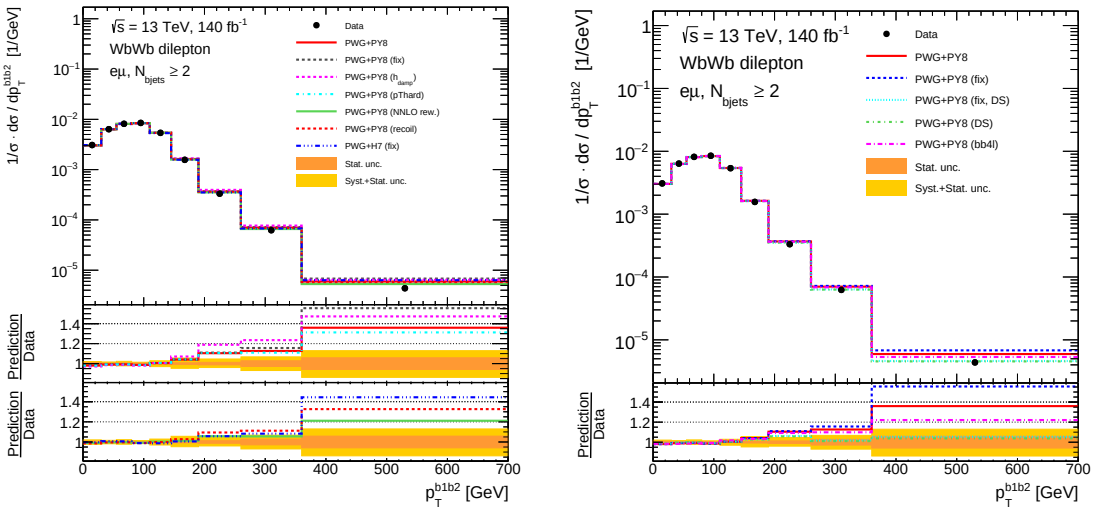

Figure 8.22: Relative differential cross-section measurement through QUnfold as a function of the p_{T} of the *bb* system compared to interference generators (right) and MC generators (left).

Conclusions and outlook

In this study, we presented the results of the first ever differential cross-section measurement of the $WbWb$ final state in the whole phase space available (even if the measurement as a function of the m^{bl}_{minimax} variable was already performed by ATLAS using a partial Run 2 dataset) using data collected by the ATLAS detector at the LHC. The analysis focuses on the fiducial phase-space defined by requiring two b-tagged jets and two leptons with opposite charge and different flavor.

The results indicate that none of the considered predictions, including the *bb4l* sample, can accurately describe all observables in the fiducial phase-space. This finding is consistent with previous publications in both the dilepton and semi-leptonic final states. The best-performing predictions are the nominal Powheg+Pythia 8 and Powheg+Herwig 7 models, with the latter being the only one capable of describing the p_{T} of the leading lepton and jet. Models with alternative h_{damp} and $p_{\text{T,hard}}$ variations are only compatible with a single observable.

The total fiducial cross-sections are also measured in the 2b-exclusive and 2b-inclusive regions. The measured cross-sections are found to be 5.77 ± 0.01 (stat.)$^{+0.27}_{-0.30}$ (syst.) pb and 5.97 ± 0.01 (stat.)$^{+0.28}_{-0.31}$ (syst.) pb, respectively. These measurements are primarily limited by uncertainties in the signal modeling and flavor-tagging efficiency, as well as other sources such as lepton isolation and jet energy scale.

This measurement represents a significant improvement over previous publications, as the uncertainty has been reduced by half, allowing for better discrimination between models. The sensitivity for most observables is currently limited primarily by uncertainties in signal modeling, including those related to the treatment of $t\bar{t}/tW$ interference, and by statistical uncertainties in the tails of the distributions. Further improvements are expected with the data collected during the LHC Run 3 data-taking period and through the use of new Monte Carlo simulations optimized based on these measurements.

Additionally, the development and usage of a novel unfolding method based on quantum annealing and its related `QUnfold` software has been developed and tested on the same data using the simulated annealing backend of the DWave quantum annealer, demonstrating that it is possible to use quantum computation to perform the unfolding procedure and therefore to measure differential cross-sections. Since this is the first software capable of handling a quantum computing based unfolding technique on large scale

LHC data, this is considered a good result and a step forward in the world of applications of quantum computing to particle physics.

In conclusion, the results of this study provide valuable insights into the modeling of the $WbWb$ final state in the fiducial phase-space. The observed discrepancies between the measured cross-sections and theoretical predictions highlight the need for further improvements in the modeling of this process.

Appendix A

The DCSAnalysisTools framework

In Sections A.1 and A.2 the DCS and gas system of the ATLAS detector are described respectively. Finally, in Section A.3 the main work of my qualification task is explained.

A.1 The RPC DCS

The RPC DCS (see Figure A.1) is a computing infrastructure used to monitor the RPC conditions and to control all its related subsystems, which are:

- Supply of low and high voltages.
- Trigger electronics.
- Detector infrastructure.
- Environment conditions.

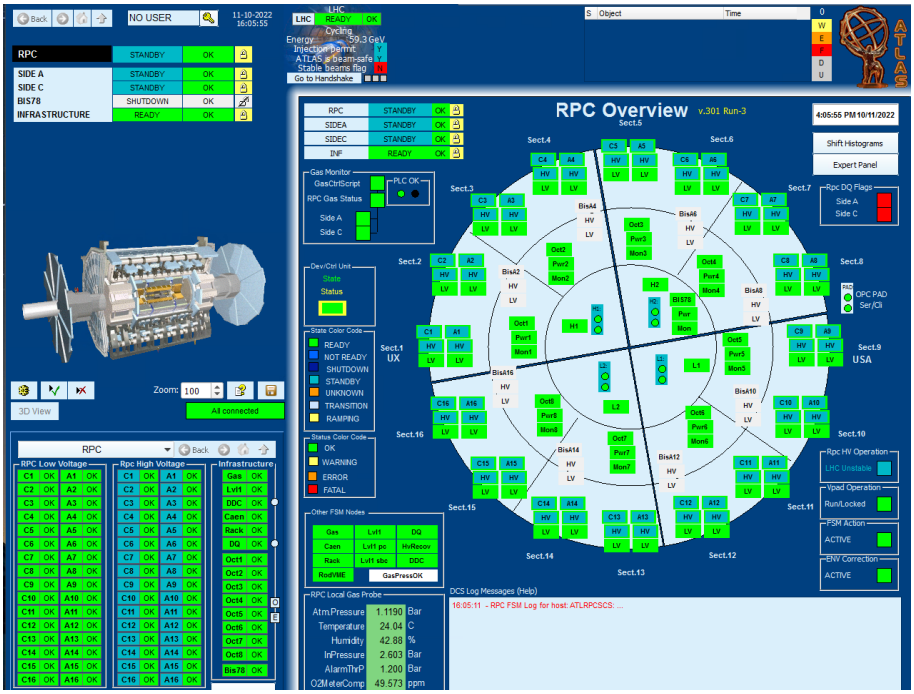

Figure A.1: Screenshot of the main page of the ATLAS RPC DCS.

The hardware chosen for the power system of the RPCs was based on the commercial CAEN EASY (*Embedded Assembly SYstem*) solution [180]. It consists of a magnetic field (up to 2 T) and radiation tolerant electronics; it is based on a master-slave architecture.

The branch controllers hosted in a CAEN mainframe act as *master boards* and monitor the electronics in several crates, located in the experimental area [181].

An updated picture of the Run-2 DCS architecture is shown in Figure A.2. The *software system* is composed of 7 multi-core rack-mounted PCs all running Scientific Linux. For the communication to the CAEN mainframes a Windows 2008 Server virtual machine is run on one of the cores of local computers to allow the communication with OPC-DA.

The relevant DCS information is stored into the ATLAS database for future analyses. Data are accessed through the *DCS variables* which are: HV (*High Voltage*), I_{gap} (gap current), gas variables, temperature and many others.

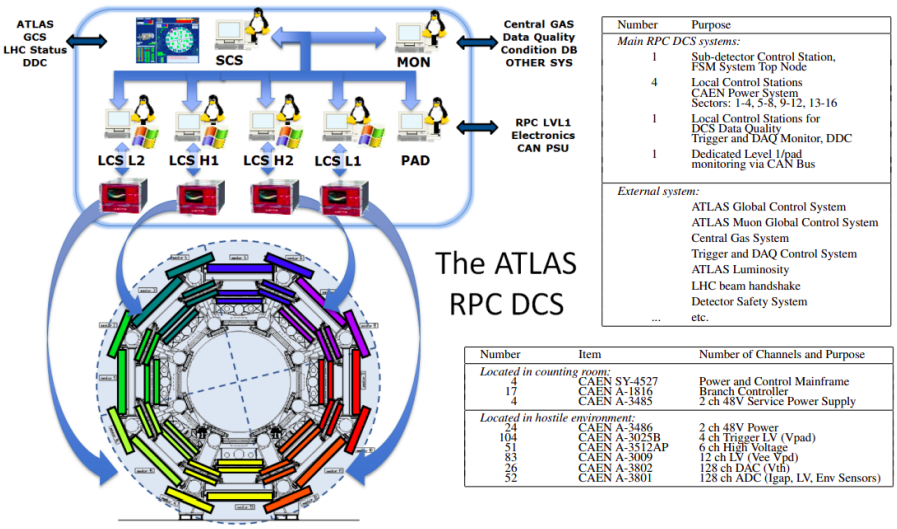

Number	Purpose
Main RPC DCS systems:	
1	Sub-detector Control Station, FSM System Top Node
4	Local Control Stations CAEN Power System Sectors: 1-4, 5-8, 9-12, 13-16
1	Local Control Stations for DCS Data Quality Trigger and DAQ Monitor, DDC
1	Dedicated Level 1/pad monitoring via CAN Bus
External system:	
	ATLAS Global Control System
	ATLAS Muon Global Control System
	Central Gas System
	Trigger and DAQ Control System
	ATLAS Luminosity
	LHC beam handshake
	Detector Safety System
...	etc.

Number	Item	Number of Channels and Purpose
Located in counting room:		
4	CAEN SY-4527	Power and Control Mainframe
17	CAEN A-1816	Branch Controller
4	CAEN A-3485	2 ch 48V Service Power Supply
Located in hostile environment:		
24	CAEN A-3486	2 ch 48V Power
104	CAEN A-3025B	4 ch Trigger LV (Vpad)
51	CAEN A-3512AP	6 ch High Voltage
83	CAEN A-3009	12 ch LV (Vee Vpd)
26	CAEN A-3802	128 ch DAC (Vth)
52	CAEN A-3801	128 ch ADC (Igap, LV, Env Sensors)

Figure A.2: Layout the hardware infrastructure of the ATLAS RPC Detector Control System. In the top-right table the computing hardware information is listed.

A.2 The gas system

In August 2023, after the completion of proton-proton data-taking, the ATLAS collaboration replaced the standard gas mixture (94.7% $C_2H_2F_4$, 5.0% i-C_4H_10, 0.3% SF_6) with a new mixture with CO_2 added: 64% $C_2H_2F_4$, 30% i-CO_2, 1% SF_6. The total gas volume amount at $\sim 15\,m^3$[182].

There are some reasons for the choice of this particular mixture and in particular of *tetrafluoroethane*:

- Its high density, through which it is possible to obtain better primary ionization with more or less 60 primary electron-ion pairs per cm.
- Its relatively low operating voltage.

The basic function of the whole gas system is to mix the previously mentioned components in the correct proportions and then to distribute the gas mixture into each chamber.

A.2.1 Gas system design

This whole gas system consists of modules designed as far as possible uniformly among all the ATLAS RPC system. These modules are:

- **Primary gas supplies**.

- **Mixer**: to ensure the correct gas component mixing.
- **Inside closed circulation loop**: the RPC chamber gas is circulated in a closed loop. This circulation loop is distributed over three different areas which are:
- – *Chamber distribution systems.*
  – *Purifier*: for gas purification.
  – *Pump and return gas analysis*: which regulate gas pressure.
- ($C_2H_2F_4$) **exhaust gas recovery**: to monitor the recovery of *tetrafluoroethane* which is very expensive.

There are in total 3714 gas modules, with volumes ranging from 1.36 L to 10.77 L [183]. Several distribution systems situated in five distinct height zones regulate the chamber pressure relative to the atmospheric pressure, correcting hydrostatic differences. In total, *ten racks* house the distribution system, serving the A and C side of the barrel, respectively (see Figure A.3). The flow needed in each RPC gas volume is proportional

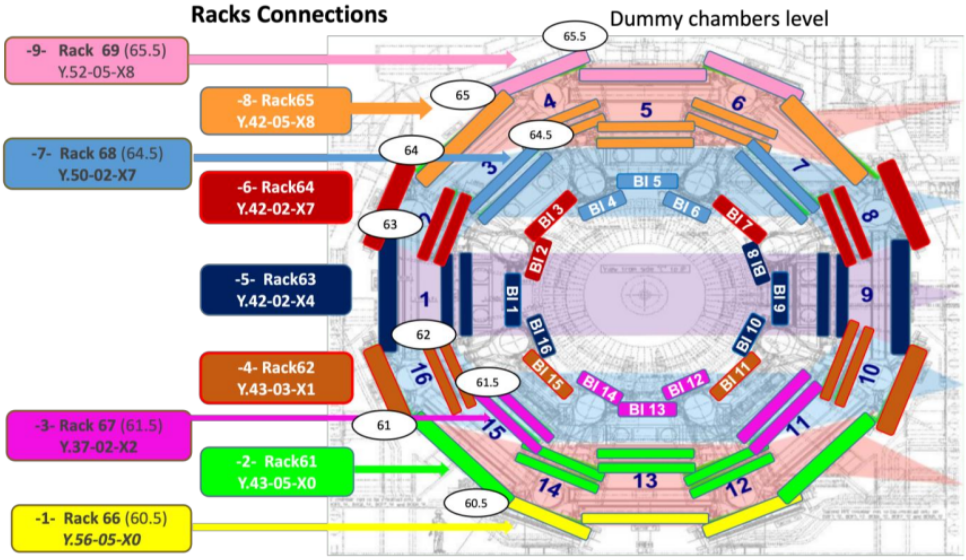

Figure A.3: RPC gas system overview with racks position with respect to each sector chamber.

to the total charge rate delivered in the gas, which is in turn proportional to the electric current flowing through each RPC gap.

The gas is distributed by 128 input manifold lines (up to 24 RPC layers each) called *flowmeters*, with an overpressure of around 10 mbar falling on input impedances, which

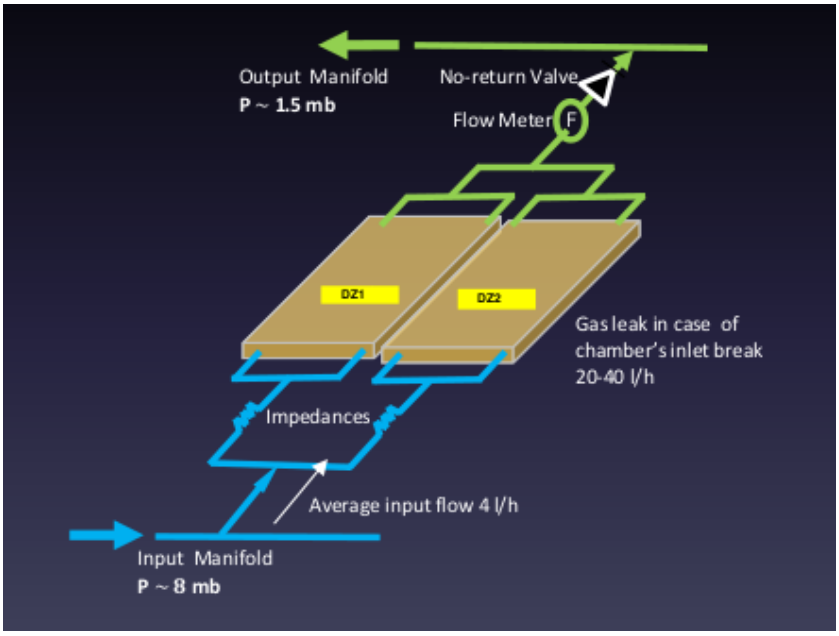

Figure A.4: Overview of a flowmeter.

determine the input flow (see Figure A.4). The gas is then recuperated by 128 output manifolds connected to a pump regulating the RPC internal pressure. This recuperated gas is purified and re-injected in the system.

A single gas layer is connected through 2 inlets and 2 outlets (see Figure A.5). There

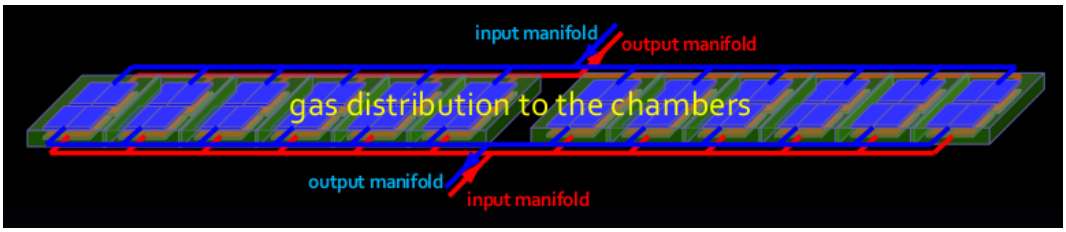

Figure A.5: Overview of the gas distribution through the chambers.

are 2136 independent gas layers in total. Per each 2 gas layers, there is an output flowmeter.

Finally, the RPC gas gap is kept at maximum 3 mbar above the atmospheric pressure.

A.2.2 Sensors distribution

There are two flow sensors groups in the ATLAS RPC system to monitor: 128 sensors lie in the manifold lines, while 1168 lie directly on the chambers.

These two groups are useful to study the gas system from two different perspectives since both them can be used to study in a complementary way the whole system.

The 1168 sensors are used to monitor the **FullFlow** of each channel, which is the total flow passing through the chamber itself; while the 128 sensors get information from the **InFlow** and **OutFlow** which are respectively the entering and exiting flows passing through a chamber.

A.3 The framework

During the three years of my PhD, we have developed a framework used to monitor the ATLAS RPC detectors condition by analyzing the DCS (*Detector Control System*) data.

This framework is called `DCSAnalysisTools` and is used as follows: data are extracted from the DCS database (Section A.1), then they are processed (Section A.3.1) and finally are used to monitor and check different RPC performances:

- Mapping of HV and I_{gap} channels (Section A.3.2).
- Possible gas leakages (Section A.3.3).
- Proper functioning of all the I_{gap} channels (Section A.3.4).

See Figure A.6 for an example workflow of a DCS analysis which uses `DCSAnalysisTools` framework. The software is open-source and is hosted on `GitLab` [184]. Some of the main

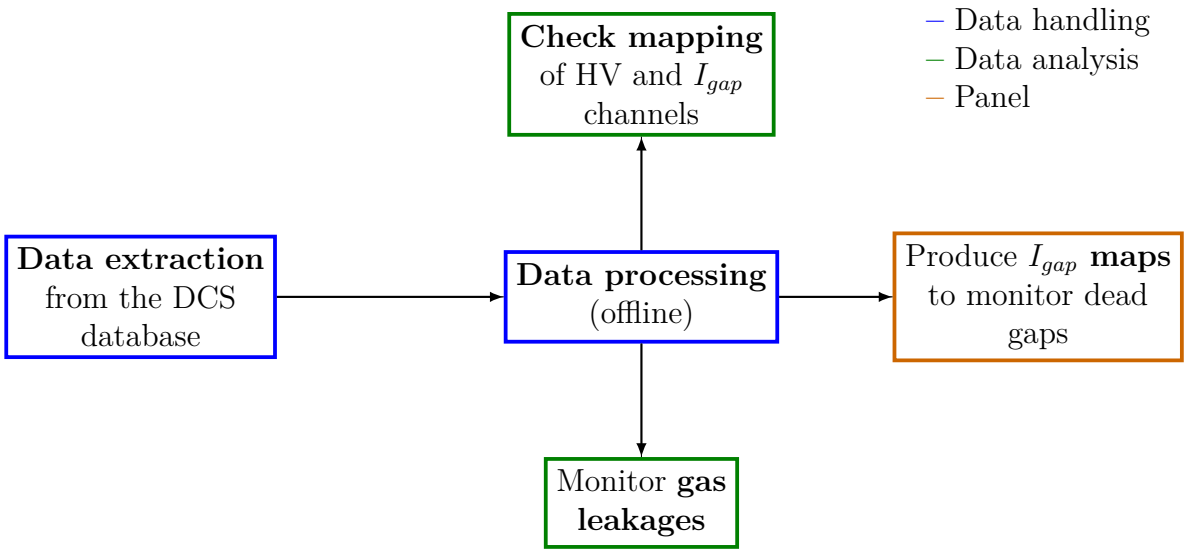

Figure A.6: Typical workflow of an analysis performed with the `DCSAnalysisTools` framework.

results of the framework are saved on specific web pages[1].

A.3.1 Data extraction and processing

As mentioned at the beginning of Section A.3, `DCSAnalysisTools` is a `Python` which extracts data from the RPC DCS and analyze them, in order to spot possible problems related to the detector behavior.

Data are downloaded manually from the DCS panel, or automatically using the `RPCOfflineFW` framework [185].

A.3.2 Check of correct DCS mapping for HV and I_{gap} channels mapping

Due to the HV boards increase during LS2, to improve the granularity of the HV distributions, correct mapping of the DCS channels needs to be checked. One of the goal of the previously mentioned framework is to check that I_{gaps} channels response follow the HV one. To do this, 2D plots are produced: the x-axis is used for time values, while two y-axes, one for HV and the other one for I_{gaps} variables, are used.

The DCS variables used here are:

- HV − `actual.vMon` (V): which is the voltage of the HV channel.
- I_{gap} − `actual.vMean` (μA): which is the current of the I_{gap} channel.

These plots are produced for each HV channel with respect to each of the corresponding I_{gap} ones.

I_{gap} channels which variation was less or equal than 0.01 µA have been considered as **OFF** (not mapped or disconnected), otherwise they have been considered as **ON** (correctly mapped). An example of HV channel plot with 100% correct mapping with its I_{gaps} is shown in Figure A.7, while an example for one with problematic I_{gaps} is show in Figure A.8. Another interesting cross-check to the previous method is to simply plot I_{gap} as a function of the HV and be sure that the trend is increasing: the expected trend is linear up to 6000 V and becomes exponential beyond. An example plot is shown in Figure A.9.

[1] https://atlas-rpc-perf.cern.ch/RPCWeb/DCSAnalysis/

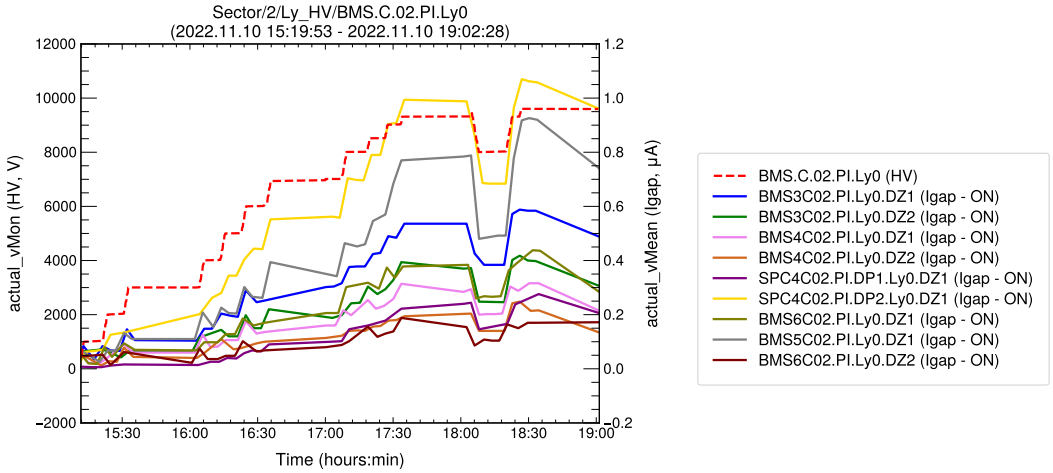

Figure A.7: Example of HV channel with 100% correct mapping.

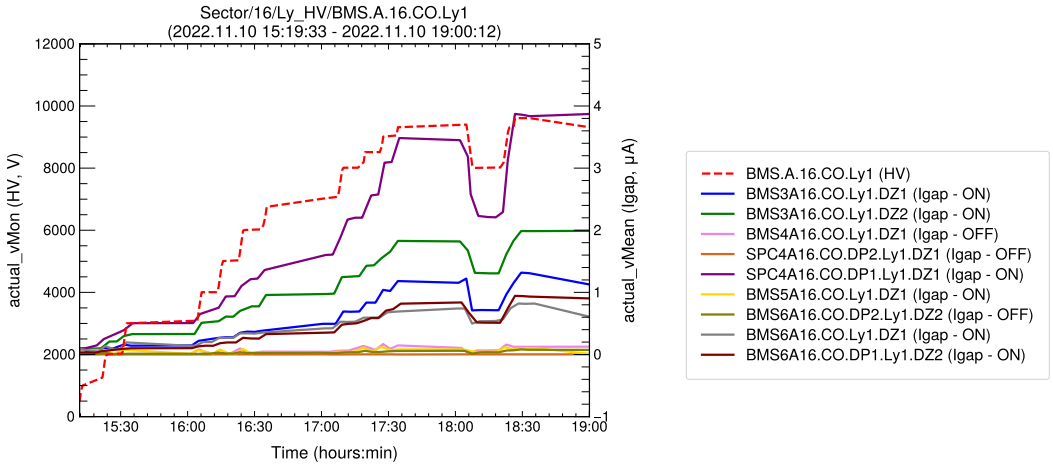

Figure A.8: Example of HV channel with mapping problems or disconnected channels. Problematic I_{gap} channels are for example.

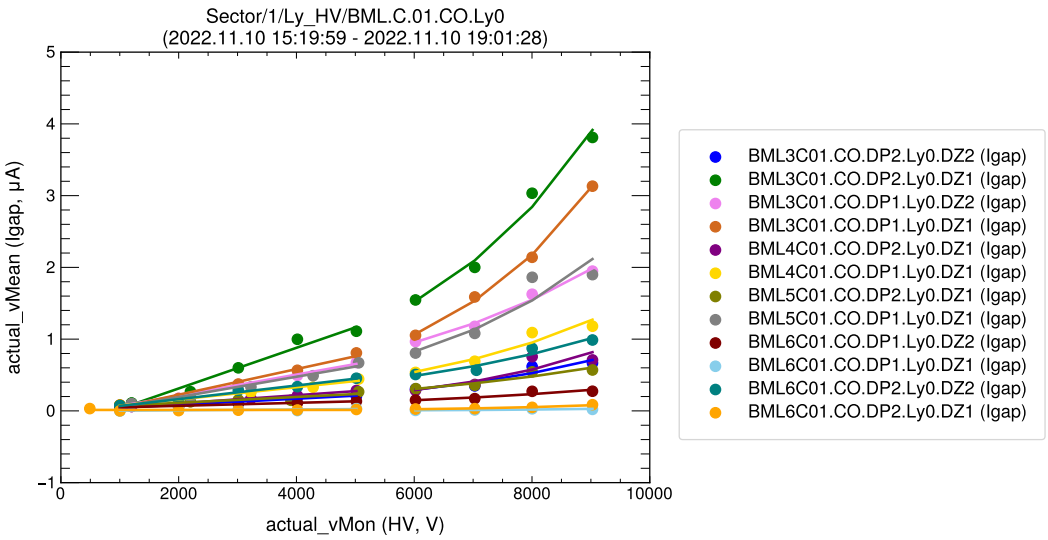

Figure A.9: Example of 2D plot of I_{gap} as a function of the HV. Up to 6000 V the behavior is linear, then becomes exponential.

A.3.3 Monitor of the gas flow

The framework has also a tool to identify chambers having negative gas flux as candidate for leaking chambers. This procedure is performed studying the FullFlow variable, from the 1168 chambers sensors and InFlow and OutFlow variables from the 128 flowmeters sensors.

The procedure is the following:

- Compute the mean of each channel data of *newer dataset* for a given time-period.
- Compute the mean of each channel data of *older dataset* for a given time-period.
- Compute the difference between each mean-value of newer and older data-points and add a point to a bar plot for each channel.

Therefore, bar plots are created and have as y-axis the difference between mean values while for x-axis the chambers name (see Figure A.10). Same plots have been produced also for separated chambers sectors (see Figure A.11), in order to deeply investigate the behavior of each single sector itself. Within this plots also some histograms of mean differences are produced (see Figure A.12). Channels which difference between mean values is less than 0.5 have been considered as problematic. A full list of chambers with old, new and difference flux is then produced and can be consulted for further clarification.

Same procedure is performed also for InFlow (see Figures A.13 and A.14) and OutFlow (see Figures A.15, A.16) variables, as a crosscheck.

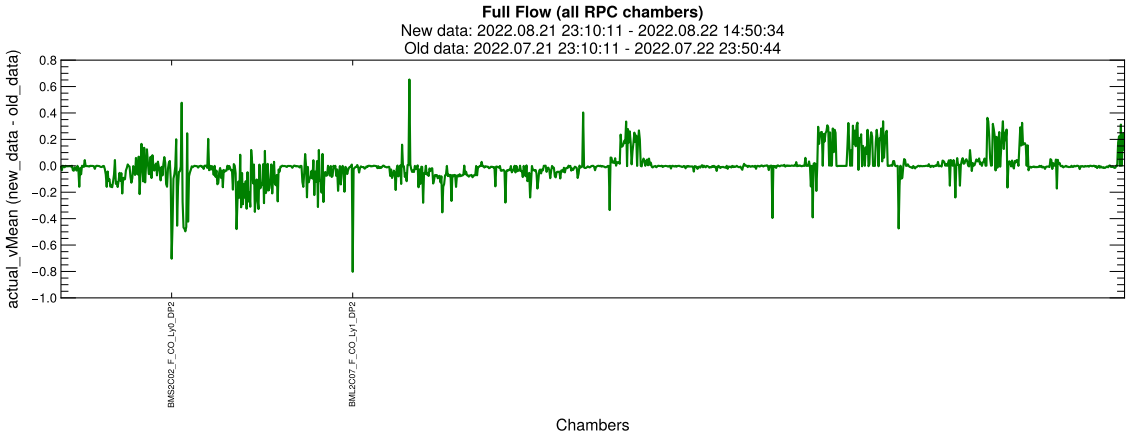

Figure A.10: Bar plot example for FullFlow variable.

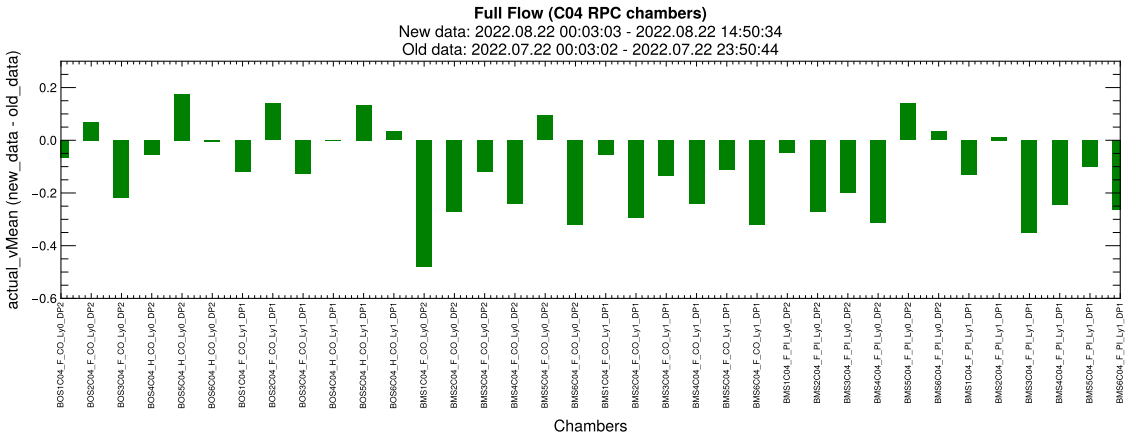

Figure A.11: Bar plot example for FullFlow variable for a single sector.

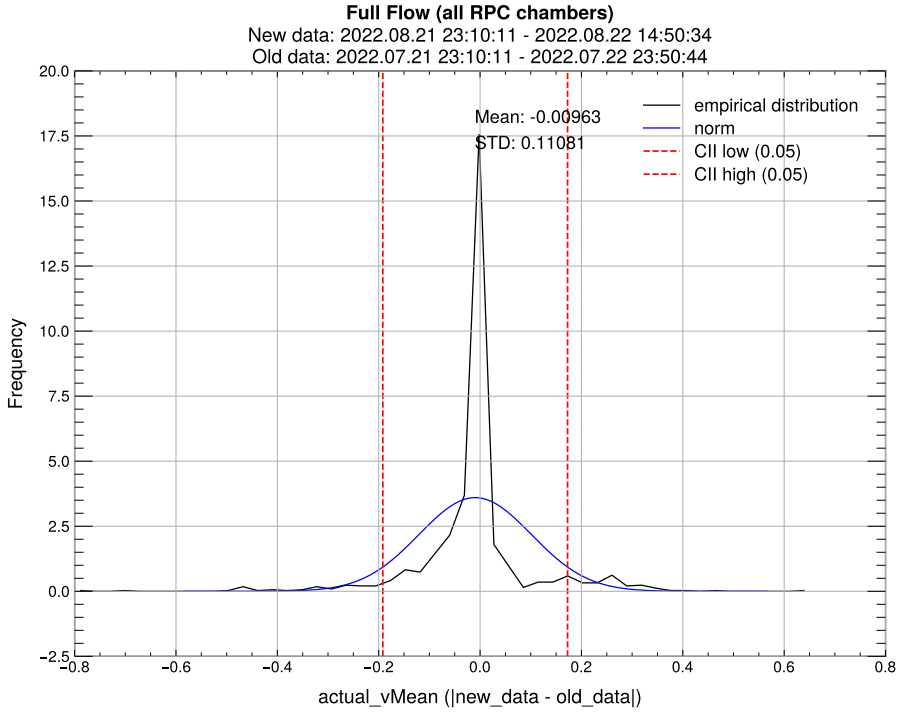

Figure A.12: Example of mean differences distribution of chambers for FullFlow variable.

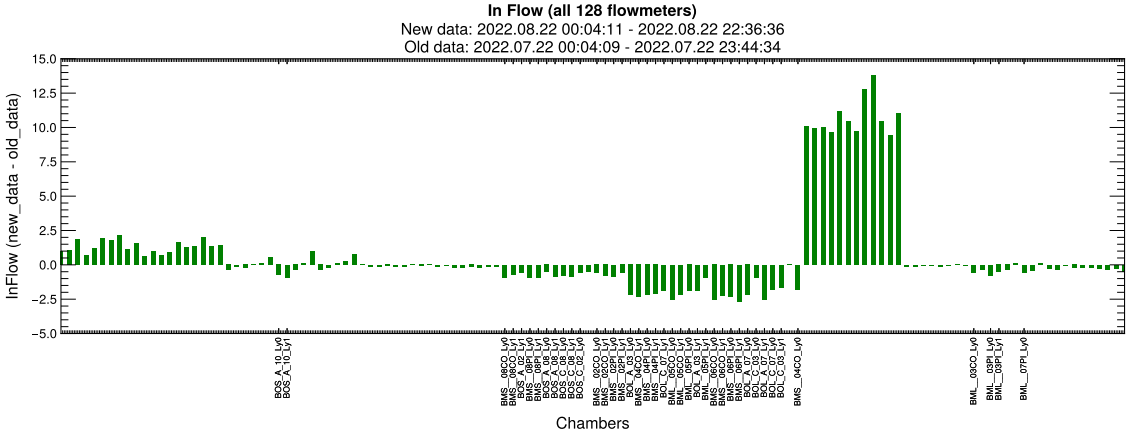

Figure A.13: Bar plot example for InFlow variable.

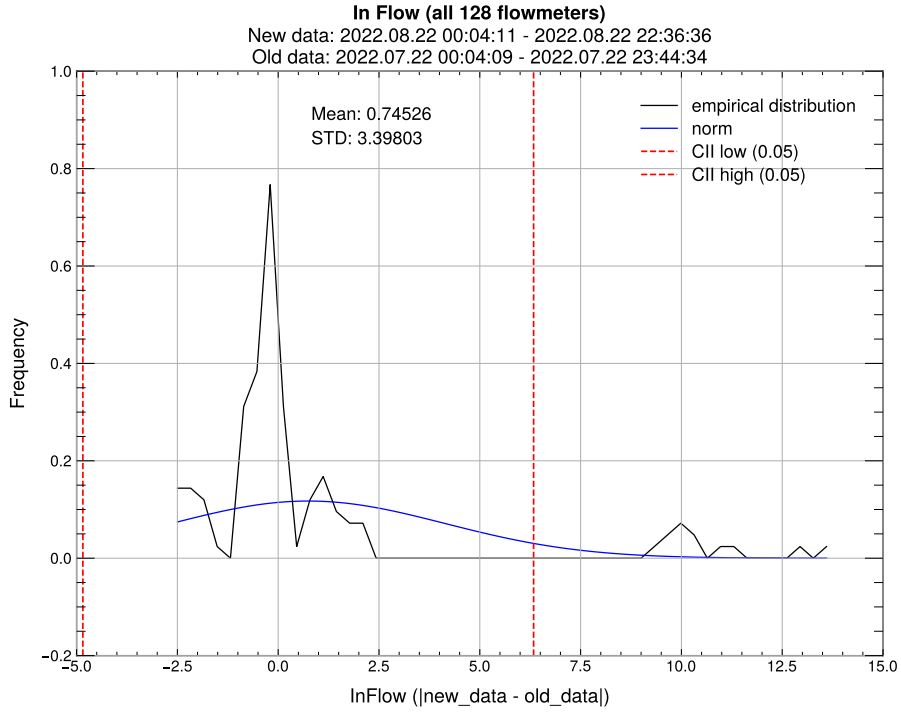

Figure A.14: Example of mean differences distribution of chambers for InFlow variable.

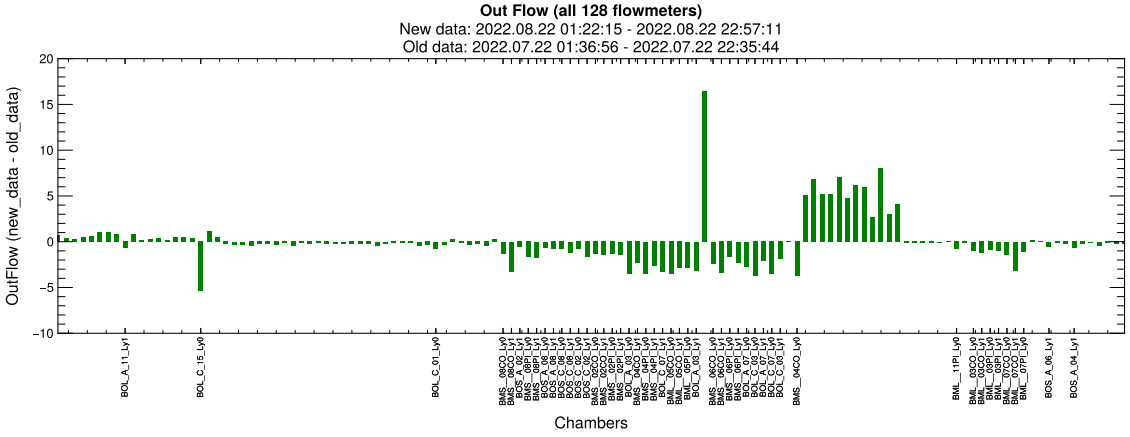

Figure A.15: Bar plot example for OutFlow variable.

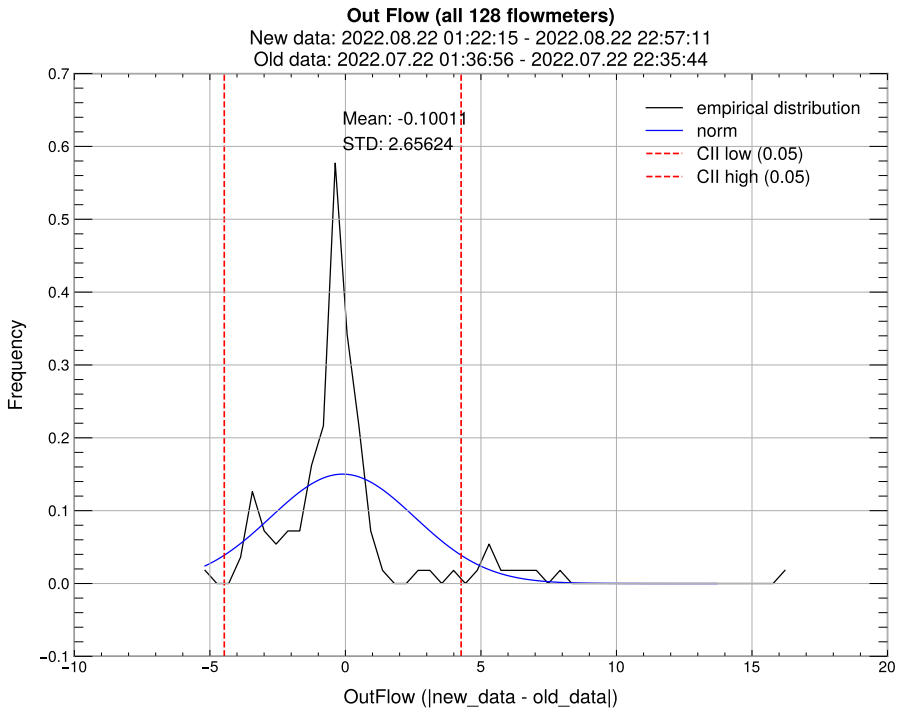

Figure A.16: Example of mean differences distribution of chambers for OutFlow variable.

A.3.4 Map of I_{gap} channels

Proper functioning of all the I_{gap} channels is provided through the production of a channels map, which contains a display of all the I_{gap} channels which correct functioning ones are colored in green while disconnected or problematic ones are colored in red (See Figure A.17). An input file containing the list of *dead gaps* (malfunctioning ones) is given to the main script, in order to produce a new map when needed.

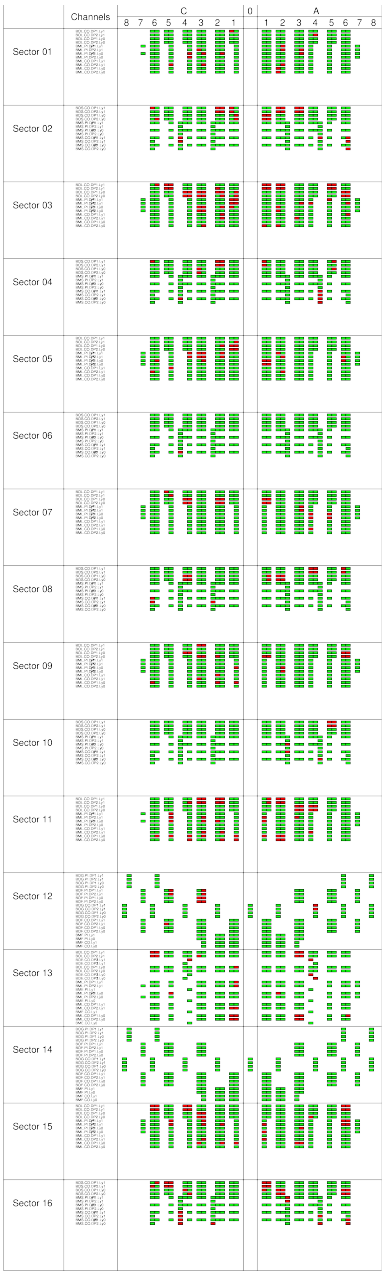

Figure A.17: Map of all the RPC I_{gap} channels. Correct functioning ones are colored in green, while disconnected or malfunctioning ones are colored in red.

Appendix B

Analysis data, samples and definitions complements

B.1 Other control plots

B.1.1 $2b$-exclusive signal region

In Figures B.1 - B.3 additional detector-level plots for the $2b$-exclusive region are presented.

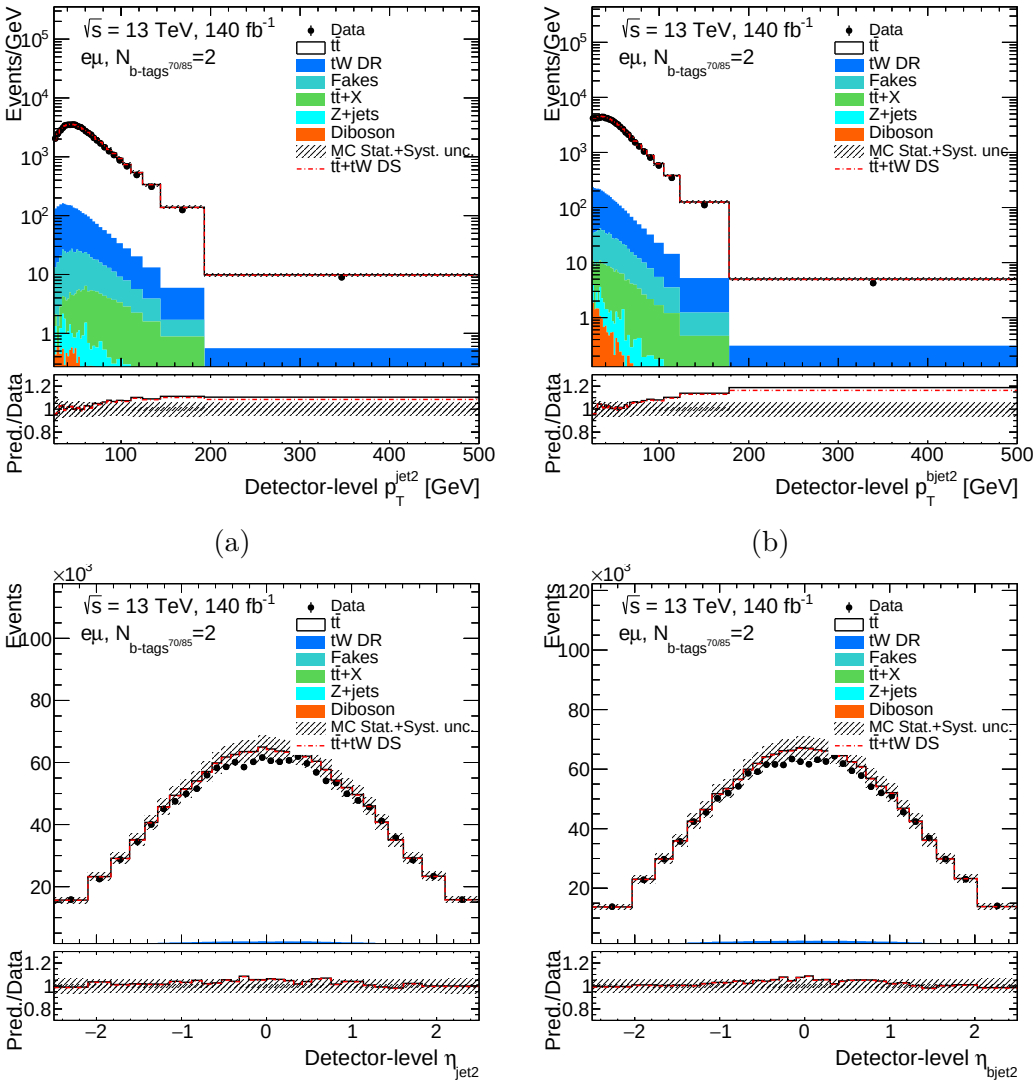

Figure B.1: Comparison of data and MC predictions for the p_{T} of a the subleading jet and b the subleading b-jet and the η of c the subleading jet and d the subleading b-jet in the 2b-exclusive region.

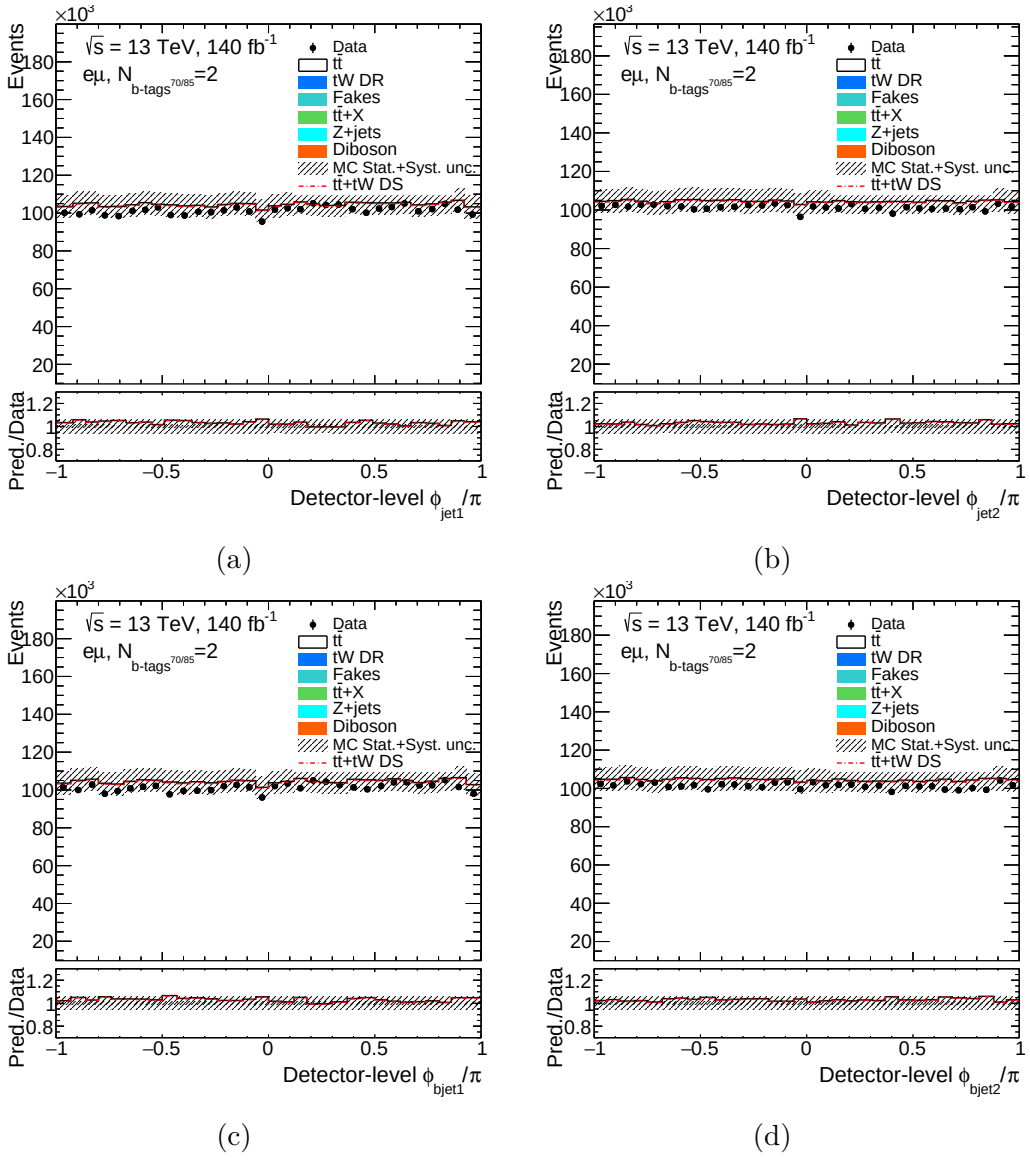

Figure B.2: Comparison of data and MC predictions for the ϕ of a the leading and b subleading jet and of c the leading and d subleading b-jet in the $2b$-exclusive region.

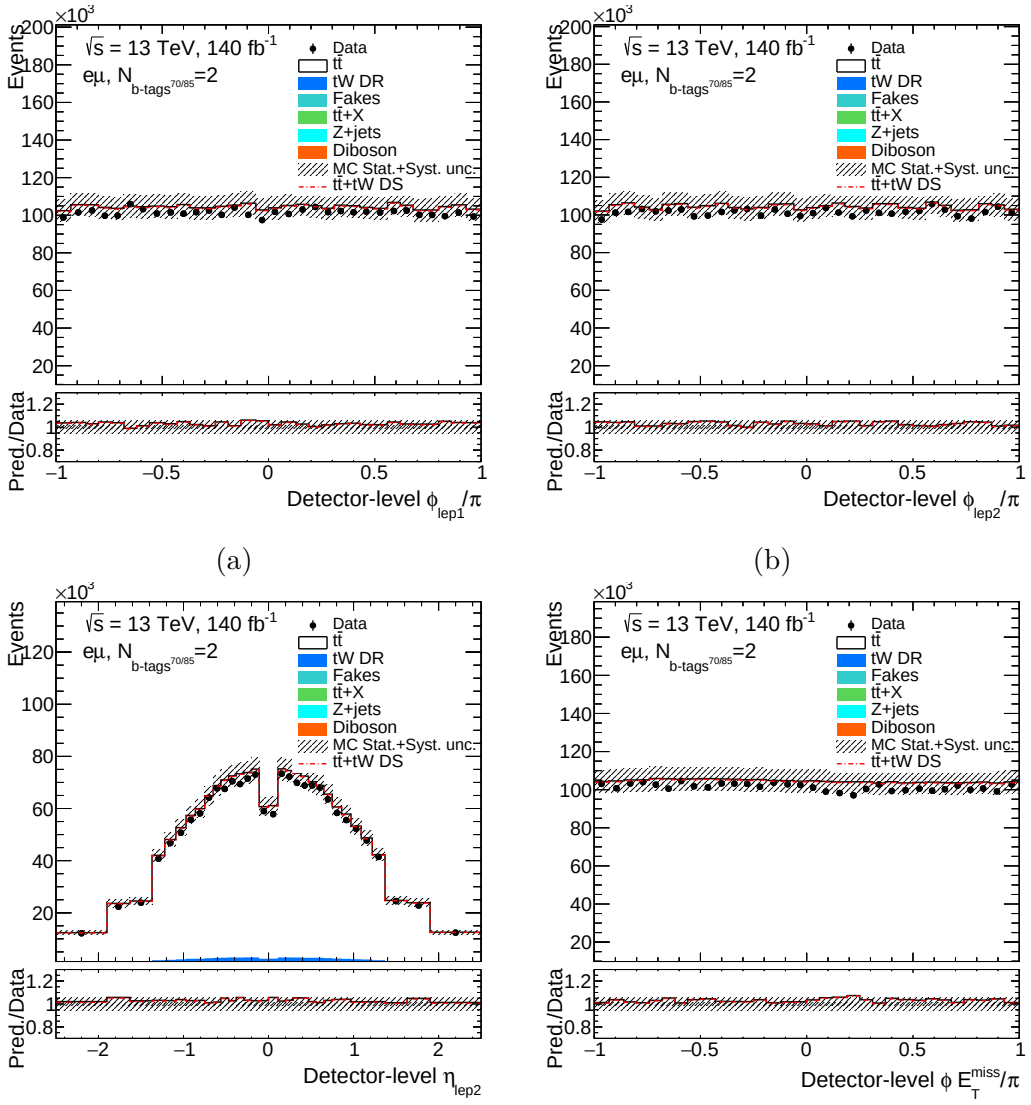

Figure B.3: Comparison of data and MC predictions for the ϕ of a the leading and b the subleading lepton, c the η of the subleading lepton and d the ϕ of the $E_{\mathrm{T}}^{\mathrm{miss}}$ in the 2b-exclusive region.

B.1.2 2b-inclusive signal region

In Figures B.4 - B.8 additional detector-level plots in the 2b-inclusive region are presented.

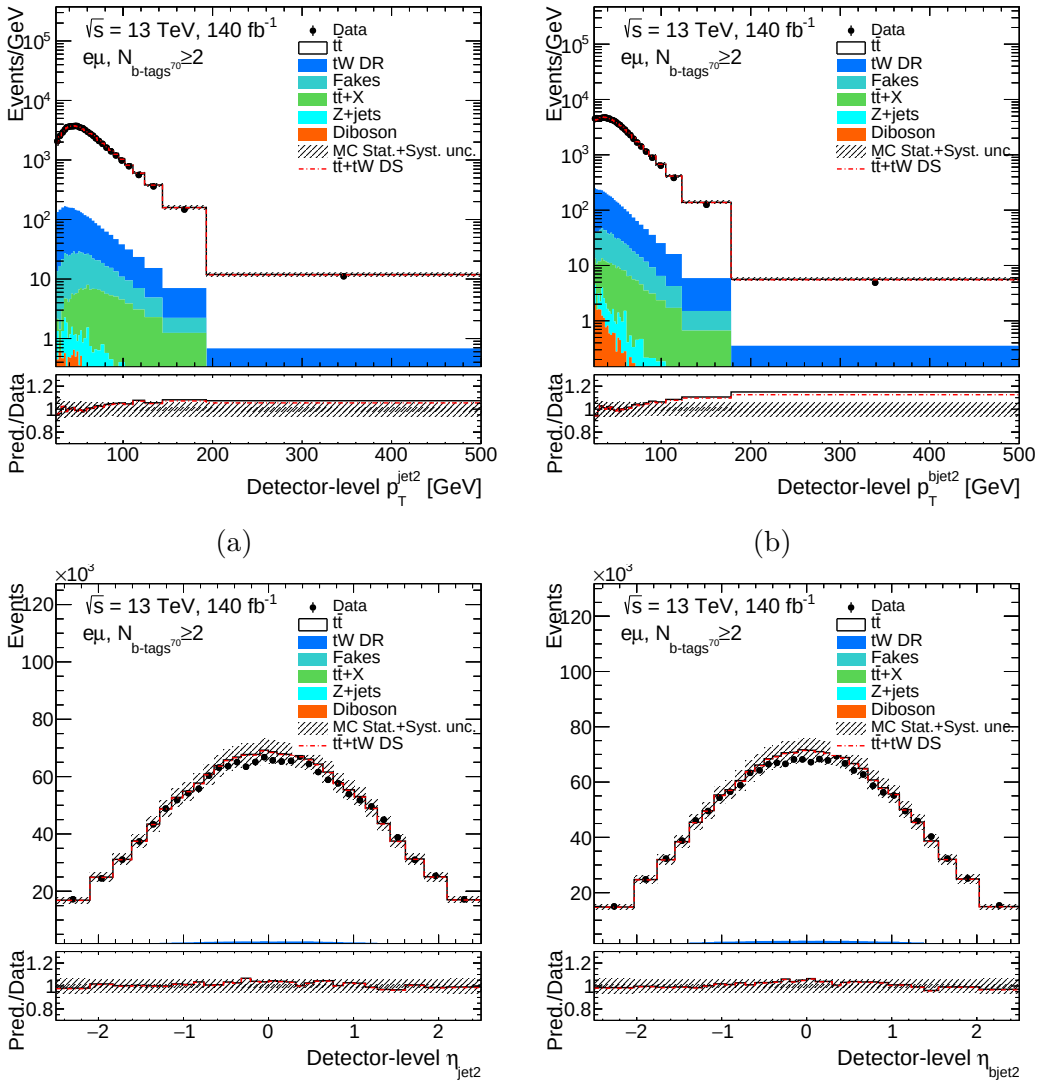

(a) (b)

(c) (d)

Figure B.4: Comparison of data and MC predictions for the p_{T} of a the subleading jet and b the subleading b-jet and the η of c the subleading jet and d the subleading b-jet in the 2b-inclusive region.

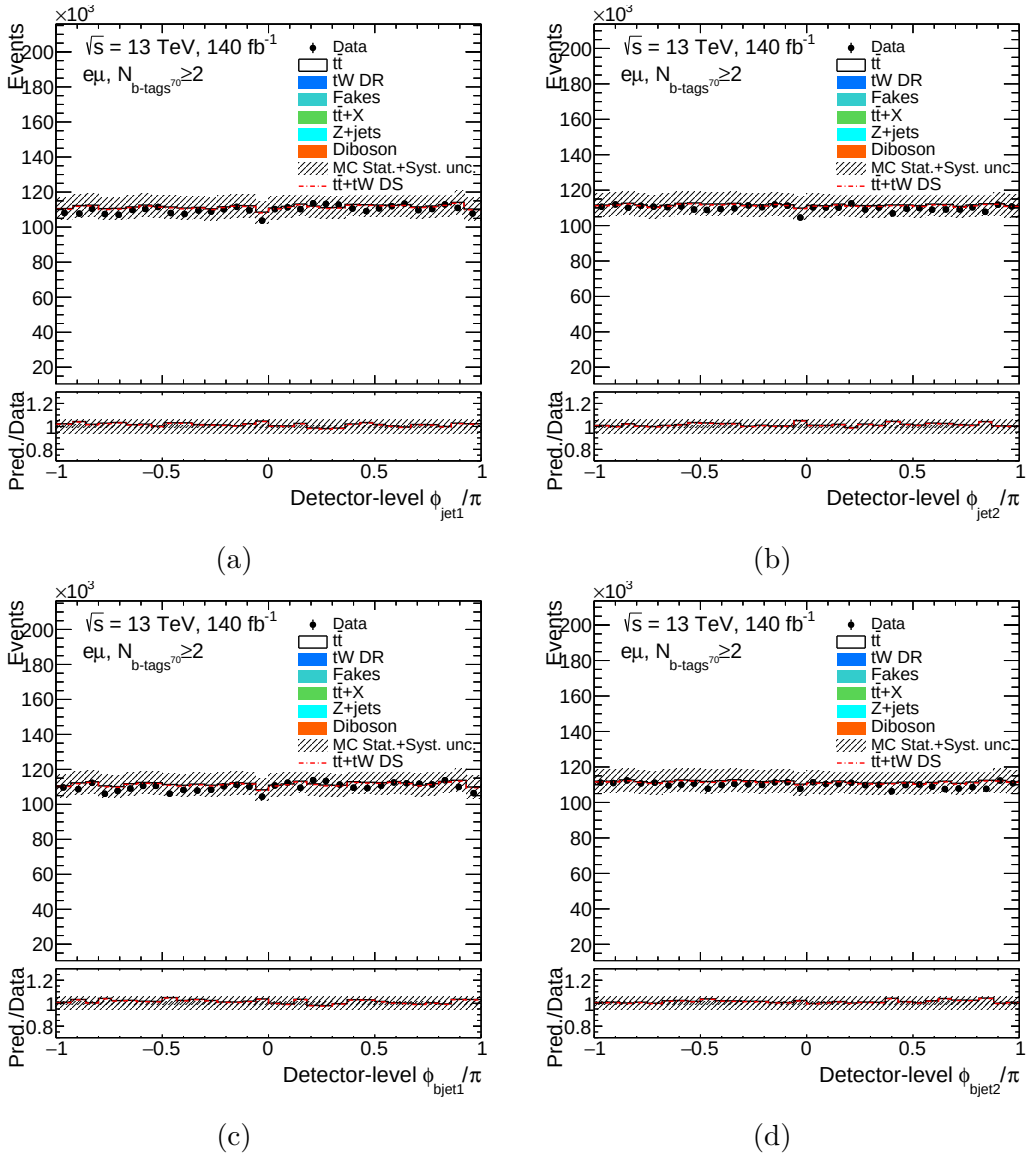

Figure B.5: Comparison of data and MC predictions for the ϕ of a the leading and b subleading jet and of c the leading and d subleading b-jet in the $2b$-inclusive region.

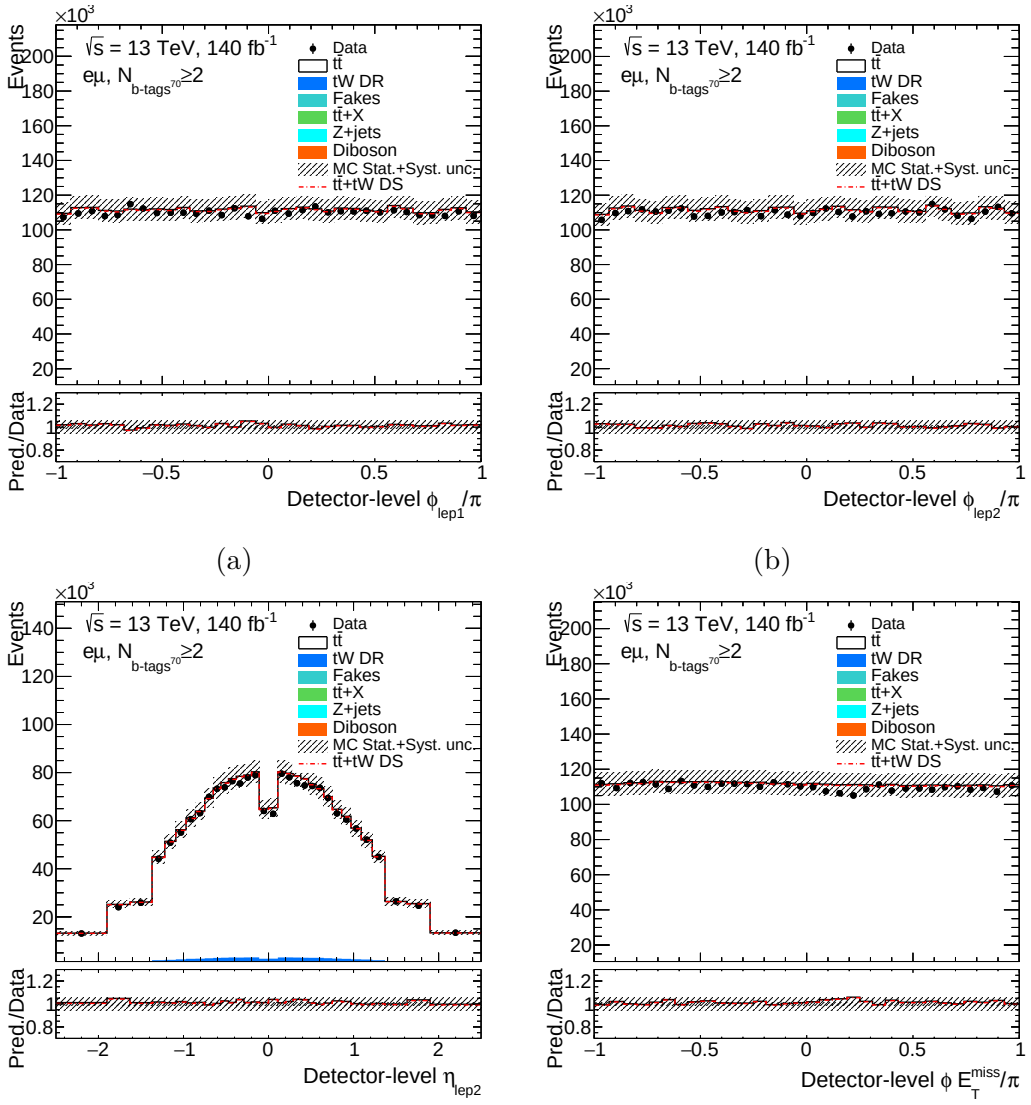

(a) (b) (c) (d)

Figure B.6: Comparison of data and MC predictions for the ϕ of a the leading and b the subleading lepton, c the η of the subleading lepton and d the ϕ of the $E_{\mathrm{T}}^{\mathrm{miss}}$ in the $2b$-inclusive region.

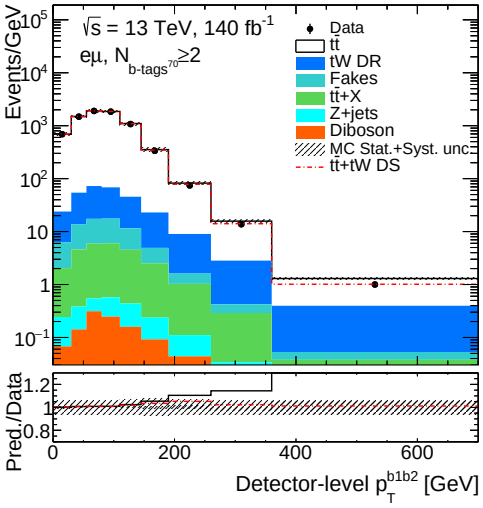

(a)

Figure B.7: Comparison of data and MC predictions for the a $p_{\mathrm{T}}^{b_1,b_2}$ variable in the $2b$-inclusive region.

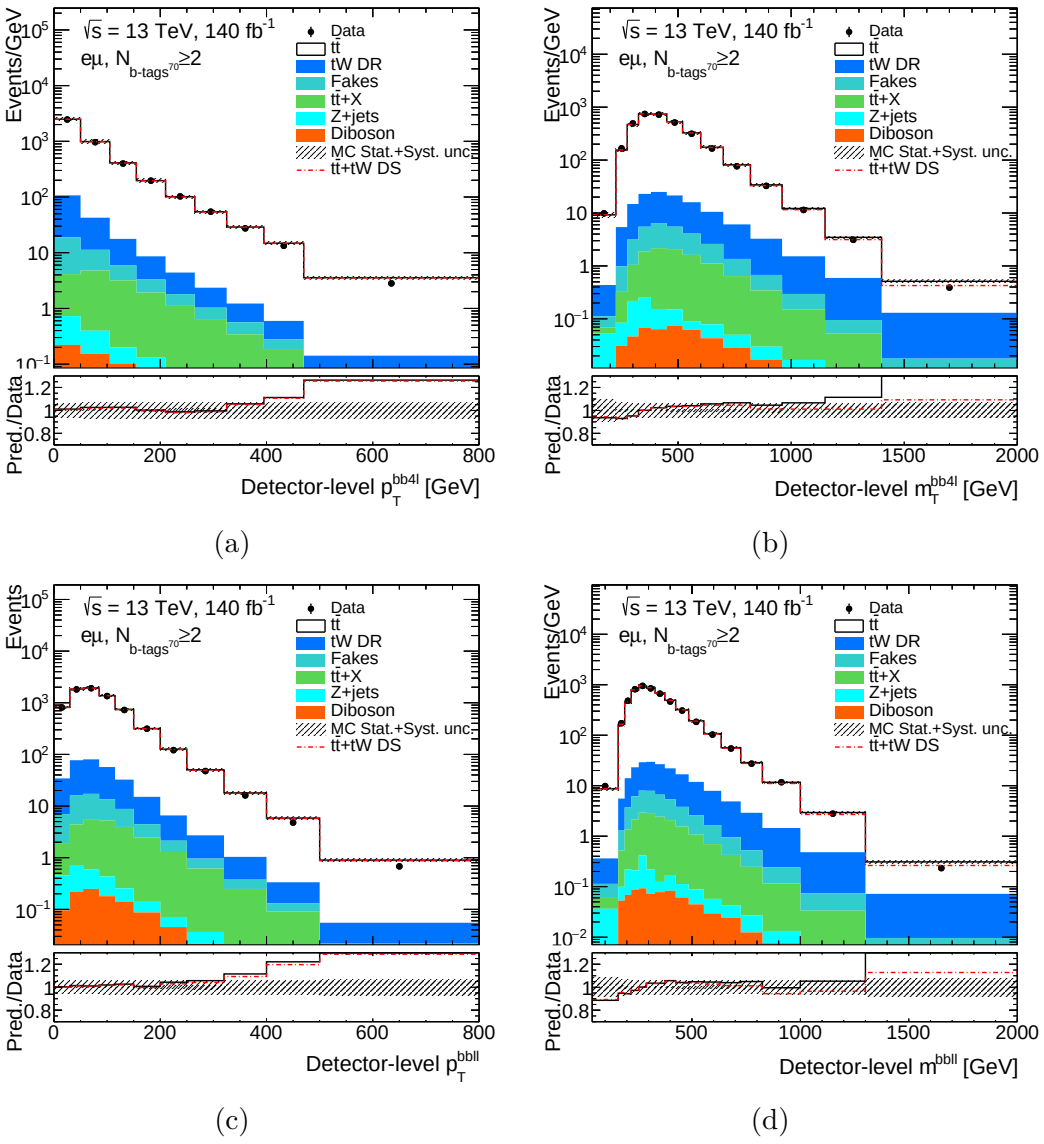

(a) (b)

(c) (d)

Figure B.8: Comparison of data and MC predictions for the a p_{T}^{bb4l}, the b m_{T}^{bb4l}, the c p_{T}^{bbll} and the d m^{bbll} variables in the $2b$-inclusive region.

B.2 The m_{bl}^{minimax} variable

B.2.1 Studies on the b-quark used in the variable construction

Some truth-level tests have been performed in order to check which of the b-quarks produced in a $t\bar{t}$ process has been used in the m^{bl}_{minimax} variable construction. This can be achieved by matching the parton-level b-quarks and leptons to the reco and particle level b-jet and dressed lepton chosen by the m^{bl}_{minimax} algorithm. Since the ntuples contain only information on the b-quarks coming from the top quarks, we can assume that the b-jet not matched to any of the two b-quarks comes from the radiation. The studies have been performed on the nominal $t\bar{t}$ sample, in the $2b$-exclusive region.

Events are categorized based on how they are matched:

- Lepton and b from the same t (referred to as `l_and_b_from_same_t` in the plots and tables below).
- Lepton from t and b from the other t (`l_from_t_b_from_other_t`)[1].
- `b_or_lep_unmatched`: b from radiation, i.e. $\Delta R > 0.4$ from any b-quark coming from top, or lepton unmatched, i.e. $\Delta R > 0.2$ from any truth lepton (which is a very rare occurrence).

This workflow has been applied to both for reco- and particle-level events.

In Figures B.9 and B.10 angular distances between the b-jet and closest b-quark and reconstructed lepton and closest truth lepton for the detector- and particle-level selections are provided, respectively.

Table B.1 shows the composition of the three categories for the reco- and particle-level selections. b-quarks from the same top are the most populated category, followed by b-quarks from the other top. The b-quarks from radiation are the least populated category. The composition of the three categories is similar for the reco- and particle-level selections. This general ranking is strongly dependant on the m^{bl}_{minimax} region considered.

Category	Reco-level	Particle-level
`l_and_b_from_same_t`	78%	80%
`l_from_t_b_from_other_t`	15%	16%
`b_or_lep_unmatched`	7%	4%

Table B.1: Composition of the three categories for the reco- and particle-level selections.

The distributions of m^{bl}_{minimax} for the three categories at reco- and particle-level are shown in Figures B.11 and B.12, respectively. Specifically, the plot on the left shows the

[1]When referring to "t" or "other t" we mean that they can be t or $\bar{t}$.

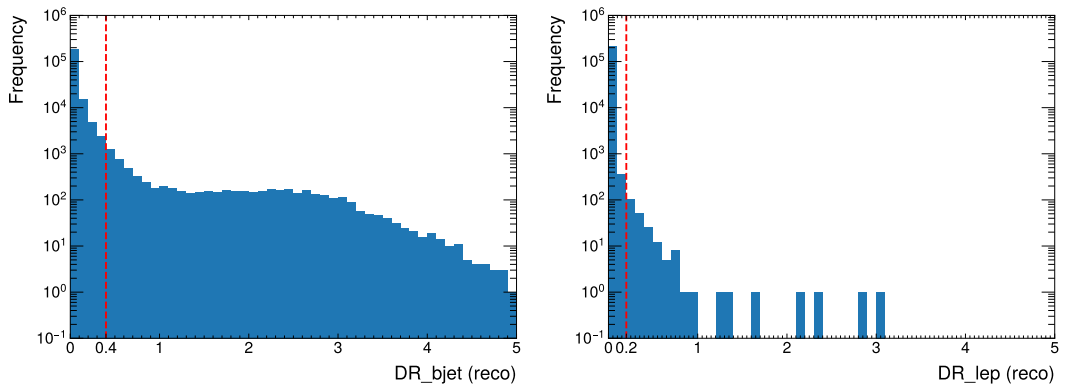

(a) (b)

Figure B.9: Angular distance ΔR between a the b-jet and closest b-quark and b the reconstructed lepton and truth lepton at detector level. The vertical red line indicates the cut value beyond which the jet and the lepton are considered "unmatched".

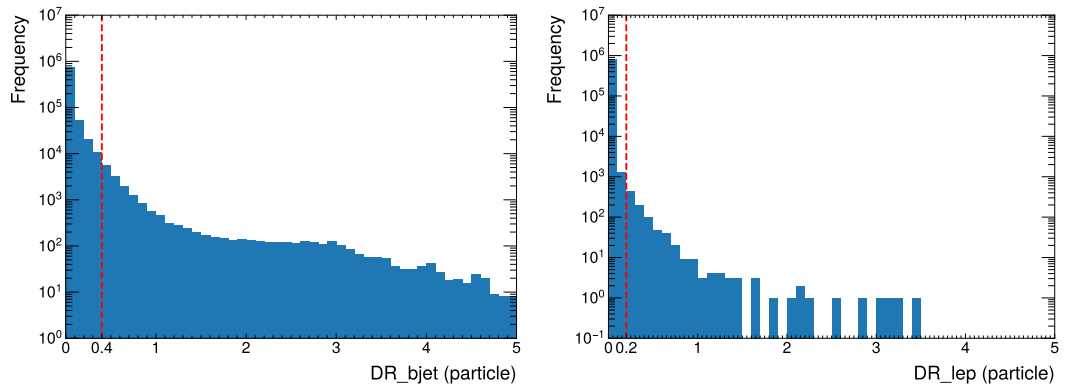

(a) (b)

Figure B.10: Angular distance ΔR between a the b-jet and closest b-quark and b the reconstructed lepton and truth lepton at particle level. The vertical red line indicates the cut value beyond which the jet and the lepton are considered "unmatched".

absolute distribution while the one on the right shows the relative distribution, where the the difference in shapes among the three categories is more evident. In particular, the events where the b-jets comes from additional radiation show a broader distribution, both at low m^{bl}_{minimax} and at high m^{bl}_{minimax} without a clear cutoff.

Finally, the relative bin-per-bin composition for the three categories is shown in Figure B.13. It can be seen that, even if the b-quarks from the same top are the most populated category, the b-quarks from the other top and from radiation are the most important categories in the regions of m^{bl}_{minimax} away from the top-quark mass (with the former dominating over the latter at low m^{bl}_{minimax} and viceversa at high m^{bl}_{minimax}), while the b-quarks from the same top are the most important category in the region around the mass of the top, showing a very strong cut-off above the top mass.

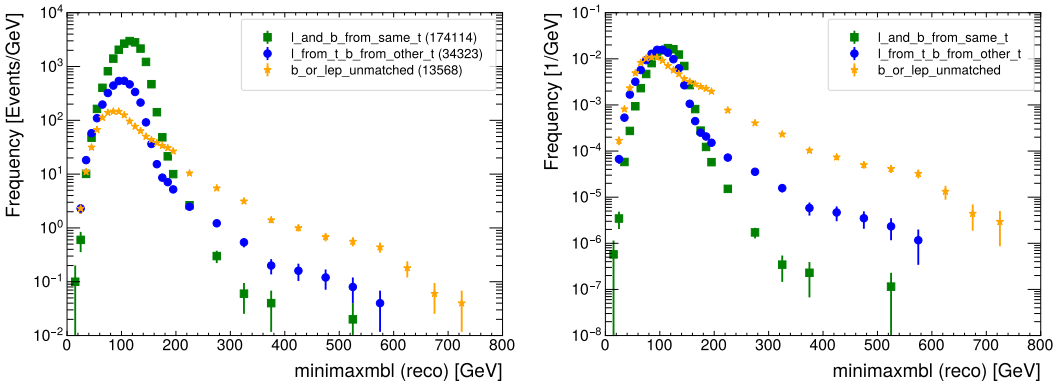

(a) (b)

Figure B.11: Absolute a and relative b m^{bl}_{minimax} variable distribution at reco-level.

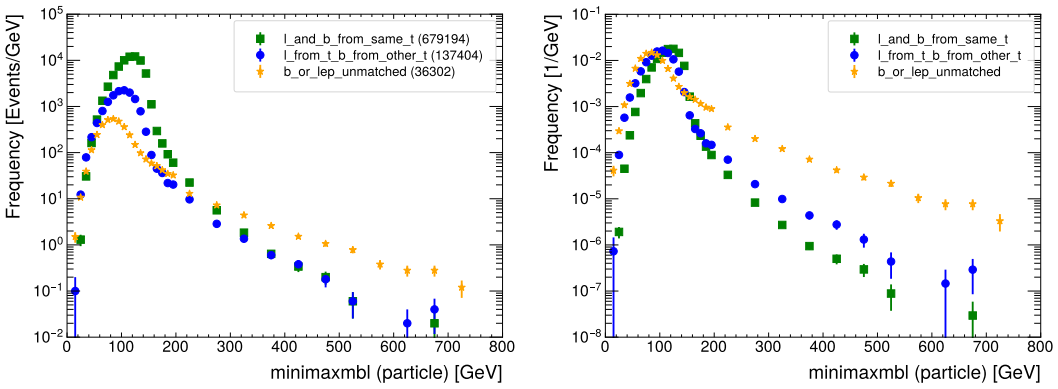

(a) (b)

Figure B.12: Absolute a and relative b m^{bl}_{minimax} variable distribution at particle-level.

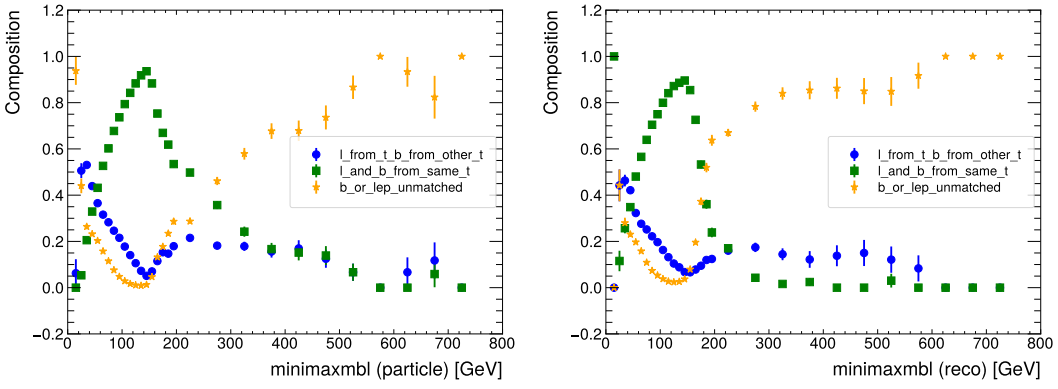

(a) (b)

Figure B.13: Sample composition at particle- a and reco-level b for the m^{bl}_{minimax} variable distribution.

B.3 Selection optimization studies

Several selections have been studied evaluating both sensitivity to interference (DR vs DS) and the total uncertainty.

The options considered in the various selections and the limitations of each options can be summarised as:

- Leptons: $e\mu$ or $e\mu + \mu\mu + ee$. Using the latter provide almost twice statistics but introduces the background from Z+jets. There is not best choice as the background contribution depends on other object selections too. In particular the 2 b-jets at 60/70/77% WP + 3° b-jet with veto at 70/77/85% WP combinations have been considered.

- Jets: 2-jet exclusive or 2-jet inclusive with a veto on third jet. The latter has a higher statistics than the former but is more affected by signal modelling.

- B-jets: 2 b-jets at 60/70/77% WP, if a veto is request on a third b-jet, considered all higher WP.

Since the number of combinations is high, only a limited number of selections were really considered as some options clearly suffered from either high uncertainty due to the MC statistics or high background from Z+jets. The sensitivity to the interference, defined as the difference between the old DR and DS samples, was studies for a subset of selections; an example of the two most promising selection is shown in Figure B.14. The 2-jet

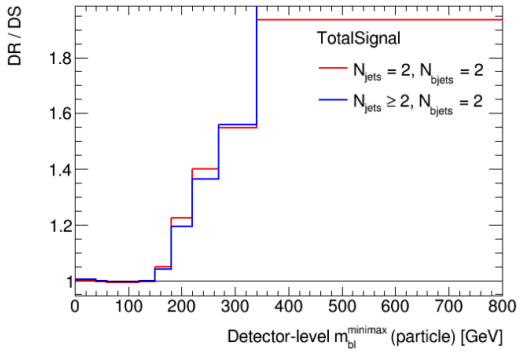

Figure B.14: Sensitivity of DR/DS ratio in different regions ot the $m_{\mathrm{bl}}^{\mathrm{minimax}}$ variable for $e\mu$ selections. For the 2 jets exclusive case there is more sensitivity in the 200-300 GeV region, while for the 2 b-jets exclusive one there is more sensitivity in the region above 400 GeV.

exclusive selection has a higher sensitivity in the middle of the range but at the highest mass the more inclusive selection has a higher sensitivity. As mentioned amove, the 2-jet

exclusive selection has a larger statistical uncertainty as shown in the Figure B.15 (left). However, using all three lepton final states (labelled ll in Figure B.15 on the right), allows to reach almost the same statistical uncertainty as the 2 b-jets exclusive selections. The

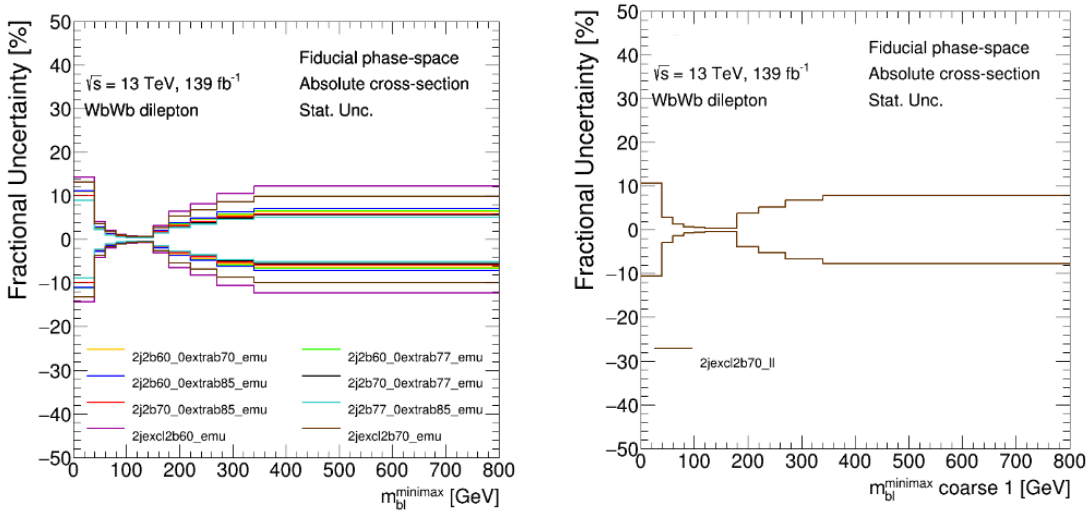

Figure B.15: statistical uncertainty comparison among $e\mu$ (left) and ll (right) channels selections.

b-tagging working point optimisation is performed looking at more uncertainties and evaluating the effect on background and modelling too. The results are summarised in Figure B.16. This study used the binning from the previous analysis. However, this does not affect the conclusions, as there are no significant differences between bins. The best b-tagging working point is the 70% WP for both jet options; for the b-jet exclusive selection, the best result is obtained with veto at 85% WP. The final selection candidates after these optimisation are two selection:

- $e\mu$, at least 2 jets with 2 b-jets at 70% WP and a veto on additional b-jets at 85% WP.
- $e\mu + \mu\mu + ee$, at least 2 jets with 2 b-jets at 70% WP and a veto on additional b-jets at 85% WP.
- $e\mu + \mu\mu + ee$, exactly 2 jets tagged at 70% WP.

The total uncertainty in the three scenarios is compared to select the best selection and is presented in Figure B.17. The Z+jets is dominant for the $e\mu + \mu\mu + ee$ with a veto on third b-jets while it is very small for the 2-jet exclusive selection. The lowest uncertainty in all bins of the tail is achieved by the $e\mu$ with a veto on third b-jets selection; in the four last bins the uncertainty is 10% or lower while for the 2-jet exclusive selection the error

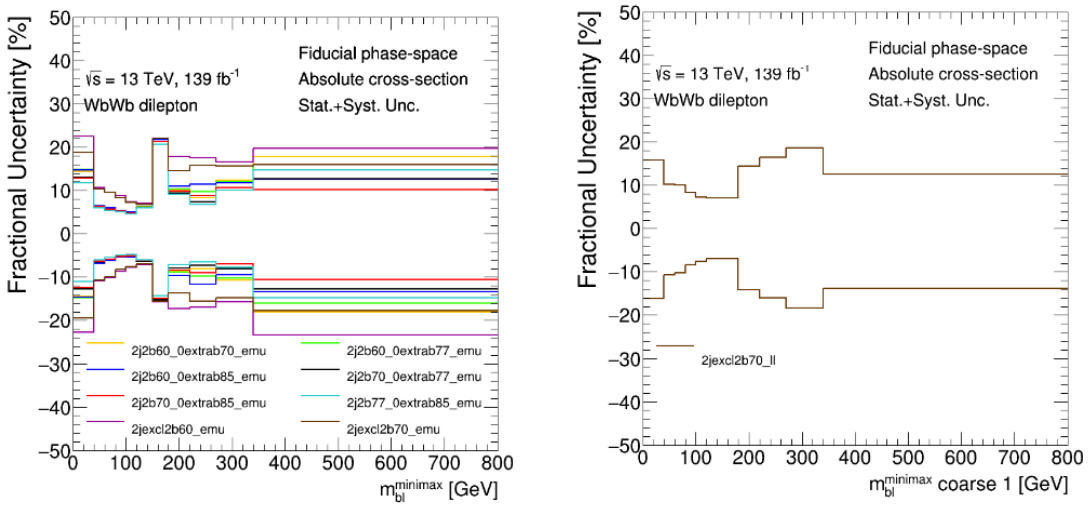

Figure B.16: Total uncertainties (without HF) comparison among $e\mu$ (left) and ll (right) channels selection.

is 12%. It should be noted that the largest uncertainty in the tail of the distribution in the 2-jet exclusive selection is the statistical uncertainty as well as the tW modeliling uncertainty. Hence, if a new prescription will be introduced in Run3 and beyond, this selection will be the best one to use in future publication given the expected additional statistics that should significantly lower the total uncertainty. A further test was carried out to confirm the chosen selection; the χ^2 for several prediction was calculated for the two best selections and summarized in Figure B.2. The chosen selection has a higher discriminating power as fewer samples are compatible with the data, hence it is the most sensitive selection.

Table B.2: χ^2 and p-values to quantify the agreement for different selections.

Observable	PWG+PY8		PWG+H7		MC@NLO+H7		MC@NLO+PY8		bb4l 950540		tW DS		hdamp3mt		pThard1	
	χ^2/NDF	p-value	χ^2/NDF	p-value	χ^2/NDF	p-value	χ^2/NDF	p-value	χ^2/NDF	p-value	χ^2/NDF	p-value	χ^2/NDF	p-value	χ^2/NDF	p-value
$e\mu$ 2-b-jet excl	12/9	0.23	22/9	< 0.01	19/9	0.03	18/9	0.04	39/9	< 0.01	62/9	< 0.01	25/9	< 0.01	25/9	< 0.01
$e\mu + \mu\mu + ee$ 2-jet excl	10/10	0.40	18/10	0.06	10/10	0.41	10/10	0.45	23/10	0.01	35/10	< 0.01	18/10	0.05	17/10	0.08

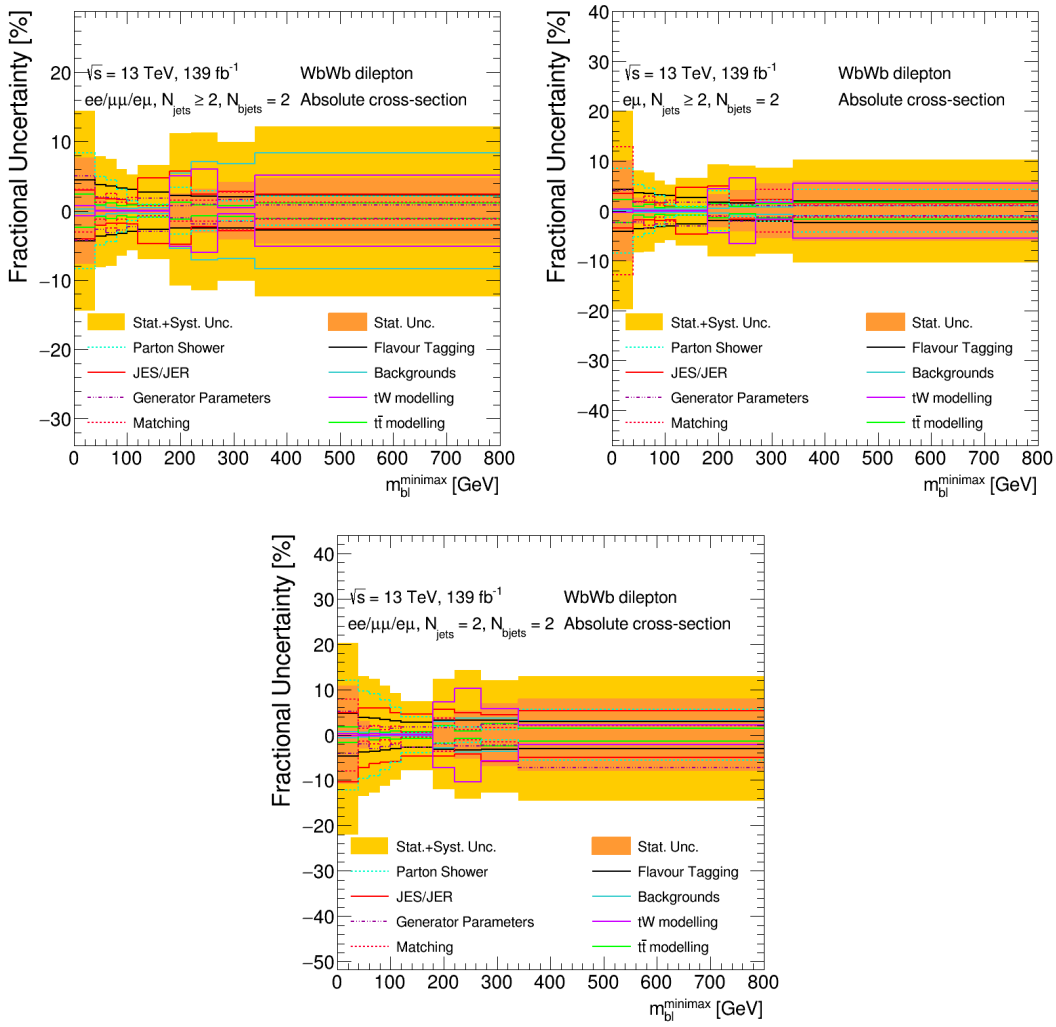

Figure B.17: Total uncertainties for $e\mu + \mu\mu + ee$ (left) and $e\mu$ (right) 2-b-jets exclusive selection (left), as well as 2-jets exclusive selection (bottom).

Appendix C

Analysis strategy and results complements

C.1 Unfolding corrections

Examples of acceptance, efficiency and migration matrices variables defined in the 2b-inclusive signal region are shown in Figures C.1 - C.9.

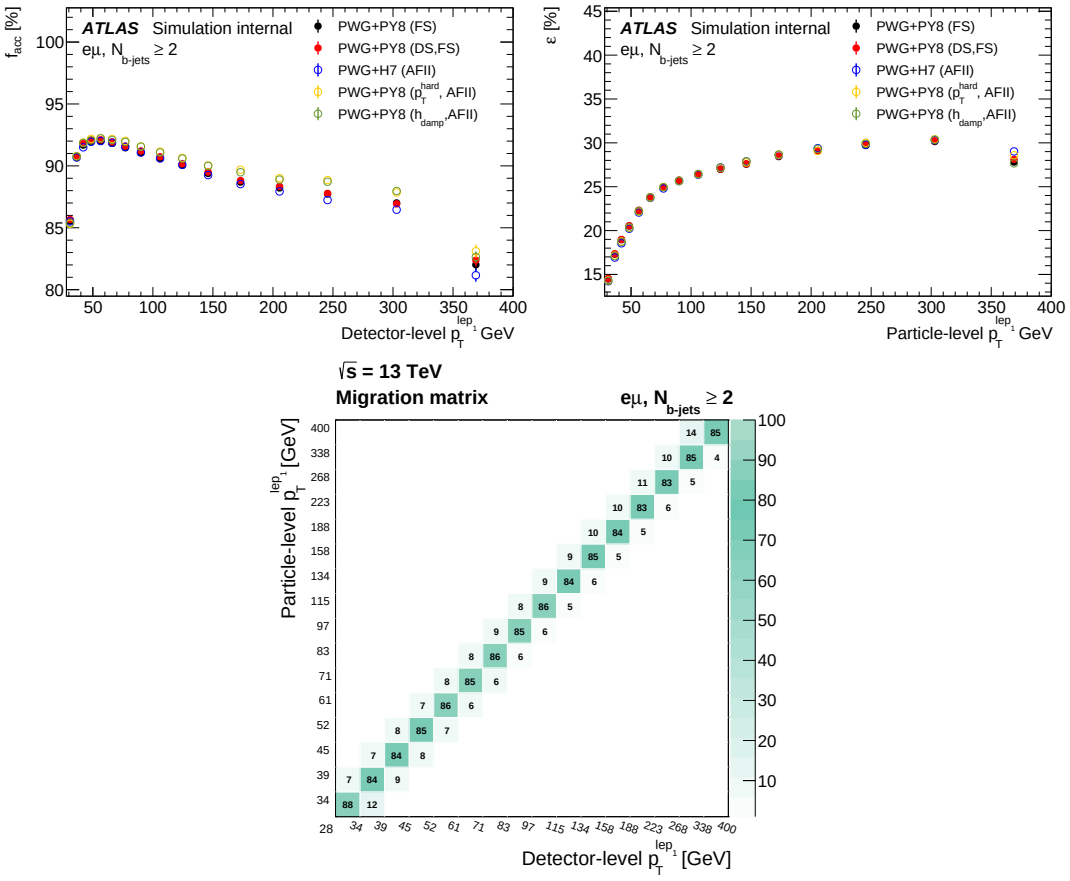

Figure C.1: The (left) acceptance (f_{acc}) and (right) efficiency ε corrections and (bottom) the migration matrix for the p_T^{lep1} variable. The nominal acceptance and efficiency corrections, in black, are compared to the corrections obtained with some MC generators used to evaluate the signal modelling uncertainties. In the migration matrix, only bins where the migration is greater than 1% are shown.

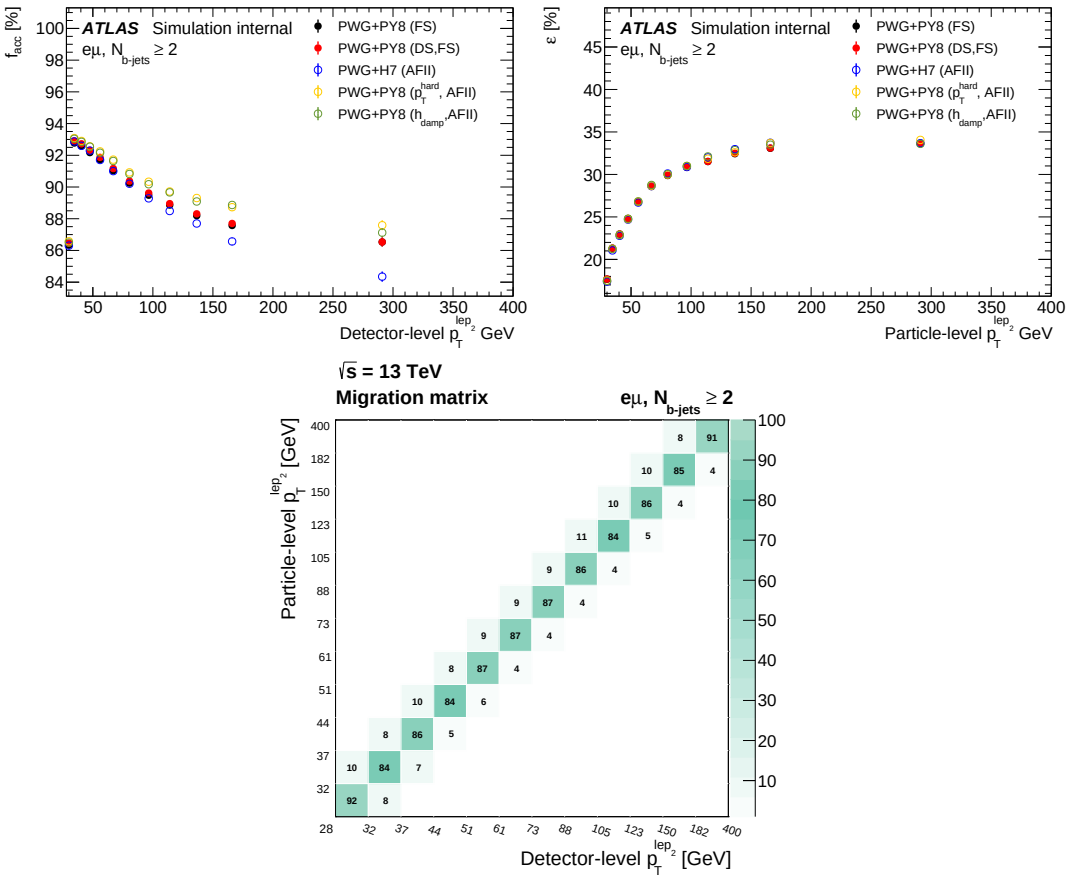

Figure C.2: The (left) acceptance (f_{acc}) and (right) efficiency ε corrections and (bottom) the migration matrix for the p_T^{lep2} variable. The nominal acceptance and efficiency corrections, in black, are compared to the corrections obtained with some MC generators used to evaluate the signal modelling uncertainties. In the migration matrix, only bins where the migration is greater than 1% are shown.

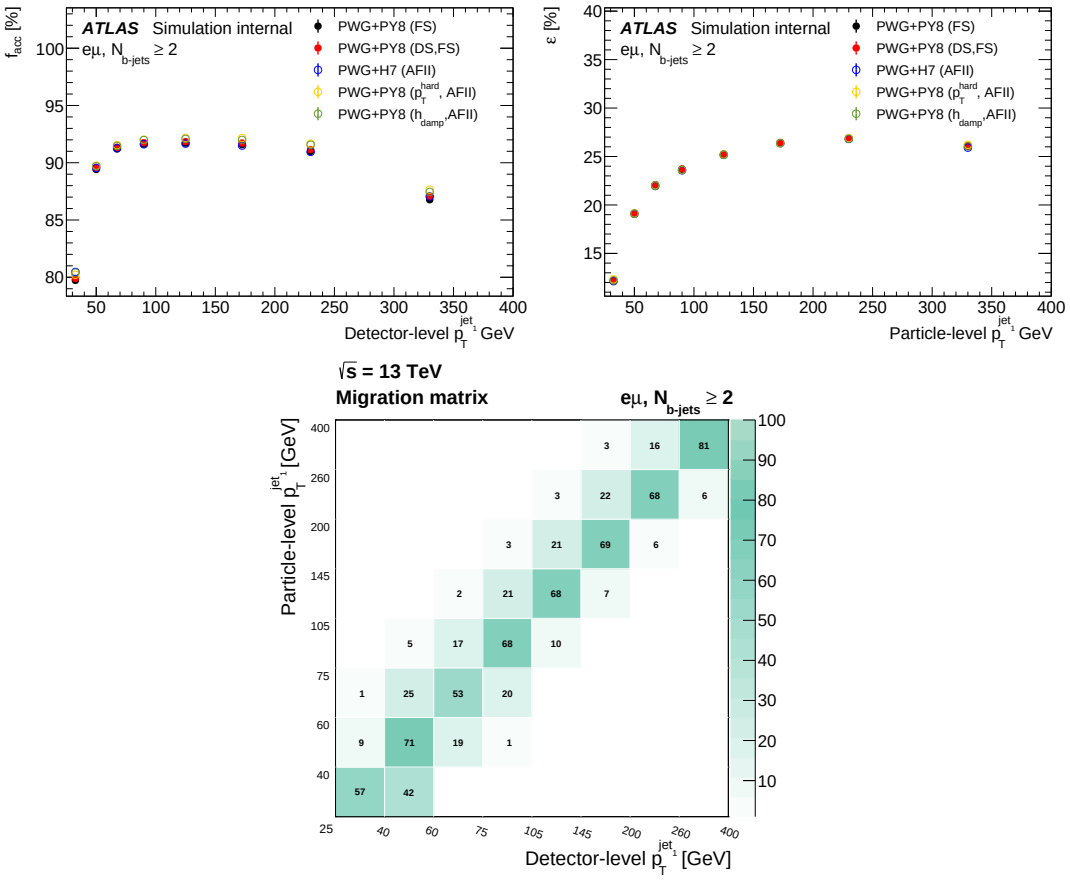

Figure C.3: The (left) acceptance (f_{acc}) and (right) efficiency ε corrections and (bottom) the migration matrix for the p_T^{jet1} variable. The nominal acceptance and efficiency corrections, in black, are compared to the corrections obtained with some MC generators used to evaluate the signal modelling uncertainties. In the migration matrix, only bins where the migration is greater than 1% are shown.

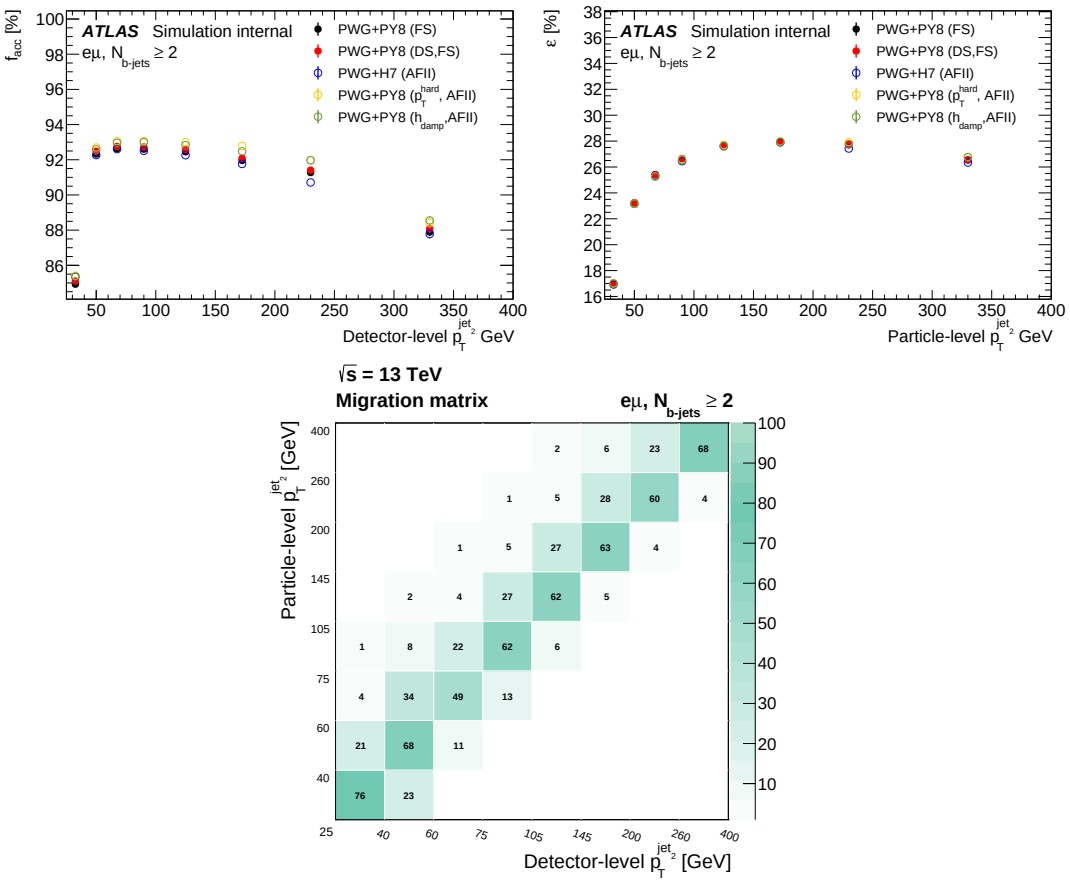

Figure C.4: The (left) acceptance (f_{acc}) and (right) efficiency ε corrections and (bottom) the migration matrix for the p_T^{jet2} variable. The nominal acceptance and efficiency corrections, in black, are compared to the corrections obtained with some MC generators used to evaluate the signal modelling uncertainties. In the migration matrix, only bins where the migration is greater than 1% are shown.

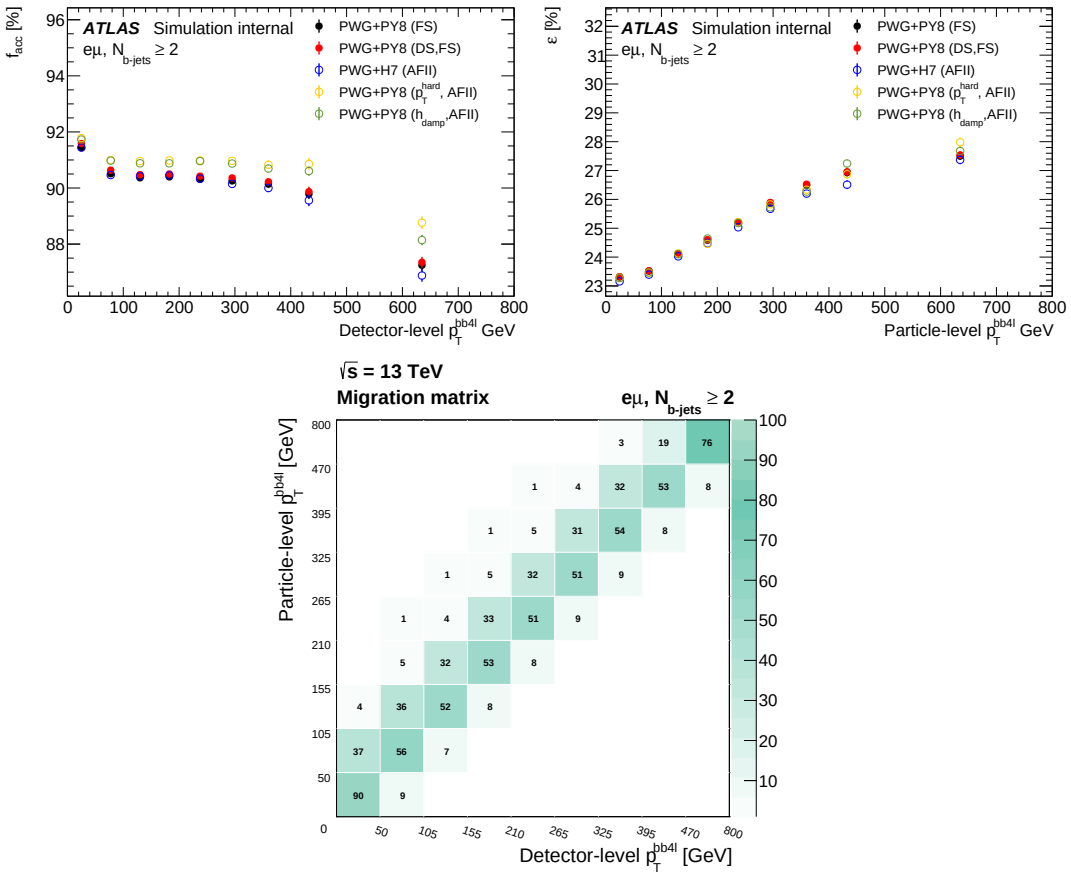

Figure C.5: The (left) acceptance (f_{acc}) and (right) efficiency ε corrections and (bottom) the migration matrix for the $p_T^{t\bar{t}}$ variable. The nominal acceptance and efficiency corrections, in black, are compared to the corrections obtained with some MC generators used to evaluate the signal modelling uncertainties. In the migration matrix, only bins where the migration is greater than 1% are shown.

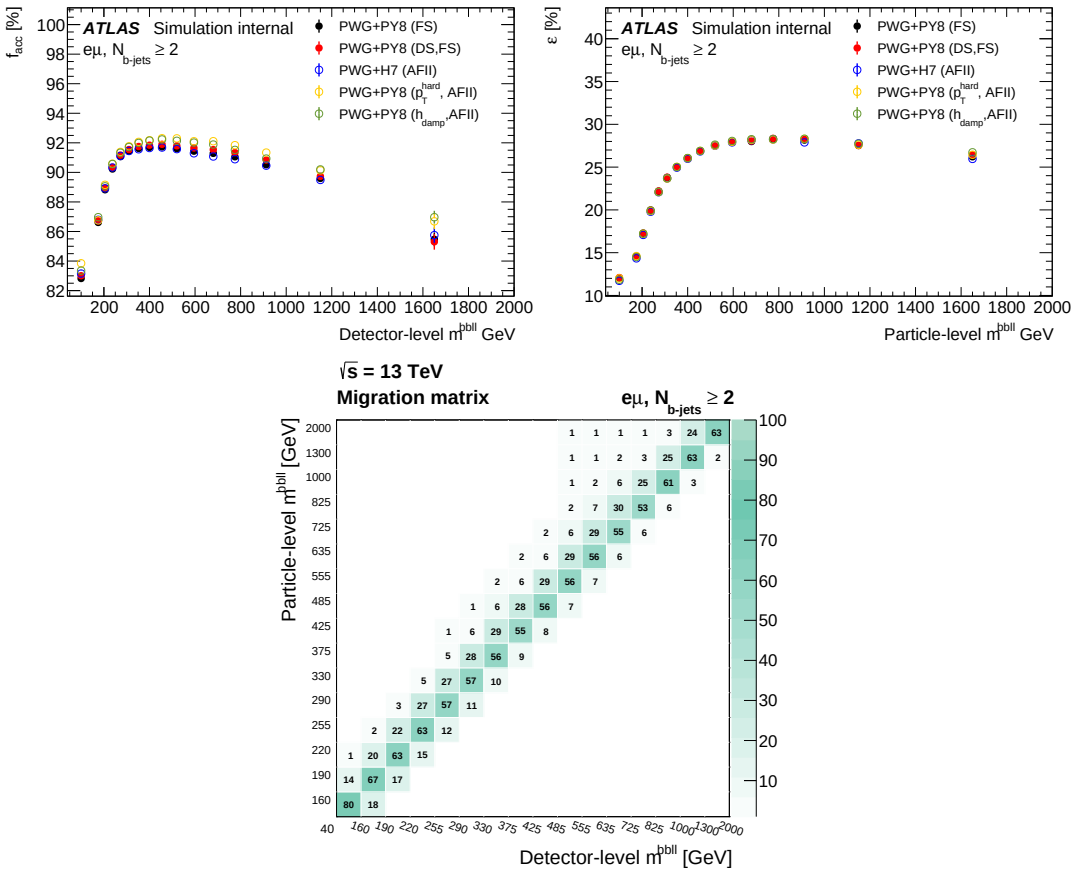

Figure C.6: The (left) acceptance (f_{acc}) and (right) efficiency ε corrections and (bottom) the migration matrix for the m_{bbll} variable. The nominal acceptance and efficiency corrections, in black, are compared to the corrections obtained with some MC generators used to evaluate the signal modelling uncertainties. In the migration matrix, only bins where the migration is greater than 1% are shown.

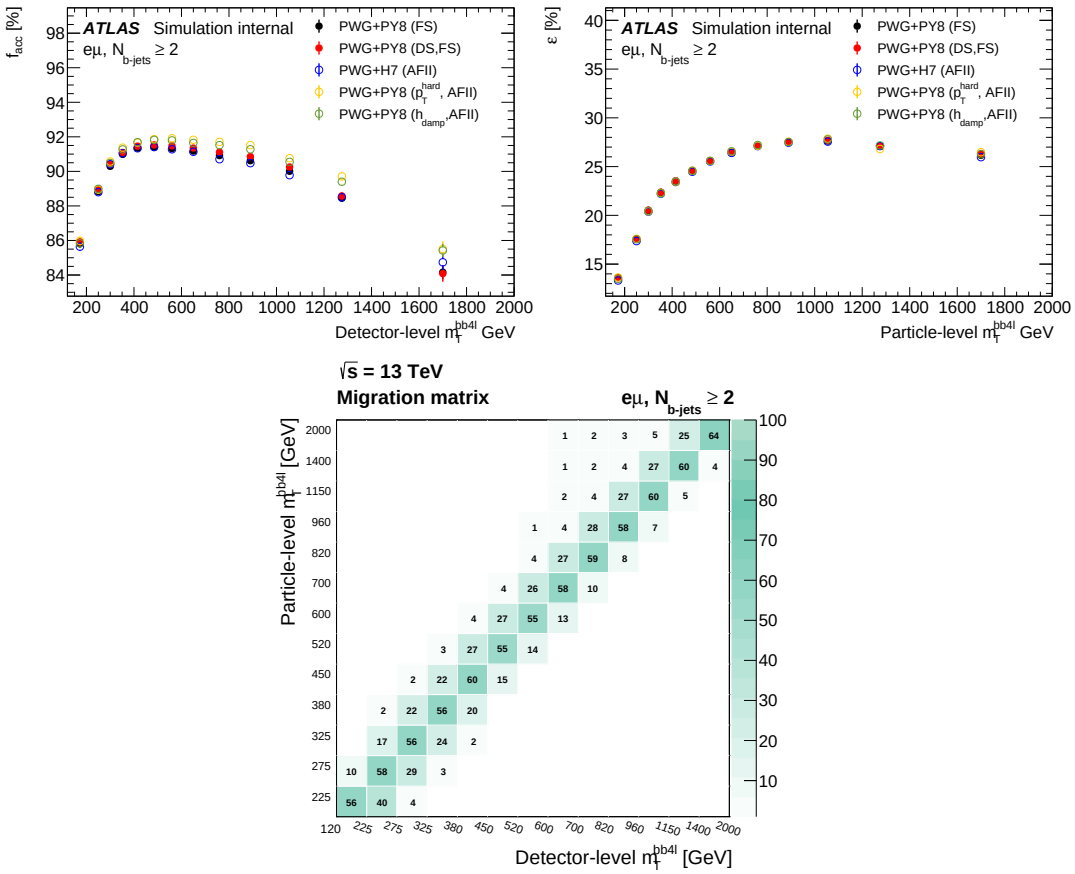

Figure C.7: The (left) acceptance (f_{acc}) and (right) efficiency ε corrections and (bottom) the migration matrix for the $m_T^{t\bar{t}}$ variable. The nominal acceptance and efficiency corrections, in black, are compared to the corrections obtained with some MC generators used to evaluate the signal modelling uncertainties. In the migration matrix, only bins where the migration is greater than 1% are shown.

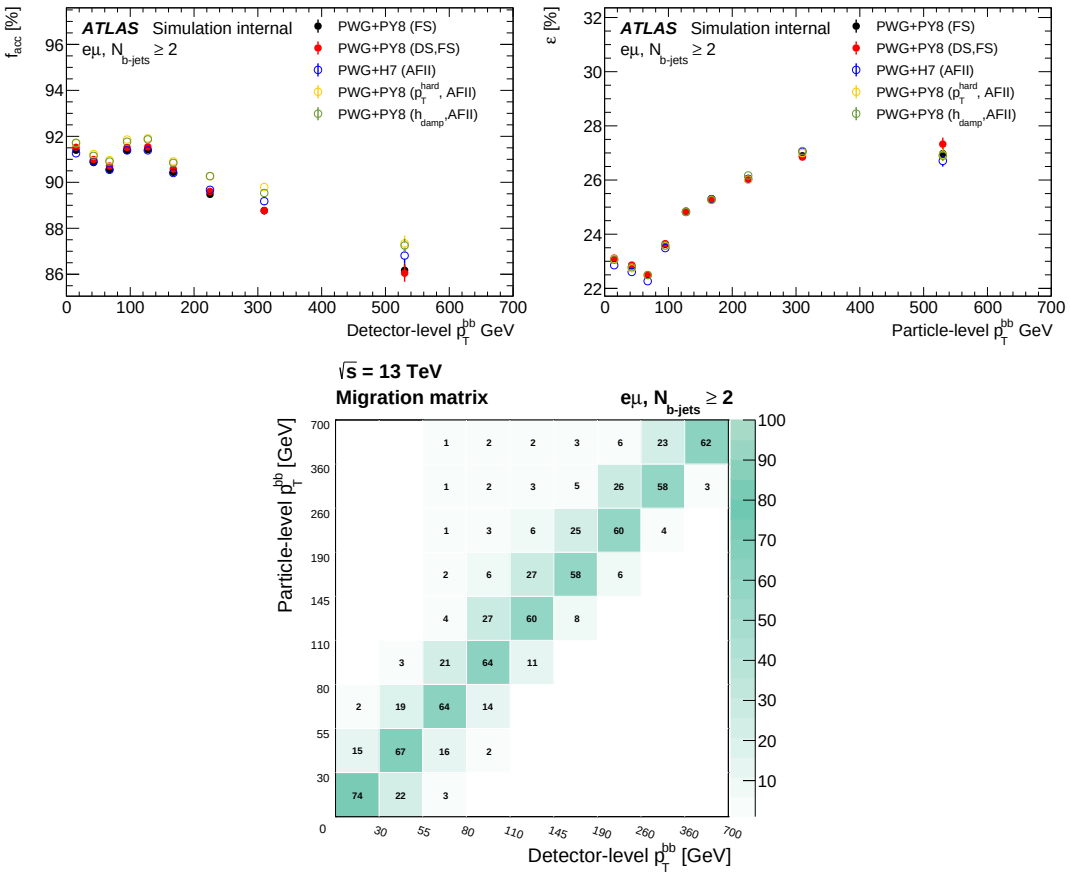

Figure C.8: The (left) acceptance (f_{acc}) and (right) efficiency ε corrections and (bottom) the migration matrix for the p_T^{b1b2} variable. The nominal acceptance and efficiency corrections, in black, are compared to the corrections obtained with some MC generators used to evaluate the signal modelling uncertainties. In the migration matrix, only bins where the migration is greater than 1% are shown.

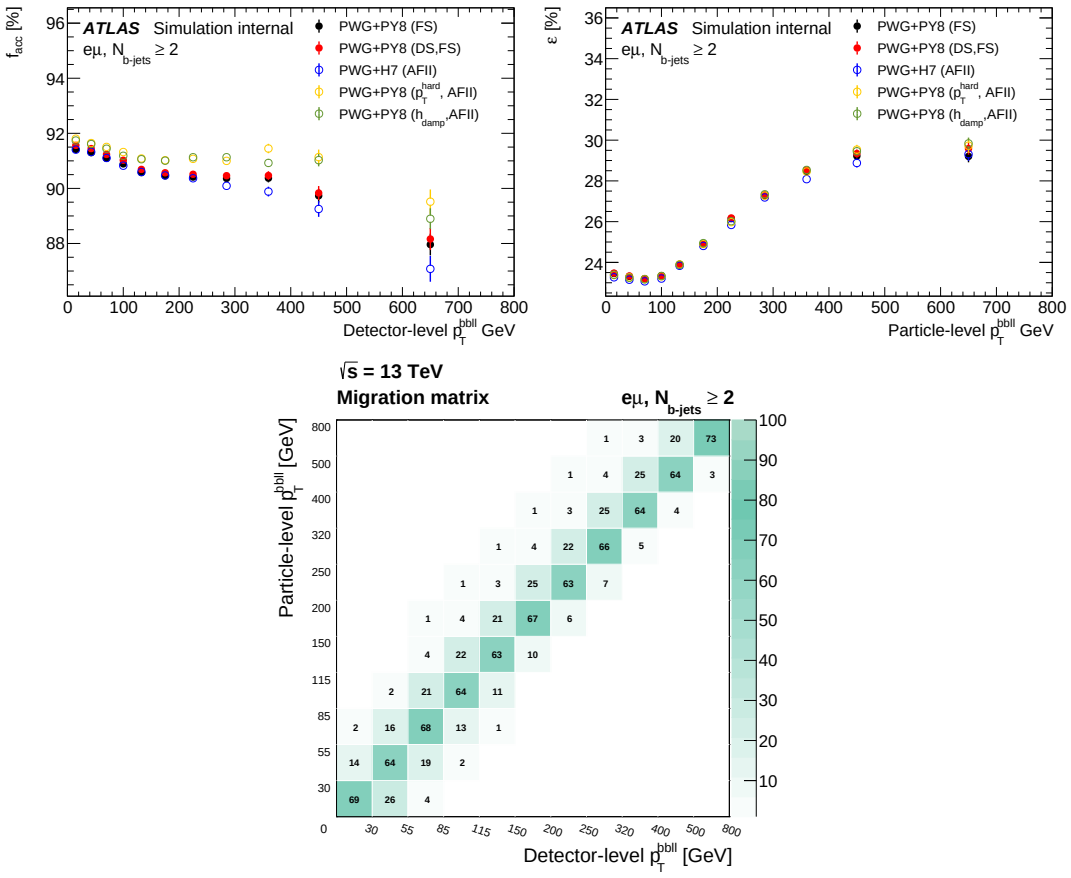

Figure C.9: The (left) acceptance (f_{acc}) and (right) efficiency ε corrections and (bottom) the migration matrix for the p_T^{bbll} variable. The nominal acceptance and efficiency corrections, in black, are compared to the corrections obtained with some MC generators used to evaluate the signal modelling uncertainties. In the migration matrix, only bins where the migration is greater than 1% are shown.

C.2 Other closure tests

In Figures C.10 - C.19 closure tests for 2b-inclusive signal region variables are shown. Here `half0` is used as pseudo-data and `half1` as MC sample.

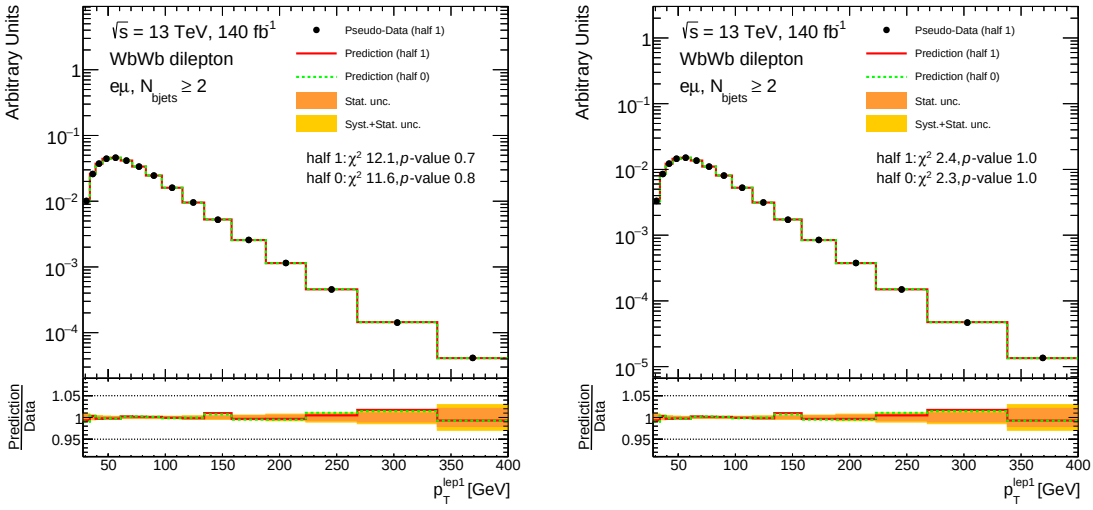

Figure C.10: Unfolding closure tests for the absolute (left) and relative (right) cross-section measurement of the leading lepton p_{T}. The yellow band includes both the statistical uncertainty on the pseudo-data sample (`half0`) and the uncertainty on the MC sample (`half1`).

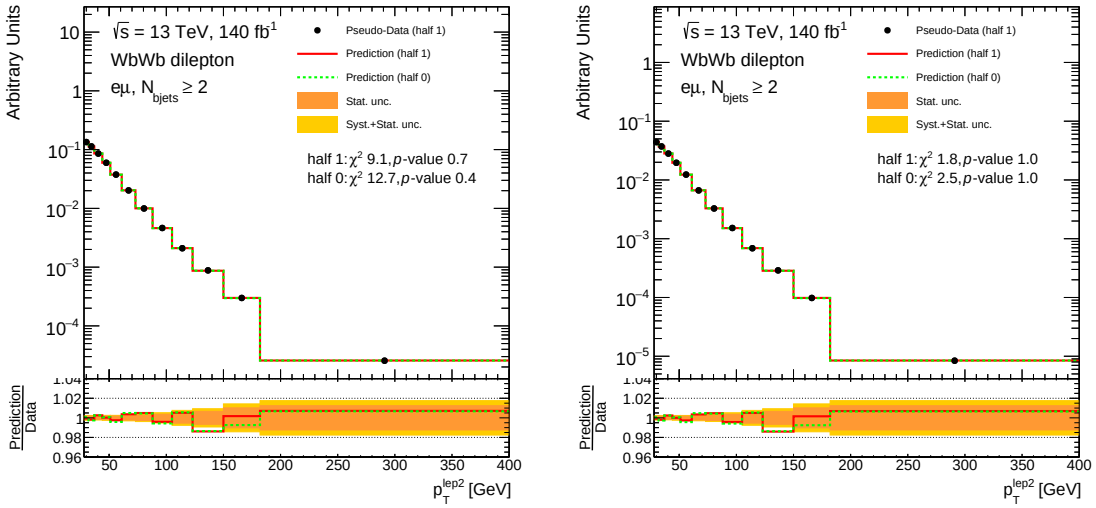

Figure C.11: Unfolding closure tests for the absolute (left) and relative (right) cross-section measurement of the subleading lepton p_{T}. The yellow band includes both the statistical uncertainty on the pseudo-data sample (`half0`) and the uncertainty on the MC sample (`half1`).

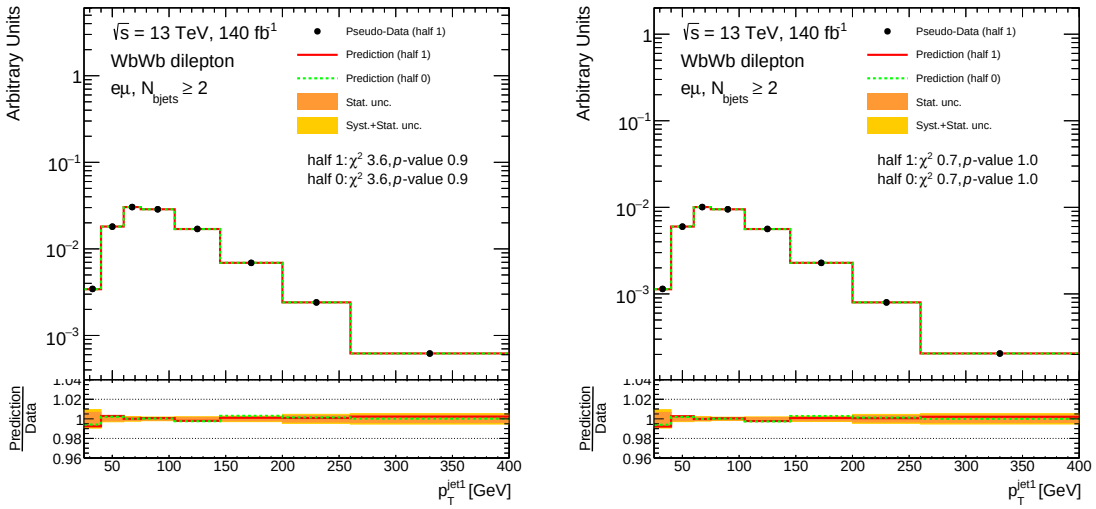

Figure C.12: Unfolding closure tests for the absolute (left) and relative (right) cross-section measurement of the leading jet p_{T}. The yellow band includes both the statistical uncertainty on the pseudo-data sample (`half0`) and the uncertainty on the MC sample (`half1`).

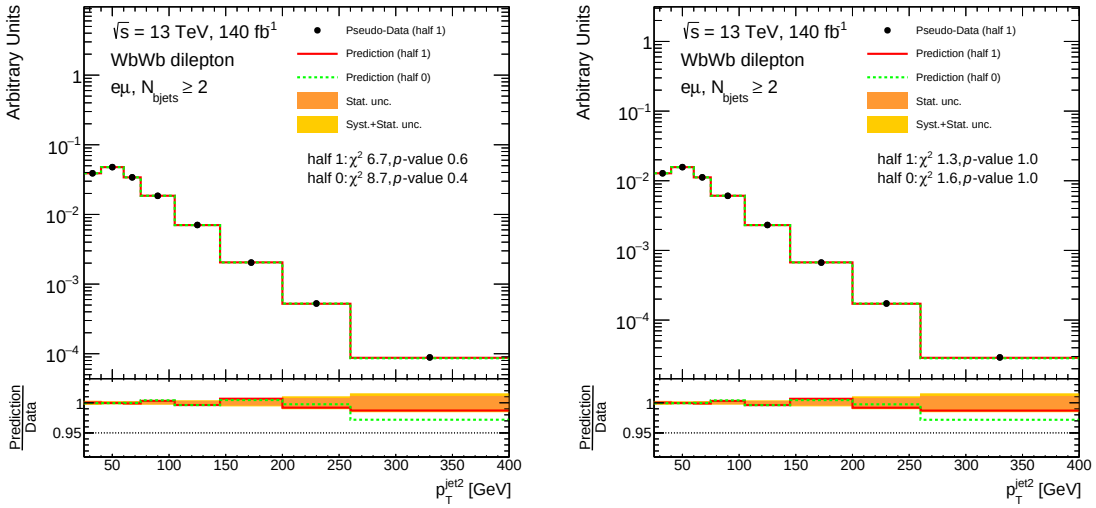

Figure C.13: Unfolding closure tests for the absolute (left) and relative (right) cross-section measurement of the subleading lepton p_{T}. The yellow band includes both the statistical uncertainty on the pseudo-data sample (`half0`) and the uncertainty on the MC sample (`half1`).

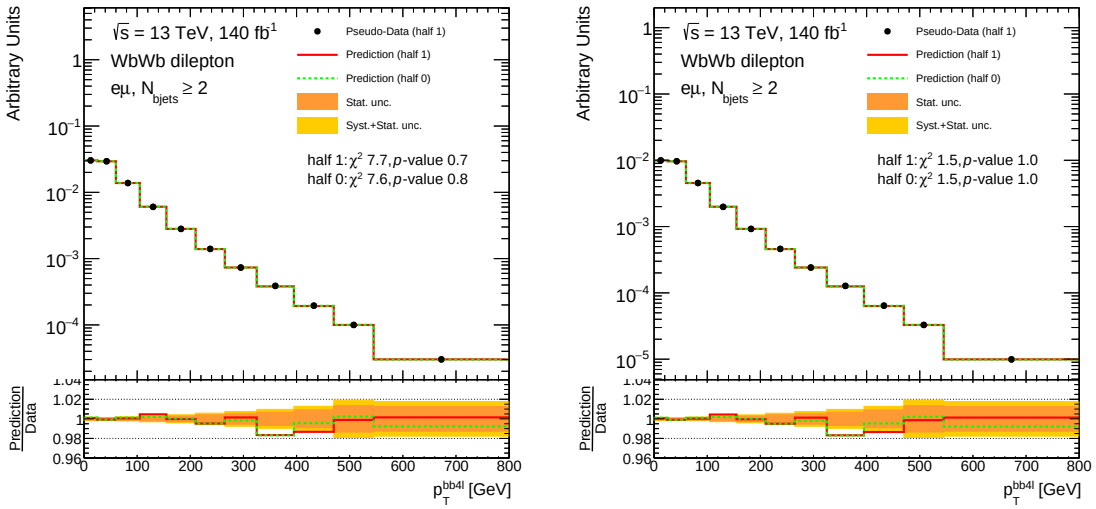

Figure C.14: Unfolding closure tests for the absolute (left) and relative (right) cross-section measurement of the p_T^{bb4l}. The yellow band includes both the statistical uncertainty on the pseudo-data sample (`half0`) and the uncertainty on the MC sample (`half1`).

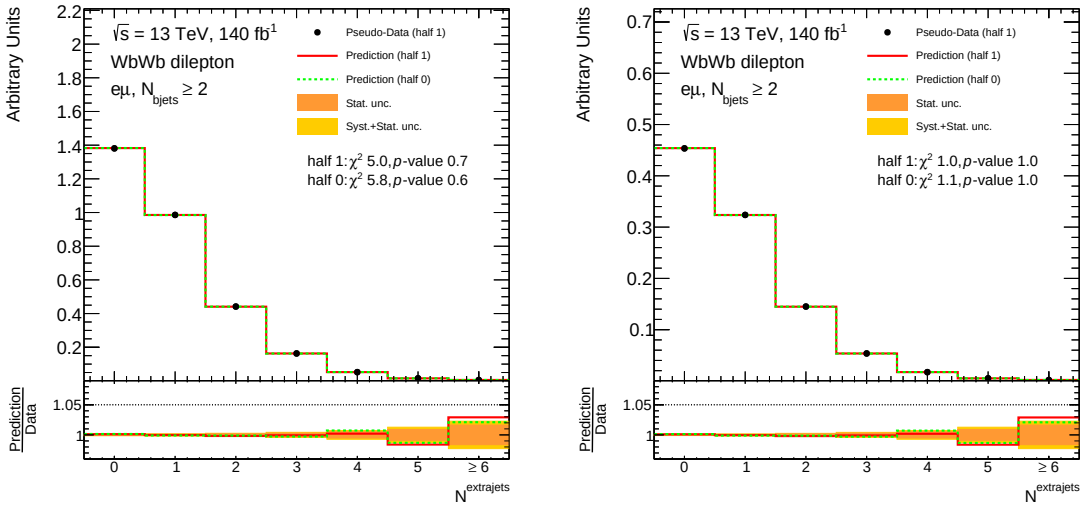

Figure C.15: Unfolding closure tests for the absolute (left) and relative (right) cross-section measurement of the number of jets. The yellow band includes both the statistical uncertainty on the pseudo-data sample (`half0`) and the uncertainty on the MC sample (`half1`).

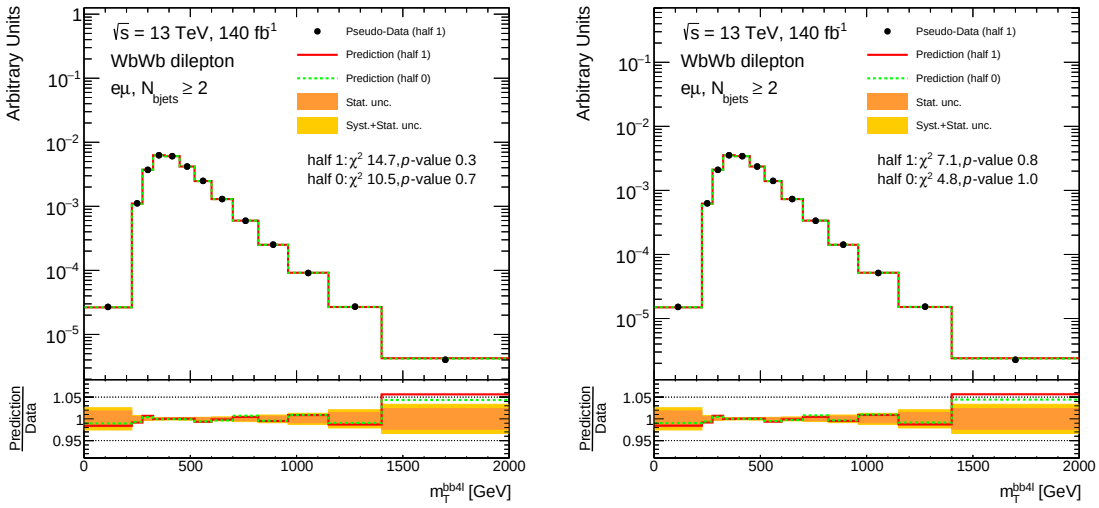

Figure C.16: Unfolding closure tests for the absolute (left) and relative (right) cross-section measurement of the $m_T^{t\bar{t}}$ variable. The yellow band includes both the statistical uncertainty on the pseudo-data sample (`half0`) and the uncertainty on the MC sample (`half1`).

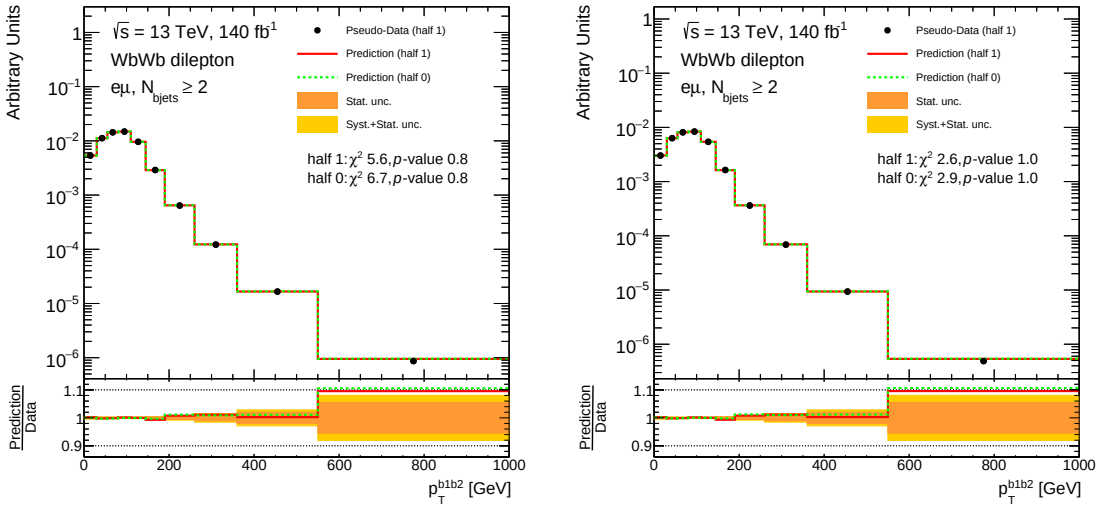

Figure C.17: Unfolding closure tests for the absolute (left) and relative (right) cross-section measurement of the p_T^{b1b2} variable. The yellow band includes both the statistical uncertainty on the pseudo-data sample (`half0`) and the uncertainty on the MC sample (`half1`).

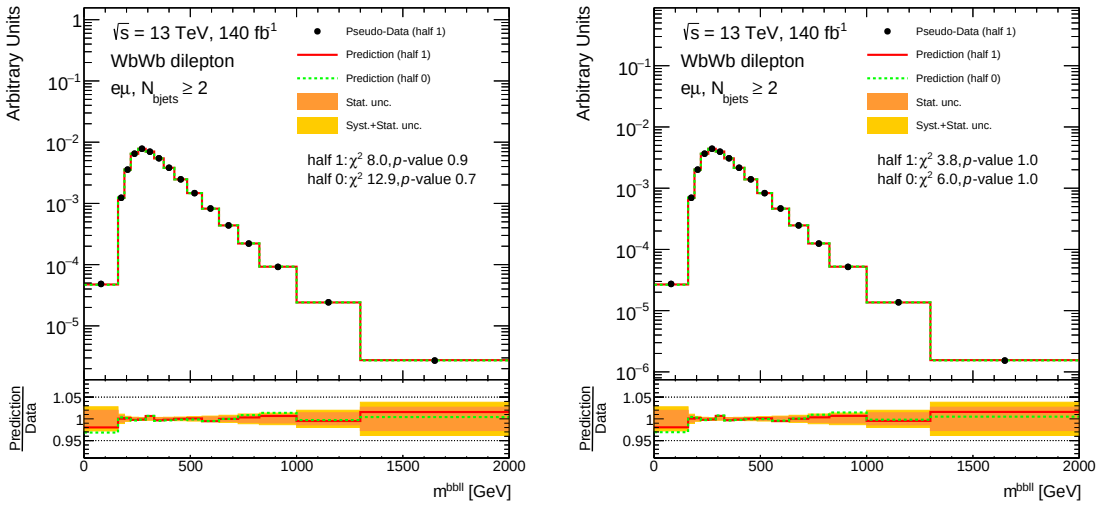

Figure C.18: Unfolding closure tests for the absolute (left) and relative (right) cross-section measurement of the m_{bbll} variable. The yellow band includes both the statistical uncertainty on the pseudo-data sample (`half0`) and the uncertainty on the MC sample (`half1`).

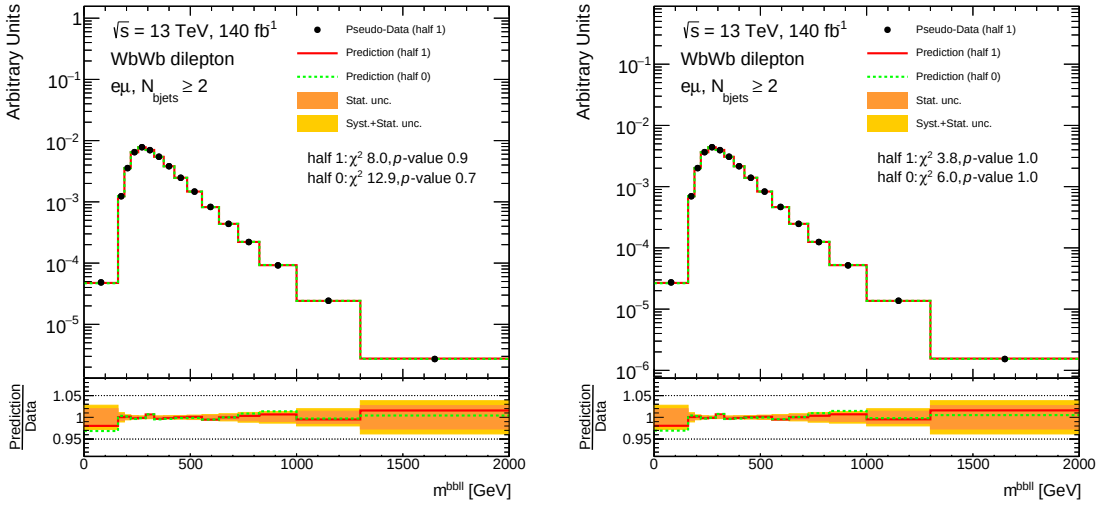

Figure C.19: Unfolding closure tests for the absolute (left) and relative (right) cross-section measurement of the m_{bbll} variable. The yellow band includes both the statistical uncertainty on the pseudo-data sample (`half0`) and the uncertainty on the MC sample (`half1`).

C.3 Other stress tests

In Figures C.20 - C.22 stress tests for the leading lepton p_{T} variable using reweighting functions based on the data/MC discrepancy for the $p_{\mathrm{T}}^{\mathrm{lep1}}$, $p_{\mathrm{T}}^{\mathrm{jet1}}$ and p_T^{bb4l} spectrums are shown.

In Figures C.23 - C.26 same tests are performed on the subleading lepton p_{T} variable.
In Figures C.27 - C.30 same tests are performed on the leading jet p_{T} variable.
In Figures C.31 - C.34 same tests are performed on the subleading jet p_{T} variable.
In Figures C.35 - C.38 same tests are performed on the p_T^{bb4l} variable.
In Figures C.39 - C.42 same tests are performed on the number of jets variable.
In Figures C.43 - C.46 same tests are performed on the $m_T^{t\bar{t}}$ variable.
In Figures C.47 - C.50 same tests are performed on the p_T^{b1b2} variable.
In Figures C.51 - C.54 same tests are performed on the p_T^{bbll} variable.
In Figures C.55 C.58 same tests are performed on the m^{bbll} variable.

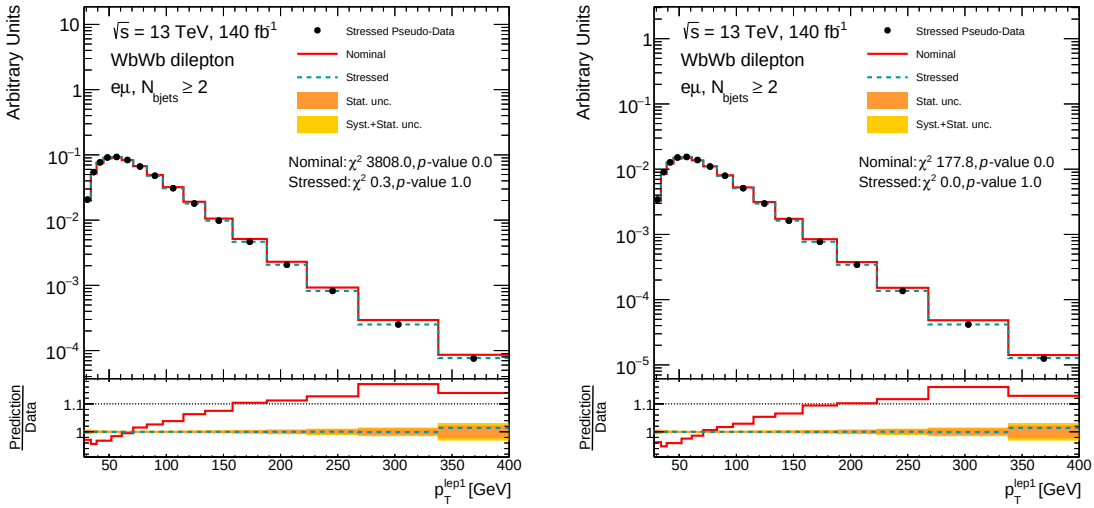

Figure C.20: Unfolding stress tests for the absolute (left) and relative (right) cross-section measurement of the leading lepton p_{T} variable using the leading lepton p_{T} reweighting function. The yellow band includes both the statistical uncertainty on the pseudo-data sample and the uncertainty on the MC sample.

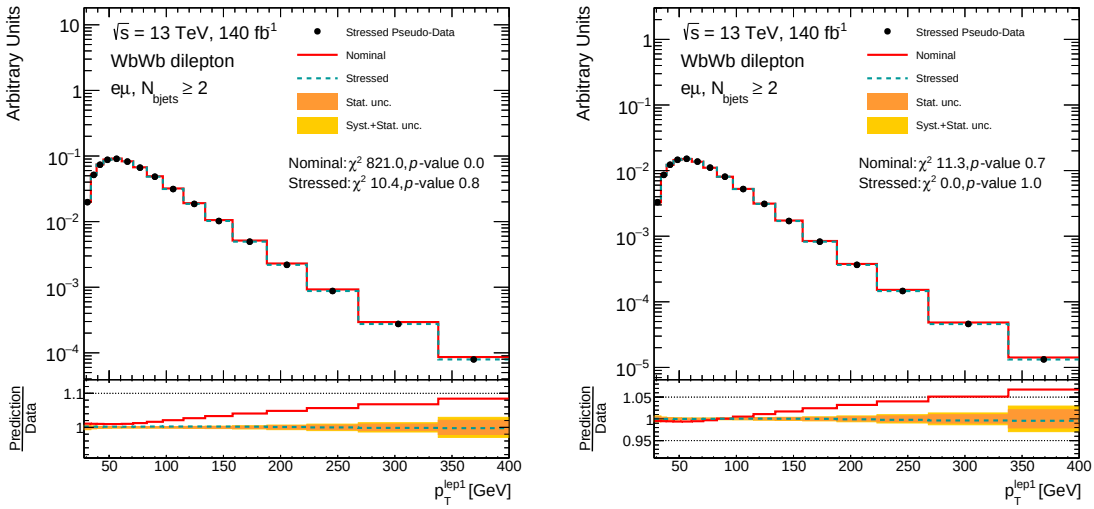

Figure C.21: Unfolding stress tests for the absolute (left) and relative (right) cross-section measurement of the leading lepton p_{T} variable using the leading jet p_{T} reweighting function. The yellow band includes both the statistical uncertainty on the pseudo-data sample and the uncertainty on the MC sample.

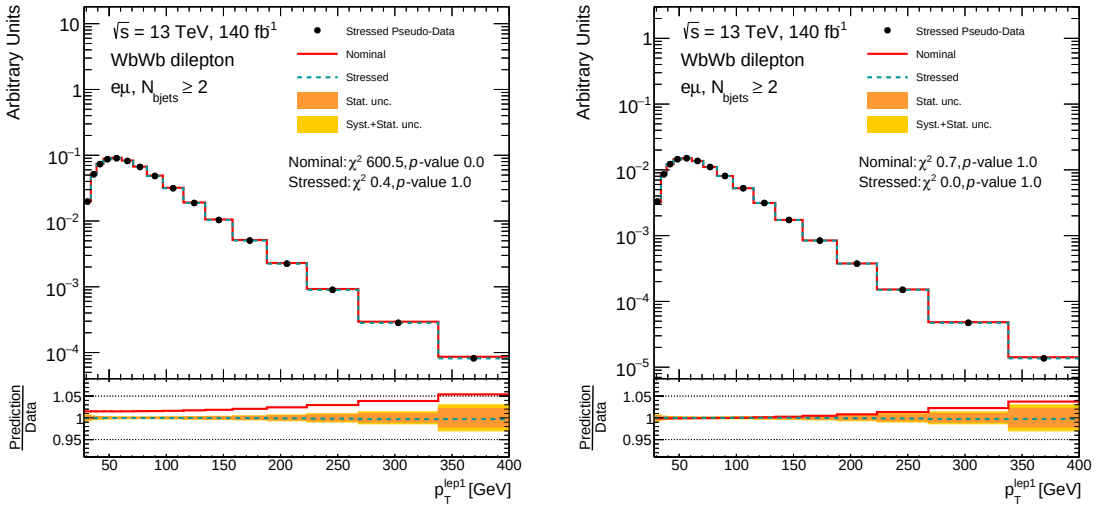

Figure C.22: Unfolding stress tests for the absolute (left) and relative (right) cross-section measurement of the leading lepton p_{T} variable using the p_T^{bb4l} reweighting function. The yellow band includes both the statistical uncertainty on the pseudo-data sample and the uncertainty on the MC sample.

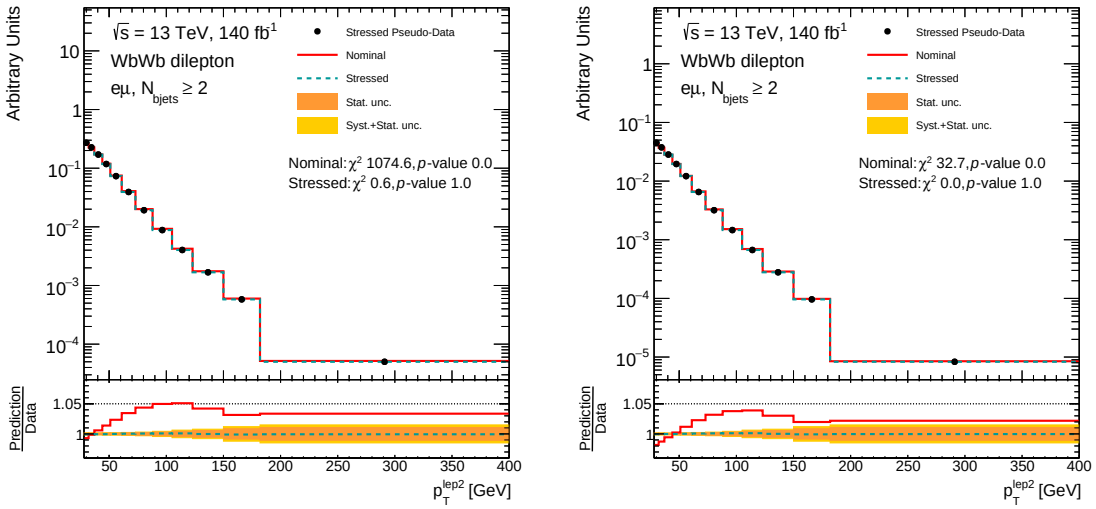

Figure C.23: Unfolding stress tests for the absolute (left) and relative (right) cross-section measurement of the subleading lepton p_{T} variable using the m_{l1l2} reweighting function. The yellow band includes both the statistical uncertainty on the pseudo-data sample and the uncertainty on the MC sample.

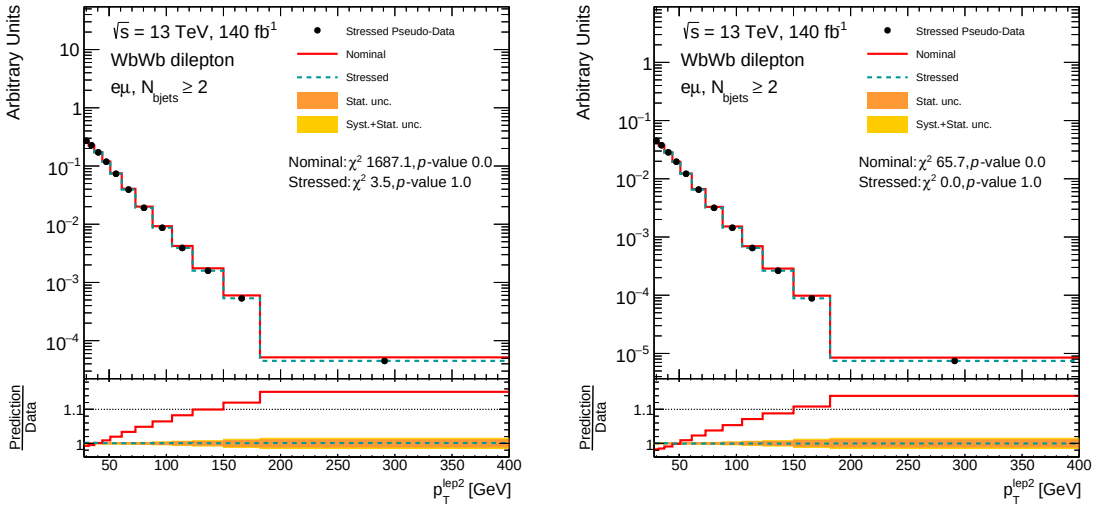

Figure C.24: Unfolding stress tests for the absolute (left) and relative (right) cross-section measurement of the subleading lepton p_{T} variable using the leading lepton p_{T} reweighting function. The yellow band includes both the statistical uncertainty on the pseudo-data sample and the uncertainty on the MC sample.

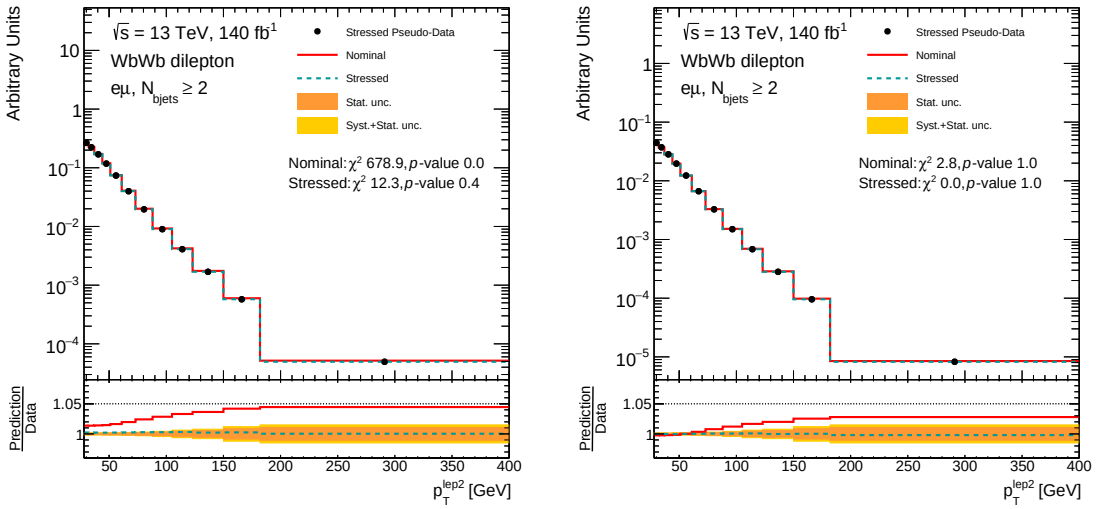

Figure C.25: Unfolding stress tests for the absolute (left) and relative (right) cross-section measurement of the subleading lepton p_{T} variable using the leading jet p_{T} reweighting function. The yellow band includes both the statistical uncertainty on the pseudo-data sample and the uncertainty on the MC sample.

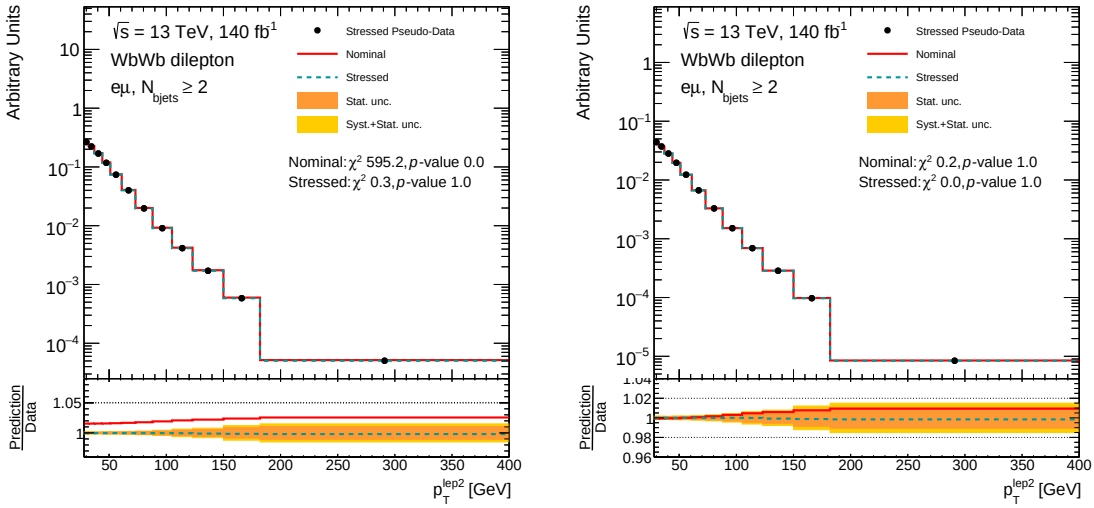

Figure C.26: Unfolding stress tests for the absolute (left) and relative (right) cross-section measurement of the subleading lepton p_{T} variable using the p_T^{bb4l} reweighting function. The yellow band includes both the statistical uncertainty on the pseudo-data sample and the uncertainty on the MC sample.

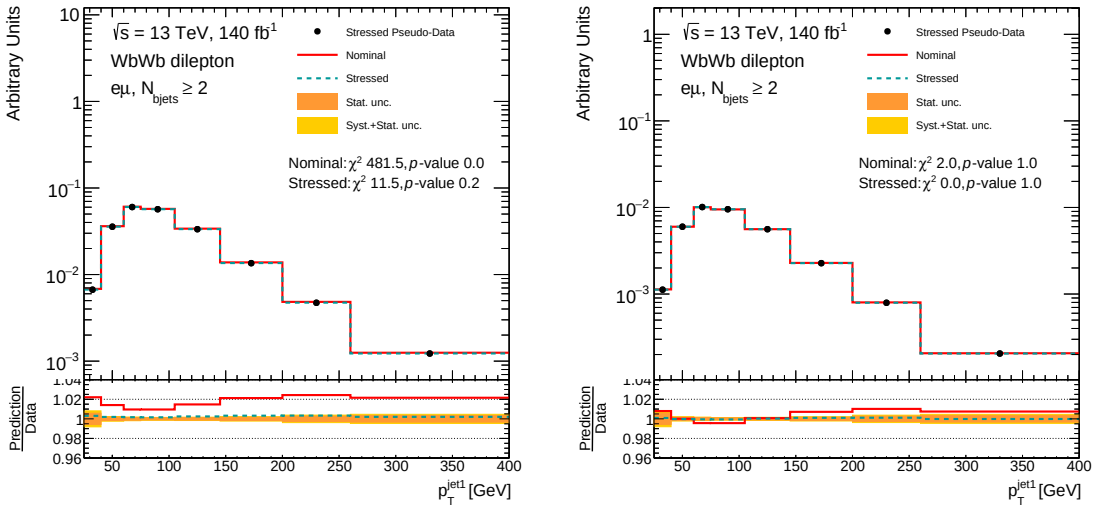

Figure C.27: Unfolding stress tests for the absolute (left) and relative (right) cross-section measurement of the leading jet p_{T} variable using the m_{l1l2} reweighting function. The yellow band includes both the statistical uncertainty on the pseudo-data sample and the uncertainty on the MC sample.

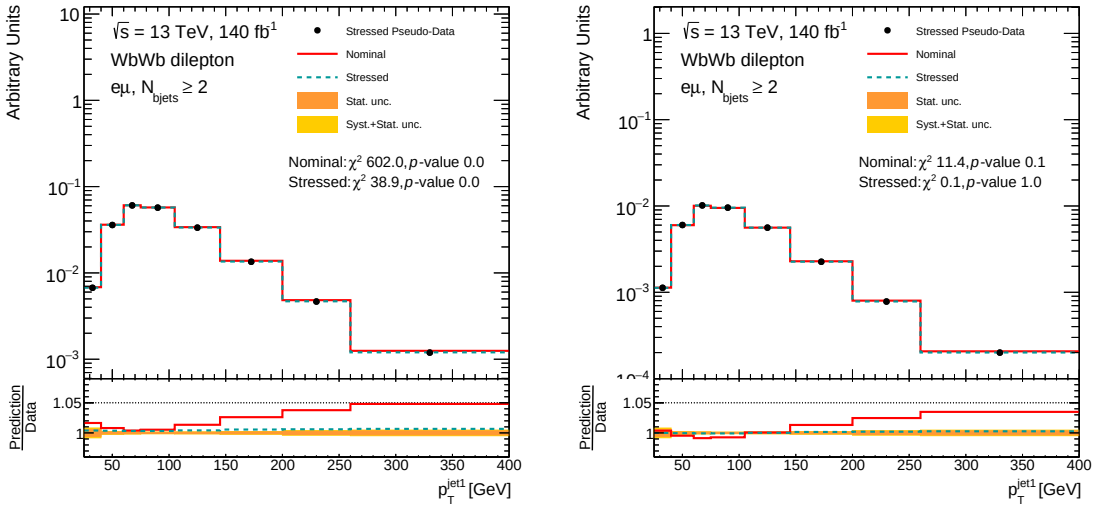

Figure C.28: Unfolding stress tests for the absolute (left) and relative (right) cross-section measurement of the leading jet p_{T} variable using the leading lepton p_{T} reweighting function. The yellow band includes both the statistical uncertainty on the pseudo-data sample and the uncertainty on the MC sample.

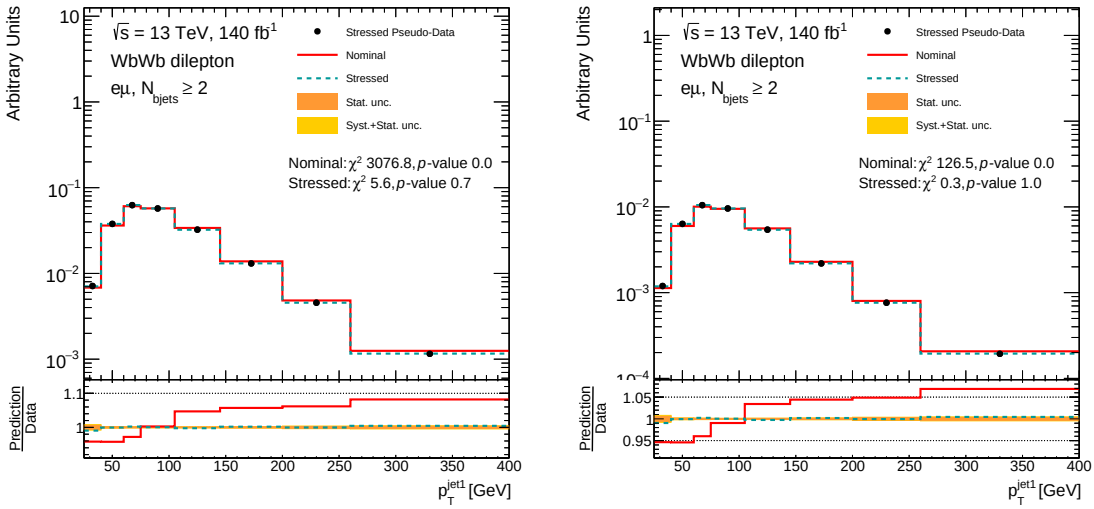

Figure C.29: Unfolding stress tests for the absolute (left) and relative (right) cross-section measurement of the leading jet p_{T} variable using the leading jet p_{T} reweighting function. The yellow band includes both the statistical uncertainty on the pseudo-data sample and the uncertainty on the MC sample.

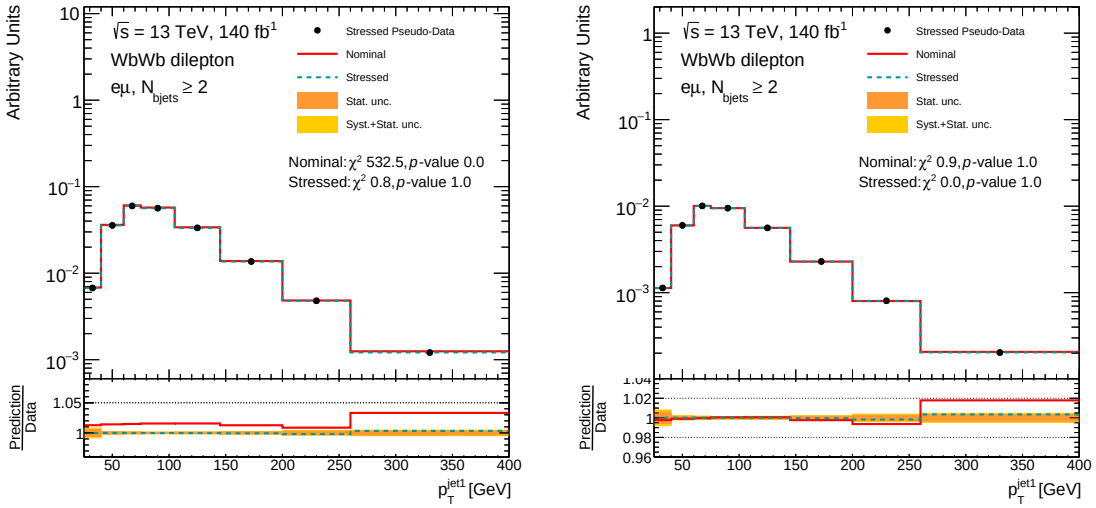

Figure C.30: Unfolding stress tests for the absolute (left) and relative (right) cross-section measurement of the leading jet p_{T} variable using the p_T^{bb4l} reweighting function. The yellow band includes both the statistical uncertainty on the pseudo-data sample and the uncertainty on the MC sample.

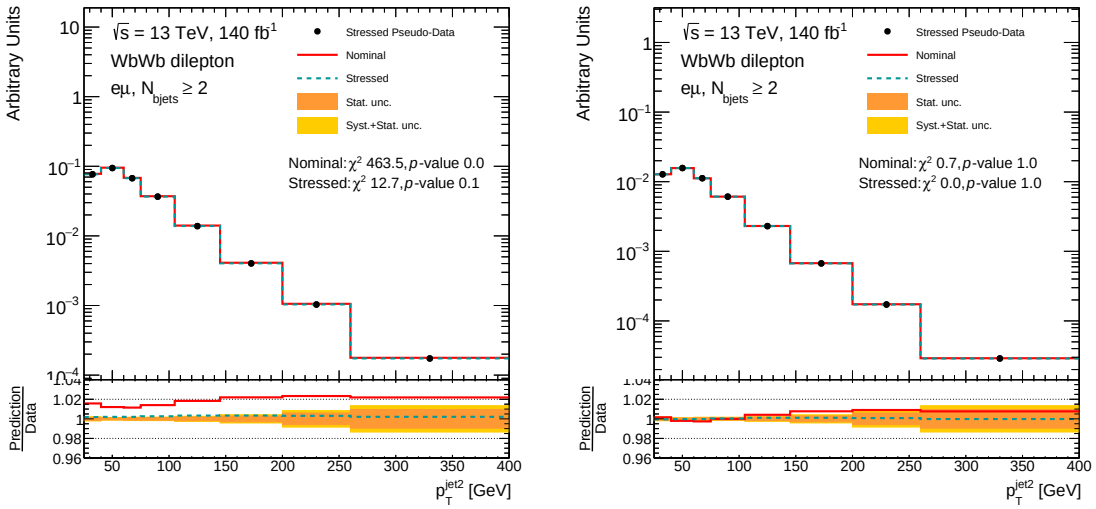

Figure C.31: Unfolding stress tests for the absolute (left) and relative (right) cross-section measurement of the subleading jet p_{T} variable using the m_{l1l2} reweighting function. The yellow band includes both the statistical uncertainty on the pseudo-data sample and the uncertainty on the MC sample.

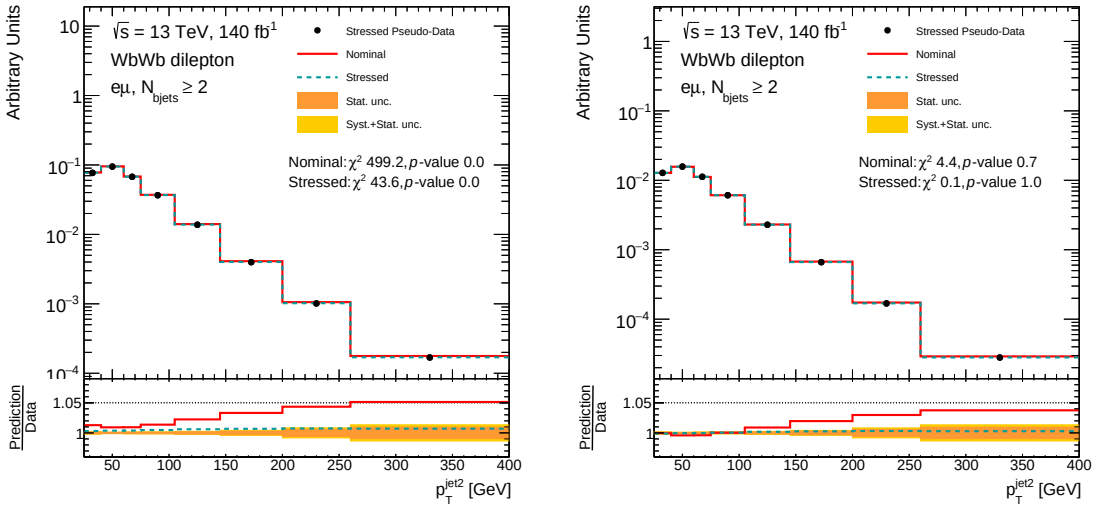

Figure C.32: Unfolding stress tests for the absolute (left) and relative (right) cross-section measurement of the subleading jet p_{T} variable using the leading lepton p_{T} reweighting function. The yellow band includes both the statistical uncertainty on the pseudo-data sample and the uncertainty on the MC sample.

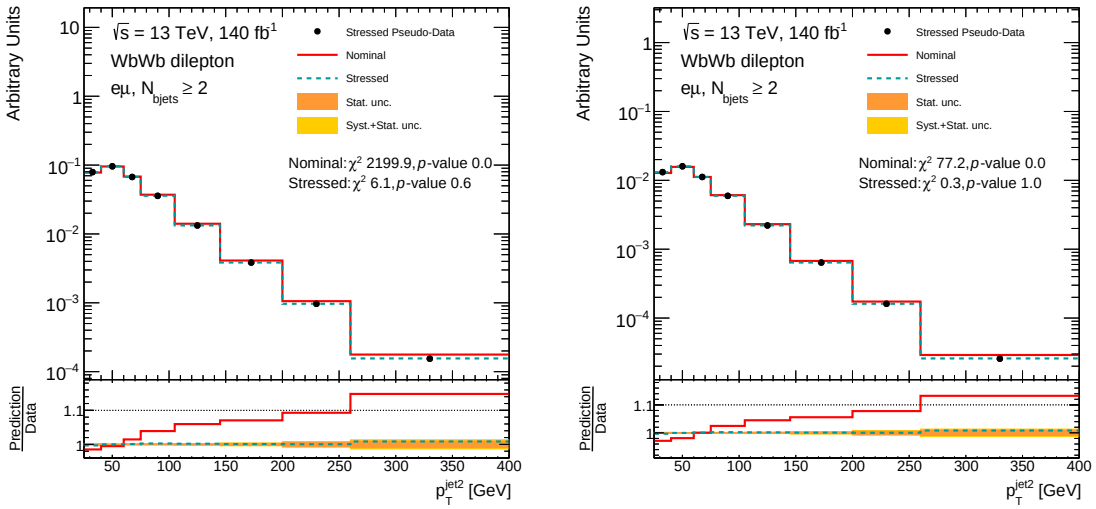

Figure C.33: Unfolding stress tests for the absolute (left) and relative (right) cross-section measurement of the subleading jet p_{T} variable using the leading jet p_{T} reweighting function. The yellow band includes both the statistical uncertainty on the pseudo-data sample and the uncertainty on the MC sample.

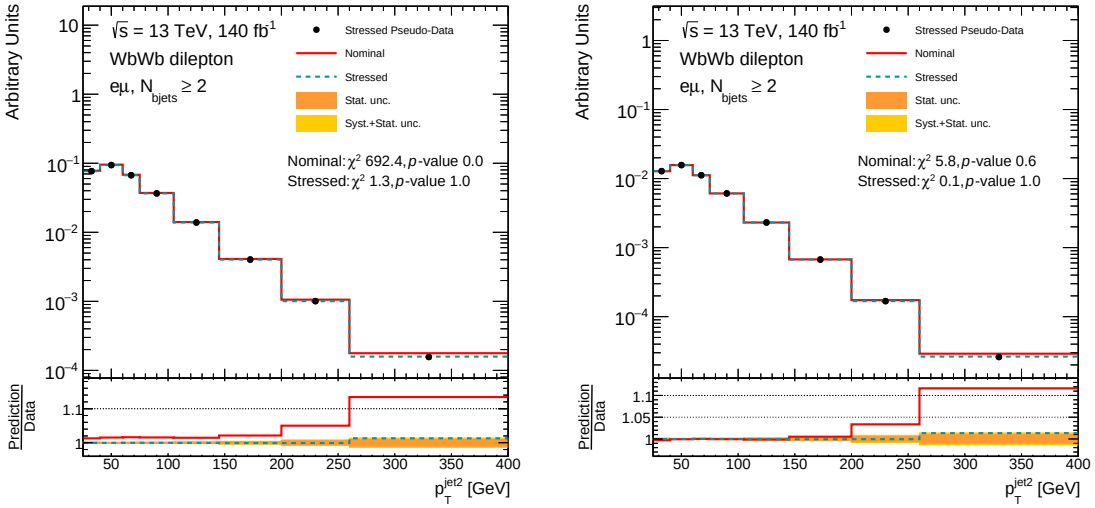

centering

Figure C.34: Unfolding stress tests for the absolute (left) and relative (right) cross-section measurement of the subleading jet p_{T} variable using the p_T^{bb4l} reweighting function. The yellow band includes both the statistical uncertainty on the pseudo-data sample and the uncertainty on the MC sample.

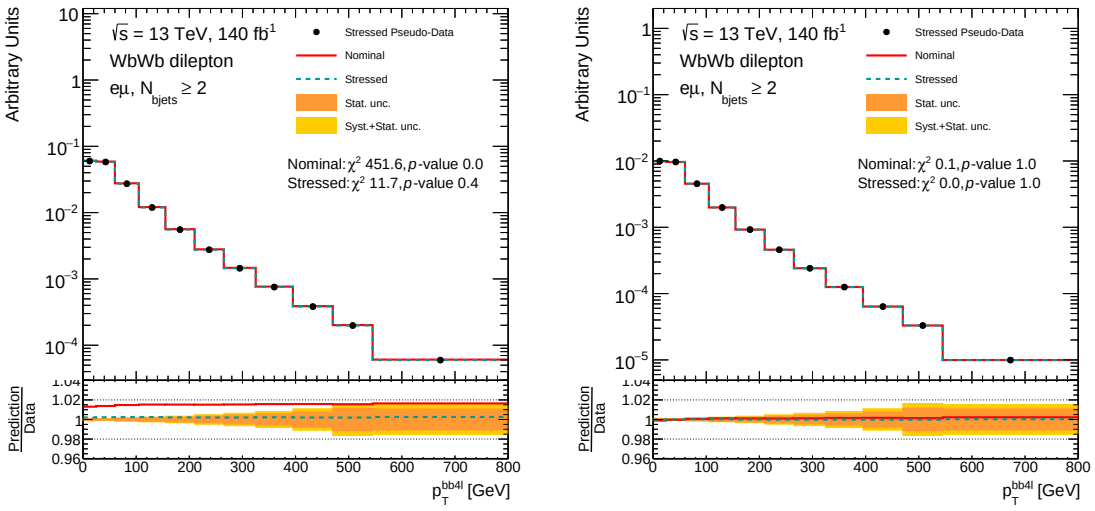

Figure C.35: Unfolding stress tests for the absolute (left) and relative (right) cross-section measurement of the p_T^{bb4l} variable using the m_{l1l2} reweighting function. The yellow band includes both the statistical uncertainty on the pseudo-data sample and the uncertainty on the MC sample.

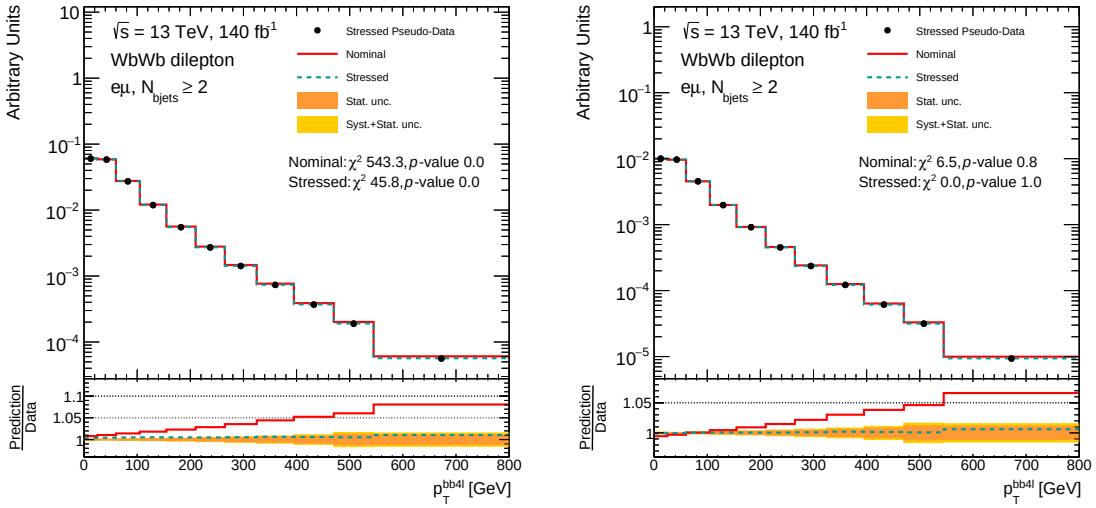

Figure C.36: Unfolding stress tests for the absolute (left) and relative (right) cross-section measurement of the p_T^{bb4l} variable using the leading lepton p_{T} reweighting function. The yellow band includes both the statistical uncertainty on the pseudo-data sample and the uncertainty on the MC sample.

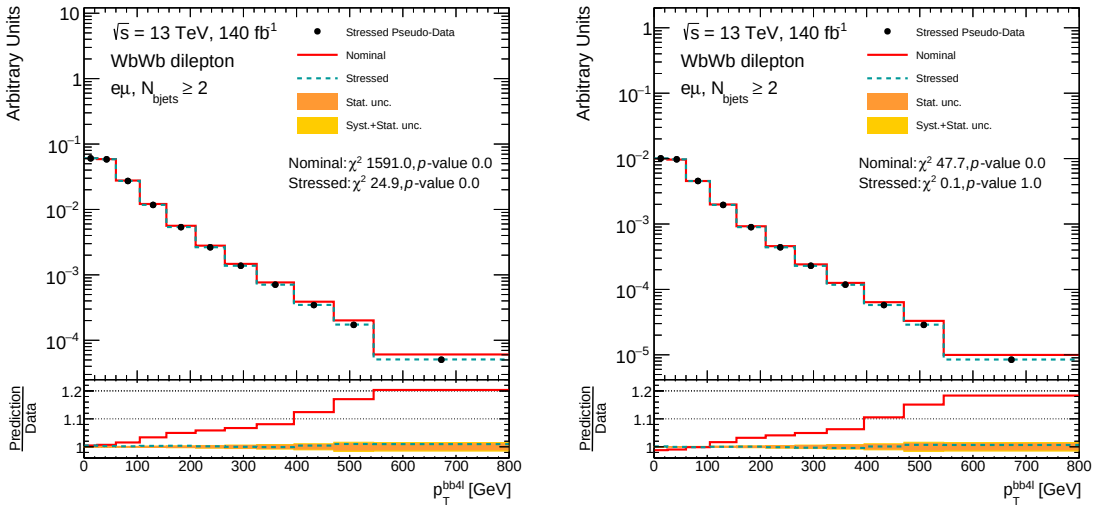

Figure C.37: Unfolding stress tests for the absolute (left) and relative (right) cross-section measurement of the p_T^{bb4l} variable using the leading jet p_{T} reweighting function. The yellow band includes both the statistical uncertainty on the pseudo-data sample and the uncertainty on the MC sample.

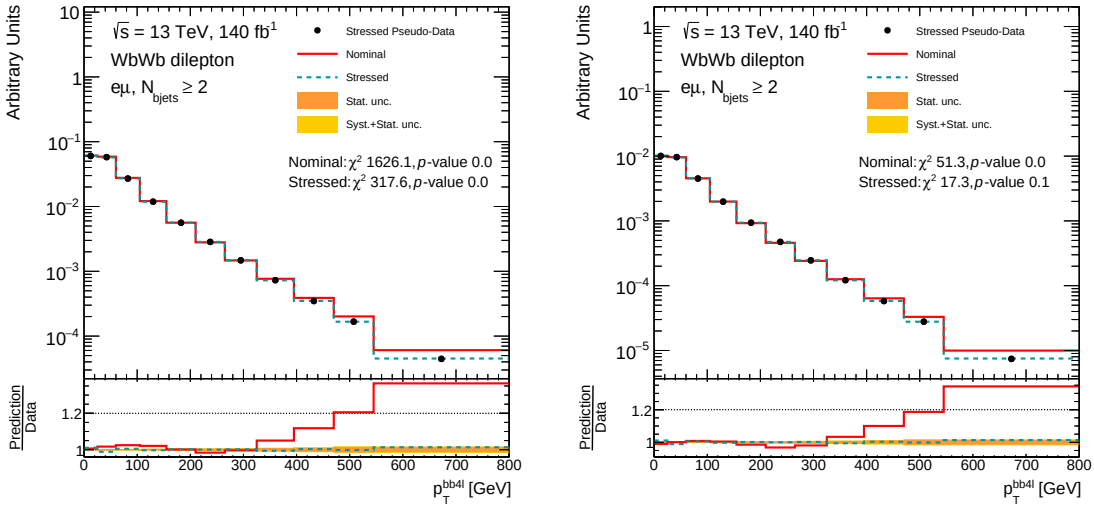

Figure C.38: Unfolding stress tests for the absolute (left) and relative (right) cross-section measurement of the p_T^{bb4l} variable using the p_T^{bb4l}reweighting function. The yellow band includes both the statistical uncertainty on the pseudo-data sample and the uncertainty on the MC sample.

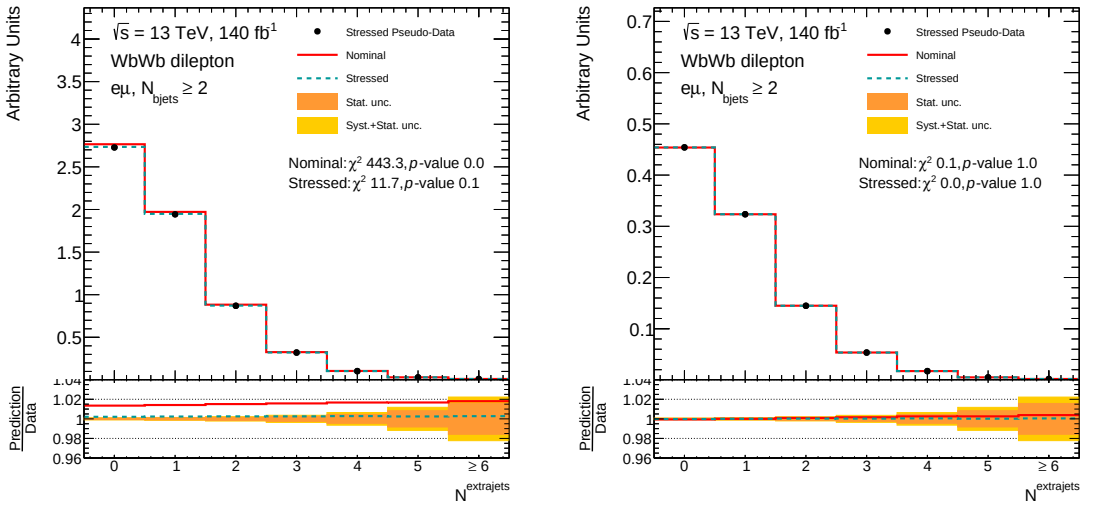

Figure C.39: Unfolding stress tests for the absolute (left) and relative (right) cross-section measurement of the number of jets variable using the m_{l1l2} reweighting function. The yellow band includes both the statistical uncertainty on the pseudo-data sample and the uncertainty on the MC sample.

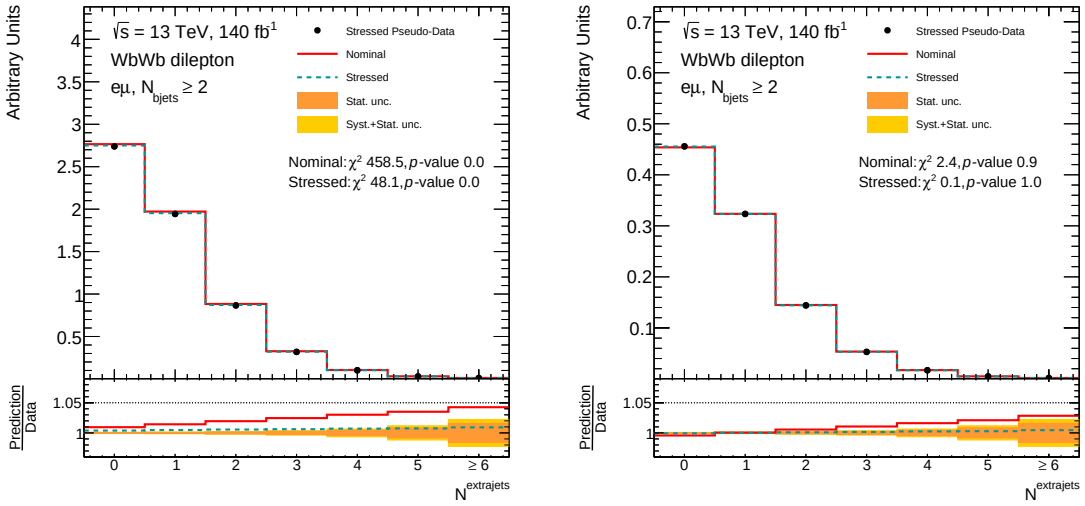

Figure C.40: Unfolding stress tests for the absolute (left) and relative (right) cross-section measurement of the number of jets variable using the leading lepton p_{T} reweighting function. The yellow band includes both the statistical uncertainty on the pseudo-data sample and the uncertainty on the MC sample.

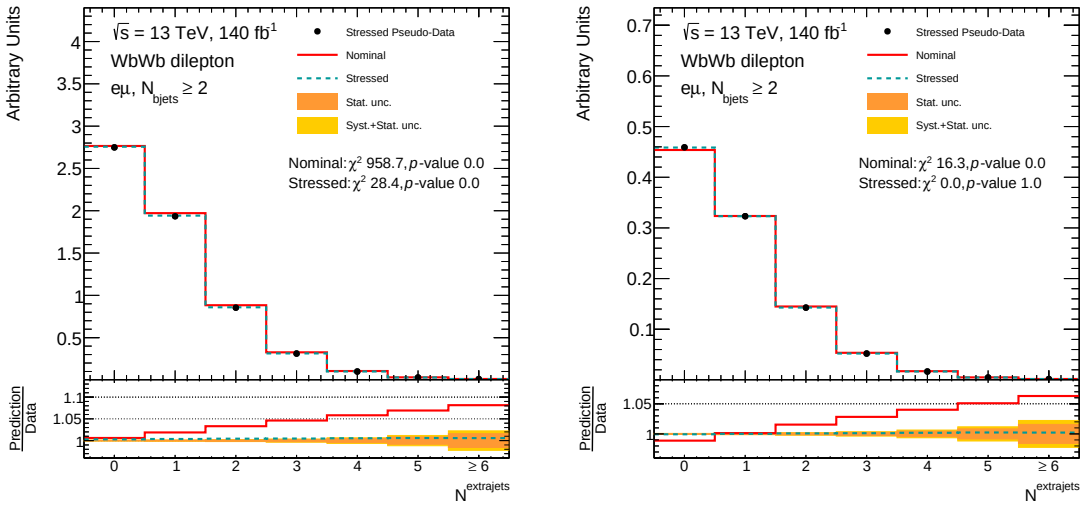

Figure C.41: Unfolding stress tests for the absolute (left) and relative (right) cross-section measurement of the number of jets variable using the leading jet p_{T} reweighting function. The yellow band includes both the statistical uncertainty on the pseudo-data sample and the uncertainty on the MC sample.

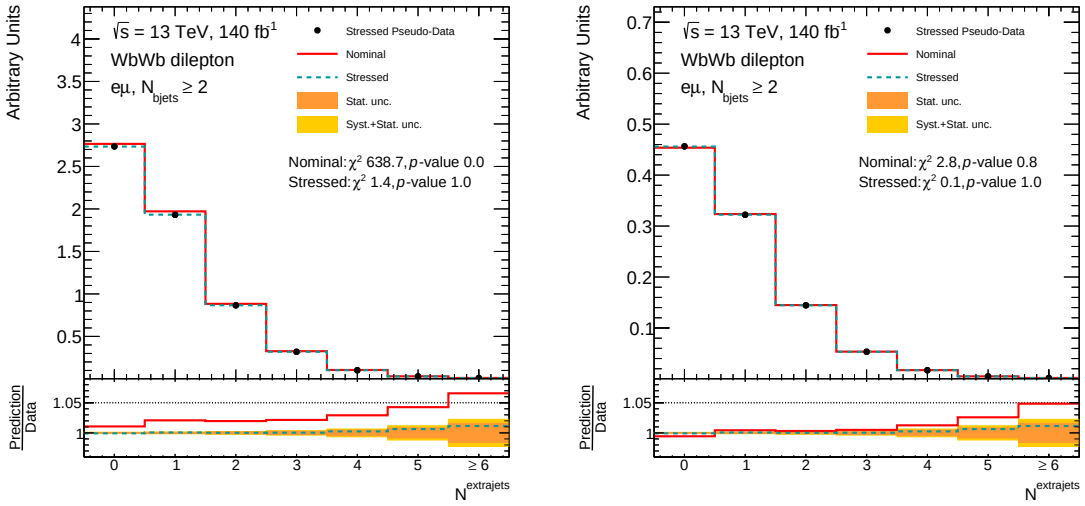

Figure C.42: Unfolding stress tests for the absolute (left) and relative (right) cross-section measurement of the number of jets variable using the p_T^{bb4l} reweighting function. The yellow band includes both the statistical uncertainty on the pseudo-data sample and the uncertainty on the MC sample.

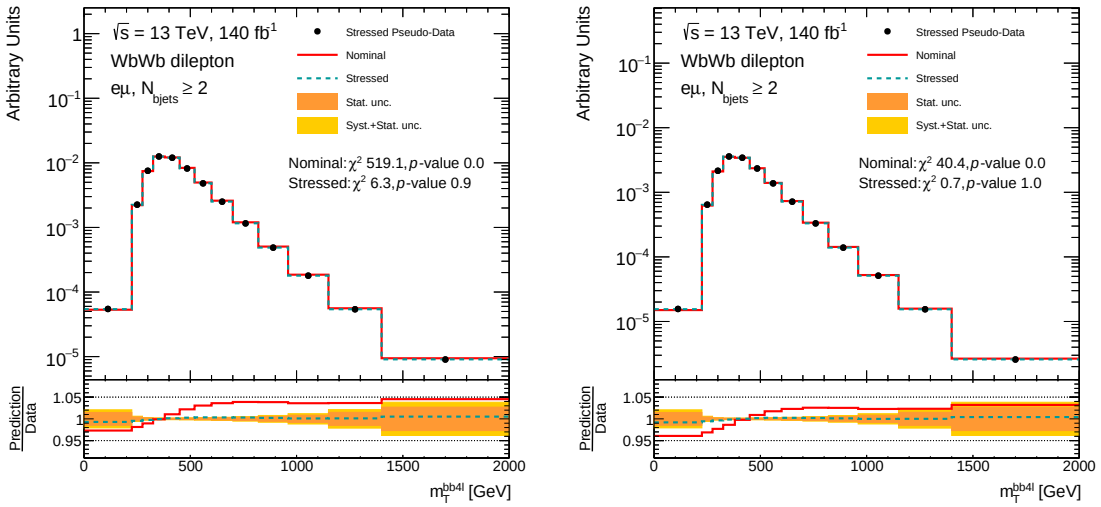

Figure C.43: Unfolding stress tests for the absolute (left) and relative (right) cross-section measurement of the $m_T^{t\bar{t}}$ variable using the m_{l1l2} reweighting function. The yellow band includes both the statistical uncertainty on the pseudo-data sample and the uncertainty on the MC sample.

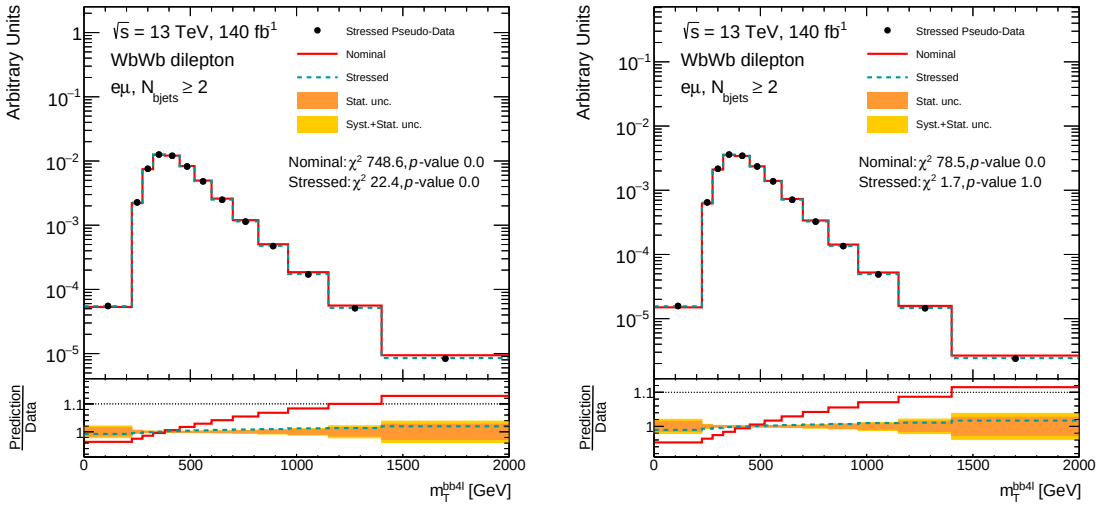

Figure C.44: Unfolding stress tests for the absolute (left) and relative (right) cross-section measurement of the $m_T^{t\bar{t}}$ variable using the leading lepton p_{T} reweighting function. The yellow band includes both the statistical uncertainty on the pseudo-data sample and the uncertainty on the MC sample.

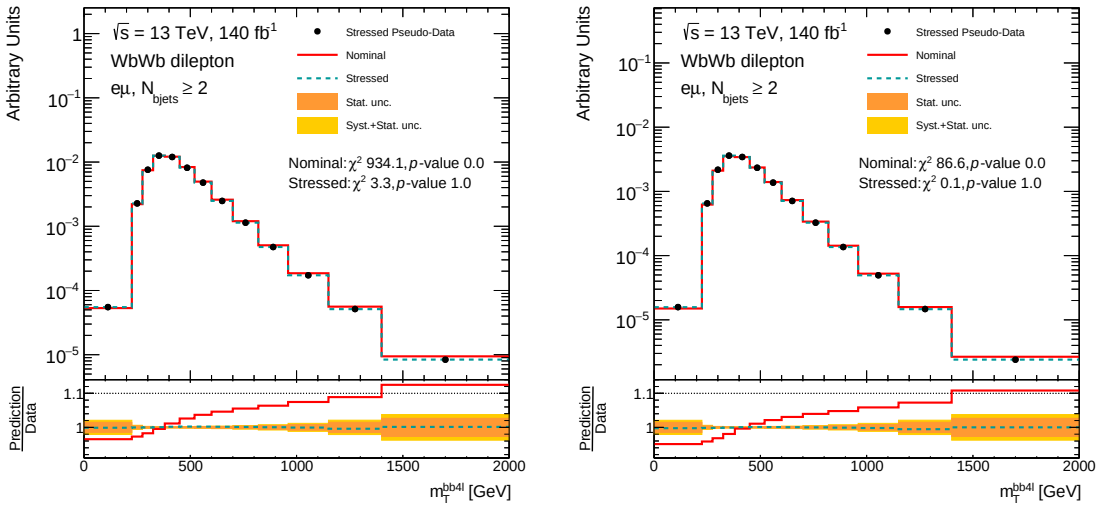

Figure C.45: Unfolding stress tests for the absolute (left) and relative (right) cross-section measurement of the $m_T^{t\bar{t}}$ variable using the leading jet p_{T} reweighting function. The yellow band includes both the statistical uncertainty on the pseudo-data sample and the uncertainty on the MC sample.

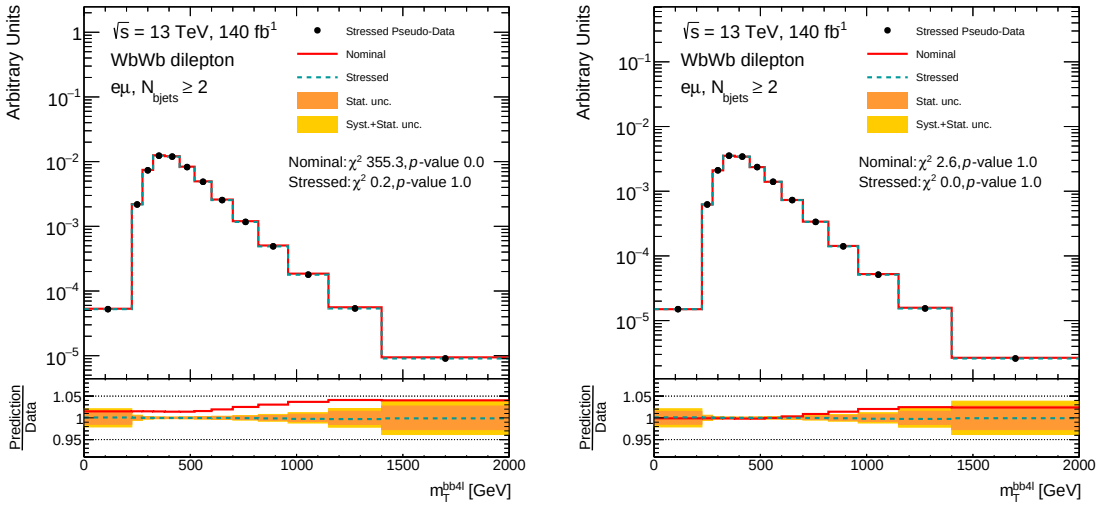

Figure C.46: Unfolding stress tests for the absolute (left) and relative (right) cross-section measurement of the $m_T^{t\bar{t}}$ variable using the p_T^{bb4l} reweighting function. The yellow band includes both the statistical uncertainty on the pseudo-data sample and the uncertainty on the MC sample.

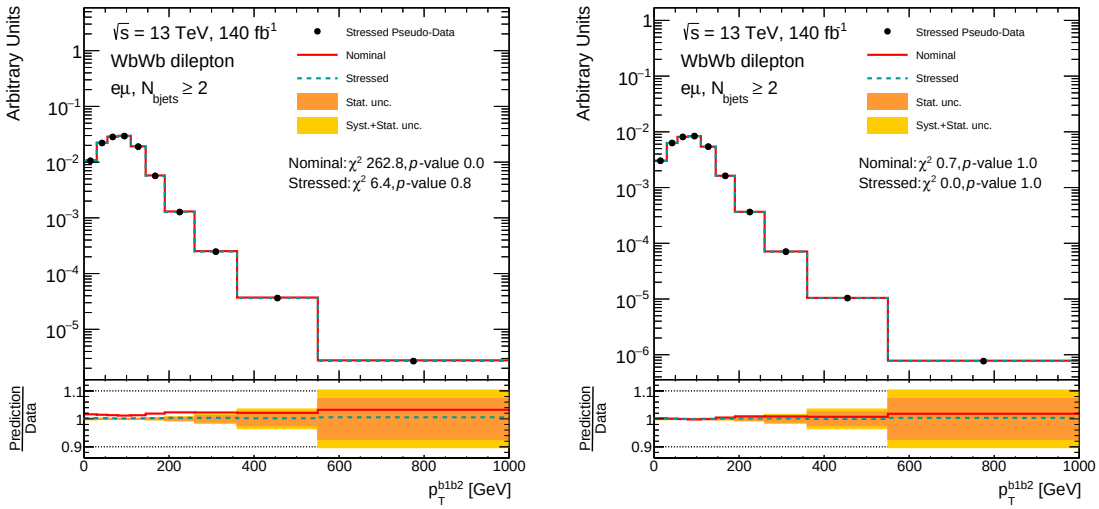

Figure C.47: Unfolding stress tests for the absolute (left) and relative (right) cross-section measurement of the p_T^{b1b2} variable using the m_{l1l2} reweighting function. The yellow band includes both the statistical uncertainty on the pseudo-data sample and the uncertainty on the MC sample.

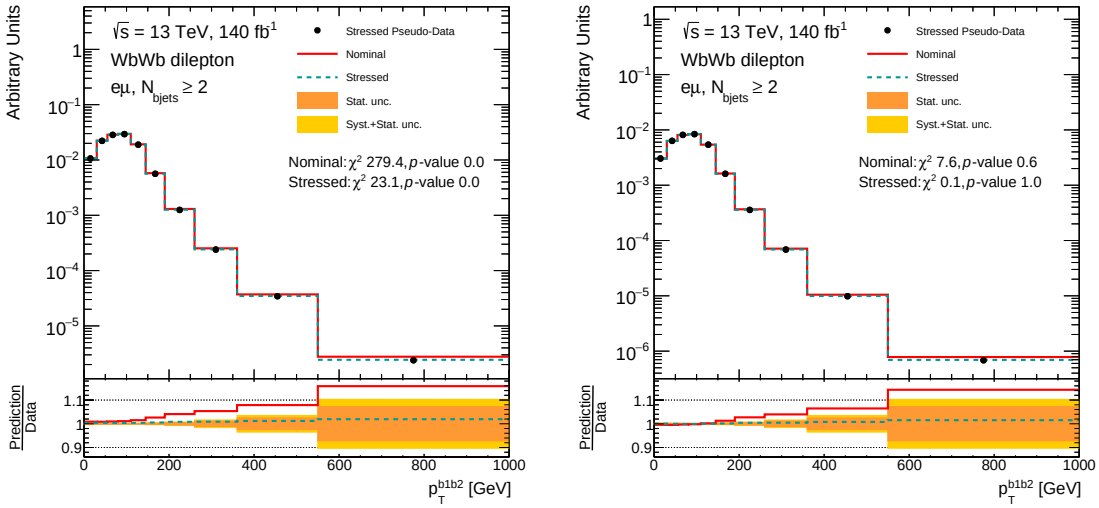

Figure C.48: Unfolding stress tests for the absolute (left) and relative (right) cross-section measurement of the p_T^{b1b2} variable using the leading lepton p_{T} reweighting function. The yellow band includes both the statistical uncertainty on the pseudo-data sample and the uncertainty on the MC sample.

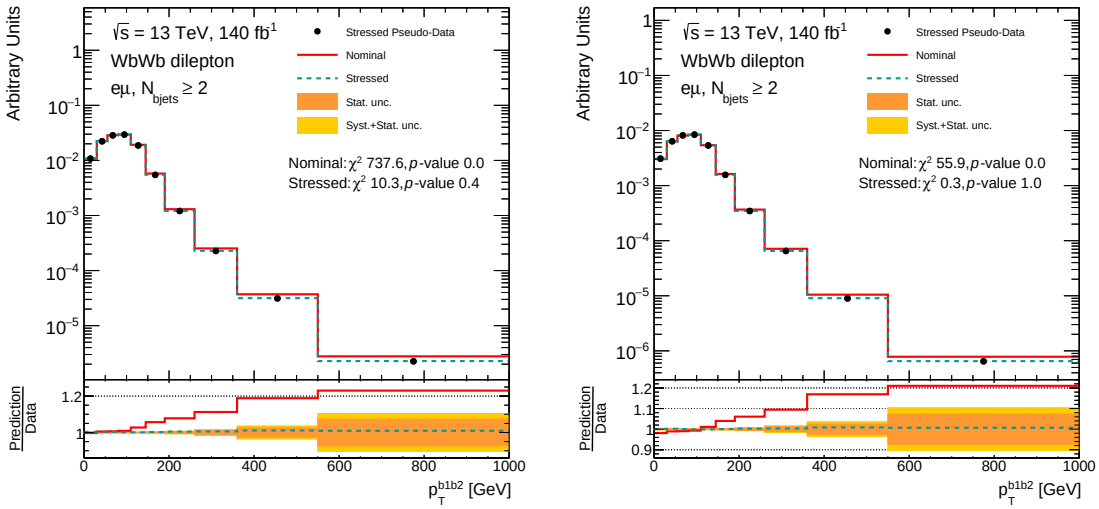

Figure C.49: Unfolding stress tests for the absolute (left) and relative (right) cross-section measurement of the p_T^{b1b2} variable using the leading jet p_{T} reweighting function. The yellow band includes both the statistical uncertainty on the pseudo-data sample and the uncertainty on the MC sample.

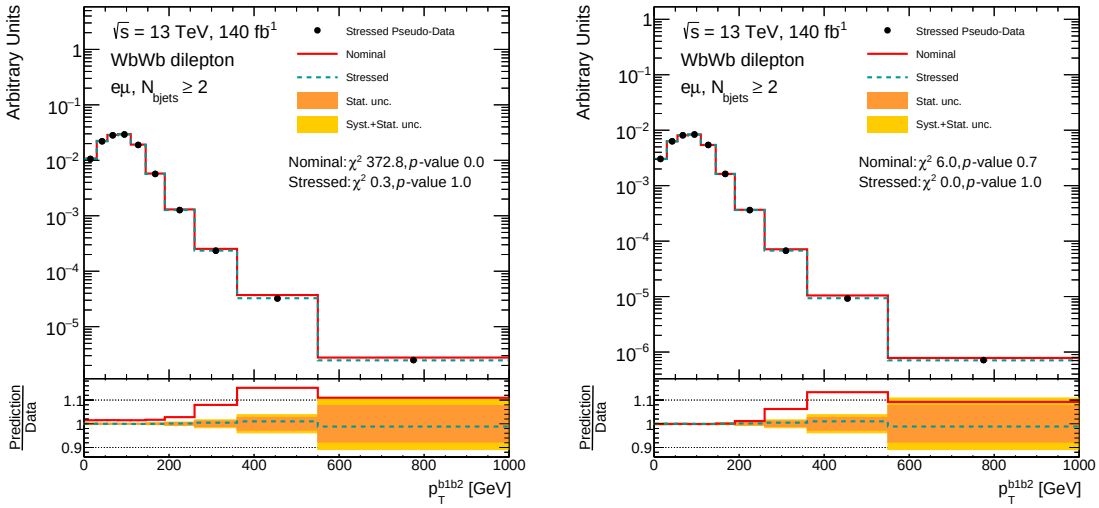

Figure C.50: Unfolding stress tests for the absolute (left) and relative (right) cross-section measurement of the p_T^{b1b2} variable using the p_T^{bb4l} reweighting function. The yellow band includes both the statistical uncertainty on the pseudo-data sample and the uncertainty on the MC sample.

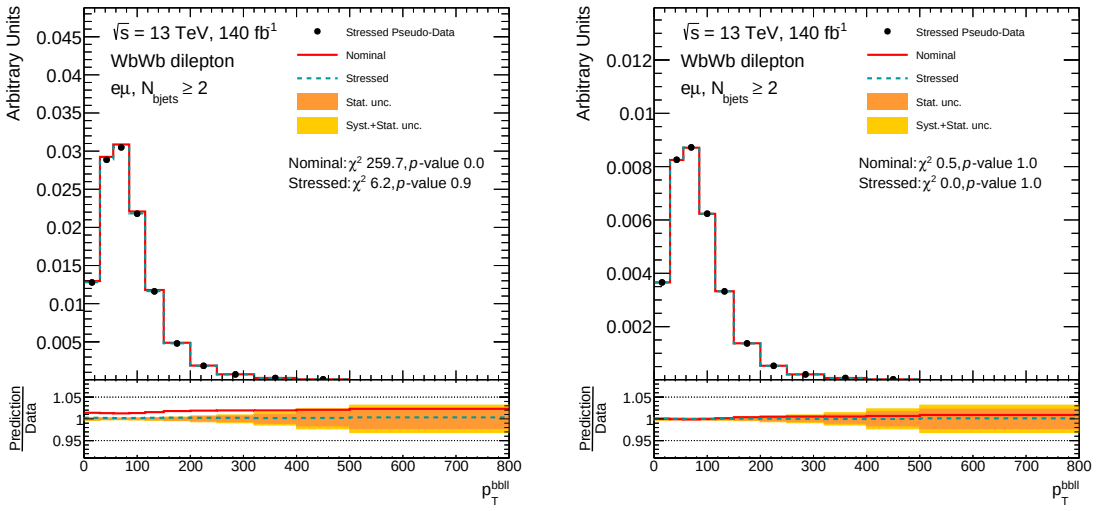

Figure C.51: Unfolding stress tests for the absolute (left) and relative (right) cross-section measurement of the p_T^{bbll} variable using the m_{l1l2} reweighting function. The yellow band includes both the statistical uncertainty on the pseudo-data sample and the uncertainty on the MC sample.

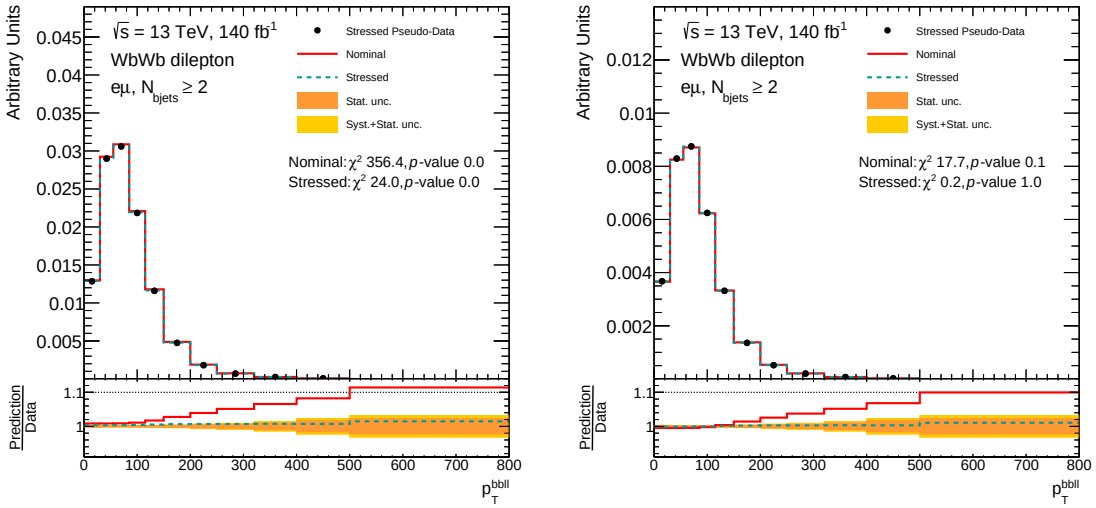

Figure C.52: Unfolding stress tests for the absolute (left) and relative (right) cross-section measurement of the p_T^{bbll} variable using the leading lepton p_{T} reweighting function. The yellow band includes both the statistical uncertainty on the pseudo-data sample and the uncertainty on the MC sample.

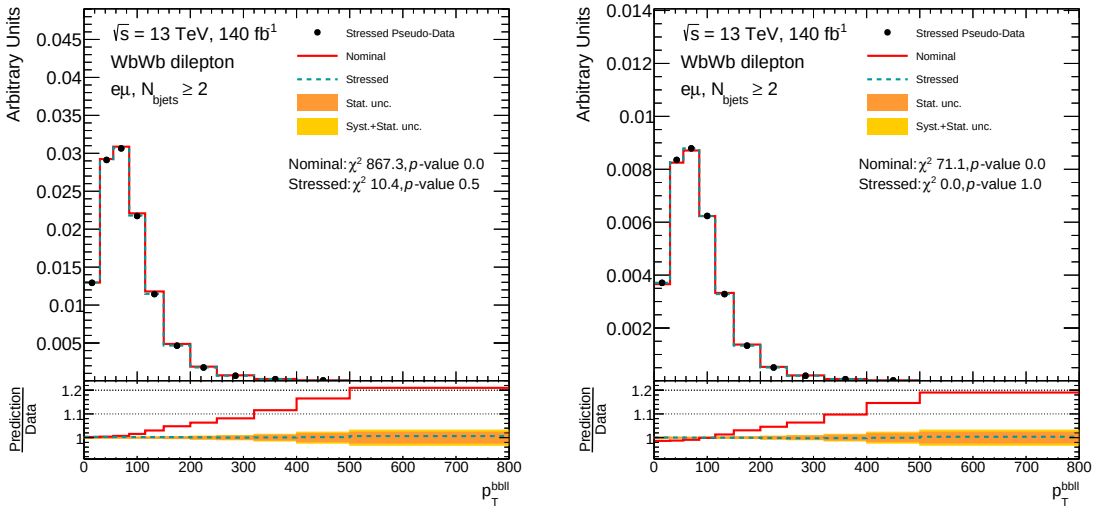

Figure C.53: Unfolding stress tests for the absolute (left) and relative (right) cross-section measurement of the p_T^{bbll} variable using the leading jet p_{T} reweighting function. The yellow band includes both the statistical uncertainty on the pseudo-data sample and the uncertainty on the MC sample.

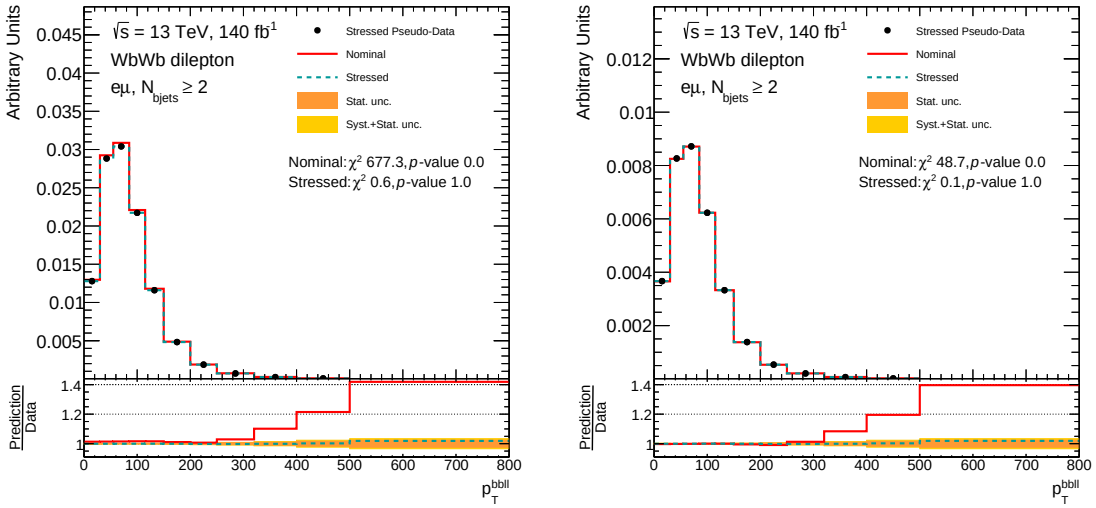

Figure C.54: Unfolding stress tests for the absolute (left) and relative (right) cross-section measurement of the p_T^{bbll} variable using the p_T^{bb4l} reweighting function. The yellow band includes both the statistical uncertainty on the pseudo-data sample and the uncertainty on the MC sample.

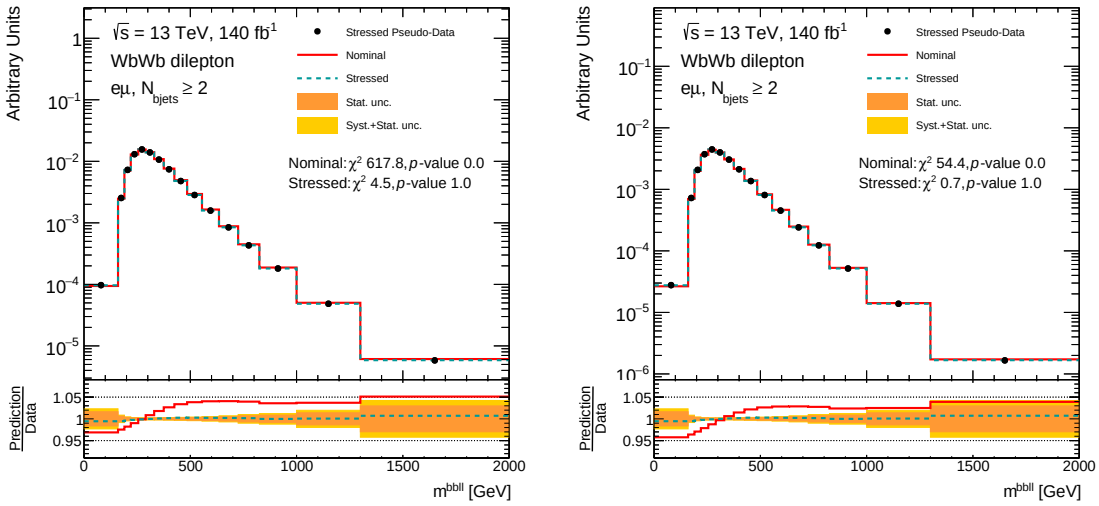

Figure C.55: Unfolding stress tests for the absolute (left) and relative (right) cross-section measurement of the m^{bbll} variable using the m_{l1l2} reweighting function. The yellow band includes both the statistical uncertainty on the pseudo-data sample and the uncertainty on the MC sample.

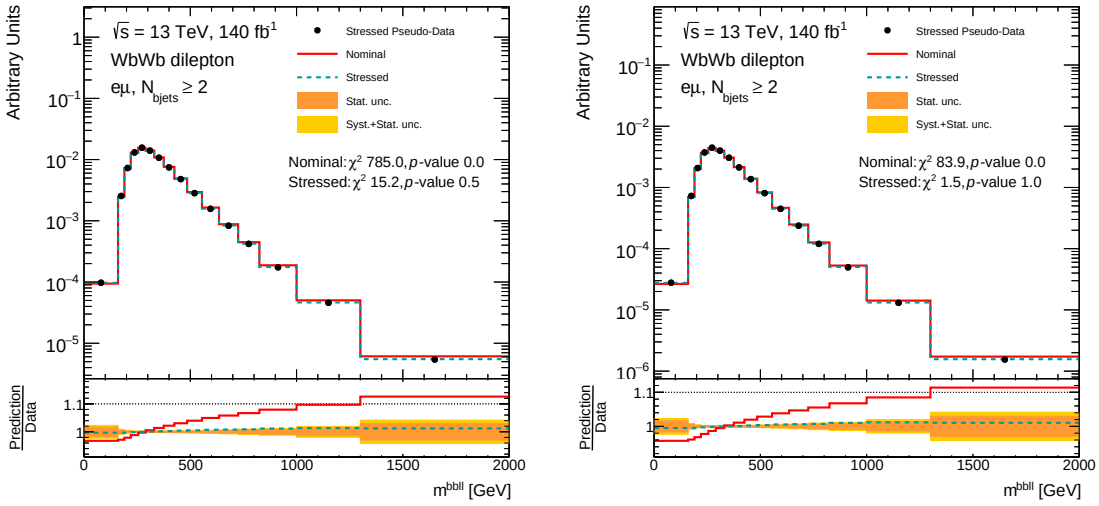

Figure C.56: Unfolding stress tests for the absolute (left) and relative (right) cross-section measurement of the m^{bbll} variable using the leading lepton p_{T} reweighting function. The yellow band includes both the statistical uncertainty on the pseudo-data sample and the uncertainty on the MC sample.

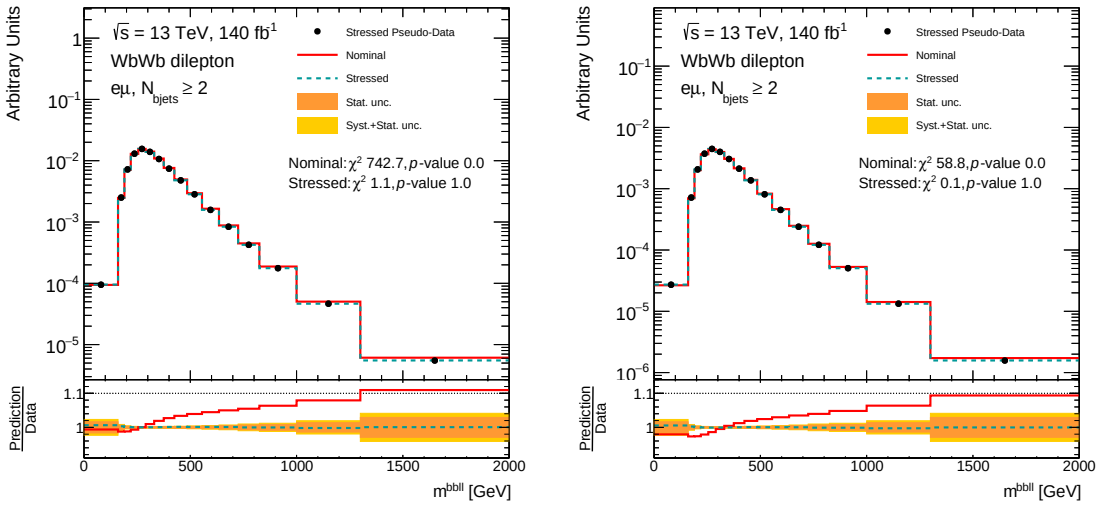

Figure C.57: Unfolding stress tests for the absolute (left) and relative (right) cross-section measurement of the m^{bbll} variable using the leading jet p_{T} reweighting function. The yellow band includes both the statistical uncertainty on the pseudo-data sample and the uncertainty on the MC sample.

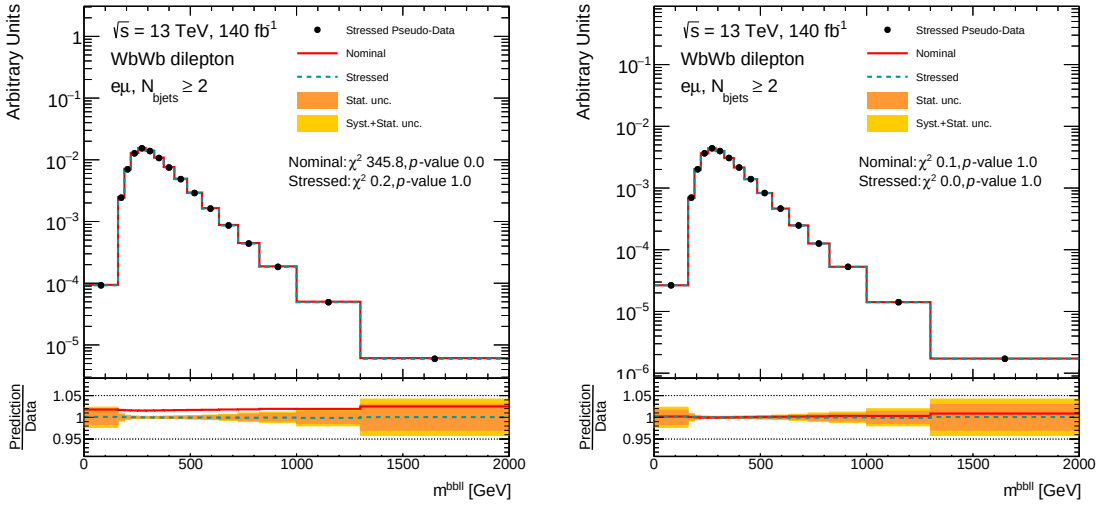

Figure C.58: Unfolding stress tests for the absolute (left) and relative (right) cross-section measurement of the m^{bbll} variable using the p_T^{bb4l} reweighting function. The yellow band includes both the statistical uncertainty on the pseudo-data sample and the uncertainty on the MC sample.

C.4 Other systematics breakdown

C.4.1 Absolute differential cross-sections

Systematics summary plots for absolute cross-sections of the $WbWb$ final-state objects are presented in Figures C.59 - C.61.

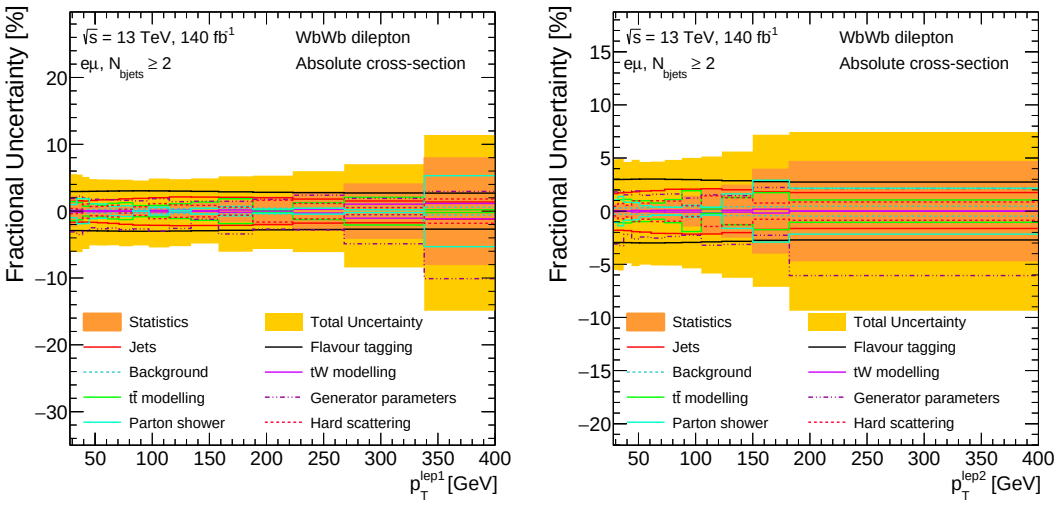

(a) (b)

Figure C.59: Uncertainties breakdown for the absolute cross-section measurement of the a leading and b subleading lepton p_{T}.

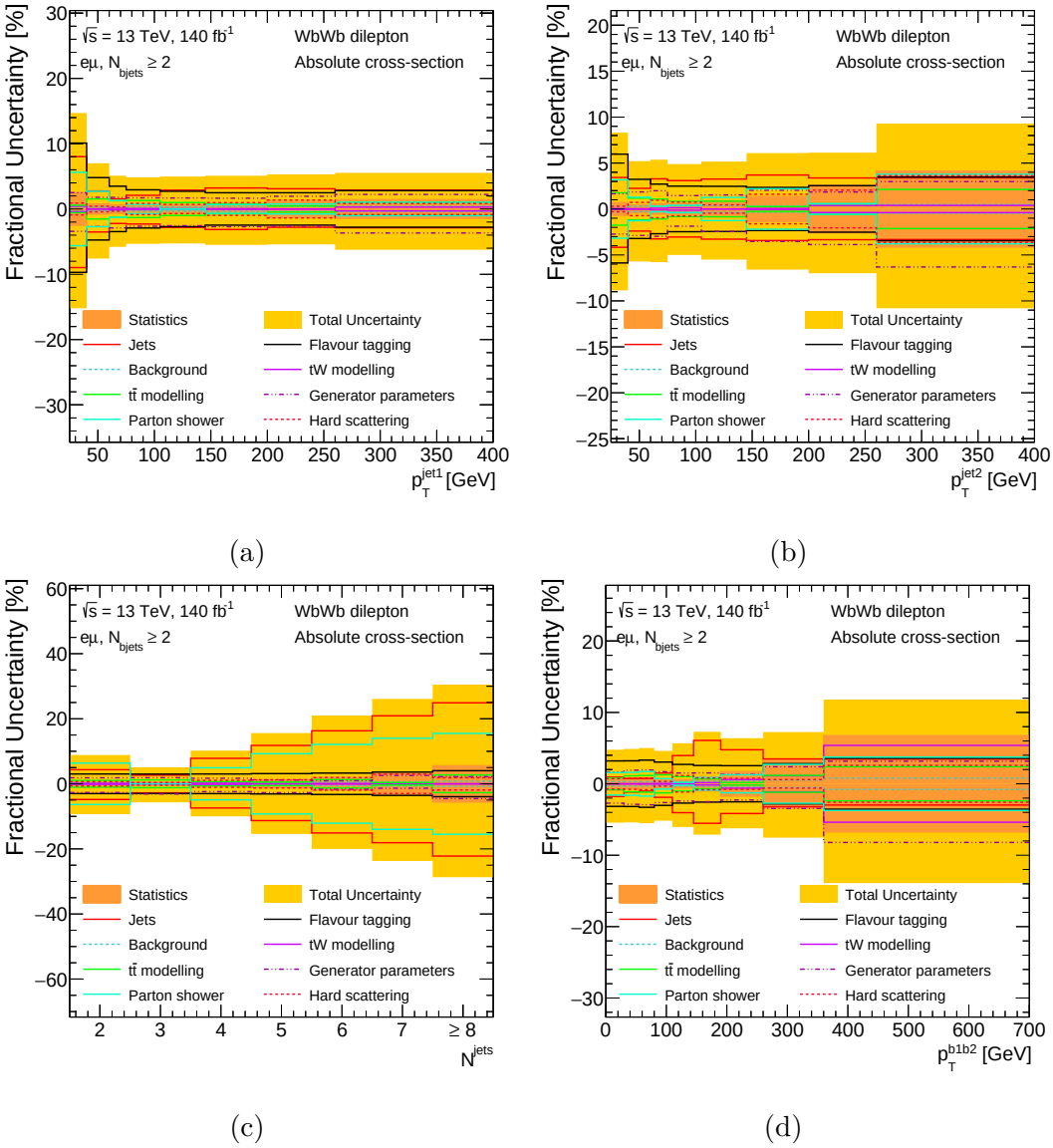

Figure C.60: Uncertainties breakdown for the absolute cross-section measurement of the a leading and b subleading jet p_{T}, c number of jets and d the p_{T} of the bb system.

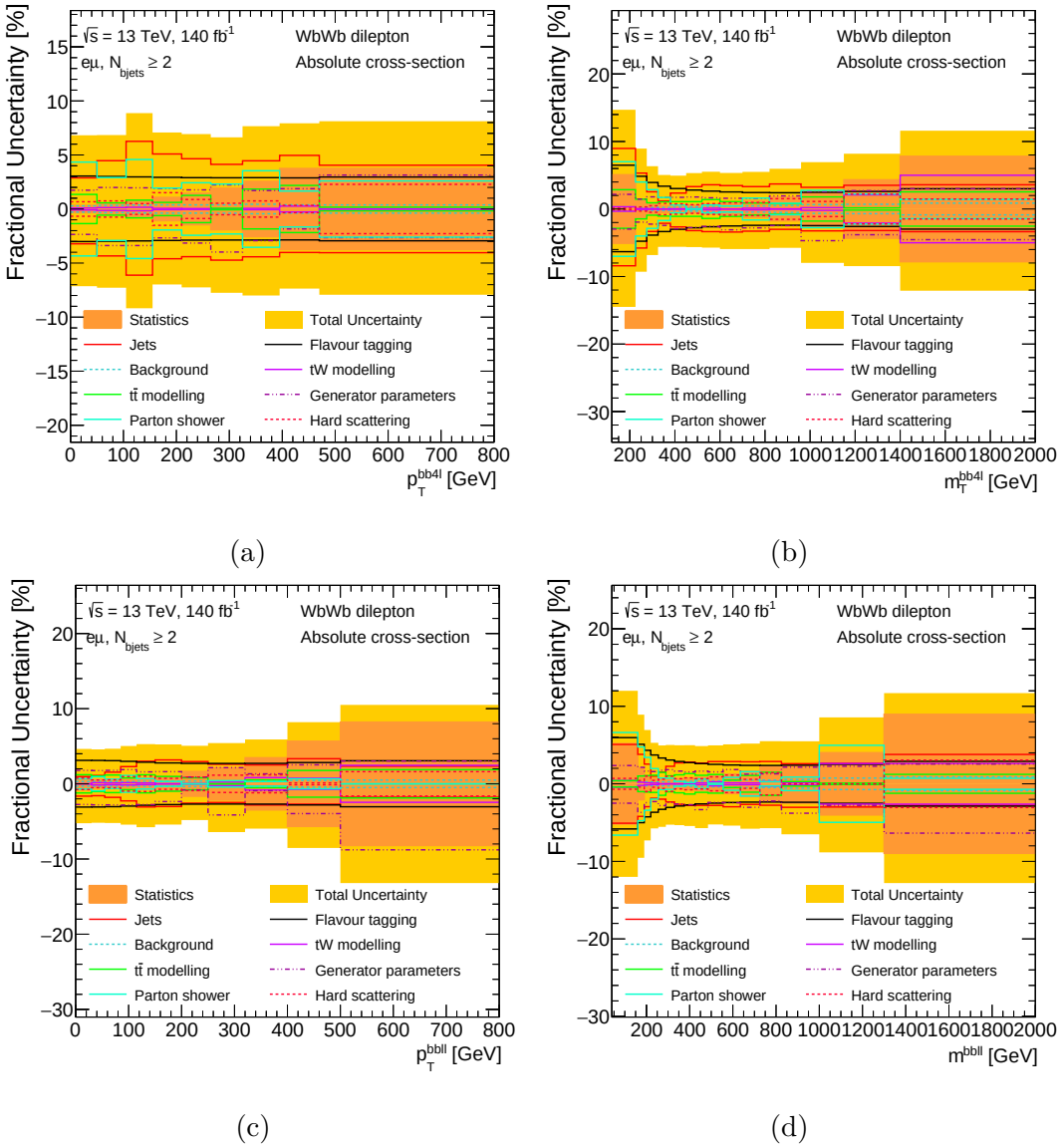

Figure C.61: Uncertainties breakdown for the absolute cross-section measurement of the a p_{T} and b m_{T} of the $bb4l$ system, and c p_{T} and d mass of the $bbll$system.

C.4.2 Relative differential cross-sections with `QUnfold`

Systematics summary plots for relative cross-sections of the $WbWb$ final-state objects measured using the `QUnfold` package are presented in Figures C.62 - C.65.

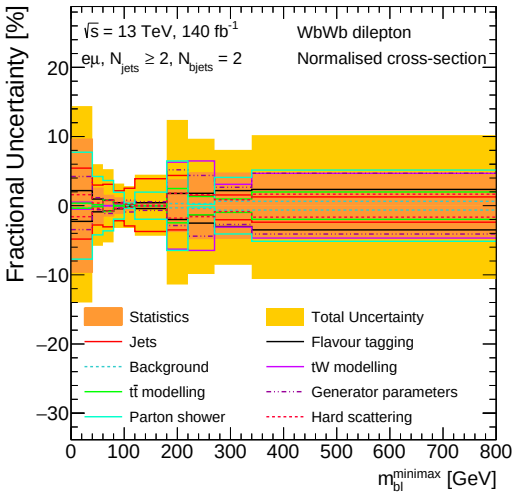

Figure C.62: Uncertainties breakdown for the relative cross-section measurement of the m^{bl}_{minimax} observable, measured using the `QUnfold` package.

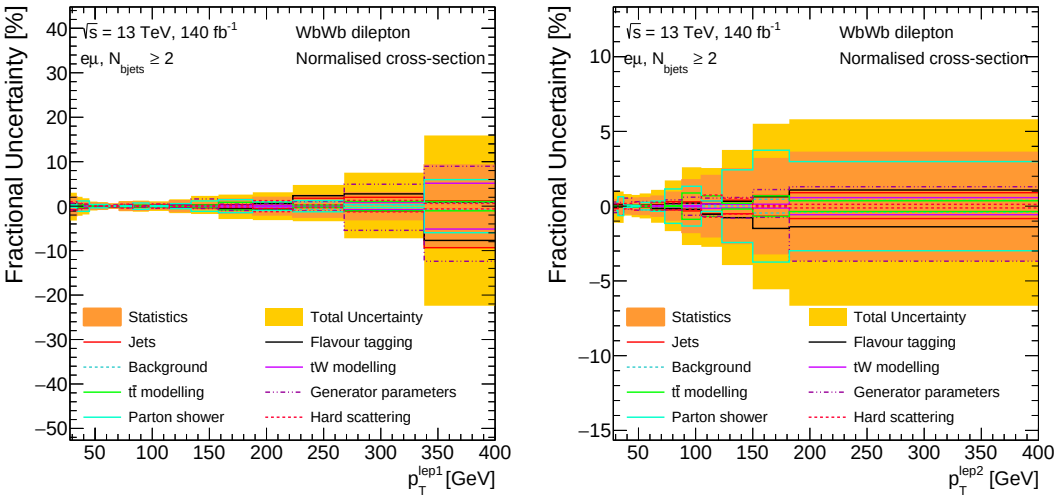

(a) (b)

Figure C.63: Uncertainties breakdown for the relative cross-section measurement of the a leading and b subleading lepton p_{T}, measured using the `QUnfold` package.

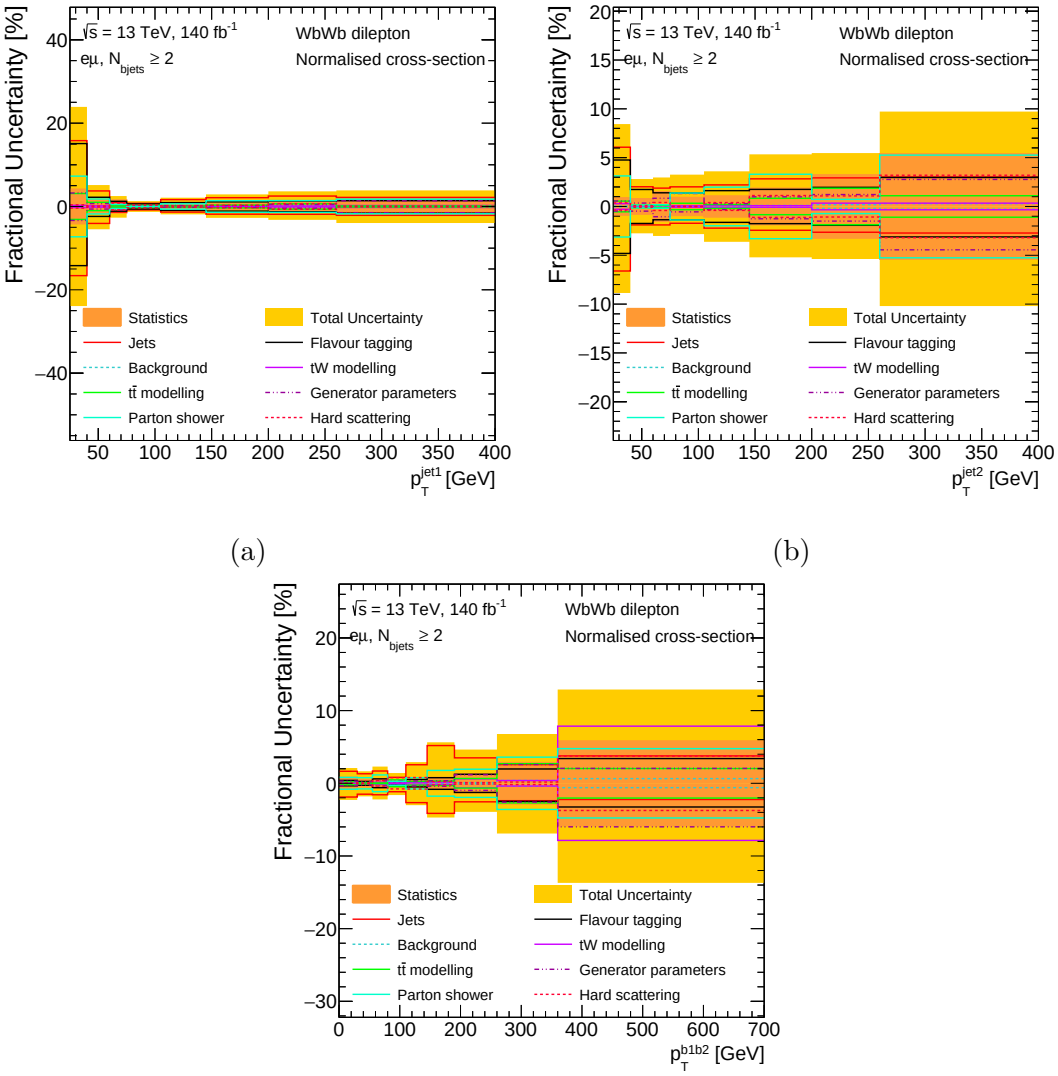

Figure C.64: Uncertainties breakdown for the relative cross-section measurement of the a leading and b subleading jet p_{T}, and c the p_{T} of the bb system, measured using the `QUnfold` package.

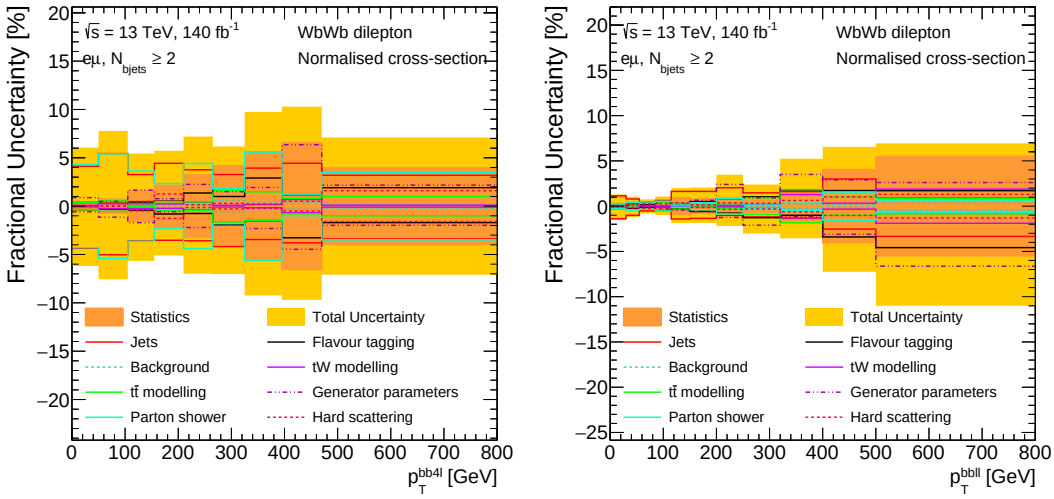

(a) (b)

Figure C.65: Uncertainties breakdown for the relative cross-section measurement of the a p_{T} of the *bb4l* system, and b p_{T} of the *bbll*system, measured using the `QUnfold` package.

C.4.3 Absolute differential cross-sections with `QUnfold`

Systematics summary plots for absolute cross-sections of the $WbWb$ final-state objects measured using the `QUnfold` package are presented in Figures C.66 - C.69.

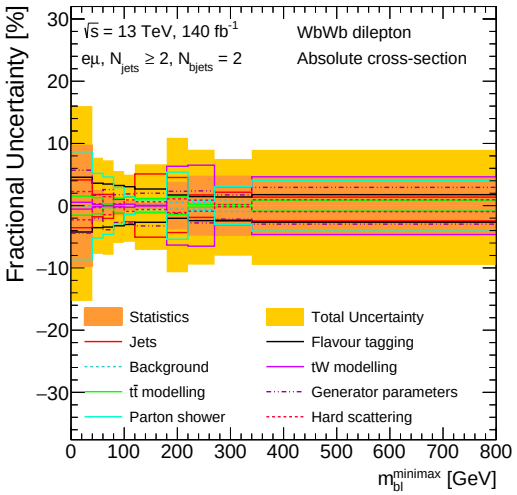

Figure C.66: Uncertainties breakdown for the absolute cross-section measurement of the m^{bl}_{minimax} observable, measured using the `QUnfold` package.

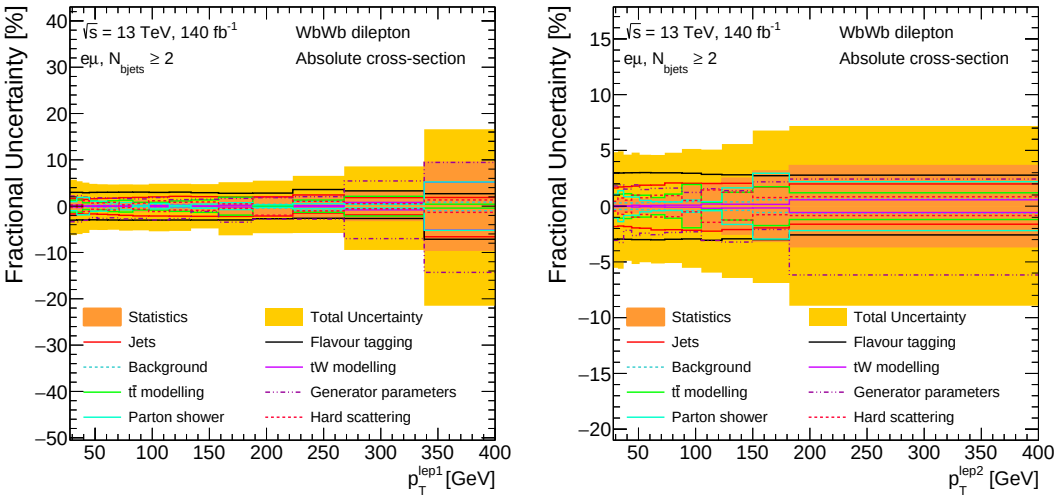

(a) (b)

Figure C.67: Uncertainties breakdown for the absolute cross-section measurement of the a leading and b subleading lepton p_{T}, measured using the `QUnfold` package.

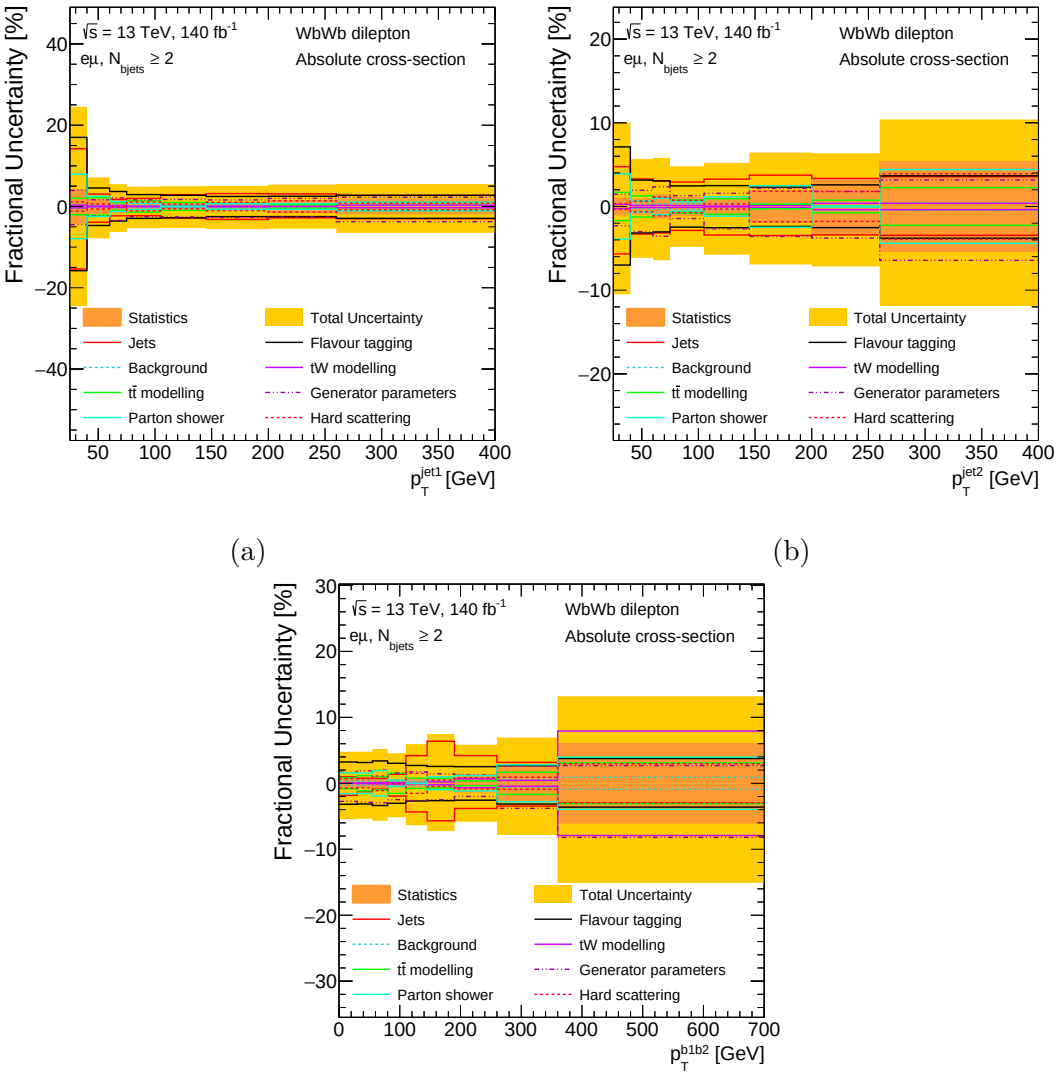

Figure C.68: Uncertainties breakdown for the absolute cross-section measurement of the a leading and b subleading jet p_{T}, and c the p_{T} of the bb system, measured using the `QUnfold` package.

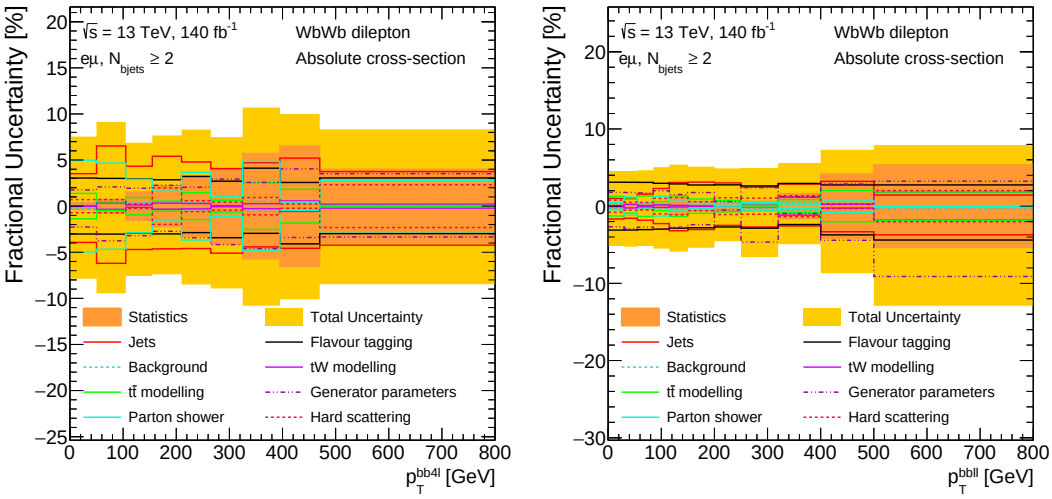

(a) (b)

Figure C.69: Uncertainties breakdown for the absolute cross-section measurement of the a p_{T} of the *bb4l* system, and b p_{T} of the *bbll*system, measured using the `QUnfold` package.

Appendix D

Complementary material for results

D.1 Correlation matrices

Correlation matrices are computed using this equation:

$$\mathrm{Corr}_{ij} = \frac{\mathrm{Cov}_{ij}}{\sqrt{\mathrm{Cov}_{ii} * \mathrm{Cov}_{jj}}} \tag{D.1}$$

In Figures D.1 - D.10, correlation matrices for each variable are shown.

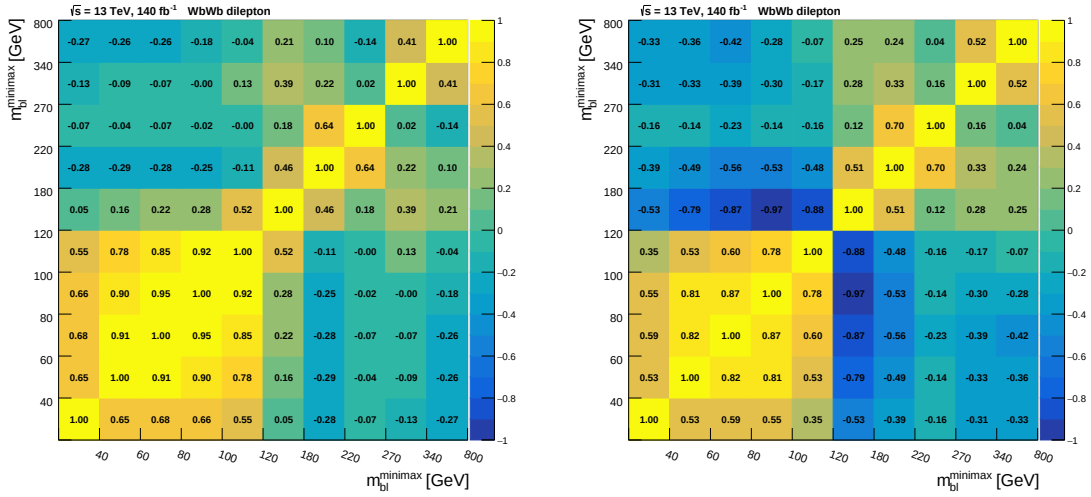

Figure D.1: Correlation matrices for the m^{bl}_{minimax} variable for the absolute cross-section measurement (left) and the relative cross-section measurement (right).

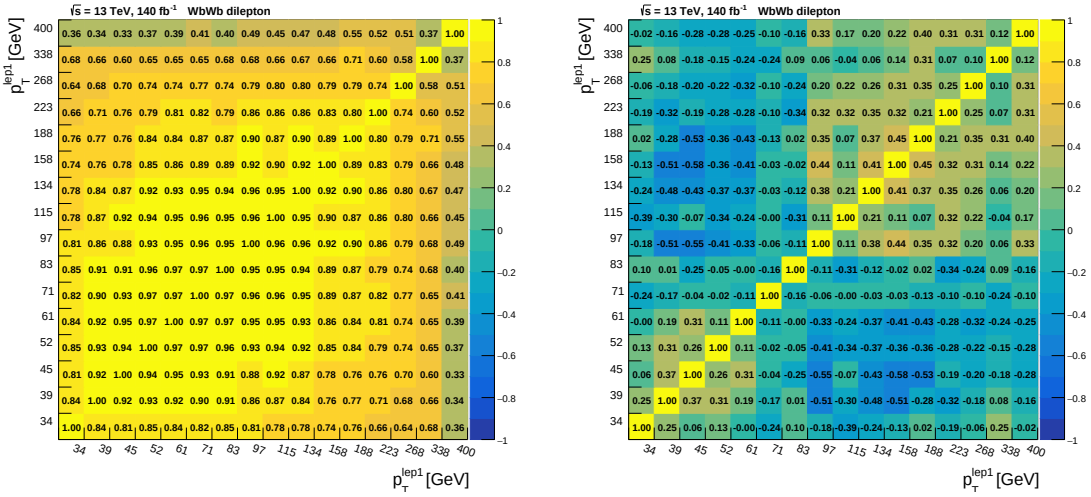

Figure D.2: Correlation matrices for the $p_{\text{T}}^{\text{lep1}}$ variable for the absolute cross-section measurement (left) and the relative cross-section measurement (right).

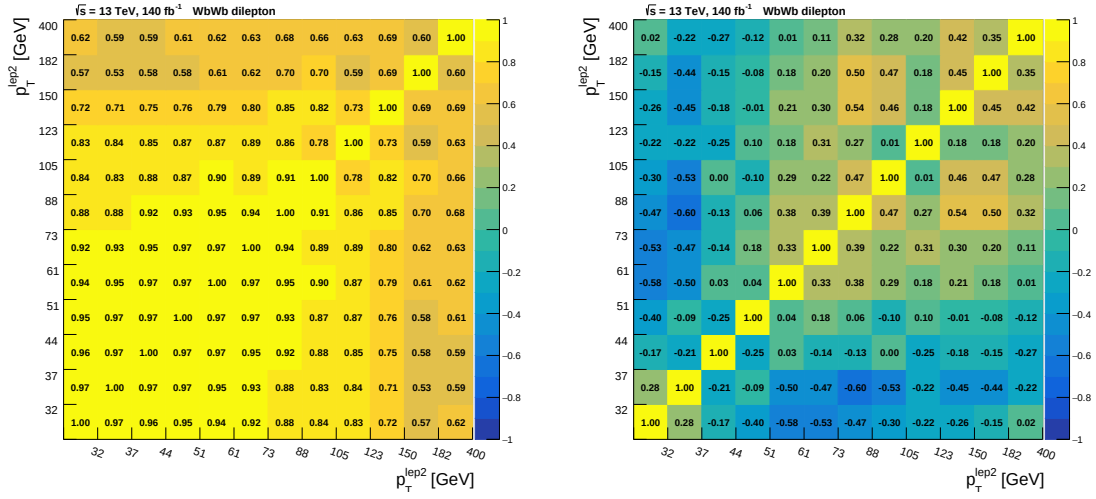

Figure D.3: Correlation matrices for the $p_{\mathrm{T}}^{\mathrm{lep2}}$ variable for the absolute cross-section measurement (left) and the relative cross-section measurement (right).

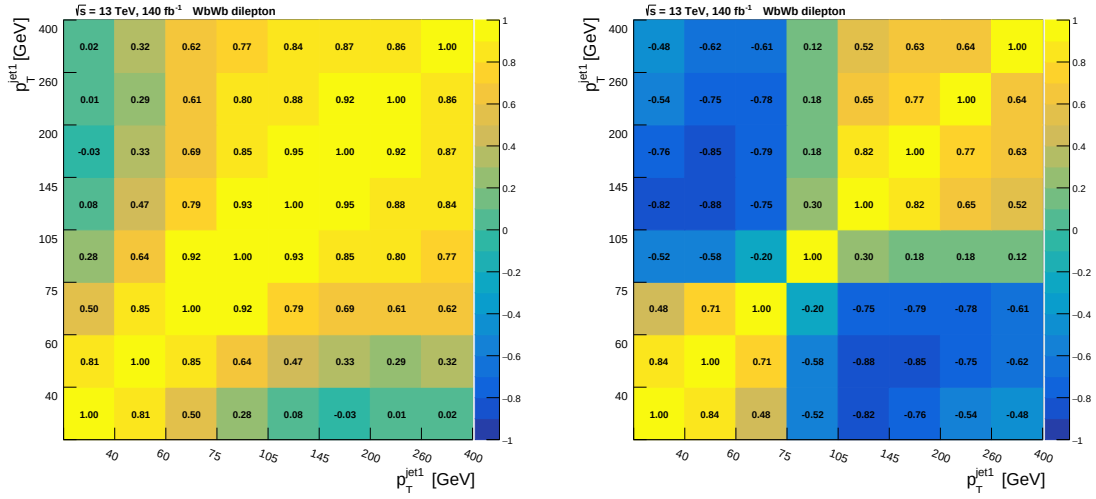

Figure D.4: Correlation matrices for the $p_{\mathrm{T}}^{\mathrm{jet1}}$ variable for the absolute cross-section measurement (left) and the relative cross-section measurement (right).

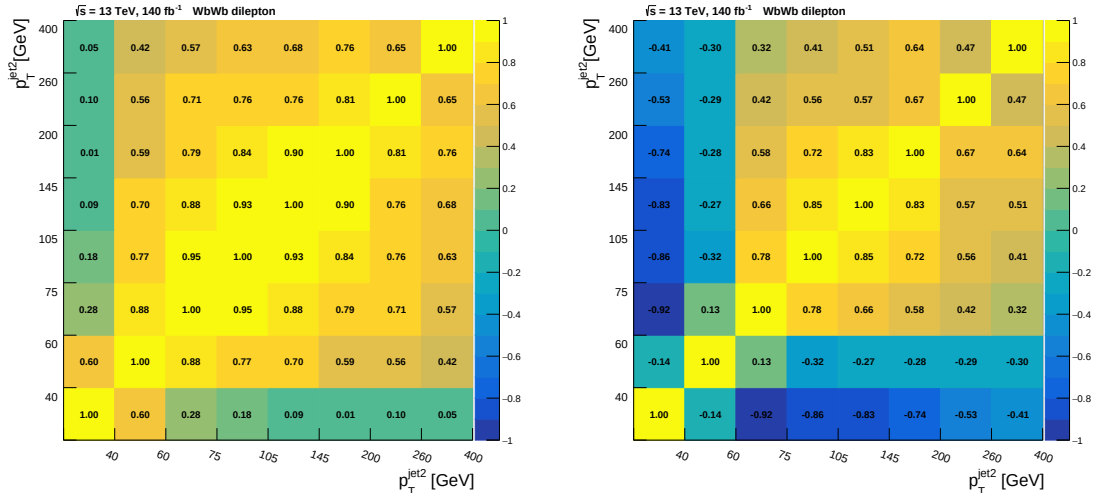

Figure D.5: Correlation matrices for the $p_{\mathrm{T}}^{\mathrm{jet2}}$ variable for the absolute cross-section measurement (left) and the relative cross-section measurement (right).

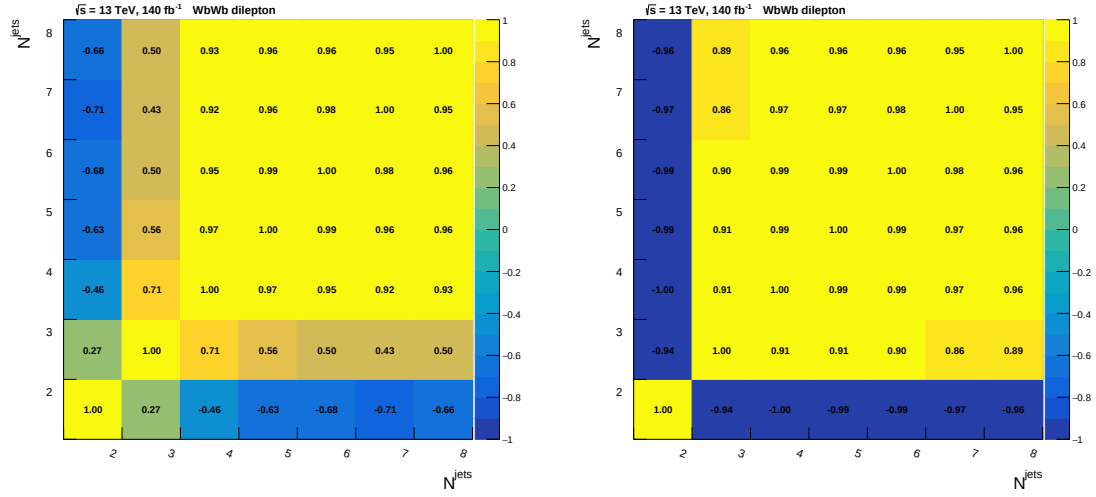

Figure D.6: Correlation matrices for the number of extra jets variable for the absolute cross-section measurement (left) and the relative cross-section measurement (right).

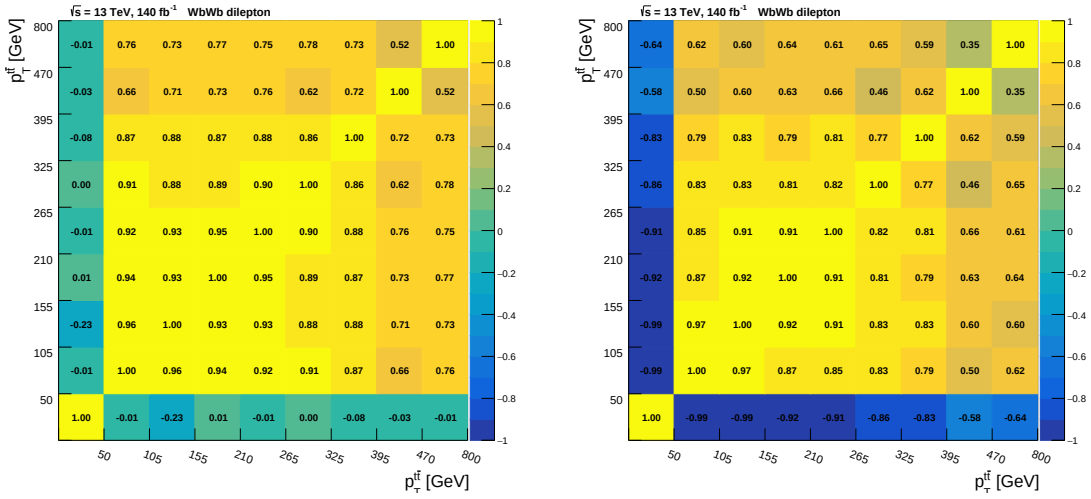

Figure D.7: Correlation matrices for the $p_{\mathrm{T}}^{t\bar{t}}$ variable for the absolute cross-section measurement (left) and the relative cross-section measurement (right).

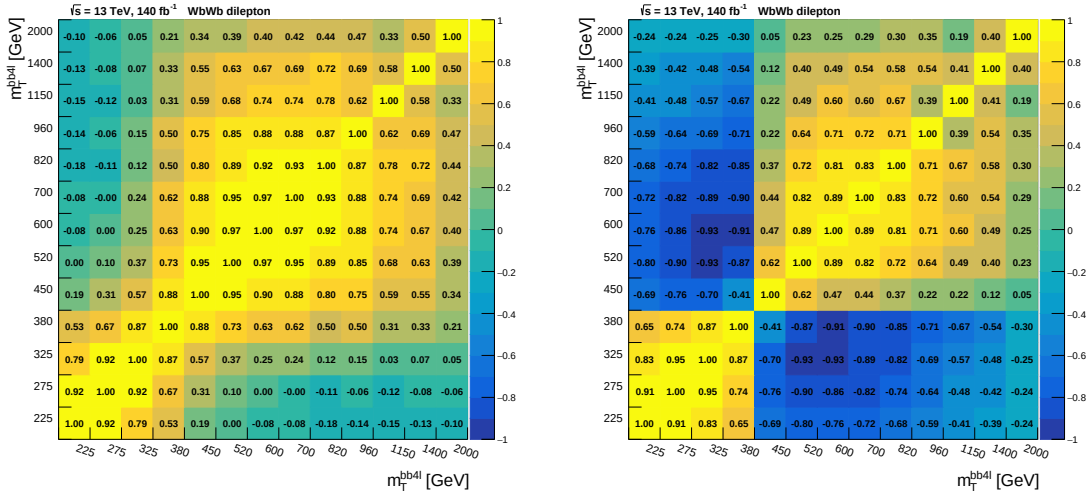

Figure D.8: Correlation matrices for the $m_T^{t\bar{t}}$ variable for the absolute cross-section measurement (left) and the relative cross-section measurement (right).

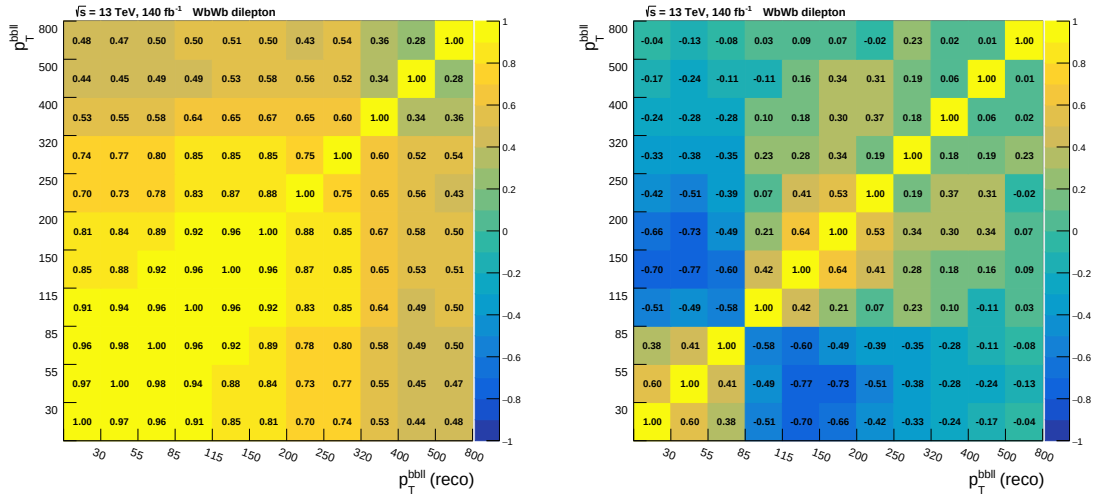

Figure D.9: Correlation matrices for the p_{T}^{bbll} variable for the absolute cross-section measurement (left) and the relative cross-section measurement (right).

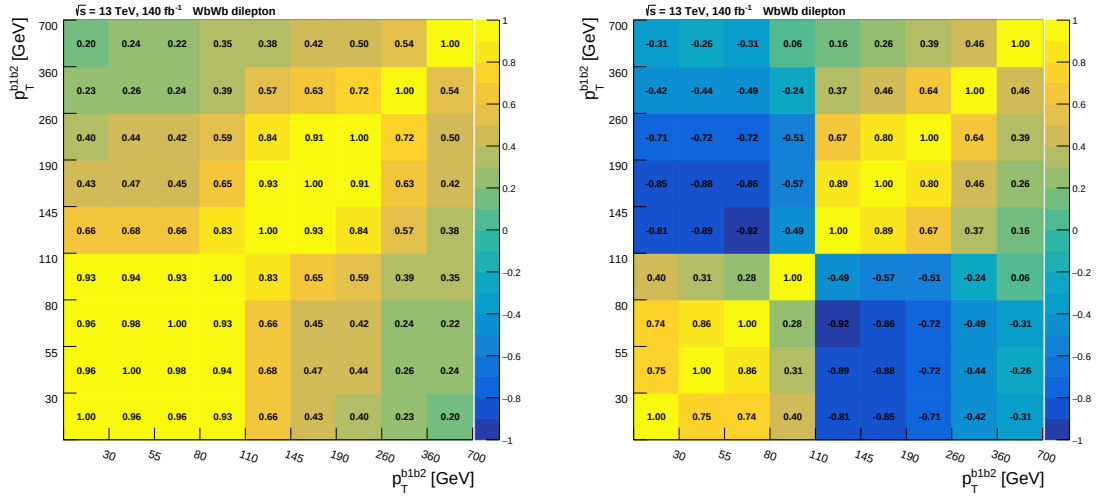

Figure D.10: Correlation matrices for the p_{T}^{b1b2} variable for the absolute cross-section measurement (left) and the relative cross-section measurement (right).

D.2 Absolute cross-section results

The absolute cross-sections measurements as a function of the kinematic variables of the $WbWb$ final-state objects are presented in Figures D.11 - D.12 for leading lepton and sub-leading lepton p_{T} and in Figures D.13 - D.14 for leading jet and sub-leading jet p_{T}. Cross-sections as a function of the additional jet multiplicity and the p_{T} of the $bb4l$ system are shown in Figures D.15 - D.16 respectively.

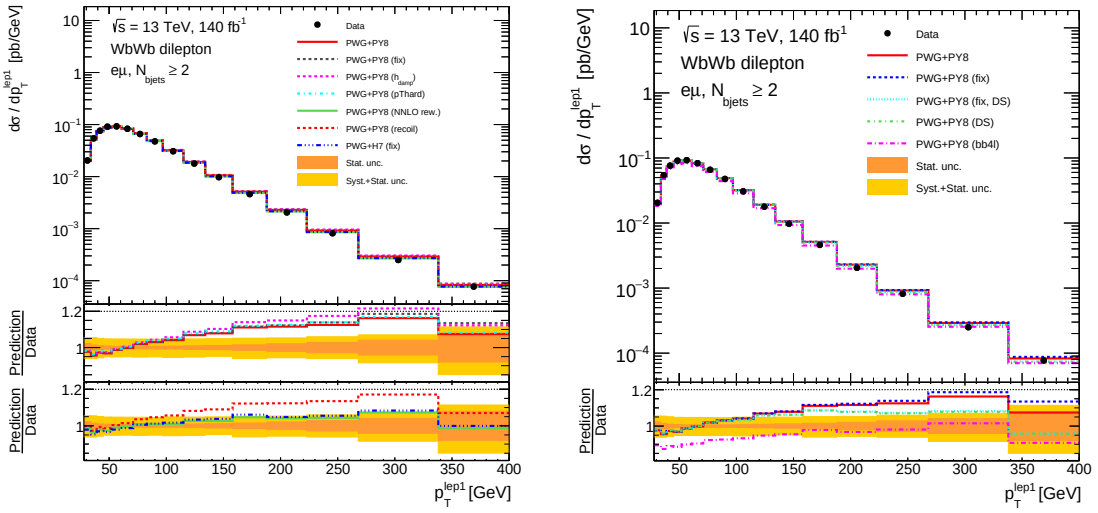

Figure D.11: Absolute differential cross-section measurement as a function of the leading lepton p_{T} compared to interference generators (right) and MC generators (left).

χ^2 and p-values of absolute results are shown in Table D.1 and **??** for the different predictions.

Observable	PWG+PY8 (h_{damp})		PWG+PY8 ($p_{\mathrm{T,hard}}$)		PWG+PY8 (NNLO REW.)		PWG+PY8 (RECOIL)		PWG+H7 (FIX)	
	χ^2/NDF	p-value	χ^2/NDF	p-value	χ^2/NDF	p-value	χ^2/NDF	p-value	χ^2/NDF	p-value
$p_{\mathrm{T}}^{\mathrm{jet}_1}$	37.9/7	<0.01	18.0/7	0.01	7.1/7	0.42	12.0/7	0.10	10.1/7	0.18
$p_{\mathrm{T}}^{\mathrm{jet}_2}$	17.1/7	0.02	8.2/7	0.31	2.9/7	0.89	3.3/7	0.86	1.9/7	0.97
$p_{\mathrm{T}}^{l_1}$	60.1/15	<0.01	44.7/15	<0.01	13.3/15	0.58	39.1/15	<0.01	20.5/15	0.15
$p_{\mathrm{T}}^{l_2}$	30.1/11	<0.01	27.9/11	<0.01	9.3/11	0.59	22.7/11	0.02	15.3/11	0.17
N^{jets}	7.9/6	0.24	23.1/6	<0.01	5.6/6	0.47	9.1/6	0.17	23.3/6	<0.01
p_{T}^{bb4l}	69.8/8	<0.01	41.0/8	<0.01	12.0/8	0.15	46.6/8	<0.01	43.6/8	<0.01
m_{T}^{bb4l}	23.4/12	0.02	18.1/12	0.11	17.3/12	0.14	16.1/12	0.18	25.5/12	0.01
m^{bbll}	30.8/15	<0.01	29.8/15	0.01	25.8/15	0.04	25.8/15	0.04	37.1/15	<0.01
p_{T}^{bbll}	78.6/10	<0.01	26.4/10	<0.01	13.0/10	0.22	31.7/10	<0.01	28.8/10	<0.01
p_{T}^{bb}	33.0/8	<0.01	10.8/8	0.21	4.4/8	0.81	10.9/8	0.20	17.7/8	0.02

Table D.1: χ^2 and p-values quantifying the level of agreement between the measured absolute differential cross-sections and predictions provided by different MC generators.

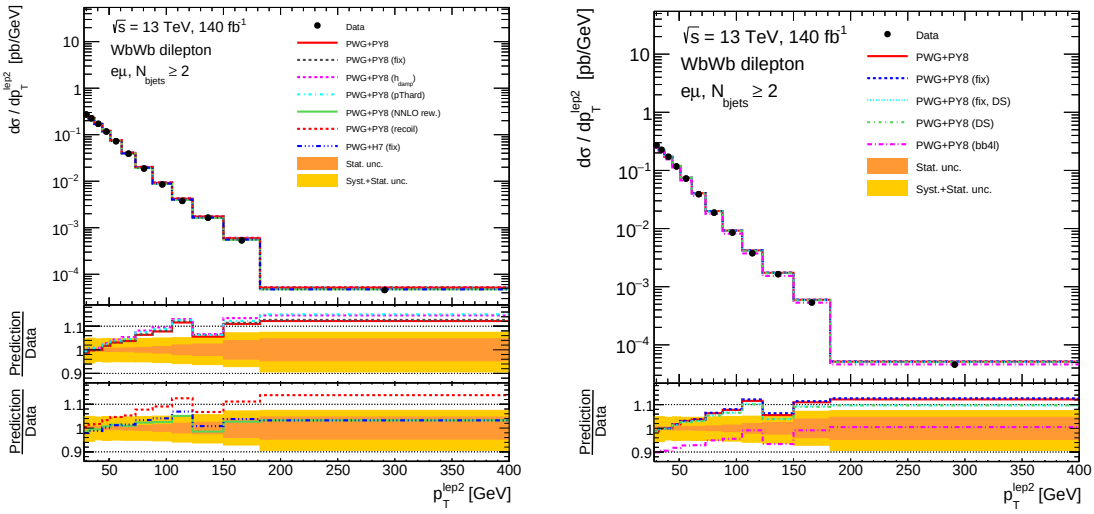

Figure D.12: Absolute differential cross-section measurement as a function of the subleading lepton p_{T} compared to interference generators (right) and MC generators (left).

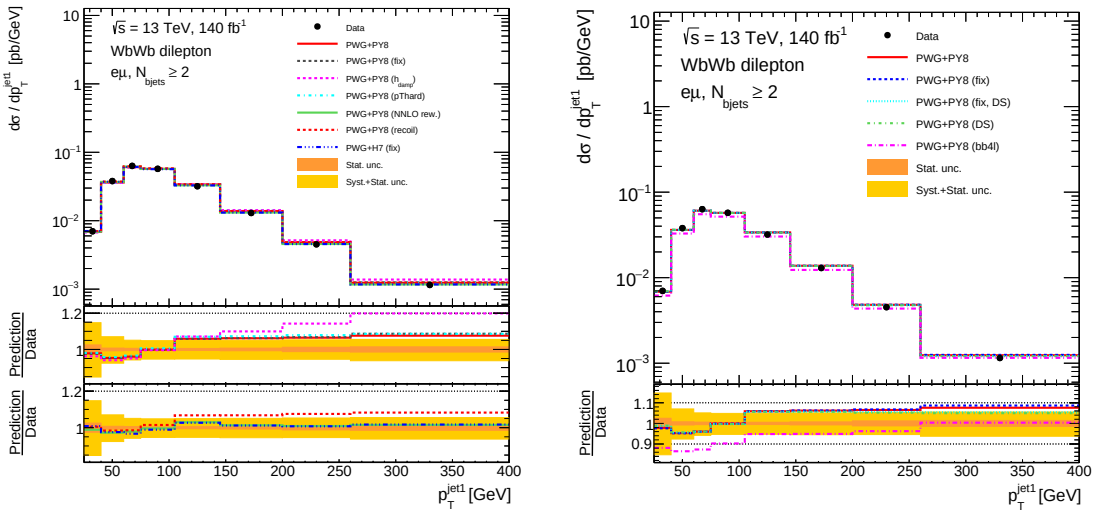

Figure D.13: Absolute differential cross-section measurement as a function of the leading jet p_{T} compared to interference generators (right) and MC generators (left).

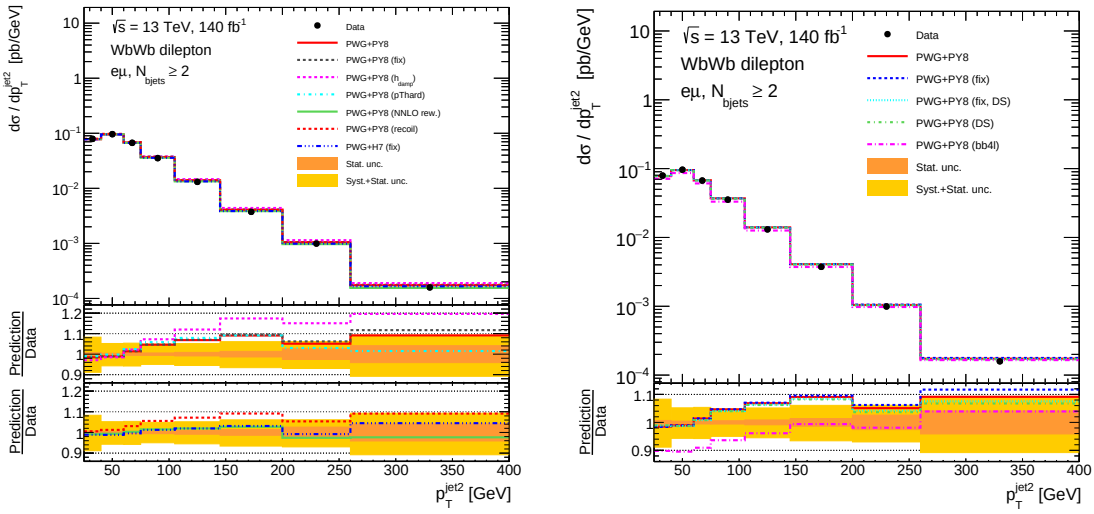

Figure D.14: Absolute differential cross-section measurement as a function of the subleading jet p_{T} compared to interference generators (right) and MC generators (left).

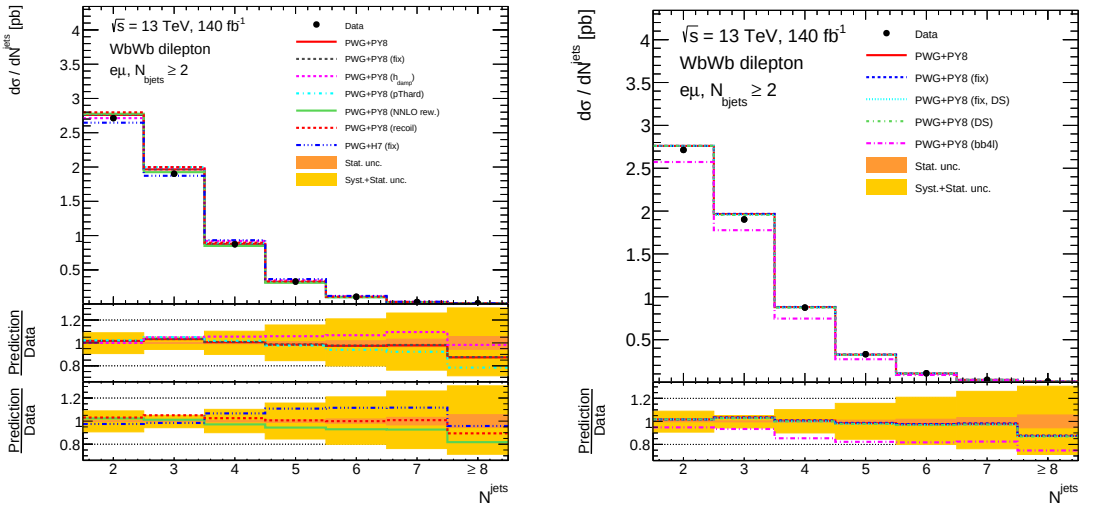

Figure D.15: Absolute differential cross-section measurement as a function of the jet multiplicity compared to interference generators (right) and MC generators (left).

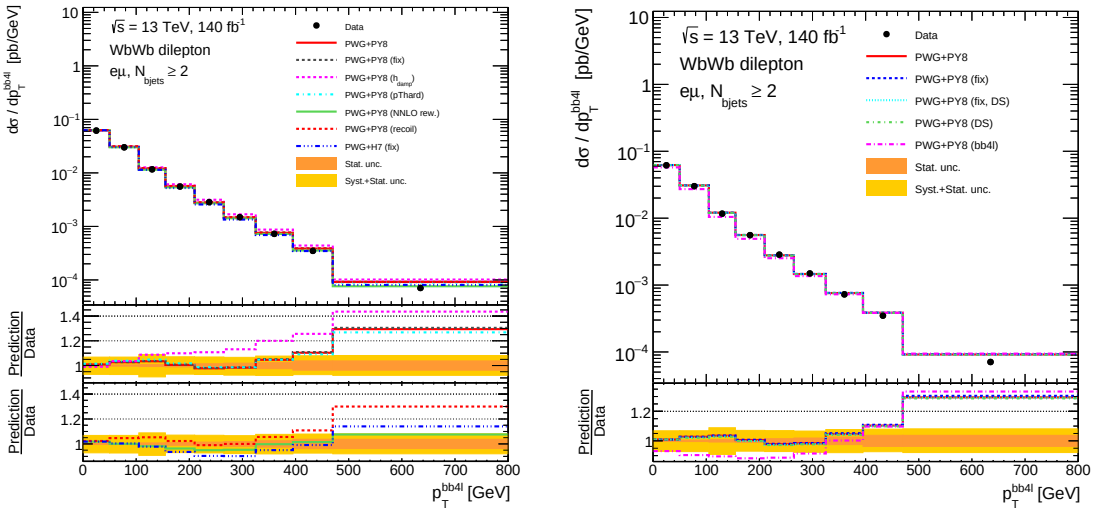

Figure D.16: Absolute differential cross-section measurement as a function of the p_{T} of the *bb4l* system compared to interference generators (right) and MC generators (left).

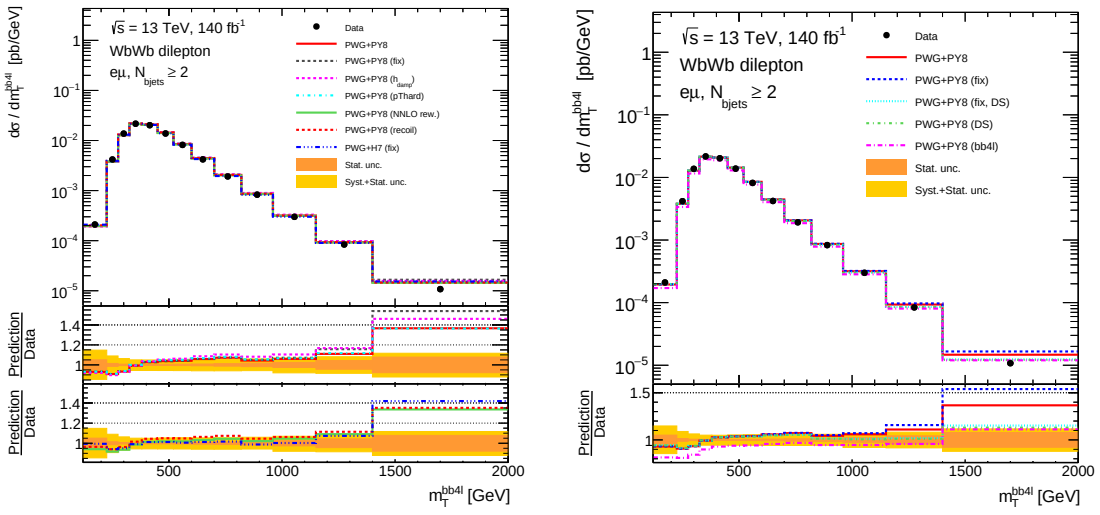

Figure D.17: Absolute differential cross-section measurement as a function of the m_{T} of the *bb4l* system compared to interference generators (right) and MC generators (left).

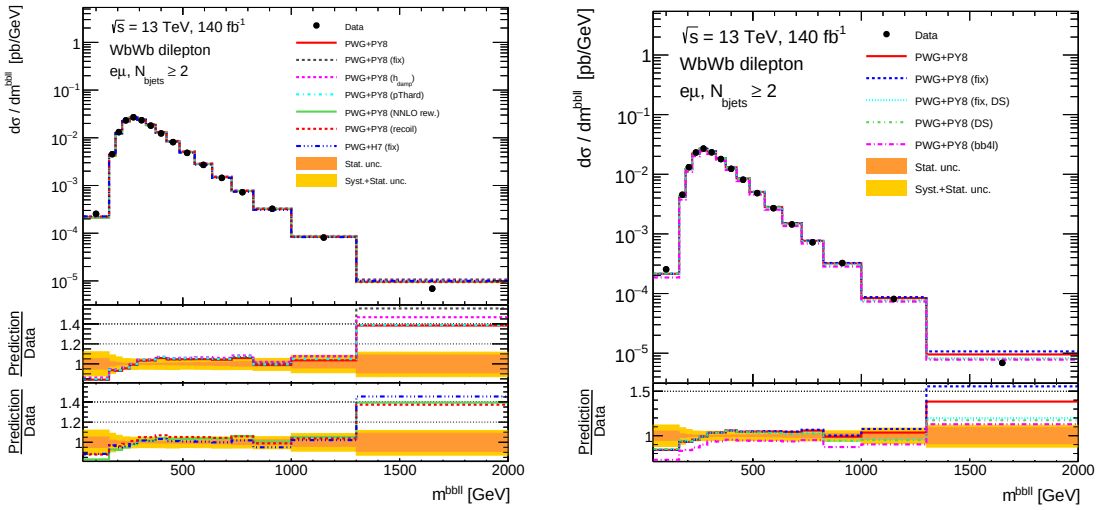

Figure D.18: Absolute differential cross-section measurement as a function of the mass of the *bbll* system compared to interference generators (right) and MC generators (left).

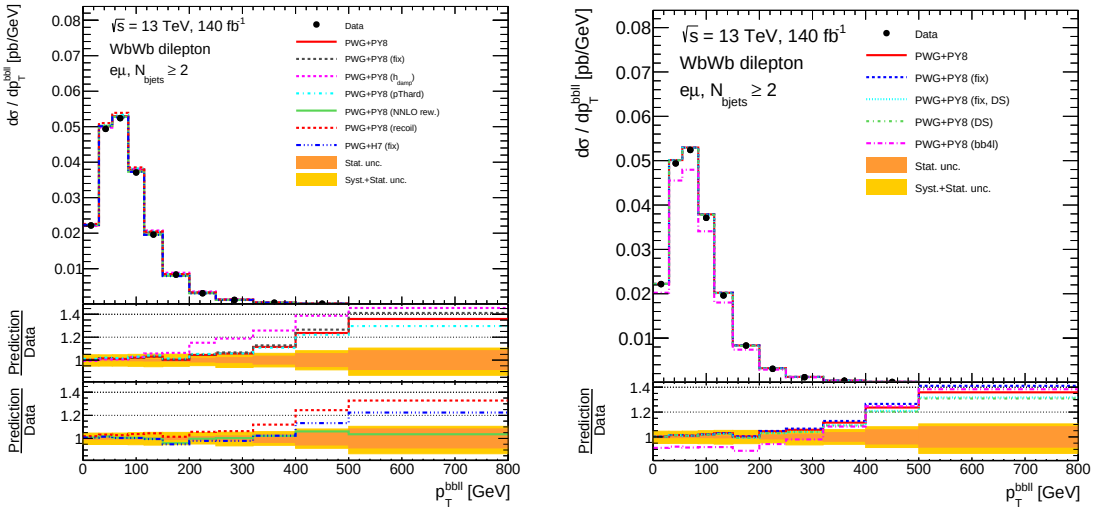

Figure D.19: Absolute differential cross-section measurement as a function of the p_{T} of the *bbll* system compared to interference generators (right) and MC generators (left).

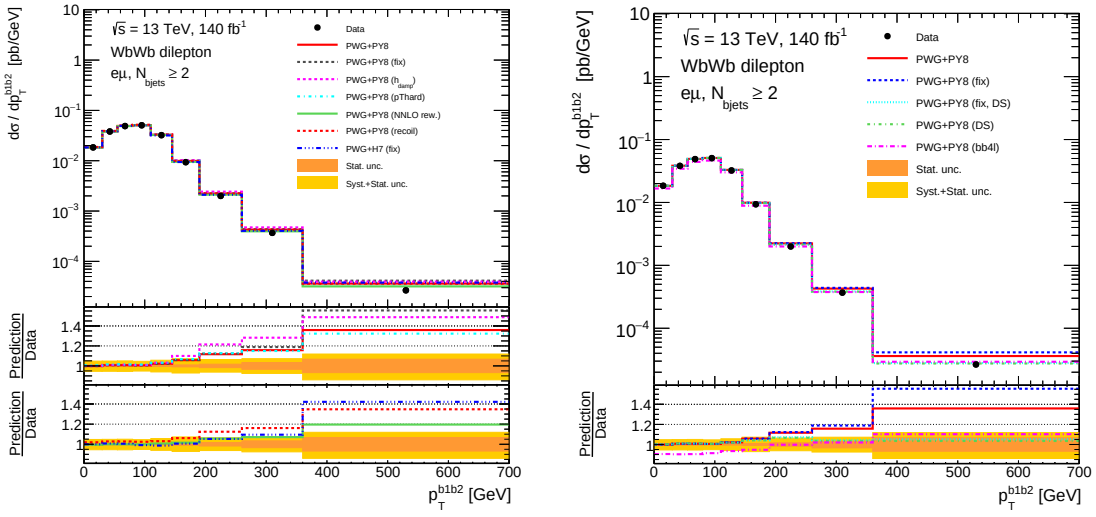

Figure D.20: Absolute differential cross-section measurement as a function of the p_{T} of the bb system compared to interference generators (right) and MC generators (left).

Observable	PWG+PY8		PWG+PY8 (FIX)		PWG+PY8 ($bb4l$)		PWG+PY8 (FIX, DS)		PWG+PY8 (DS)	
	χ^2/NDF	p-value	χ^2/NDF	p-value	χ^2/NDF	p-value	χ^2/NDF	p-value	χ^2/NDF	p-value
$p_{\mathrm{T}}^{\mathrm{jet}_1}$	17.7/8	0.02	18.2/8	0.02	15.7/8	0.05	17.6/8	0.02	17.7/8	0.02
$p_{\mathrm{T}}^{\mathrm{jet}_2}$	7.5/8	0.49	7.5/8	0.48	7.2/8	0.52	7.5/8	0.48	7.6/8	0.48
$p_{\mathrm{T}}^{l_1}$	46.3/16	< 0.01	48.9/16	< 0.01	23.9/16	0.09	32.6/16	< 0.01	33.1/16	< 0.01
$p_{\mathrm{T}}^{l_2}$	27.6/12	< 0.01	29.3/12	< 0.01	17.5/12	0.13	21.8/12	0.04	22.5/12	0.03
N^{jets}	9.3/7	0.23	9.4/7	0.23	21.7/7	< 0.01	7.9/7	0.34	8.0/7	0.34
p_{T}^{bb4l}	56.0/9	< 0.01	58.4/9	< 0.01	107.2/9	< 0.01	55.7/9	< 0.01	56.9/9	< 0.01
m_T^{bb4l}	19.4/13	0.11	31.8/13	< 0.01	15.0/13	0.31	13.6/13	0.40	13.7/13	0.39
m^{bbll}	29.6/16	0.02	41.2/16	< 0.01	27.5/16	0.04	28.4/16	0.03	27.7/16	0.03
p_{T}^{bbll}	38.7/11	< 0.01	47.7/11	< 0.01	81.4/11	< 0.01	32.2/11	< 0.01	33.5/11	< 0.01
p_{T}^{bb}	14.2/9	0.12	27.2/9	< 0.01	7.7/9	0.56	2.9/9	0.97	3.2/9	0.96

D.3 Absolute cross-section results with QUnfold

The absolute cross-sections measurements as a function of some of the kinematic variables of the $WbWb$ final-state objects are presented in Figures D.21 - D.27.

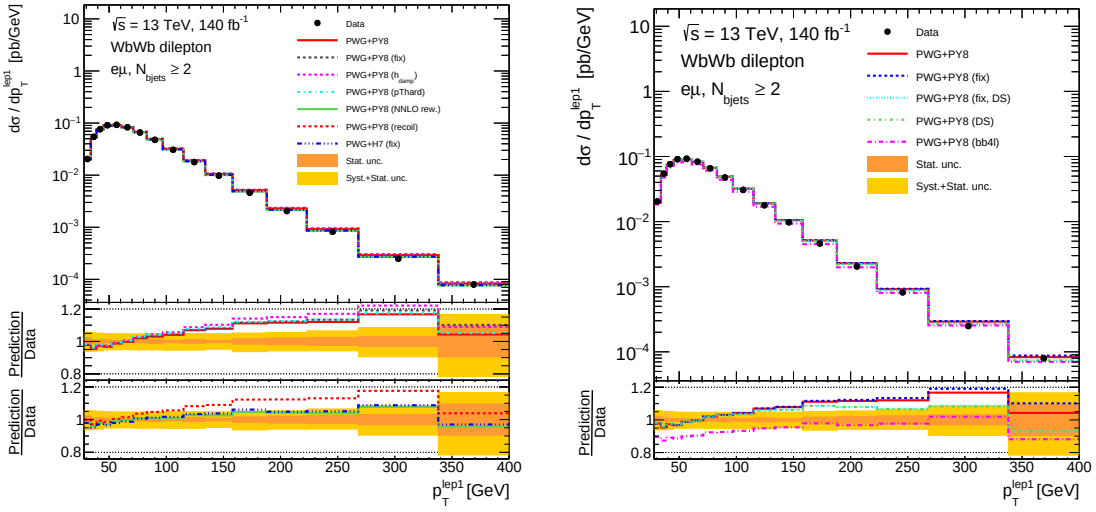

Figure D.21: Absolute differential cross-section measurement through QUnfold as a function of the leading lepton p_{T} compared to interference generators (right) and MC generators (left).

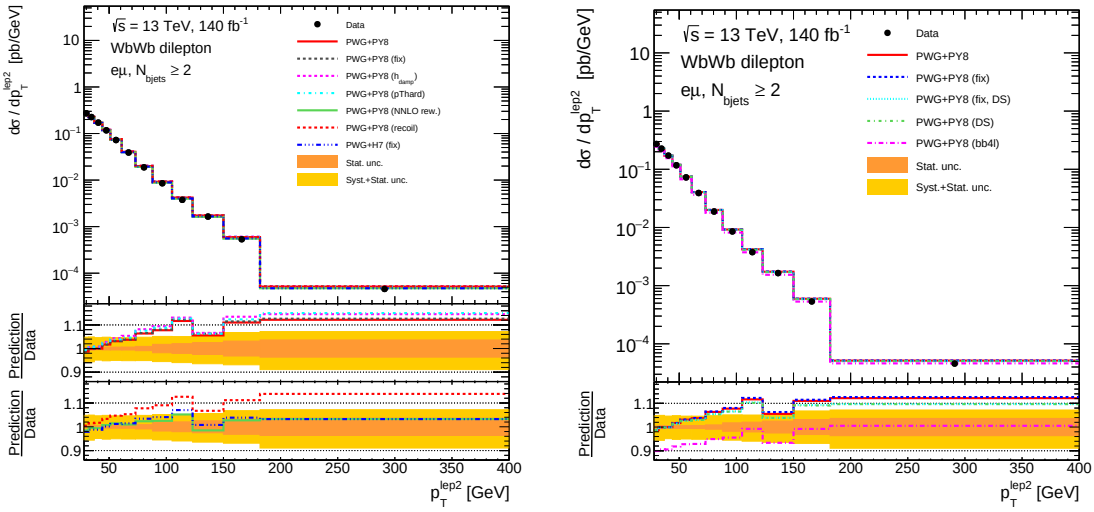

Figure D.22: Absolute differential cross-section measurement through QUnfold as a function of the sub-leading lepton p_{T} compared to interference generators (right) and MC generators (left).

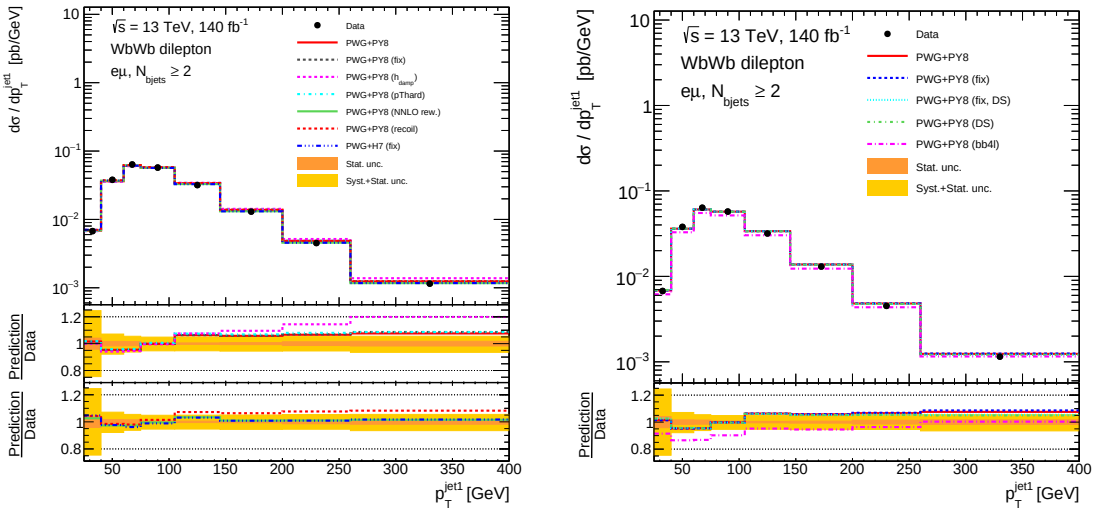

Figure D.23: Absolute differential cross-section measurement through QUnfold as a function of the leading jet p_{T} compared to interference generators (right) and MC generators (left).

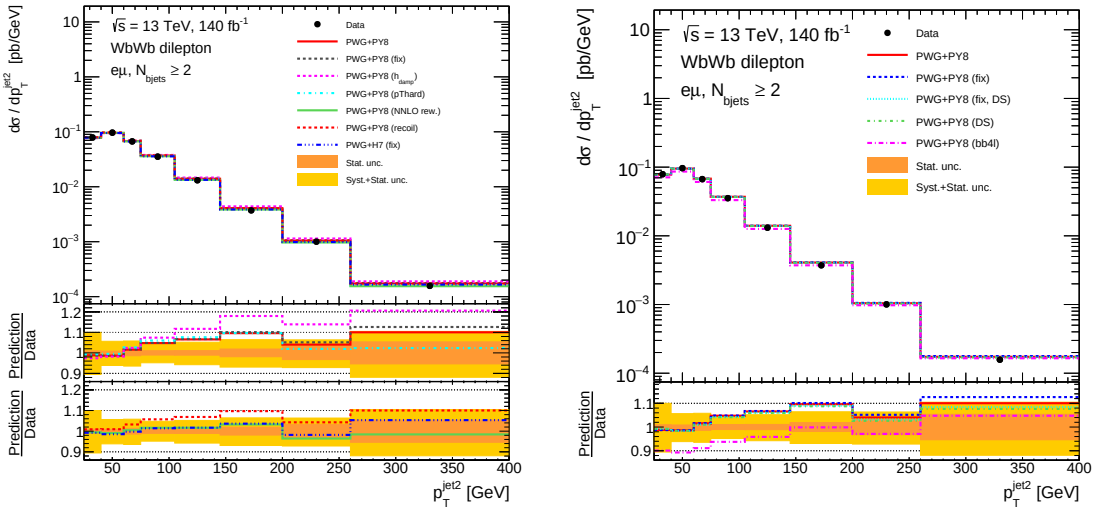

Figure D.24: Absolute differential cross-section measurement through QUnfold as a function of the sub-leading jet p_{T} compared to interference generators (right) and MC generators (left).

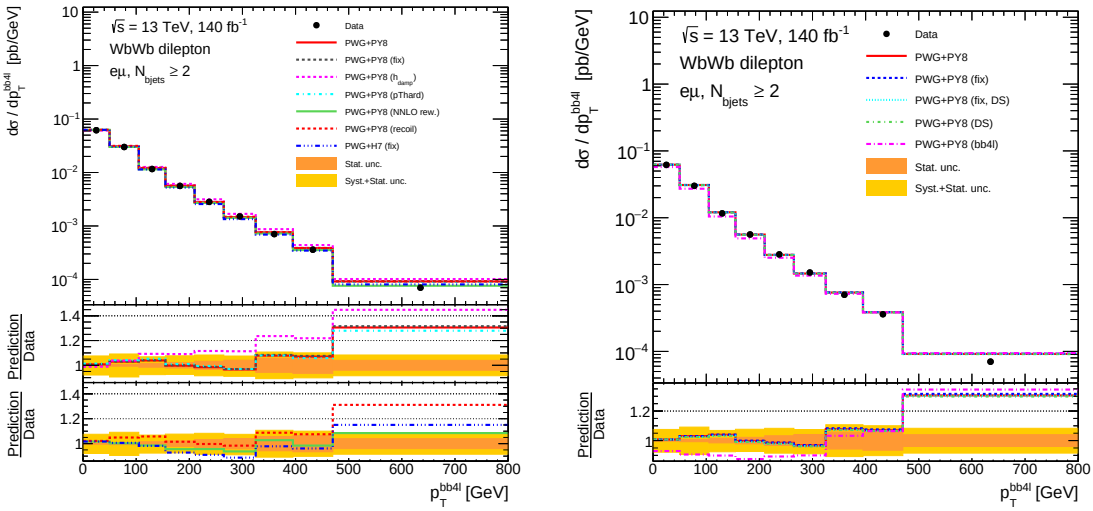

Figure D.25: Absolute differential cross-section measurement through QUnfold as a function of the p_{T} of the *bb4l* system compared to interference generators (right) and MC generators (left).

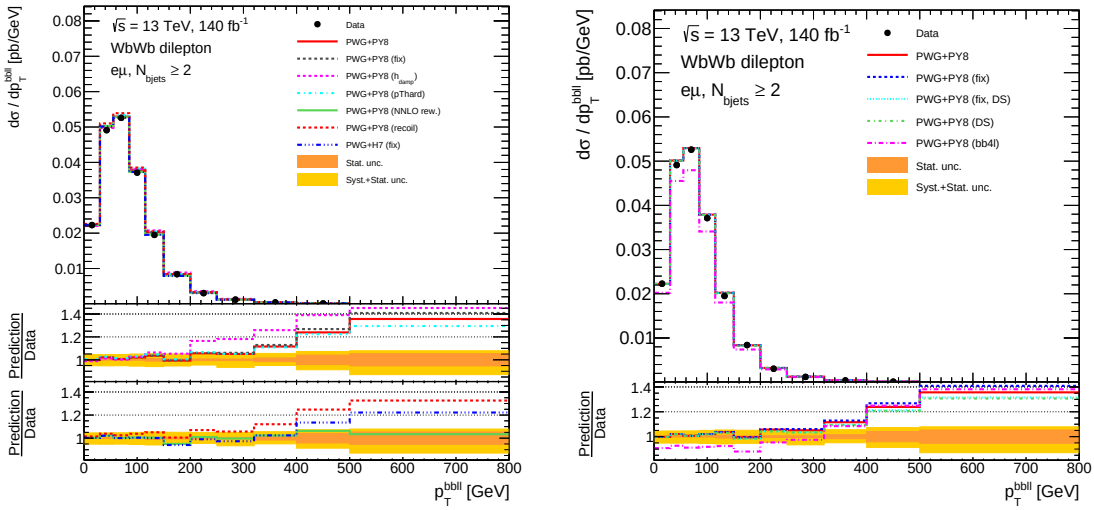

Figure D.26: Absolute differential cross-section measurement through QUnfold as a function of the p_{T} of the *bbll* system compared to interference generators (right) and MC generators (left).

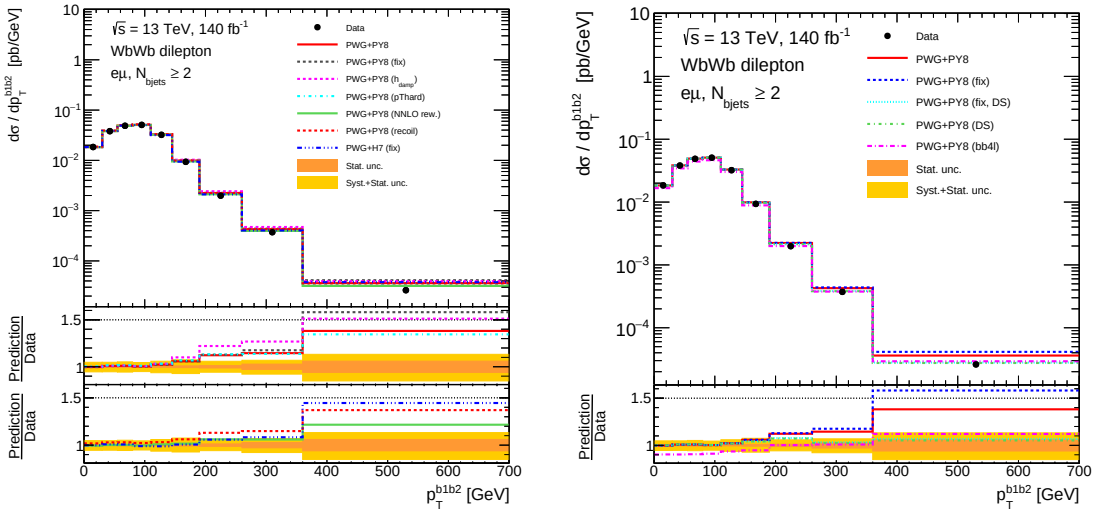

Figure D.27: Absolute differential cross-section measurement through QUnfold as a function of the p_{T} of the *bb* system compared to interference generators (right) and MC generators (left).

Bibliography

[1] Mark Thomson. *Modern particle physics*. New York: Cambridge University Press, 2013. ISBN: 978-1-107-03426-6.

[2] S. Braibant, G. Giacomelli, and M. Spurio. *Particelle e interazioni fondamentali: Il mondo delle particelle*. UNITEXT. Springer Milan, 2010. ISBN: 9788847011618. URL: https://books.google.it/books?id=6YKRe94BTKAC.

[3] Sheldon L. Glashow. "Partial-symmetries of weak interactions". In: *Nuclear Physics* 22.4 (1961), pp. 579–588. ISSN: 0029-5582. DOI: DOI:10.1016/0029-5582(61)90469-2. URL: http://www.sciencedirect.com/science/article/B73DR-470FCCY-3/2/73adaafe245cc26ee7aa3aa7215f18e1.

[4] Steven Weinberg. "A Model of Leptons". In: *Phys. Rev. Lett.* 19 (1967), pp. 1264–1266. DOI: 10.1103/PhysRevLett.19.1264.

[5] Abdus Salam. "Weak and Electromagnetic Interactions". In: *Conf. Proc. C* 680519 (1968), pp. 367–377. DOI: 10.1142/9789812795915_0034.

[6] Murray Gell-Mann. "A Schematic Model of Baryons and Mesons". In: *Phys. Lett.* 8 (1964), pp. 214–215. DOI: 10.1016/S0031-9163(64)92001-3.

[7] G. Zweig. "An SU(3) model for strong interaction symmetry and its breaking. Version 1". In: (Jan. 1964). DOI: 10.17181/CERN-TH-401.

[8] Peter W. Higgs. "Broken Symmetries and the Masses of Gauge Bosons". In: *Phys. Rev. Lett.* 13 (16 Oct. 1964), pp. 508–509. DOI: 10.1103/PhysRevLett.13.508. URL: https://link.aps.org/doi/10.1103/PhysRevLett.13.508.

[9] Tanabashi et al. "Review of Particle Physics". In: *Phys. Rev. D* 98 (3 Aug. 2018), p. 030001. DOI: 10.1103/PhysRevD.98.030001. URL: https://link.aps.org/doi/10.1103/PhysRevD.98.030001.

[10] Edgardo T. Garcia Alvarez and Fabian H. Gaioli. "Feynman's proper time approach to QED". In: *Found. Phys.* 28 (1998). Ed. by J. R. Fanchi and L. P. Horwitz, pp. 1529–1538. DOI: 10.1023/A:1018882101146. arXiv: hep-th/9807132.

[11] Joshua P. Ellis. "TikZ-Feynman: Feynman diagrams with TikZ". In: *Computer Physics Communications* 210 (2017), pp. 103–123. ISSN: 0010-4655. DOI: https://doi.org/10.1016/j.cpc.2016.08.019. URL: http://www.sciencedirect.com/science/article/pii/S0010465516302521.

[12] C. Quigg. *Gauge Theories of the Strong, Weak and Electromagnetic Interactions*. Vol. 56. 1983. ISBN: 978-0-8053-6020-2.

[13] Ernst Carl Gerlach Stueckelberg de Breidenbach and Andreas Petermann. "Normalization of constants in the quanta theory". In: *Helv. Phys. Acta* 26 (1953), pp. 499–520. DOI: 10.5169/seals-112426.

[14] G. Rajasekaran. "Fermi and the Theory of Weak Interactions". In: *Resonance J. Sci. Educ.* 19.1 (2014), pp. 18–44. DOI: 10.1007/s12045-014-0005-2. arXiv: 1403.3309 [physics.hist-ph].

[15] C. S. Wu et al. "Experimental Test of Parity Conservation in Beta Decay". In: *Physical Review* 105.4 (1957), pp. 1413–1415. DOI: 10.1103/PhysRev.105.1413.

[16] A. Lesov. *The Weak Force: From Fermi to Feynman*. 2009. arXiv: 0911.0058 [physics.hist-ph].

[17] Peter Skands. "Introduction to QCD". In: *Theoretical Advanced Study Institute in Elementary Particle Physics: Searching for New Physics at Small and Large Scales*. 2013, pp. 341–420. DOI: 10.1142/9789814525220_0008. arXiv: 1207.2389 [hep-ph].

[18] Antonio Pich. "The Standard model of electroweak interactions". In: *2006 European School of High-Energy Physics*. 2008, pp. 1–49. arXiv: 0705.4264 [hep-ph].

[19] Simone Amoroso et al. "Compatibility and combination of world W-boson mass measurements". In: *Eur. Phys. J. C* 84.5 (2024), p. 451. DOI: 10.1140/epjc/s10052-024-12532-z. arXiv: 2308.09417 [hep-ex].

[20] M. Gell-Mann. "A schematic model of baryons and mesons". In: *Physics Letters* 8.3 (1964), pp. 214–215. ISSN: 0031-9163. DOI: https://doi.org/10.1016/S0031-9163(64)92001-3. URL: https://www.sciencedirect.com/science/article/pii/S0031916364920013.

[21] Luciano Maiani. *The GIM Mechanism: origin, predictions and recent uses*. 2013. arXiv: 1303.6154 [hep-ph].

[22] Martin L. Perl. "The Discovery of the tau lepton and the changes in elementary particle physics in forty years". In: *Phys. Perspect.* 6 (2004), pp. 401–427. DOI: 10.1007/s00016-003-0218-3.

[23] L M Lederman. "Upsilon particle. [Historical review]". In: *Sci. Am.; (United States)* 4.239 (Oct. 1978). URL: https://www.osti.gov/biblio/6500405.

[24] F. Abe et al. "A Limit on the top quark mass from $p\bar{p}$ collisions at $\sqrt{s} = 1.8$ TeV". In: *Phys. Rev. D* 45 (1992), pp. 3921–3948. DOI: 10.1103/PhysRevD.45.3921.

[25] *ALEPH suggestions for 1990 LEP running*. Tech. rep. Geneva: CERN, 1990. URL: https://cds.cern.ch/record/700758.

[26] S. et al Abachi. "Observation of the Top Quark". In: *Physical Review Letters* 74.14 (Apr. 1995), pp. 2632–2637. ISSN: 1079-7114. DOI: 10.1103/physrevlett.74.2632. URL: http://dx.doi.org/10.1103/PhysRevLett.74.2632.

[27] Arnulf Quadt. "Top quark physics at hadron colliders". In: *Eur. Phys. J. C* 48 (2006), pp. 835–1000. DOI: 10.1140/epjc/s2006-02631-6.

[28] M. Jeżabek and J.H. Kühn. "QCD corrections to semileptonic decays of heavy quarks". In: *Nuclear Physics B* 314.1 (1989), pp. 1–6. ISSN: 0550-3213. DOI: https://doi.org/10.1016/0550-3213(89)90108-9. URL: https://www.sciencedirect.com/science/article/pii/0550321389901089.

[29] TIM GERSHON. "Overview of the Cabibbo–Kobayashi–Maskawa matrix†". In: *Pramana* 79.5 (Nov. 2012), pp. 1091–1108. ISSN: 0973-7111. DOI: 10.1007/s12043-012-0418-y. URL: http://dx.doi.org/10.1007/s12043-012-0418-y.

[30] Martin C. Smith and Scott S. Willenbrock. "Top-quark pole mass". In: arXiv:hep-ph/9612329. 1997. DOI: 10.1103/PhysRevLett.79.3825.

[31] Giorgio Cortiana. "Top-quark mass measurements: Review and perspectives". In: *Reviews in Physics* 1 (2016), pp. 60–76. ISSN: 2405-4283. DOI: https://doi.org/10.1016/j.revip.2016.04.001. URL: http://www.sciencedirect.com/science/article/pii/S2405428316300028.

[32] Aram Hayrapetyan et al. "Combination of Measurements of the Top Quark Mass from Data Collected by the ATLAS and CMS Experiments at s=7 and 8 TeV". In: *Phys. Rev. Lett.* 132.26 (2024), p. 261902. DOI: 10.1103/PhysRevLett.132.261902. arXiv: 2402.08713 [hep-ex].

[33] Peter Athron et al. "Precise calculation of the W boson pole mass beyond the standard model with FlexibleSUSY". In: *Physical Review D* 106.9 (Nov. 2022). ISSN: 2470-0029. DOI: 10.1103/physrevd.106.095023. URL: http://dx.doi.org/10.1103/PhysRevD.106.095023.

[34] Jens Erler and Matthias Schott. "Electroweak Precision Tests of the Standard Model after the Discovery of the Higgs Boson". In: *Prog. Part. Nucl. Phys.* 106 (2019), pp. 68–119. DOI: 10.1016/j.ppnp.2019.02.007. arXiv: 1902.05142 [hep-ph].

[35] Giuseppe Degrassi et al. "Higgs mass and vacuum stability in the Standard Model at NNLO". In: *Journal of High Energy Physics* 2012 (May 2012). DOI: 10.1007/JHEP08(2012)098.

[36] Michele Gallinaro. "Top quark physics: A tool for discoveries". In: *Journal of Physics: Conference Series* 447 (July 2013), p. 012012. DOI: 10.1088/1742-6596/447/1/012012. URL: https://doi.org/10.1088%2F1742-6596%2F447%2F1%2F012012.

[37] Morad Aaboud et al. "Probing the quantum interference between singly and doubly resonant top-quark production in pp collisions at $\sqrt{s} = 13$ TeV with the ATLAS detector". In: *Phys. Rev. Lett.* 121.15 (2018), p. 152002. DOI: 10.1103/PhysRevLett.121.152002. arXiv: 1806.04667 [hep-ex].

[38] Richard D. Ball et al. "Parton distributions from high-precision collider data." In: *Eur. Phys. J. C* 77.CAVENDISH-HEP-17-06. 10 (June 2017), 663. 95 p. DOI: 10.1140/epjc/s10052-017-5199-5. URL: https://cds.cern.ch/record/2267455.

[39] Michal Czakon, Paul Fiedler, and Alexander Mitov. "Total Top-Quark Pair-Production Cross Section at Hadron Colliders Through $O(\alpha_S^4)$". In: *Phys. Rev. Lett.* 110 (2013), p. 252004. DOI: 10.1103/PhysRevLett.110.252004. arXiv: 1303.6254 [hep-ph].

[40] *Top cross section summary plots - April 2024*. Tech. rep. All figures including auxiliary figures are available at https://atlas.web.cern.ch/Atlas/GROUPS/PHYSICS/PUBNOTES PHYS-PUB-2024-006. Geneva: CERN, 2024. URL: https://cds.cern.ch/record/2896104.

[41] F. Cascioli et al. "A unified NLO description of top-pair and associated Wt production". In: *The European Physical Journal C* 74.3 (Mar. 2014). ISSN: 1434-6052. DOI: 10.1140/epjc/s10052-014-2783-9. URL: http://dx.doi.org/10.1140/epjc/s10052-014-2783-9.

[42] Stefano Frixione et al. "Single-top hadroproduction in association with aWboson". In: *Journal of High Energy Physics* 2008.07 (July 2008), pp. 029–029. DOI: 10.1088/1126-6708/2008/07/029. URL: https://doi.org/10.1088%2F1126-6708%2F2008%2F07%2F029.

[43] Shouhua Zhu. "Next-to-leading order QCD corrections to bg→tW− at the CERN Large Hadron Collider". In: *Physics Letters B* 524.3 (2002), pp. 283–288. ISSN: 0370-2693. DOI: https://doi.org/10.1016/S0370-2693(01)01404-6. URL: http://www.sciencedirect.com/science/article/pii/S0370269301014046.

[44] CERN (Conseil Européen pour la Recherche Nucléaire). URL: https://twiki.cern.ch/twiki/bin/view/LHCPhysics/LHCTopWGSummaryPlots.

[45] Chris D. White et al. "Isolating Wt production at the LHC". In: *Journal of High Energy Physics* 2009 (2009), p. 074.

[46] CERN (Conseil Européen pour la Recherche Nucléaire). URL: https://home.cern/. (accessed: 12.04.2020).

[47] Alexander Gude. "Measurement of the phistar distribution of Z bosons decaying to electron pairs with the CMS experiment at a center-of-mass energy of 8 TeV". PhD thesis. May 2015.

[48] Lyndon Evans and Philip Bryant. "The CERN Large Hadron Collider: Accelerator and Experiments". In: *JINST* **3** S08001 (2008).

[49] X. Buffat et al. "Stability diagrams of colliding beams in the Large Hadron Collider". In: *Physical Review Special Topics - Accelerators and Beams* 17 (Nov. 2014). DOI: 10.1103/PhysRevSTAB.17.111002.

[50] Ewa Stanecka and on Collaboration. "The ATLAS Inner Detector operation, data quality and tracking performance". In: *Proceedings of 32nd International Symposium on Physics in Collision, PIC 2012* (Mar. 2013). arXiv: 1303.3630v1.

[51] ATLAS Collaboration. *ATLAS data quality operations and performance for 2015-2018 data-taking*. Tech. rep. arXiv:1911.04632. Geneva: CERN, Nov. 2019. URL: https://cds.cern.ch/record/2700249.

[52] Rafal Noga. "Modeling and control of the String2 LHC Prototype at CERN". PhD thesis. Sept. 2007.

[53] Helmut Wiedemann. *Particle Accelerator Physics*. Springer, 2015.

[54] K. Schindl. "The injector chain for the LHC". In: *LEP performance. Proceedings, 9th Workshop, Chamonix, France, January 26-29, 1999*. Mar. 1999, pp. 47–52.

[55] The ATLAS collaboration et al. "The ATLAS experiment at the CERN Large Hadron Collider". In: *JINST* **3** S08003 (2008).

[56] ATLAS. URL: https://atlas.cern/Discover/Detector/.

[57] David E Baynham et al. "ATLAS end cap toroid magnets cryostat design, manufacture and integration at CERN". In: *Applied Superconductivity, IEEE Transactions on* 14 (July 2004), pp. 522–525. DOI: 10.1109/TASC.2004.829710.

[58] Benjamin Pearson. "Searches for a high-mass Higgs-like diboson resonance in the $H \to WW \to \ell\nu qq$ decay channel using pp collisions at both $\sqrt{s} = 8$ and 13 TeV with the ATLAS detector at the LHC". PhD thesis. Oklahoma U., 2016.

[59] Fabian Kuger. "Signal Formation Processes in Micromegas Detectors and Quality Control for large size Detector Construction for the ATLAS New Small Wheel". In: (Aug. 2017).

[60] P Strizenec. "Performance of the ATLAS Liquid Argon Calorimeter after three years of LHC, operation and plans for a future upgrade". In: *Journal of Instrumentation* 9.09 (Sept. 2014), pp. C09007–C09007. DOI: 10.1088/1748-0221/9/09/c09007. URL: https://doi.org/10.1088%2F1748-0221%2F9%2F09%2Fc09007.

[61] N C Benekos et al. "ATLAS muon spectrometer simulation and its validation algorithms". In: *Journal of Physics: Conference Series* 119.3 (July 2008), p. 032009. DOI: 10.1088/1742-6596/119/3/032009. URL: https://doi.org/10.1088%2F1742-6596%2F119%2F3%2F032009.

[62] ATLAS Collaboration. *Operation of the ATLAS trigger system in Run 2*. 2020. arXiv: 2007.12539 [physics.ins-det].

[63] ATLAS Collaboration. *Technical Design Report for the Phase-II Upgrade of the ATLAS TDAQ System*. Tech. rep. CERN-LHCC-2017-020. ATLAS-TDR-029. Geneva: CERN, Sept. 2017. URL: https://cds.cern.ch/record/2285584.

[64] The ATLAS Collaboration. "Electron reconstruction and identification in the ATLAS experiment using the 2015 and 2016 LHC proton-proton collision data at s=13 TeV". In: *The European Physical Journal C* 79 (Aug. 2019).

[65] Morad Aaboud et al. "Electron reconstruction and identification in the ATLAS experiment using the 2015 and 2016 LHC proton-proton collision data at $\sqrt{s}$ = 13 TeV". In: *Eur. Phys. J. C* 79.8 (2019), p. 639. DOI: 10.1140/epjc/s10052-019-7140-6. arXiv: 1902.04655 [physics.ins-det].

[66] Leonor Alberich. "Photon and electron identification with the ATLAS detector". In: *PoS* ICHEP2016 (2017), p. 1235. DOI: 10.22323/1.282.1235.

[67] The ATLAS Collaboration. "Performance of electron and photon triggers in ATLAS during LHC Run 2". In: *Eur. Phys. J. C* 80.arXiv:1909.00761. 1 (Sept. 2019), 47. 56 p. DOI: 10.1140/epjc/s10052-019-7500-2. URL: https://cds.cern.ch/record/2688248.

[68] The ATLAS Collaboration. "Muon reconstruction performance of the ATLAS detector in proton–proton collision data at $\sqrt{s}$ =13 TeV". In: *Eur. Phys. J. C* 76.5 (2016), p. 292. DOI: 10.1140/epjc/s10052-016-4120-y. arXiv: 1603.05598 [hep-ex].

[69] Sebastien Rettie. *Muon identification and performance in the ATLAS experiment*. Tech. rep. ATL-PHYS-PROC-2018-052. Geneva: CERN, June 2018. DOI: 10.22323/1.316.0097. URL: https://cds.cern.ch/record/2626330.

[70] Andrea Ventura and ATLAS Collaboration. "ATLAS Muon Trigger Performance". In: (Sept. 2019). URL: https://cds.cern.ch/record/2688754.

[71] Morad Aaboud et al. "Jet reconstruction and performance using particle flow with the ATLAS Detector". In: *Eur. Phys. J. C* 77.7 (2017), p. 466. DOI: 10.1140/epjc/s10052-017-5031-2. arXiv: 1703.10485 [hep-ex].

[72] Matteo Cacciari, Gavin P. Salam, and Gregory Soyez. "The anti-k_t jet clustering algorithm". In: *JHEP* 04 (2008), p. 063.

[73] *Optimisation and performance studies of the ATLAS b-tagging algorithms for the 2017-18 LHC run*. Tech. rep. All figures including auxiliary figures are available at https://atlas.web.cern.ch/Atlas/GROUPS/PHYSICS/PUBNOTES/ATL-PHYS-PUB-2017-013. Geneva: CERN, 2017. URL: https://cds.cern.ch/record/2273281.

[74] *Identification of Jets Containing b-Hadrons with Recurrent Neural Networks at the ATLAS Experiment*. Tech. rep. All figures including auxiliary figures are available at https://atlas.web.cern.ch/Atlas/GROUPS/PHYSICS/PUBNOTES/ATL-PHYS-PUB-2017-003. Geneva: CERN, 2017. URL: https://cds.cern.ch/record/2255226.

[75] Aliaksei Hrynevich. *ATLAS jet and missing energy reconstruction, calibration and performance in LHC Run-2*. Tech. rep. ATL-PHYS-PROC-2017-045. 06. Geneva: CERN, May 2017. DOI: 10.1088/1748-0221/12/06/C06038. URL: https://cds.cern.ch/record/2263777.

[76] ATLAS Collaboration. *Tagging and suppression of pileup jets with the ATLAS detector*. ATLAS-CONF-2014-018. 2014. URL: https://cds.cern.ch/record/1700870.

[77] ATLAS Collaboration. "Performance of the ATLAS trigger system in 2015". In: *Eur. Phys. J. C* 77 (2017), p. 317. DOI: 10.1140/epjc/s10052-017-4852-3. arXiv: 1611.09661 [hep-ex].

[78] ATLAS Collaboration. *2015 start-up trigger menu and initial performance assessment of the ATLAS trigger using Run-2 data*. ATL-DAQ-PUB-2016-001. 2016. URL: https://cds.cern.ch/record/2136007.

[79] ATLAS Collaboration. *Trigger Menu in 2016*. ATL-DAQ-PUB-2017-001. 2017. URL: https://cds.cern.ch/record/2242069.

[80] ATLAS Collaboration. *Trigger Menu in 2017*. ATL-DAQ-PUB-2018-002. 2018. URL: https://cds.cern.ch/record/2625986.

[81] ATLAS Collaboration. *Trigger Menu in 2018*. ATL-DAQ-PUB-2019-001. 2019. URL: https://cds.cern.ch/record/2693402.

[82] ATLAS Collaboration. "The ATLAS Simulation Infrastructure". In: *Eur. Phys. J. C* 70 (2010), p. 823. DOI: 10.1140/epjc/s10052-010-1429-9. arXiv: 1005.4568 [physics.ins-det].

[83] Torbjörn Sjöstrand et al. "An introduction to PYTHIA 8.2". In: *Comput. Phys. Commun.* 191 (2015), p. 159. DOI: 10.1016/j.cpc.2015.01.024. arXiv: 1410.3012 [hep-ph].

[84] ATLAS Collaboration. *Summary of ATLAS Pythia 8 tunes*. ATL-PHYS-PUB-2012-003. 2012. URL: https://cds.cern.ch/record/1474107.

[85] A. D. Martin et al. "Parton distributions for the LHC". In: *Eur. Phys. J. C* 63 (2009), p. 189. DOI: 10.1140/epjc/s10052-009-1072-5. arXiv: 0901.0002 [hep-ph].

[86] S. Agostinelli et al. "GEANT4 – a simulation toolkit". In: *Nucl. Instrum. Meth. A* 506 (2003), p. 250. DOI: 10.1016/S0168-9002(03)01368-8.

[87] William Buttinger. *Using Event Weights to account for differences in Instantaneous Luminosity and Trigger Prescale in Monte Carlo and Data*. Geneva, May 2015. URL: https://cds.cern.ch/record/2014726.

[88] Stefano Frixione, Giovanni Ridolfi, and Paolo Nason. "A positive-weight next-to-leading-order Monte Carlo for heavy flavour hadroproduction". In: *JHEP* 09 (2007), p. 126. DOI: 10.1088/1126-6708/2007/09/126. arXiv: 0707.3088 [hep-ph].

[89] Paolo Nason. "A new method for combining NLO QCD with shower Monte Carlo algorithms". In: *JHEP* 11 (2004), p. 040. DOI: 10.1088/1126-6708/2004/11/040. arXiv: hep-ph/0409146.

[90] Stefano Frixione, Paolo Nason, and Carlo Oleari. "Matching NLO QCD computations with parton shower simulations: the POWHEG method". In: *JHEP* 11 (2007), p. 070. DOI: 10.1088/1126-6708/2007/11/070. arXiv: 0709.2092 [hep-ph].

[91] Simone Alioli et al. "A general framework for implementing NLO calculations in shower Monte Carlo programs: the POWHEG BOX". In: *JHEP* 06 (2010), p. 043. DOI: 10.1007/JHEP06(2010)043. arXiv: 1002.2581 [hep-ph].

[92] The NNPDF Collaboration, Richard D. Ball, et al. "Parton distributions for the LHC run II". In: *JHEP* 04 (2015), p. 040. DOI: 10.1007/JHEP04(2015)040. arXiv: 1410.8849 [hep-ph].

[93] ATLAS Collaboration. *Studies on top-quark Monte Carlo modelling for Top2016*. ATL-PHYS-PUB-2016-020. 2016. URL: https://cds.cern.ch/record/2216168.

[94] ATLAS Collaboration. *ATLAS Pythia 8 tunes to 7 TeV data*. ATL-PHYS-PUB-2014-021. 2014. URL: https://cds.cern.ch/record/1966419.

[95] NNPDF Collaboration, Richard D. Ball, et al. "Parton distributions with LHC data". In: *Nucl. Phys. B* 867 (2013), p. 244. DOI: 10.1016/j.nuclphysb.2012.10.003. arXiv: 1207.1303 [hep-ph].

[96] D. J. Lange. "The EvtGen particle decay simulation package". In: *Nucl. Instrum. Meth. A* 462 (2001), p. 152. DOI: 10.1016/S0168-9002(01)00089-4.

[97] M. Beneke et al. "Hadronic top-quark pair production with NNLL threshold resummation". In: *Nucl. Phys. B* 855 (2012), pp. 695–741. DOI: 10.1016/j.nuclphysb.2011.10.021. arXiv: 1109.1536 [hep-ph].

[98] Matteo Cacciari et al. "Top-pair production at hadron colliders with next-to-next-to-leading logarithmic soft-gluon resummation". In: *Phys. Lett. B* 710 (2012), pp. 612–622. DOI: 10.1016/j.physletb.2012.03.013. arXiv: 1111.5869 [hep-ph].

[99] Peter Bärnreuther, Michal Czakon, and Alexander Mitov. "Percent-Level-Precision Physics at the Tevatron: Next-to-Next-to-Leading Order QCD Corrections to $q\bar{q} \to t\bar{t} + X$". In: *Phys. Rev. Lett.* 109 (2012), p. 132001. DOI: 10.1103/PhysRevLett.109.132001. arXiv: 1204.5201 [hep-ph].

[100] Michal Czakon and Alexander Mitov. "NNLO corrections to top-pair production at hadron colliders: the all-fermionic scattering channels". In: *JHEP* 12 (2012), p. 054. DOI: 10.1007/JHEP12(2012)054. arXiv: 1207.0236 [hep-ph].

[101] Michal Czakon and Alexander Mitov. "NNLO corrections to top pair production at hadron colliders: the quark-gluon reaction". In: *JHEP* 01 (2013), p. 080. DOI: 10.1007/JHEP01(2013)080. arXiv: 1210.6832 [hep-ph].

[102] Michal Czakon and Alexander Mitov. "Top++: A program for the calculation of the top-pair cross-section at hadron colliders". In: *Comput. Phys. Commun.* 185 (2014), p. 2930. DOI: 10.1016/j.cpc.2014.06.021. arXiv: 1112.5675 [hep-ph].

[103] Michiel Botje et al. "The PDF4LHC Working Group Interim Recommendations". In: (2011). arXiv: 1101.0538 [hep-ph].

[104] A. D. Martin et al. "Uncertainties on α_S in global PDF analyses and implications for predicted hadronic cross sections". In: *Eur. Phys. J. C* 64 (2009), pp. 653–680. DOI: 10.1140/epjc/s10052-009-1164-2. arXiv: 0905.3531 [hep-ph].

[105] H.-L. Lai et al. "New parton distributions for collider physics". In: *Phys. Rev. D* 82 (2010), p. 074024. DOI: 10.1103/PhysRevD.82.074024. arXiv: 1007.2241 [hep-ph].

[106] J. Gao et al. "CT10 next-to-next-to-leading order global analysis of QCD". In: *Phys. Rev. D* 89 (2014), p. 033009. DOI: 10.1103/PhysRevD.89.033009. arXiv: 1302.6246 [hep-ph].

[107] Emanuele Re. "Single-top Wt-channel production matched with parton showers using the POWHEG method". In: *Eur. Phys. J. C* 71 (2011), p. 1547. DOI: 10.1140/epjc/s10052-011-1547-z. arXiv: 1009.2450 [hep-ph].

[108] Nikolaos Kidonakis. "Two-loop soft anomalous dimensions for single top quark associated production with a W^- or H^-". In: *Phys. Rev. D* 82 (2010), p. 054018. DOI: 10.1103/PhysRevD.82.054018. arXiv: 1005.4451 [hep-ph].

[109] Nikolaos Kidonakis. "Top Quark Production". In: *Proceedings, Helmholtz International Summer School on Physics of Heavy Quarks and Hadrons (HQ 2013)* (JINR, Dubna, Russia, July 15–28, 2013), pp. 139–168. DOI: 10.3204/DESY-PROC-2013-03/Kidonakis. arXiv: 1311.0283 [hep-ph].

[110] Johannes Bellm et al. "Herwig 7.0/Herwig++ 3.0 release note". In: *Eur. Phys. J. C* 76.4 (2016), p. 196. DOI: 10.1140/epjc/s10052-016-4018-8. arXiv: 1512.01178 [hep-ph].

[111] M. Bähr et al. "Herwig++ physics and manual". In: *Eur. Phys. J. C* 58 (2008), p. 639. DOI: 10.1140/epjc/s10052-008-0798-9. arXiv: 0803.0883 [hep-ph].

[112] L. A. Harland-Lang et al. "Parton distributions in the LHC era: MMHT 2014 PDFs". In: *Eur. Phys. J. C* 75.5 (2015), p. 204. DOI: 10.1140/epjc/s10052-015-3397-6. arXiv: 1412.3989 [hep-ph].

[113] Stefan Höche et al. "A Study of QCD Radiation in VBF Higgs Production with Vincia and Pythia". In: *SciPost Phys.* 12 (2022), p. 010. DOI: 10.21468/SciPostPhys.12.1.010. URL: https://scipost.org/10.21468/SciPostPhys.12.1.010.

[114] Federica Fabbri et al. *Studies on the improvement of the matching uncertainty definition in top-quark processes simulated with* `Powheg` *+*`Pythia8`. Tech. rep. Geneva: CERN, 2023. URL: https://cds.cern.ch/record/2867549.

[115] ATLAS Collaboration. *Studies of $t\bar{t}/tW$ interference effects in $b\bar{b}\ell^+\ell^{-\prime}\nu\bar{\nu}'$ final states with* POWHEG *and* MADGRAPH5_AMC@NLO *setups*. ATL-PHYS-PUB-2021-042. 2021. URL: https://cds.cern.ch/record/2792254.

[116] Tomáš Ježo et al. "An NLO+PS generator for $t\bar{t}$ and Wt production and decay including non-resonant and interference effects". In: *Eur. Phys. J. C* 76.12 (2016), p. 691. DOI: 10.1140/epjc/s10052-016-4538-2. arXiv: 1607.04538 [hep-ph].

[117] Tomáš Ježo et al. "New NLOPS predictions for $t\bar{t}+b$-jet production at the LHC". In: *Eur. Phys. J. C* 78.6 (2018), p. 502. DOI: 10.1140/epjc/s10052-018-5956-0. arXiv: 1802.00426 [hep-ph].

[118] Tomáš Ježo and Paolo Nason. "On the Treatment of Resonances in Next-to-Leading Order Calculations Matched to a Parton Shower". In: *JHEP* 12 (2015), p. 065. DOI: 10.1007/JHEP12(2015)065. arXiv: 1509.09071 [hep-ph].

[119] Michal Czakon et al. "Top-pair production at the LHC through NNLO QCD and NLO EW". In: *JHEP* 10 (2017), p. 186. DOI: 10.1007/JHEP10(2017)186. arXiv: 1705.04105 [hep-ph].

[120] Stefano Catani et al. "Top-quark pair production at the LHC: Fully differential QCD predictions at NNLO". In: *JHEP* 07 (2019), p. 100. DOI: 10.1007/JHEP07(2019)100. arXiv: 1906.06535 [hep-ph].

[121] Massimiliano Grazzini, Stefan Kallweit, and Marius Wiesemann. "Fully differential NNLO computations with MATRIX". In: *Eur. Phys. J. C* 78.7 (2018), p. 537. DOI: 10.1140/epjc/s10052-018-5771-7. arXiv: 1711.06631 [hep-ph].

[122] Leonid Serkin. "Treatment of top-quark backgrounds in extreme phase spaces: the "top p_{T} reweighting" and novel data-driven estimations in ATLAS and CMS". In: *13th International Workshop on Top Quark Physics*. May 2021. arXiv: 2105.03977 [hep-ex].

[123] Michele Pinamonti et al. *TTbarNNLOReweighter package*. https://gitlab.cern.ch/pinamont/TTbarNNLOReweighter. 2021.

[124] J. Alwall et al. "The automated computation of tree-level and next-to-leading order differential cross sections, and their matching to parton shower simulations". In: *JHEP* 07 (2014), p. 079. DOI: 10.1007/JHEP07(2014)079. arXiv: 1405.0301 [hep-ph].

[125] Stefano Frixione et al. "Angular correlations of lepton pairs from vector boson and top quark decays in Monte Carlo simulations". In: *JHEP* 04 (2007), p. 081. DOI: 10.1088/1126-6708/2007/04/081. arXiv: hep-ph/0702198.

[126] Pierre Artoisenet et al. "Automatic spin-entangled decays of heavy resonances in Monte Carlo simulations". In: *JHEP* 03 (2013), p. 015. DOI: 10.1007/JHEP03(2013)015. arXiv: 1212.3460 [hep-ph].

[127] D. de Florian et al. "Handbook of LHC Higgs Cross Sections: 4. Deciphering the Nature of the Higgs Sector". In: (2016). DOI: 10.23731/CYRM-2017-002. arXiv: 1610.07922 [hep-ph].

[128] ATLASPMG. *ttV NLO cross section*. 2017. URL: https://twiki.cern.ch/twiki/bin/view/AtlasProtected/CrossSectionNLOttV.

[129] Heribertus B. Hartanto et al. "Higgs boson production in association with top quarks in the POWHEG BOX". In: *Phys. Rev. D* 91.9 (2015), p. 094003. DOI: 10.1103/PhysRevD.91.094003. arXiv: 1501.04498 [hep-ph].

[130] Enrico Bothmann et al. "Event generation with Sherpa 2.2". In: *SciPost Phys.* 7.3 (2019), p. 034. DOI: 10.21468/SciPostPhys.7.3.034. arXiv: 1905.09127 [hep-ph].

[131] Tanju Gleisberg and Stefan Höche. "Comix, a new matrix element generator". In: *JHEP* 12 (2008), p. 039. DOI: 10.1088/1126-6708/2008/12/039. arXiv: 0808.3674 [hep-ph].

[132] Federico Buccioni et al. "OpenLoops 2". In: *Eur. Phys. J. C* 79.10 (2019), p. 866. DOI: 10.1140/epjc/s10052-019-7306-2. arXiv: 1907.13071 [hep-ph].

[133] Fabio Cascioli, Philipp Maierhöfer, and Stefano Pozzorini. "Scattering Amplitudes with Open Loops". In: *Phys. Rev. Lett.* 108 (2012), p. 111601. DOI: 10.1103/PhysRevLett.108.111601. arXiv: 1111.5206 [hep-ph].

[134] Ansgar Denner, Stefan Dittmaier, and Lars Hofer. "COLLIER: A fortran-based complex one-loop library in extended regularizations". In: *Comput. Phys. Commun.* 212 (2017), pp. 220–238. DOI: 10.1016/j.cpc.2016.10.013. arXiv: 1604.06792 [hep-ph].

[135] Steffen Schumann and Frank Krauss. "A parton shower algorithm based on Catani–Seymour dipole factorisation". In: *JHEP* 03 (2008), p. 038. DOI: 10.1088/1126-6708/2008/03/038. arXiv: 0709.1027 [hep-ph].

[136] Stefan Höche et al. "A critical appraisal of NLO+PS matching methods". In: *JHEP* 09 (2012), p. 049. DOI: 10.1007/JHEP09(2012)049. arXiv: 1111.1220 [hep-ph].

[137] Stefan Höche et al. "QCD matrix elements + parton showers. The NLO case". In: *JHEP* 04 (2013), p. 027. DOI: 10.1007/JHEP04(2013)027. arXiv: 1207.5030 [hep-ph].

[138] S. Catani et al. "QCD Matrix Elements + Parton Showers". In: *JHEP* 11 (2001), p. 063. DOI: 10.1088/1126-6708/2001/11/063. arXiv: hep-ph/0109231.

[139] Stefan Höche et al. "QCD matrix elements and truncated showers". In: *JHEP* 05 (2009), p. 053. DOI: 10.1088/1126-6708/2009/05/053. arXiv: 0903.1219 [hep-ph].

[140] Charalampos Anastasiou et al. "High-precision QCD at hadron colliders: Electroweak gauge boson rapidity distributions at next-to-next-to leading order". In: *Phys. Rev. D* 69 (2004), p. 094008. DOI: 10.1103/PhysRevD.69.094008. arXiv: hep-ph/0312266.

[141] ATLAS Collaboration. "Inclusive and differential cross-sections for dilepton $t\bar{t}$ production measured in $\sqrt{s} = 13\,\text{TeV}$ pp collisions with the ATLAS detector". In: *JHEP* 07 (2023), p. 141. DOI: 10.1007/JHEP07(2023)141. arXiv: 2303.15340 [hep-ex].

[142] CMS Collaboration. "Measurements of $t\bar{t}$ differential cross sections in proton–proton collisions at $\sqrt{s} = 13\,\text{TeV}$ using events containing two leptons". In: *JHEP* 02 (2019), p. 149. DOI: 10.1007/JHEP02(2019)149. arXiv: 1811.06625 [hep-ex].

[143] Matteo Cacciari, Gavin P. Salam, and Gregory Soyez. "The Catchment Area of Jets". In: *JHEP* 04 (2008), p. 005. DOI: 10.1088/1126-6708/2008/04/005. arXiv: 0802.1188 [hep-ph].

[144] G. Cowan. *Statistical data analysis*. Oxford University Press, USA, 1998.

[145] William T Eadie et al. *Statistical methods in experimental physics*. Amsterdam: North-Holland, 1971. URL: https://cds.cern.ch/record/100342.

[146] G. D'Agostini. "A Multidimensional unfolding method based on Bayes' theorem". In: *Nucl. Instrum. Meth.* A362 (1995), pp. 487–498. DOI: 10.1016/0168-9002(95)00274-X.

[147] Tim Adye. "Unfolding algorithms and tests using RooUnfold". In: *PHYSTAT 2011*. Geneva: CERN, 2011, pp. 313–318. DOI: 10.5170/CERN-2011-006.313. arXiv: 1105.1160 [physics.data-an].

[148] Tim Adye. *Unfolding algorithms and tests using RooUnfold*. 2011. arXiv: 1105.1160 [physics.data-an].

[149] ATLAS Collaboration. "Electron and photon performance measurements with the ATLAS detector using the 2015–2017 LHC proton–proton collision data". In: *JINST* 14 (2019), P12006. DOI: 10.1088/1748-0221/14/12/P12006. arXiv: 1908.00005 [hep-ex].

[150] ATLAS Collaboration. "Muon reconstruction performance of the ATLAS detector in proton–proton collision data at $\sqrt{s} = 13\,\text{TeV}$". In: *Eur. Phys. J. C* 76 (2016), p. 292. DOI: 10.1140/epjc/s10052-016-4120-y. arXiv: 1603.05598 [hep-ex].

[151] ATLAS Collaboration. "Jet energy scale and resolution measured in proton–proton collisions at $\sqrt{s} = 13\,\text{TeV}$ with the ATLAS detector". In: *Eur. Phys. J. C* 81 (2020), p. 689. DOI: 10.1140/epjc/s10052-021-09402-3. arXiv: 2007.02645 [hep-ex].

[152] *Tagger Recommendations for Release 21*. https://twiki.cern.ch/twiki/bin/viewauth/AtlasProtected/BTagTaggerRecommendationsRelease21. Accessed: 2023-05-06.

[153] ATLAS Collaboration. "ATLAS b-jet identification performance and efficiency measurement with $t\bar{t}$ events in pp collisions at $\sqrt{s} = 13\,\text{TeV}$". In: *Eur. Phys. J. C* 79 (2019), p. 970. DOI: 10.1140/epjc/s10052-019-7450-8. arXiv: 1907.05120 [hep-ex].

[154] ATLAS Collaboration. *Measurement of b-tagging efficiency of c-jets in $t\bar{t}$ events using a likelihood approach with the ATLAS detector*. ATLAS-CONF-2018-001. 2018. URL: https://cds.cern.ch/record/2306649.

[155] ATLAS Collaboration. *Calibration of light-flavour b-jet mistagging rates using ATLAS proton–proton collision data at $\sqrt{s} = 13$ TeV*. ATLAS-CONF-2018-006. 2018. URL: https://cds.cern.ch/record/2314418.

[156] ATLAS Collaboration. *Release 21 MET recommendations*. https://twiki.cern.ch/twiki/bin/view/AtlasProtected/EtmissRecommendationsFullRun2. 2020.

[157] ATLAS Collaboration. *E_T^{miss} performance in the ATLAS detector using 2015–2016 LHC pp collisions*. ATLAS-CONF-2018-023. 2018. URL: https://cds.cern.ch/record/2625233.

[158] ATLAS Collaboration. *Studies on top-quark Monte Carlo modelling with Sherpa and MG5_aMC@NLO*. ATL-PHYS-PUB-2017-007. 2017. URL: https://cds.cern.ch/record/2261938.

[159] ATLAS Collaboration. "Measurement of the top quark mass in the $t\bar{t} \to$ lepton+jets channel from $\sqrt{s} = 8$ TeV ATLAS data and combination with previous results". In: *Eur. Phys. J. C* 79 (2019), p. 290. DOI: 10.1140/epjc/s10052-019-6757-9. arXiv: 1810.01772 [hep-ex].

[160] Jon Butterworth et al. "PDF4LHC recommendations for LHC Run II". In: *J. Phys. G* 43 (2016), p. 023001. DOI: 10.1088/0954-3899/43/2/023001. arXiv: 1510.03865 [hep-ph].

[161] ATLAS Collaboration. *ATLAS simulation of boson plus jets processes in Run 2*. ATL-PHYS-PUB-2017-006. 2017. URL: https://cds.cern.ch/record/2261937.

[162] ATLAS Collaboration. "Luminosity determination in pp collisions at $\sqrt{s} = 13$ TeV using the ATLAS detector at the LHC". In: (2022). arXiv: 2212.09379 [hep-ex].

[163] G. Avoni et al. "The new LUCID-2 detector for luminosity measurement and monitoring in ATLAS". In: *JINST* 13.07 (2018), P07017. DOI: 10.1088/1748-0221/13/07/P07017.

[164] Peter W. Shor. "Polynomial time algorithms for prime factorization and discrete logarithms on a quantum computer". In: *SIAM J. Sci. Statist. Comput.* 26 (1997), p. 1484. DOI: 10.1137/S0097539795293172. arXiv: quant-ph/9508027.

[165] Lov K. Grover. "A Fast quantum mechanical algorithm for database search". In: (May 1996). arXiv: quant-ph/9605043.

[166] Michael A. Nielsen and Isaac L. Chuang. *Quantum Computation and Quantum Information: 10th Anniversary Edition*. Cambridge University Press, 2011. ISBN: 9781107002173.

[167] Qiskit contributors. *Qiskit: An Open-source Framework for Quantum Computing*. 2023. DOI: 10.5281/zenodo.2573505.

[168] DWave. URL: https://www.dwavesys.com/.

[169] Mark W. Lewis and Fred W. Glover. "Quadratic Unconstrained Binary Optimization Problem Preprocessing: Theory and Empirical Analysis". In: *CoRR* abs/1705.09844 (2017). arXiv: 1705.09844. URL: http://arxiv.org/abs/1705.09844.

[170] Tadashi Kadowaki and Hidetoshi Nishimori. "Quantum annealing in the transverse Ising model". In: *Physical Review E* 58.5 (Nov. 1998), pp. 5355–5363. ISSN: 1095-3787. DOI: 10.1103/physreve.58.5355. URL: http://dx.doi.org/10.1103/PhysRevE.58.5355.

[171] He-Liang Huang et al. "Superconducting Quantum Computing: A Review". In: *Science China Information Sciences* 63 (June 2020). DOI: 10.1007/s11432-020-2881-9.

[172] Kyle Cormier, Riccardo Di Sipio, and Peter Wittek. "Unfolding measurement distributions via quantum annealing". In: *JHEP* 11 (2019), p. 128. DOI: 10.1007/JHEP11(2019)128. arXiv: 1908.08519 [physics.data-an].

[173] Daniel O'Malley and Velimir V. Vesselinov. "ToQ.jl: A high-level programming language for D-Wave machines based on Julia". In: *2016 IEEE High Performance Extreme Computing Conference (HPEC)*. 2016, pp. 1–7. DOI: 10.1109/HPEC.2016.7761616.

[174] Mashiyat Zaman, Kotaro Tanahashi, and Shu Tanaka. "PyQUBO: Python Library for QUBO Creation". In: *IEEE Transactions on Computers* (2021).

[175] Gianluca Bianco and Simone Gasperini. *QUnfold*. Version 0.3.0. Mar. 2024. DOI: https://zenodo.org/badge/latestdoi/652649177. URL: https://github.com/JustWhit3/QUnfold.

[176] Charles R. Harris et al. "Array programming with NumPy". In: *Nature* 585.7825 (Sept. 2020), pp. 357–362. DOI: 10.1038/s41586-020-2649-2. URL: https://doi.org/10.1038/s41586-020-2649-2.

[177] Rene Brun and Fons Rademakers. "ROOT - An Object Oriented Data Analysis Framework". In: *Nucl. Inst. & Meth. in Phys. Res. A* 389 (1997). Proceedings AIHENP'96 Workshop, Lausanne, Sep. 1996, pp. 81–86.

[178] Valerio Brugnami. *QUnfold a quantum annealing-based unfolding tool for HEP: a case study on entangled $t\bar{t}$ pair production at the ATLAS experiment*. Bachelor's thesis. Sept. 2024.

[179] J. de Favereau et al. "DELPHES 3, A modular framework for fast simulation of a generic collider experiment". In: *JHEP* 02 (2014), p. 057. DOI: 10.1007/JHEP02(2014)057. arXiv: 1307.6346 [hep-ex].

[180] CAEN. URL: https://www.caen.it/.

[181] A. Polini. "Monitoring and control system of the ATLAS RPCs in view of run-2". In: *Journal of Instrumentation* 9.11 (Nov. 2014), p. C11011. DOI: 10.1088/1748-0221/9/11/C11011. URL: https://dx.doi.org/10.1088/1748-0221/9/11/C11011.

[182] *ATLAS muon spectrometer: Technical Design Report*. Technical design report. ATLAS. Geneva: CERN, 1997. URL: http://cds.cern.ch/record/331068.

[183] G Aielli and E Pastori. "New gas distribution system for the ATLAS RPCs". In: *Journal of Instrumentation* 8.02 (Feb. 2013), P02014–P02014. DOI: 10.1088/1748-0221/8/02/p02014. URL: https://doi.org/10.1088/1748-0221/8/02/p02014.

[184] Bianco Gianluca. *DCSAnalysisTools*. Version 0.4.1. 2022. URL: https://gitlab.cern.ch/gbianco/DCSAnalysis.

[185] Giannini Antonio. *RPCOfflineFW*. 2022. URL: https://gitlab.cern.ch/angianni/rpcofflinefw.